

THE UNIVERSITY OF QUEENSLAND

AUSTRALIA

Progress in Photonic Quantum Information

Sebastian Andres Malewicz
Master of Science, Bachelor of Science



Sebastian Andres Malewicz ORCID

A thesis submitted for the degree of Doctor of Philosophy at
The University of Queensland in 2025

School of Mathematics and Physics

Abstract

The work presented in this thesis focuses on the improvement of quantum information by way of quantum photonics. This is done in three main parts, the first of which is the experimental demonstration of asymmetric quantum interference. This shows the destructive interference of the $|0,2\rangle$ portion of a NOON state. Secondly, the complete overhaul of a quantum dot excitation and collection scheme to be used as an essential tool for further single-photon experiments. This was done by improving the mechanical stability of the system and through including pump frequency filtering. Finally, the implementation of adaptive optics and a machine learning genetic algorithm to assist researchers in single-photon coupling optimization beyond what is achievable by hand.

Declaration by author

This thesis is composed of my original work, and contains no material previously published or written by another person except where due reference has been made in the text. I have clearly stated the contribution by others to jointly-authored works that I have included in my thesis.

I have clearly stated the contribution of others to my thesis as a whole, including statistical assistance, survey design, data analysis, significant technical procedures, professional editorial advice, financial support and any other original research work used or reported in my thesis. The content of my thesis is the result of work I have carried out since the commencement of my higher degree by research candidature and does not include a substantial part of work that has been submitted to qualify for the award of any other degree or diploma in any university or other tertiary institution. I have clearly stated which parts of my thesis, if any, have been submitted to qualify for another award.

I acknowledge that an electronic copy of my thesis must be lodged with the University Library and, subject to the policy and procedures of The University of Queensland, the thesis be made available for research and study in accordance with the Copyright Act 1968 unless a period of embargo has been approved by the Dean of the Graduate School.

I acknowledge that copyright of all material contained in my thesis resides with the copyright holder(s) of that material. Where appropriate I have obtained copyright permission from the copyright holder to reproduce material in this thesis and have sought permission from co-authors for any jointly authored works included in the thesis.

Publications included in this thesis

1. [1] **Sebastian Malewicz**, Dr Marcelo de Almeida, and Prof. Andrew White, Asymmetric Quantum Interference

Submitted manuscripts included in this thesis

No manuscripts submitted for publication.

Other publications during candidature

Conference abstracts

1. [2] **Sebastian Malewicz**, Dr Marcelo de Almeida, and Prof. Andrew White, Tunable Quantum Interference, *EQUS Annual Workshop*, 2023.

2. [3] **Sebastian Malewicz**, Dr Marcelo de Almeida, Dr Markus Rambach, Dr Till Weinhold, and Prof. Andrew White, Bending Mirrors to Collect More Photons, *12th International Conference on Quantum Dots*, 2024.

Contributions by others to the thesis

Professor Andrew White provided support as the primary supervisor with the main contributions to the conception of all experimental endeavors described in this thesis, as well as interpretation of data and editing of all written work.

Dr Marcelo de Almeida provided support as a supervisor in the conception and design of experimental procedures, as well as theoretical calculations and data analysis. Dr de Almeida also contributed to the writing and editing of publications.

Dr Markus Rambach provided support as a supervisor in laboratory technical support and experimental advice. Dr Rambach also provided feedback on all written work produced.

Dr Till Weinhold provided support as a supervisor in experimental advice and career guidance.

Fatemeh Mohit and Abhishek Roy provided support as fellow students in laboratory technical support and data collection.

Statement of parts of the thesis submitted to qualify for the award of another degree

No works submitted towards another degree have been included in this thesis.

Research involving human or animal subjects

No animal or human subjects were involved in this research.

Acknowledgments

I would like to start by acknowledging Professor Andrew White, Dr Marcelo de Almeida, Dr Markus Rambach, and Dr Till Weinhold. These are the gentlemen who make up my incredible supervisory team, and I can't imagine having completed this milestone without them. They have provided an immeasurable amount of support and guidance throughout this journey, and I will be forever grateful. I would also like to thank my fellow students, Fatemeh Mohit, Stefan Zeppetzauer, Abhishek Roy, Emerald Gayden, Jaden McKinlay, William Gunn, Melvee George, and many others for their assistance, company, and friendship. I would also like to thank Angie Bird for always being a great help and willingness to deal with my shenanigans.

Financial support

This research was supported by an Australian Government Research Training Program Scholarship.

This research was supported by a University of Queensland Research Training Stipend.

This research was supported by a University of Queensland Research Training Tuition Fee Offset.

This research was supported by a Research Higher Degree Top Up Scholarship.

I dedicate this work to my loving family. My mother, Virginia, my father, Andrzej, and my brother Raphael. You have always given me the love and support anyone could ever ask for, and then some. And to my high school physics teacher, Mr Grul. I have you to thank for starting me on this incredible journey. You are, without a doubt, the best teacher I have ever had.

Contents

Abstract ii

Contents **ix**

List of Figures **xi**

List of Abbreviations and Symbols **xv**

1 Introduction **1**

2 Foundational Concepts in Quantum Information Processes **3**
2.1 Light and Lasers 3
2.1.1 Electromagnetic Radiation 3
2.1.2 Before the Laser 4
2.1.3 The First Lasers 4
2.1.4 Types of Lasers 5
2.1.5 Lasers in Quantum Optics 8
2.2 Beamsplitter 9
2.3 Polarizing Beamsplitters 11
2.4 Bloch Sphere 13
2.5 Hong-Ou-Mandel Effect 15

3 Photonic Quantum Information **17**
3.1 A Brief History of Quantum Information 17
3.2 Qubits and Gate Operations 18
3.3 Kraus Representation Theorem 21
3.4 Photons as Qubits 22
3.5 Spontaneous Parametric Down Conversion 23
3.6 Quantum Dots 25

4 Asymmetric Quantum Interference **31**
4.1 Two-Photon Interference: Theory 31
4.2 Experimental Data: Quantum Processor 36
4.3 Bulk Optics Experimental Construction 42
4.4 Improving the Bulk Optics Theoretical Model 47
4.4.1 Higher-Order Terms in Down Conversion 48
4.4.2 System Loss and Noise 49

4.4.3 Imperfect Indistinguishability . . . 49
4.4.4 Mode Mismatch . . . 50
4.4.5 Bulk Optics Theoretical Model . . . 51
4.5 Experimental Data: Bulk Optics . . . 56

5 Improving Stability of the Micropillar Quantum Dot Single Photon Source 63
5.1 Basics of the Excitation and Collection Scheme . . . 63
5.1.1 Exciting the Quantum Dot . . . 63
5.1.2 Excitation Arm . . . 65
5.1.3 Collection Arm . . . 65
5.2 Original Excitation and Collection Setup . . . 66
5.3 Optimized Excitation and Collection Setup . . . 66
5.3.1 Excitation Laser for Quantum Dot . . . 67
5.3.2 Pulse Shaping . . . 69
5.3.3 Optimized Excitation Arm . . . 72
5.3.4 Quantum Dot Setup and Filtering . . . 72
5.3.5 Optimized Collection Arm . . . 75
5.3.6 Four Photon Demultiplexing . . . 79
5.4 Future Project: Heralded Entanglement . . . 81

6 Adaptive Optics and Machine Learning 83
6.1 Deformable Mirror . . . 83
6.2 Genetic Algorithm . . . 85

7 Conclusion 91

Bibliography 93

A Maxwell's Equations 109
A.1 Maxwell's Equations . . . 109

B Heralded Entanglement: Full Calculations 111
B.1 Notation and Optical Elements . . . 111
B.2 Event-Ready Pair Generation . . . 111
B.2.1 Sector I: At least one vacuum mode . . . 112
B.2.2 Sector II: One photon in each path . . . 113
B.3 Click Patterns Leading to Entanglement . . . 113

C Jupyter Notebook: Asymmetric Quantum Interference Modeling and Fitting 115

List of Figures

2.1 Energy level diagram of Cr^{3+} in corundum showing the relevant energy transitions to emit a pair of photons, R_1 and R_2. . . . 5
2.2 Conceptual diagram of the active mode-locking optical cavity. . . . 8
2.3 Visual description of a plate beamsplitter with an incident beam. . . . 9
2.4 Visual depiction of a cube beamsplitter. . . . 10
2.5 Visual depiction of the evanescent coupling that occurs in fiber beamsplitters. . . . 10
2.6 Probability distribution on one output mode of a 50:50 beamsplitter with N=19 photons in one input mode and either none or one in the other input mode. . . . 11
2.7 Glan-Thompson polarizer. . . . 12
2.8 Glan-Taylor prism polarizer. . . . 13
2.9 Calcite beam displacer 14
2.10 Bloch Sphere representation of a qubit. . . . 15
2.11 Visualization of the single qubit transformation from any point on the Bloch Sphere to any other point on the Bloch Sphere. . . . 16

3.1 Diagram of a spontaneous parametric downconversion source. . . . 23
3.2 Crossectional view of the downconverted light emitted by a SPDC type 1 source. . . . 24
3.3 Diagram of a type 2 SPDC source. . . . 25
3.4 Schematic of the in-situ setup used for locating and etching patterns around quantum dots. 27

4.1 Output probability of ideal asymmetric quantum interference. . . . 35
4.2 Functional diagram of 12-mode photonic processor produced by QuiX. . . . 37
4.3 Diagram of full quantum processor with inset. The values displayed for the beamsplitters are placeholders. . . . 38
4.4 Diagram of a subsection of the quantum processor and the setting used to conduct asymmetric quantum interference. . . . 39
4.5 Probability distribution of asymmetric quantum interference using Quandela's quantum processor unit. . . . 39
4.6 Probability distribution of asymmetric quantum interference using Quandela's quantum processor unit with various attenuation. . . . 40
4.7 Conceptual experimental diagram for asymmetric two-photon interference. . . . 43
4.8 Experimental setup for measuring the HOM of the first and second beamsplitter. . . . 44
4.9 Experimental construction of the variable beamsplitter and the variable attenuator. . . . 44
4.10 Pseudo-number-resolving photon detection. . . . 45
4.11 Full experimental diagram for asymmetric two-photon interference in a single mode. . . . 47

4.12 Probability distribution of the $|1,1\rangle$, $|0,2\rangle$, and $|2,0\rangle$ states using a bulk optics experimental setup with $\gamma = 0.933$. Error bars confined within points. 47
4.13 Diagram of mode mismatch calculation. (Left) Prior to the interaction on the variable beamsplitter or reflectivity "R", a portion of the light from one mode is picked off by the "mode mismatch beamsplitter" (MMBS). This portion of picked-off light is sent through the variable beamsplitter as well, but without interacting with other modes. (Right) This is modeled by sending the picked-off portion to a separate pair of modes that mimic the remainder of the original circuit. 50
4.14 Theoretical probability distribution of the state with the production of higher-order terms from the SPDC source. 54
4.15 The output state probability distribution as a function of variable beamsplitter reflectivity with decoherence and higher-order terms. 55
4.16 The output state probability distribution as a function of variable beamsplitter reflectivity with decoherence, higher-order terms, and imperfect indistinguishability. 56
4.17 HOM1 and HOM2 for experimental data. 58
4.18 Calibration curves for the variable beamsplitter HWP, and the loss HWP determining the attenuation to Mode 1. The transmission into one output mode was measured as a function of HWP from the optical axis (degrees). The respective optical axes were determined by maximal transmission. Error bars confined within points. 59
4.19 Experimental data collected of asymmetric quantum interference using bulk optics. . . . 60
4.20 Probability distribution surface plots of the $|1,1\rangle$, $|0,2\rangle$, and $|2,0\rangle$ states. 61
4.21 Probability distribution contour plots of the $|1,1\rangle$, $|0,2\rangle$, and $|2,0\rangle$ states. 61
4.22 Optimal output state probability distribution of the bulk optics experiment. The optimal output state is defined by the $P_{11} = P_{20}$ coinciding with the minimum of P_{02}. The parameters used in this calculation are identical to those used in the fitting of the bulk optics experimental data (see Figure 4.19). In this case, the attenuation value differs and is calculated to be $\gamma \approx 0.5123$, which gives the optimal point a variable beamsplitter reflectivity of $R = 0.8025$. 62

5.1 Resonant excitation pump scheme 64
5.2 Quantum dot and surrounding structure. 65
5.3 Diagram of original collection and excitation setup 66
5.4 Faraday Isolator. 68
5.5 Pump laser preparation. 69
5.6 Conceptual visual representation of a 4F pulse shaper. 70
5.7 Diagram to show the basic concept of what a 4f pulse shaper achieves. 70
5.8 Spectrum of the pump laser before the 4F filter and after the 4F filter. 71
5.9 Excitation arm. 73
5.10 Pump laser light reflected from diode. 73
5.11 Filtering of the reflected excitation light. 74
5.12 Diagram of collection arm when imaging the sample and when measuring single-photon output. 75
5.13 Diagram of full excitation, filtering, and collection system of the quantum dot. 76
5.14 Photograph of quantum dot excitation and collection 77
5.15 Second order correlation measurement. 78
5.16 Diagram of demultiplexer. 80

5.17 Scheme for creating event-ready heralded entanglement. Adapted from [4, 5]. 81

6.1 3D rendering of deformable mirror. 84
6.2 Depiction of how the movement of one actuator affects the surface of the deformable mirror and the reflection of incident light. 84
6.3 A smaller incidence angle of the laser with respect to the normal of the deformable mirror (DM) reduces the amount of clipping the laser has a large beam diameter. 85
6.4 Layout of the actuators in the deformable mirror. 86
6.5 Flow chart of the genetic algorithm. 87
6.6 Experimental data of count rates measured during the execution of the genetic algorithm on three separate runs. 89
6.7 Topological depiction of the final orientation of the deformable mirror at the end of the experimental runs. 90

B.1 Scheme for creating event ready heralded entanglement. Adapted from [4]. 112

List of Abbreviations and Symbols

Abbreviations	
QD	Quantum Dot
BS	Beam Splitter
PBS	Polarizing Beam Splitter
NA	Numerical Aperture
QWP	Quarter Waveplate
HWP	Half Waveplate
LP	Linear Polarizer
LHP	Left Hand Polarized
RHP	Right Hand Polarized
EOM	Electro-Optic Modulator
etc.	*etc.*

Symbols	
$\hat{\rho}$	Density operator
etc.	*etc.*

Chapter 1

Introduction

The aim of this thesis is to progress the field of quantum photonics, with particular regard to applications in quantum information.

This thesis is written in a manner that assumes the reader has some basic understanding of physics as well as an understanding of quantum physics at the undergraduate level. Chapters 2 and 3 are meant as a review of the relevant topics in physics and a brief introduction into the world of quantum information and photonics, respectively. These will be followed by three chapters that discuss the experimental contributions to the field conducted over the course of the candidature.

Chapter 4 is a full explanation of asymmetric quantum interference: an experimental realization of a theoretical proof presented by [6]. The experiment uses a simple set of optical components paired with a spontaneous parametric down conversion source to create tunable destructive interference. This chapter includes a full description of the experimental setup as well as an in-depth description of the theoretical model behind it. The model in this case had to be updated from the original ideal conditions to account for noise and other experimental variables. In addition to the data collected from the bulk optics experiment, data was also collected from Quandela's fully integrated quantum dot and programmable photonic chip.

Over the course of the past four years, the quantum dot experiment was completely rebuilt due to a relocation of the lab [1]. Chapter 5 describes how this was accomplished, as well as the modifications made to the system. The discussion centers around three main parts: First, how the quantum dot is excited, which includes the frequency tuning of the excitation laser and the alignment of the beam. Second, the filtering of the excitation laser reflected by the quantum dot from the single photons. And lastly, the collection of the single photons and their preparation for use in future applications.

The final chapter expands on work that was first started as a part of a masters research project [7]. Single-photon collection efficiency is a key component of system brightness in single-photon sources. This project aims to improve that by implementing adaptive optics with a machine learning algorithm. This method is implemented with the intention of correcting for any misalignment to the system, as well as compensating for beam mode aberrations. While it is not meant to replace the need for manual

[1] My supervisor's repeated muttered asides on "never, ever move a working lab, even if the old one is knee-deep in manure and the new one is gold plated" begin to make sense.

alignment, it is meant to improve upon it with a smaller time investment.

For those less familiar with the subject of quantum mechanics and quantum information, it is suggested that this thesis be read in its entirety. For those with a greater, or expert level understanding, Chapters 2 and 3 can be used as a brief reference or otherwise disregarded.

Chapter 2

Foundational Concepts in Quantum Information Processes

This chapter covers the concepts that I consider to be some of the foundations of Quantum Information. It may serve as a basic review for experts in the field, but I also believe it is necessary to explain these topics to those who are unfamiliar with this field of study. This chapter aims to bring readers up to speed so that they can better understand the more complex experimental implementations discussed in later chapters.

2.1 Light and Lasers

The carriers of electromagnetic radiation are single particles called photons. The subject of photons will be discussed more in-depth later in this work, but for now, the important information for this section is that photons are not only particles but waves as well. Furthermore, photons have wavelengths. Light usually refers to the range of wavelengths the human eye can see, when the electromagnetic wavelength spectrum is much broader. The full list of electromagnetic waves from longest to shortest is Radiowaves, Microwaves, Infrared, Visible, Ultraviolet, X-ray, and Gamma Ray. At the two ends of the spectrum, Radiowaves have wavelengths from a few millimeters to hundreds of kilometers, and Gamma Rays have wavelengths on the order 10^{-12} meters. As you can see, this range of wavelengths is quite large, and visible light only accounts for a tiny section of this range, about 400 to 700 nanometers

In this thesis, the majority of the experimental work is done using near-infrared light, defined as 780 nm to 1 μm—this is just outside the range of visible light.

2.1.1 Electromagnetic Radiation

Light sources used in technology are typically engineered to be spatially and temporally coherent, with low noise: the opposite of everyday light sources, which are typically broadband in frequency, suffering low coherence, and are noisy. Consider a laser, whose name is an acronym from ”Light Amplification by Stimulated Emission of Radiation”. When one thinks of a laser beam, one usually associates two particular qualities with it. First, a single beam maintains a relatively consistent cross-sectional diameter. Second, it has well-defined temporal and frequency behaviour. These qualities are due to the coherence of the laser: over some time and length scales, there is a fixed phase relationship between

the electric field values at different times or locations. When light is spatially coherent, it is able to be focused in a small spot, hence the consistent cross-sectional beam diameter. When it is temporally coherent, the frequency properties of the beam are well-defined, be it narrowband for a continuous laser or broadband for a pulsed laser.

2.1.2 Before the Laser

The first notion of creating a laser was first brought up by Einstein [8], although he did not know it at the time. Instead, Einstein discussed the fundamental concepts that were later used to create the first laser. Einstein based his work on the work that Planck did a few years prior [9], where he described that atoms could absorb and release chunks of energy spontaneously. Einstein used this to describe the photoelectric effect. In addition, Einstein later theorized that atoms could release excess energy as light when stimulated by incident light, which is known as stimulated emission [10]. Following this, in 1928, a fellow German scientist, Ladenburg, was able to experimentally measure stimulated emission via negative dispersion. It was not until 1947 that Lamb and Rutherford were able to create the first demonstration of stimulated emission in the microwave regime by using hydrogen atoms.

At this point, the construction of the first laser was close. But first came its predecessor, the maser. The theory for the maser was first presented by Joseph Weber in 1951, by suggesting that one could use stimulated emission to make a microwave amplifier. This was then physically realized in 1953 when Townes, Gordon, and Zeiger created the first one. Simultaneously, Soviet scientists Basov and Prokhorov were working on a quantum oscillator that released a continuous output of stimulated emission. They later suggested that optical pumping should be used to produce the population inversion needed in the quantum system. This was a significant step in laser physics, as many modern lasers still use optical pumping to achieve emission.

In 1957, two significant groups started pushing towards making masers in the optical range. One was Jun-ichi Nishizawa [11], and the other was the pair of Townes and Schawlow. Townes met with Gordon Gould and noted that an optical maser could be made using an open resonator. Gould is also credited with developing the term “Laser”.

2.1.3 The First Lasers

The first laser ever built came in 1960 when Theodore Maiman demonstrated stimulated emission in a ruby coated in silver [12]. More technically, the material used is chromium in corundum. A light at 550 *nm* was used to irradiate the material. At this point, the chromium ions are brought to the $4F^2$ state and then quickly lose some of their energy as they decay to $2E$ state through non-radiative transitions. Then, spontaneous emission takes effect and the ions emit a pair of photons at 694.3 *nm* and 692.9 *nm* (R_1 and R_2 in Figure 2.1).

Later in that same year, Javan, Bennett Jr., and Herriott developed the first-ever gas laser. This was significant as it was a continuous laser as opposed to the pulsed design of Maiman’s ruby laser. They showed that applying a voltage across of tube of helium atoms could excite them to a long-lived state. This state was very close in energy to an excited state of neon. So, combining the two gases in a tube allowed excited helium atoms to transfer their energy to neon atoms via collisions. This created the

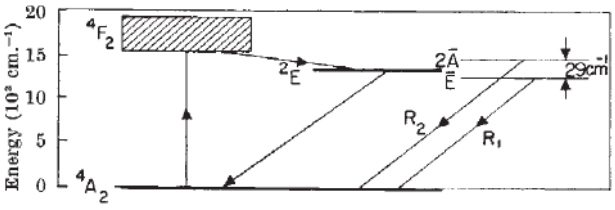


Figure 2.1: Energy level diagram of Cr^{3+} in corundum showing the relevant energy transitions to emit a pair of photons, R_1 and R_2 [12].

necessary population inversion of neon atoms [13]. This theory was put into practice by using a quartz tube filled with 10 parts helium for every 1 part of neon. The tube had two reflectors placed at each end to create an optical cavity. The strongest emission line occurred at 1153 *nm* [14]. Another laser of this form was developed in 1964 that instead used carbon dioxide (CO_2), instead of helium, with nitrogen. This provided two new things to the area of lasers. First, it was producing photons of much longer wavelengths in the infrared ($\approx 10\ \mu m$). Secondly, it was producing an output of a much higher power ($\approx 10\ W$) [15].

2.1.4 Types of Lasers

Gas lasers are one of the many different types of lasers, so let us discuss the full range of lasers that are out there. Chemical lasers are lasers that achieve population inversion by way of chemical reaction. The idea of doing such a thing was first proposed by Polanyi in 1961 [16]. The first version of this laser was physically realized in 1965 by using hydrogen-chloride as the basis for the chemical reaction [17]. The chemical reaction via vibrational excitation is as follows.

$$H + Cl_2 \rightarrow HCl^{\ddagger} + Cl \tag{2.1}$$

This laser was created using a Raman-type multiple-reflection cell containing a flash photolysis tube or a quartz laser tube fitted with normally polished sodium chloride discs oriented at the Brewster angle. Everything was placed in an optical cavity made of two large gold mirrors with a third disc that deflected some of the light out of the cavity. The output of this laser was pulsed and capable of producing 10 W. The continuous wave (CW) chemical laser was later demonstrated in 1969 using hydrogen fluoride [18]. The chemical process being

$$H_2 + F \rightarrow HF^{\ddagger} + H. \tag{2.2}$$

This laser was able to produce a continuous output in the region of 3 μm at approximately 1 W. The technique used here was similar to previous laser systems in that it used an optical cavity. However, it differed by injecting a diluted supersonic jet of fluorine atoms into an atmosphere of ambient hydrogen atoms. Chemical lasers later included the use of other chemical interactions, chemical oxygen iodine laser (COIL), all gas-phase iodine laser (AGIL), and deuterium fluoride (DL) lasers, to name a few.

The next on the list is a Dye laser. First independently realised by Sorokin [19] and Schäfer [20] in 1966, and as the name suggests, the Dye laser is a laser that uses dye as its gain medium. Most of these

dyes are composed of organic molecules in liquid form. This is not the case for all dye lasers, as some do exist with solid or vapor dyes. The solution is placed in a mirror cavity pumped with a flashtube or another laser to pump the liquid beyond the lasing threshold. The light bounces off the mirrors of the cavity and through the dye solution, and the output is amplified with each pass. The benefit of using a liquid as the medium is that it can take any shape. This allows for a range of optical cavities to be used in dye lasers.

A solid-state laser uses a solid gain medium. Starting to notice a pattern? Usually, these solids come in the form of a type of glass or crystal doped with rare-earth or transition metal ions. Looking back, one might now realize that the first laser ever built was a solid-state laser, as the gain medium was ruby. However, since then, other mediums have been used as they come with superior performance. Solid-state lasers are usually pumped by flashtubes or arc lamps, which are relatively cheap and provide a high power source, but are very power inefficient and produce a lot of heat. The modern solution to this is to use diode lasers to pump the solid-state gain medium. The advantage of this is that it is a more compact design and lasts a lot longer.

One of the nice features of solid-state lasers is that the transitions of the doped crystals are weakly allowed transitions, meaning that they have long upper-state lifetimes. This comes in handy for pulse generation. The crystal can easily store an amount of energy. When this energy is released, it is done in a nanosecond pulse. This leads to a very brief, but large spike in power output. When a laser is maintained in a mode-locked operation, it can achieve ultrashort pulse duration (picoseconds or femtoseconds).

There have been several different mediums used for solid-state lasers. Neodymium-doped yttrium aluminum garnet lasers (Nd:YAG or YAG) are pumped with a small diode laser. These lasers can produce output powers on the order of milliwatts to watts. Neodymium is also often paired with yttrium orthovanadate and yttrium lithium fluoride, all providing different peak pulse powers at different rates.

The fiber laser is a form of solid-state laser, but the gain medium is in the form of an optical fiber. An optical fiber is a very common tool used in optics, and it is used to guide light. It works by creating a long cable of two optically transmissive materials, one used for the core and one surrounding the core. The material used for the core has a higher index of refraction compared to the material surrounding it. That way, when light is coupled into the core, it experiences total internal reflection when it meets the outer surface of the core. Thus, it is contained within the core, only leaving when it reaches the other end of the cable. In the case of a fiber laser, replace the core of the fiber with a gain medium. This has a few advantages, mainly long gain regions for the pump light to interact with the gain medium and better cooling as the fiber has a large surface area to volume ratio, allowing for more efficient cooling.

For the sake of relevance to the work done in this thesis, it is beneficial to expand on the discussion of pulsed lasers. As mentioned previously, pulsed lasers differ from continuous wave lasers in that they are not constantly producing an output. Instead, the output of a pulsed laser rapidly switches on and off. This usually occurs on the time scale of nanoseconds to femtoseconds. Making a laser pulse can be achieved in a few different ways, first, by Q-switching, which is a method that implements an attenuator within the optical cavity. When the attenuator is turned on, it removes light from the cavity and reduces the cavity's q-factor (quality factor). This prevents feedback in the system and allows for population inversion to occur. However, because there is no feedback, there is no lasing. Once the

gain medium is saturated, the attenuator will turn off, allowing for feedback to occur, creating a higher q-factor in the optical resonator, and optical amplification begins. The energy in the system builds up quickly and is released quickly, causing a short burst of high-intensity light. This process repeats as the attenuator is rapidly switched on and off. Q-switched pulses are typically in the nanosecond regime.

A second, conceptually simple method to pump a pulsed laser is with a source that is itself pulsed. This usually comes in the form of some electrically driven light pulse, like the previously mentioned flashtube. These are devices that use capacitors to store electrical energy and release it quickly in the form of an intense flash of light. This light can then be used to produce the population inversion in a gain medium via the photoelectric effect.

The last method, and the most prevalent in this thesis, is mode-locking. Like most lasers, mode-locked lasers also contain an optical cavity. The light bounces back and forth within the cavity, and as light waves moving in one direction interact with those moving in the other direction, it creates a standing wave. This forms a set of discrete frequencies known as longitudinal modes. The processes that are important in a mode-locking laser are as follows [21].

1. Gain is required in mode-locking lasers just as it is required in all lasers. Gain saturation can occur in lasers, which is when the gain decreases with increasing laser power. In single-mode lasers, gain is sensitive to average laser power. In most mode-locked lasers, the gain saturates dynamically on the timescale of the pulse duration.

2. Linear loss, which is present in any laser, is the portion of light loss independent of the laser power.

3. Bandwidth limitations can occur in several ways. One is the finite bandwidth of the gain medium used in the laser. Others can come from passive filtering of frequency-dependent loss elements. These limits on the bandwidth also limit how short a pulse can be, which is undesirable.

4. Dispersion refers to passive, frequency-dependent phase variations in the pulse as it travels through the laser cavity. This usually leads to the broadening of the pulse, which can be detrimental to ultrafast laser pulses.

5. Active modulation is when an externally driven optical modulator is used to modulate either the amplitude or the phase of the pulse. The frequency of this modulator is typically synchronized to the frequency of a round trip around the optical cavity.

6. Saturable loss. The optical cavity loss may be dependent on the pulse intensity of the pulse energy. This loss changes dynamically in response to the pulse. The pulse itself is modulated by the dynamic changes in the loss. This becomes a self-induced modulation with a period that is equal to the cavity round-trip time.

7. Self-phase modulation occurs because the phase can vary nonlinearly with time-dependent pulse intensity and also occurs at the pulse round-trip time. This nonlinear phase shift usually has a very rapid response time, and so it only really depends on the instantaneous laser intensity, but this is not the case for all lasers.

There are two types of mode-locked lasers: active and passive. In the case of active mode-locking, it is one of the simplest and was one of the first techniques demonstrated. The modulator is driven at a

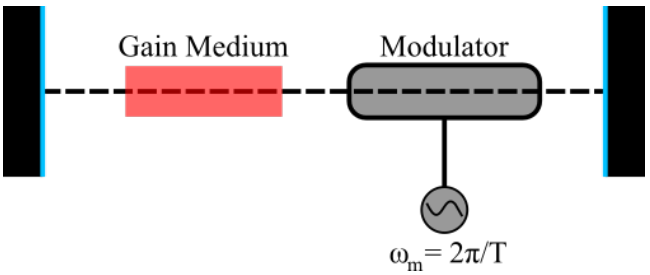


Figure 2.2: Conceptual diagram of the active mode-locking optical cavity [21].

frequency $\omega_m = 2\pi/T$, where T is the round-trip time of light in the optical cavity. The modulator acts like a periodic shutter that opens once per pulse round-trip. This causes the pulse to be shortened every time it passes through the shutter. However, this shortening of the pulse means that the modulator is introducing active loss to the system. Short laser emission pulses would ideally occur when the shutter is fully open to counteract this. However, in practice, it is often very difficult to exactly match the frequency of the modulator with the frequency of the optical cavity. Fortunately, the system allows for a degree of tolerance for this parameter, and it is typically 1 part in every 100,000. This means, for example, that for a 10MHz laser cavity, the modulator must operate in a tolerance of $\pm 1\ kHz$. This also assumes that the dimensions of the optical cavity remain stable. In the case that the modulator frequency does not match that of the optical cavity. This offset of modulator transmission during the pulse will slightly push the pulse toward the transmission peak of the modulator, creating a timing restoring mechanism. If this timing restoration is enough to fully compensate for the difference in modulation and cavity frequencies, then a stable mode lock is achieved.

2.1.5 Lasers in Quantum Optics

The laser is the central tool in almost every quantum optics experiment. This subsection will go through some of the ways that lasers are used in quantum experiments. Keep in mind that the list of examples given is not exhaustive, but instead some of the more common uses.

Starting with the use most prevalent in this body of work, pumping. Optical pumping is the process of using a laser to create a population inversion of the atoms in a given material. In other words, light is used to raise the energy level of an atom or molecule. It is important to note that optical pumping with respect to quantum optics usually refers to single-photon or photon pair emitters (eg. quantum dots and SPDC sources, see chapter3.5 and 3.6). In the case of a quantum dot, which can be described as a two-level artificial atom (ground state and excited state), the laser is focused down onto the quantum dot. Once the electron absorbs one of the incident photons, it populates the excited state before falling back down and emitting a photon of a very specific quality in the process. The laser required to make this happen is a pulsed laser (pulses are typically in the picosecond to femtosecond range). This is because these single-photon systems have a relaxation time, and it is usually favorable to regulate the single-photon production rate. In the case of the SPDC source, the demand from the laser can vary with respect to being pulsed or continuous wave, power, wavelength, etc. Typically, high beam quality, narrow linewidth, and short wavelengths are required for quality photon pair production.

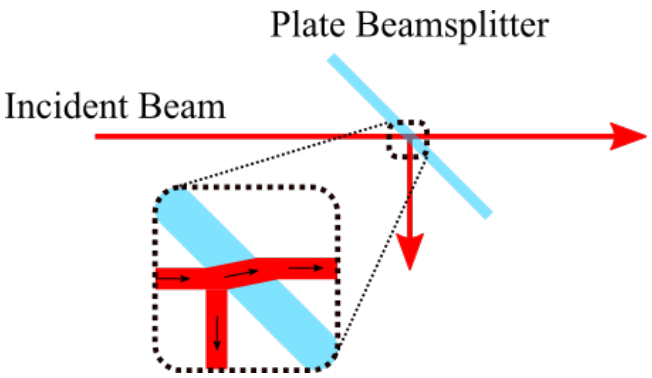


Figure 2.3: Visual description of a plate beamsplitter with an incident beam. The plate separates the beam into two distinct paths. Notice the small displacement as the beam passes through the material of the plate.

2.2 Beamsplitter

There is a running joke in quantum optics, or at least in this group, that a new paper on the beamsplitter comes out every five years. Well, I guess it was our turn this time. Before discussing the exact experiment that was performed in a later chapter, it might be useful to understand the basics of a beamsplitter first.

Beamsplitters typically rely on either tunneling or interference. Consider a plate beamsplitter, which is a partially reflective mirror, where the reflectivity can be provided by a thin layer of metal—tunneling—or by a dielectric stack—interference. In either case, if it is oriented at 45° to the incident beam[1], part of the power will be reflected at 90°, while the remaining power passes through the plate. The transmitted beam experiences a small deflection as the material used in the plate usually has a greater index of refraction compared to the air or vacuum around it. The reflection-to-transmission ratio of the plate can be changed by either varying the metallic film thickness or by varying the parameters of the dielectric coating stack.

There is a tradeoff between these choices: thin metallic films tend to absorb more of the light than dielectric stacks, but are very broadband in response; dielectric stacks typically are much less absorptive, but being based on interference, are necessarily less broadband than a metallic film.

Additionally, plate beamsplitters are polarization dependent to a degree. The orientation of the linearly polarized beam will determine how much of that light is reflected or transmitted. These two properties can be useful when separating light of different wavelengths or polarizations.

A practical issue with plate beamsplitters is that the reflective surface is exposed and physically vulnerable. In a cube beamsplitter, the reflective surface is protected by enclosing it in glass, see Figure 2.4. The cube is comprised of two identical triangular prisms that sandwich the reflective layer; they are cemented together by a transparent adhesive (resin, cement, epoxy). The entry and exit surfaces of the cubes can be coated with a thin layer of a small stack of dielectric material to provide an anti-reflection coating. This cube is comprised of two identical triangular prisms that are glued together by a transparent adhesive (resin, cement, epoxy).

[1]This is usually the most convenient angle of incidence on a plate beamsplitter, but they can also be designed to work with any angle of incidence.

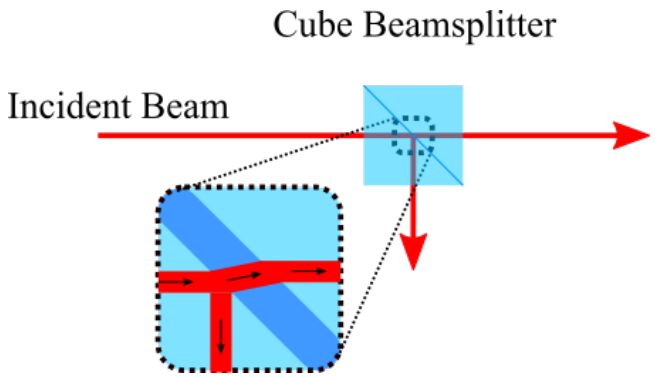


Figure 2.4: Visual depiction of a cube beamsplitter. The cube is constructed of two rectangular prisms that are adhered together by a thin film of adhesive (dark blue), which also acts as the splitting interface.

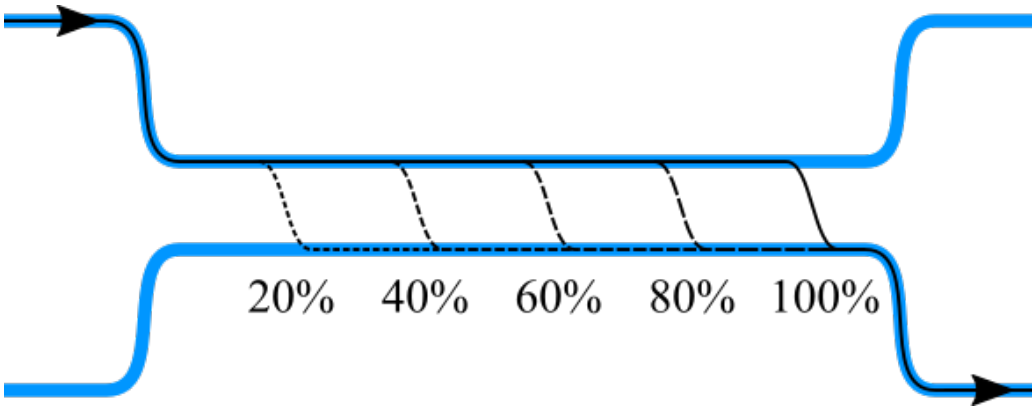


Figure 2.5: Visual depiction of he evanescent coupling that occurs in fiber beamsplitters. The cores of two parallel single-mode fibers are brought close together, allowing for light to "leak" from the mode of one fiber to the other. The longer the segment of interaction, the more light couples into the second mode. This interaction segment can be manufactured to a length that provides the desired splitting ratio of the beamsplitter.

Another fairly common version of the beamsplitter is the fiber beamsplitter. These are created by taking two single-mode fibers and placing their cores parallel to each other and close together. This allows for evanescent wave coupling between the two fibers, which can transfer light from one core to the other. The amount that is transferred is controlled by changing the length of the section of fiber in which the cores are close together (see figure 2.5).

The beamsplitter in its many forms has become quite a useful tool in the study of experimental quantum optics. Perhaps none are as famous as the Hong-Ou-Mandel effect [22], which is discussed in detail in chapter 2.5. However, the beamsplitter has contributed to other significant advancements. In 2002, it was suggested [23] and later mathematically proven [24] that quantum entanglement is possible to achieve with a single beamsplitter in the case that the input states are non-classical. Furthermore, what is interesting is that maximal entanglement did not occur when the splitting ratio of the beamsplitter is 50:50.

After his work on developing the Hong-Ou-Mandel effect, Ou went on to explore the characteristics of multiple photons interacting on a beamsplitter [25]. The specific interaction that he explored was having a group of photons in one input mode of the beamsplitter, and none in the other ($|N,0\rangle, N>1$), and comparing the output probabilities when a single photon is added to the other mode ($|N,1\rangle, N>1$).

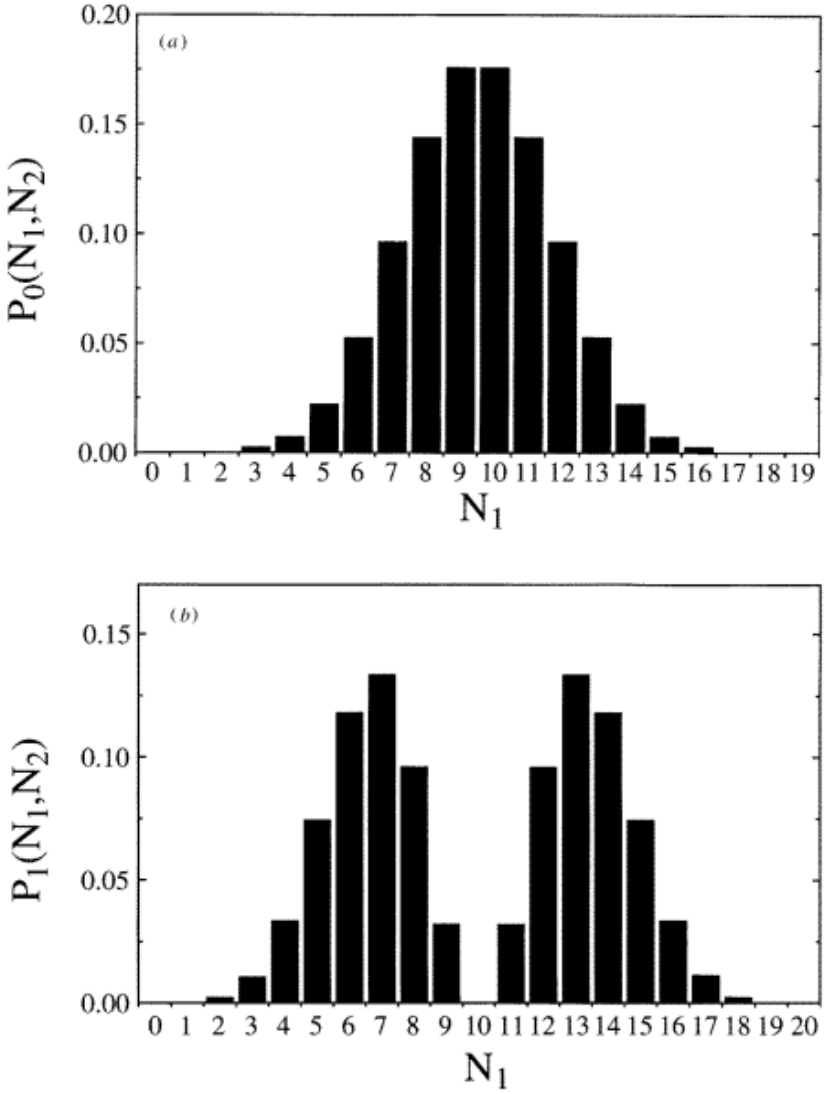


Figure 2.6: Probability distribution on one output mode of a 50:50 beamsplitter with N=19 photons in one input mode and either none (top) or one (bottom) in the other input mode [25].

The result showed that even with a weak non-classical field, the result was very non-classical, as can be seen in figure 2.6.

2.3 Polarizing Beamsplitters

Beamsplitters often come in two forms, polarizing and non-polarizing. The non-polarizing cubes require a bit of refinement to the design. This is because the incident beam hits the interface surface at a large angle (typically around 45°), and reflections at high angles typically introduce some amount of polarizing effects. These polarization effects can be minimized with a multi-layer coating on the interference surface. An important characteristic to remember about these cubes is that they are not polarization-maintaining. The polarizing beamsplitter will separate incident light into two separate beams of light of different linear polarizations. When light hits the surface of the beamsplitter at an angle, the p-polarized light is transmitted, and the s-polarized light is reflected [2]. Polarizing beamsplit-

[2]light that oscillates perpendicular to the plane of incidence is s-polarized, while light that oscillates parallel to the plane of incidence is p-polarized.

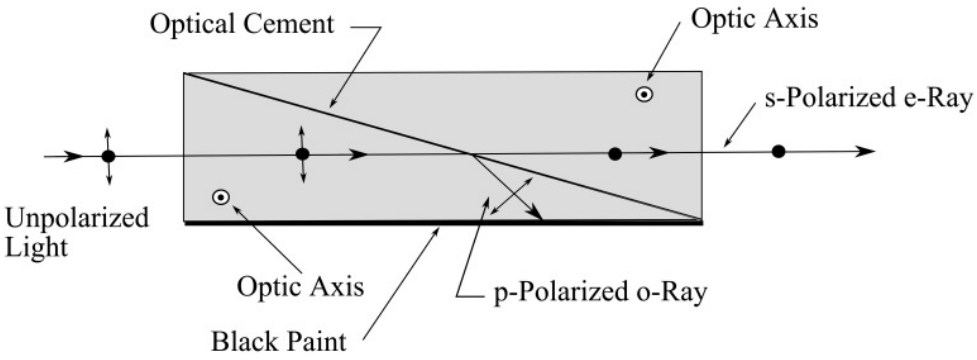


Figure 2.7: Glan-Thompson polarizer. The side of the prism is often painted black to optically absorb the p-polarized light [27].

ters make use of dielectric coating on the interaction surface to separate the s and p polarizations of light [26]. This has many uses, especially when it comes to filtering light, as can be seen in chapter 5.3.4.

Anisotropic materials can also be used to separate light based on polarization. The Glan-Thompson, Glan-Taylor, and beam-displacing polarizing prism are all optical elements constructed out of calcite[3]. The Glan-Thompson uses two calcite prisms adhered together with optical cement, and the optical axis of each prism is perpendicular to the plane of reflection. At the surface between the prism and optical cement, total internal reflection occurs, separating the s-polarized and p-polarized light (see Figure 2.7).

Similar to the Glan-Thompson, the Glan-Taylor is the joining of two calcite prisms. However, in the Glan-Taylor, the two prisms are separated by air and have optical axes parallel to the plane of reflection. Again, at the plane of reflection, total internal reflection separates the s-polarized and p-polarized light (see Figure 2.8).

A calcite crystal, if cleaved in the proper way, can also separate a beam of light by polarization. If one considers the rhombus crystalline structure of the calcite crystal with corner angles $\alpha = 78.08^\circ$ and $\beta = 101.92^\circ$, then the optical axis is defined by equally trisecting the β, β, β oblique corner (see Figure 2.9). When a beam of light enters the prism, the s-polarized o-ray vibrates perpendicular to the principal section and remains undisplaced. The p-polarized e-ray vibrates in the principal section and is displaced [4]. When the two exit beams exit the prism, they are both completely linearly polarized and orthogonal to each other [27]. The total beam displacement of the e-ray, or the spatial separation between the two rays, is dependent on the length of the crystal. The longer the crystal is, the more the e-ray is displaced.

[3]Calcite is a naturally occurring trigonal crystalline form of calcium carbonate ($CaCo_3$).

[4]Ordinary rays (o-rays) and extraordinary rays (e-rays) are ways of defining how light behaves in birefringent materials (calcite as an example). In these materials, o-rays follow Snell's Law and experience a constant refractive index, while e-rays do not follow Snell's Law and experience a direction-dependent refractive index.

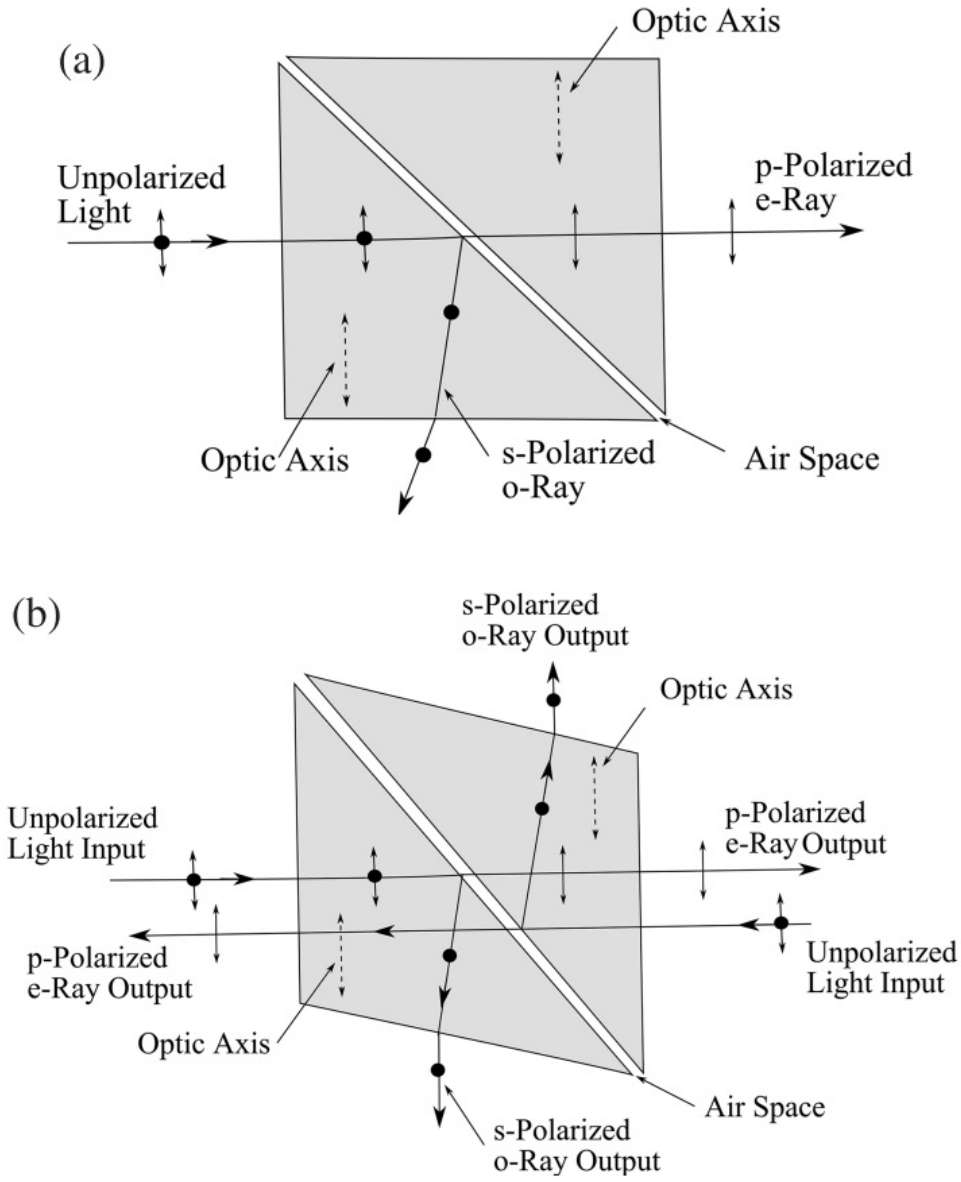


Figure 2.8: (a) Glan-Taylor prism polarizer made of calcite prisms. (b) Glan-Taylor prism polarizer designed to have orthogonal outputs [27].

2.4 Bloch Sphere

A useful way to visualize qubits is the think of them as points on a sphere. In quantum information, this is known as the Bloch Sphere [5]. First, consider the state

$$|\psi\rangle = cos\left(\frac{\theta}{2}\right)|0\rangle + e^{i\varphi} sin\left(\frac{\theta}{2}\right)|1\rangle, \tag{2.3}$$

where θ and φ are numbers that define a point on the unit three-dimensional sphere, and with imaginary i. The visual of the Bloch Sphere can be seen in Figure 2.10.

Because the information of a qubit is represented by where it is located on the surface of the Bloch Sphere, one could think that an infinite amount of information could be stored in one qubit, as there are an infinite number of values of θ and φ. However, this is not true in reality because the act of measuring

[5]The Bloch Sphere is also known as the Poincaré Sphere or the Spin 1/2 State Vector Sphere.

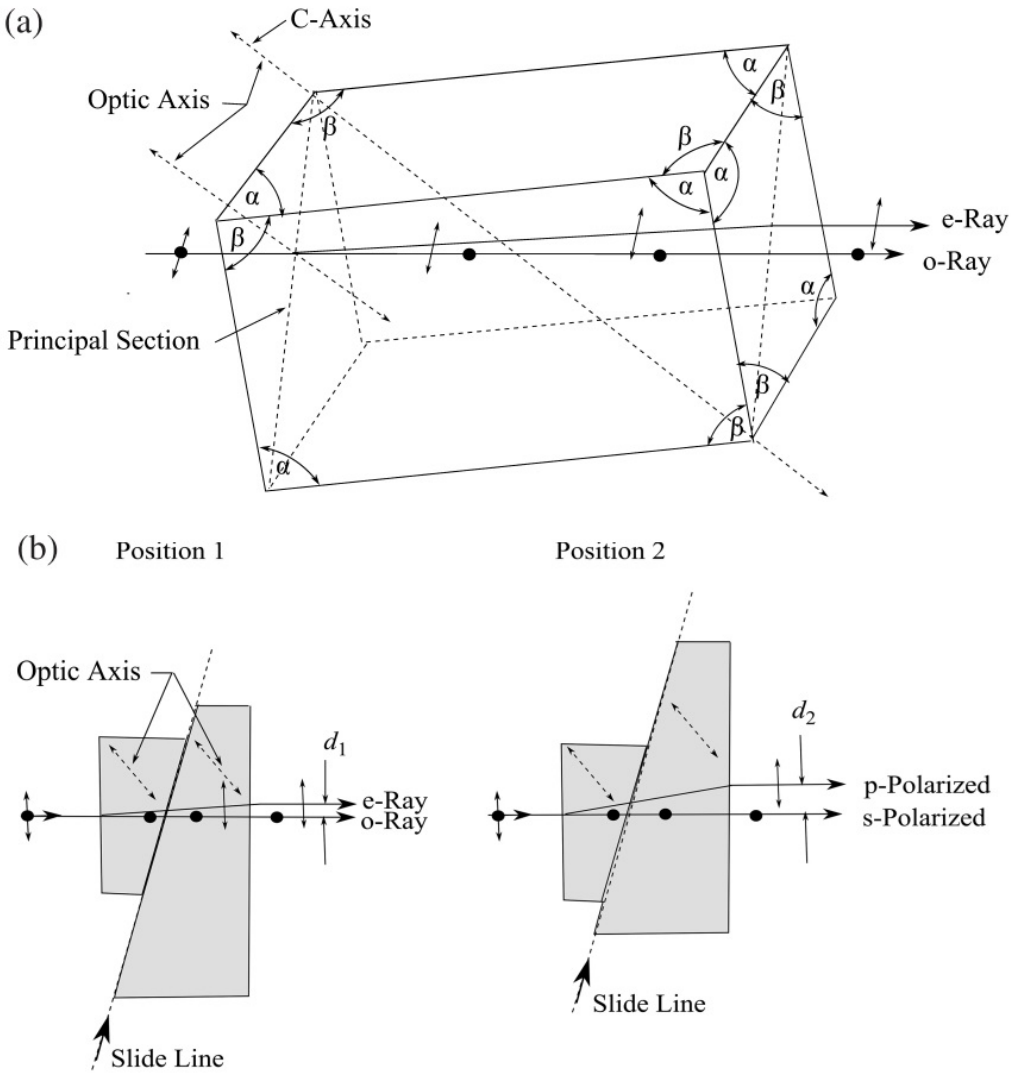


Figure 2.9: (a) Calcite beam displacer. (b) Variable calcite beam displacer. Two calcite crystals are cut at an angle and with their optical axes aligned. Depending on their relative positions, the propagation distance through the crystal varies, which in turn varies the overall displacement of the e-ray (p-polarized) [27].

a qubit changes the qubit. In the case of some arbitrary superposition state, if the measurement of $|+\rangle$ gives 0, then the state post measurement will be $|0\rangle$ [6]. So, from a single qubit, one bit of information is obtained [28]. In photonic quantum computing, in order to understand the complexity of the state that is being measured, a statistical measurement is made. This means that large numbers of photons are prepared in the same state and processed in the same way.

In the context of quantum optics, the Bloch Sphere is a great tool to visualize what is being done to photons when they go through single-photon gates. A simple way to prepare photons in a desired state in the polarization basis is to have them pass through a series of waveplates: quarter-waveplate, half-waveplate, quarter-waveplate. Quarter waveplates (QWP) rotate the state between the poles of the Bloch Sphere by an angle of θ, which is limited by $\pi/2$ radians, or a quarter of the way around the sphere. Half-waveplates (HWP) rotate the state around a point on the equatorial plane of the Bloch Sphere by 2φ. Figure 2.11 depicts these transformations and how the series of QWP-HWP-QWP can

[6] $|+\rangle = \frac{1}{\sqrt{2}}(|0\rangle + |1\rangle)$ and $|-\rangle = \frac{1}{\sqrt{2}}(|0\rangle - |1\rangle)$. These are two orthogonal states, just in a different basis.

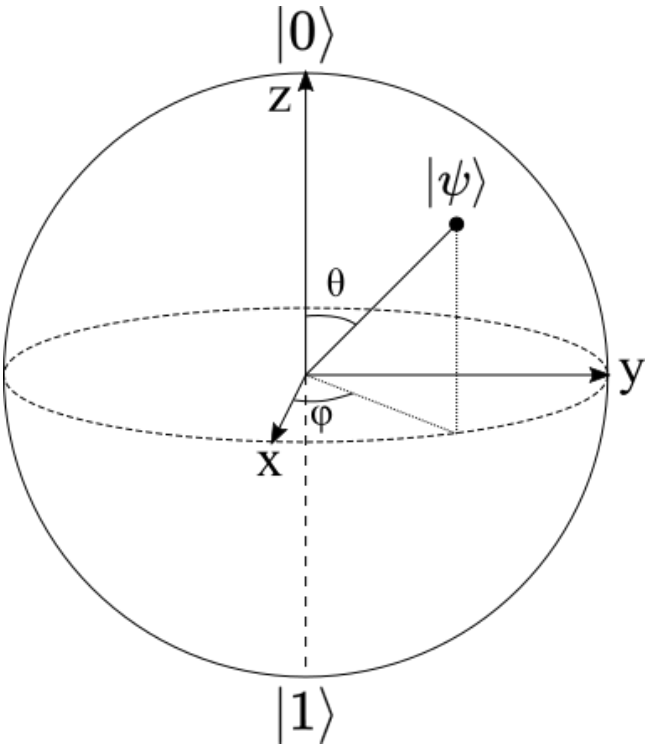


Figure 2.10: Bloch Sphere representation of a qubit.

be applied to transform a state from any point on the Bloch Sphere to another.

2.5 Hong-Ou-Mandel Effect

Back in 1987, Hong, Ou, and Mandel demonstrated that when you interfere two indistinguishable photons on a 50:50 beamsplitter, they interact in an interesting way [22]. When both photons arrive at the beamsplitter at the same time, they bunch together and both exit through the same output port. To understand this mathematically, take the simple two-photon state

$$|1,j\rangle_a |1,k\rangle_b = \hat{a}_j^\dagger \hat{b}_k^\dagger |0\rangle_{ab} \tag{2.4}$$

where j and k are placeholder variables that describe other properties of the state (such as polarization). $\hat{a}$ and $\hat{b}$ are the creation/annihilation operators for the individual photons.

Next, consider the matrix form of the beamsplitter unitary with reflectivity η.

$$U_{bs} = \begin{bmatrix} \sqrt{\eta} & \sqrt{1-\eta} \\ \sqrt{1-\eta} & -\sqrt{\eta} \end{bmatrix} \tag{2.5}$$

Applying this to the system,

$$U_{bs}(\hat{a}_j^\dagger \hat{b}_k^\dagger |0\rangle_{ab}) = \left(\sqrt{\eta(1-\eta)}\, \hat{a}_j^\dagger \hat{a}_k^\dagger + \eta \hat{a}_k^\dagger \hat{b}_j^\dagger - (1-\eta)\hat{a}_j^\dagger \hat{b}_k^\dagger + \sqrt{\eta(1-\eta)}\, \hat{b}_j^\dagger \hat{b}_k^\dagger \right) |0\rangle_{ab} \tag{2.6}$$

Recalling that in this scenario, the beamsplitter is a 50:50 beamsplitter. Thus, $\eta = 1/2$. So the final result of this general calculation is

$$|\psi_f\rangle_{ab} = \frac{1}{2} \left(\hat{a}_j^\dagger \hat{a}_k^\dagger + \hat{a}_k^\dagger \hat{b}_j^\dagger - \hat{a}_j^\dagger \hat{b}_k^\dagger - \hat{b}_j^\dagger \hat{b}_k^\dagger \right) |0\rangle_{ab} \tag{2.7}$$

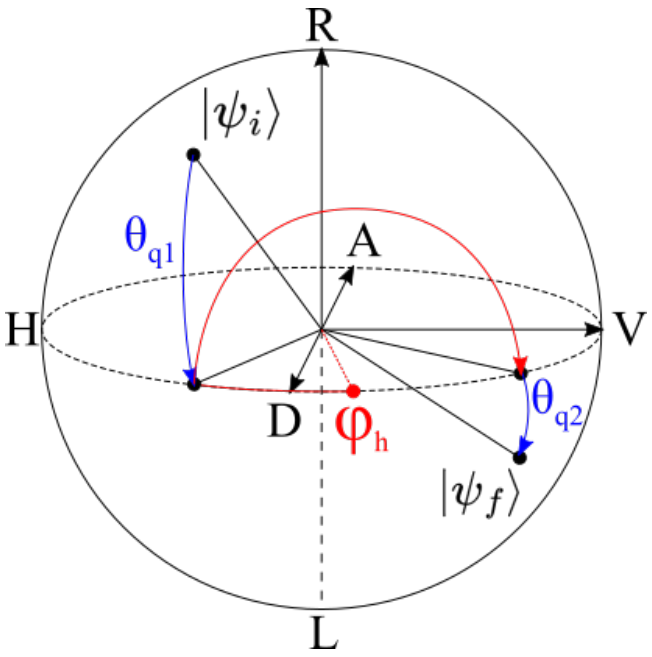


Figure 2.11: Visualization of the single qubit transformation from any point on the Bloch Sphere to any other point on the Bloch Sphere. The orthogonal basis of Vertical (V), Horizontal (H), Diagonal (D), Antidiagonal (A), Left (L), and Right (R) polarization. The initial state, $|\psi_i\rangle$, is rotated down to the equatorial plane with a QWP by the angle θ_{q1}. It is then rotated around the equatorial plane with HWP by the angle φ_h. Finally, it is rotated down (in this specific example) with a second QWP by the angle θ_{q2}.

Next, consider the case in which both photons are indistinguishable, meaning that they have the same polarization. So, $j = k = H$ (both photons are horizontally polarized).

$$|\psi_f\rangle_{ab} = \frac{1}{2}\left(\hat{a}_H^\dagger \hat{a}_H^\dagger + \hat{a}_H^\dagger \hat{b}_H^\dagger - \hat{a}_H^\dagger \hat{b}_H^\dagger - \hat{b}_H^\dagger \hat{b}_H^\dagger\right)|0\rangle_{ab} \tag{2.8}$$

Notice that two of the terms cancel each other, and thus

$$|\psi_f\rangle_{ab} = \frac{1}{2}\left(\hat{a}_H^\dagger \hat{a}_H^\dagger - \hat{b}_H^\dagger \hat{b}_H^\dagger\right)|0\rangle_{ab} = \frac{1}{\sqrt{2}}\left(|2,H\rangle_a - |2,H\rangle_b\right). \tag{2.9}$$

This final state shows that the two photons will be in one mode half the time and the other mode half the time. This, of course, assumes that both photons are in the same time bin, meaning they arrive at the beamsplitter at the same time [29].

In practice, the Hong-Ou-Mandel experiment is conducted by varying the relative lengths of the two optical input paths that each photon travels down prior to reaching the beamsplitter. Coincidence measurements are then taken between the output channels of the beamsplitter. If the two photons are highly indistinguishable, the coincidence rates between the two outputs will be high if the input path lengths are such that the two photons arrive at the beamsplitter in different time bins. As the photons are slowly brought into the same time bin (by varying the relative input path lengths), the coincidence rate will drop, and then rise again as they are brought out of the same time bin. The coincidence rates at the bottom of this dip compared to the coincidence rates on the edge of the dip gives a ratio. This ratio, subtracted from 1, gives the indistinguishability. As an example, say that at the edge of the dip, the coincidence rate is 100 counts/second, and at the bottom, it is 3 counts/second. Then the indistinguishability would be $1 - \frac{3}{100} = 0.97$.

The ideal indistinguishability is 1. However, in practice, this number is very easily reduced due to noise, dark counts, and the photons not being perfectly identical in any measurable quality.

Chapter 3

Photonic Quantum Information

This chapter discusses quantum information as it pertains to the work done in this thesis. A brief history of the development of quantum information will be provided as well as the basic mathematical concepts and components necessary to understand the experimental work demonstrated in Chapters 4, 5, and 6.

3.1 A Brief History of Quantum Information

Quantum information is a relatively new field of study—only a few decades old—but its roots begin back in the early 20th century with the birth of quantum theory [30], which discussed the atomic and subatomic world [31]. These roots started to grow and produce many wonderful technologies that heavily impacted society. Magnetic resonance imaging, lasers, computers, phones, etc, are all based on wave-particle duality—just one aspect of quantum mechanics—and all contributed to bringing the world together in a large technological community [32].

In 1935, Einstein, Podolsky, and Rosen showed that quantum theory violated local realism in fundamental physics [33]. This violation was later named entanglement by Schrödinger. This entanglement is one of the key components that sets quantum computing apart from classical computing, but more on that later. This entanglement became somewhat of a paradox, and it was suggested that there must be some local hidden variables to fill the gaps in quantum mechanics.

Later, in 1964, Bell derived a correlation qualifier that, in principle, could show that entanglement is a purely quantum effect—now known as Bell's Inequality [34]. This was turned into an experimental proposal a few years later by Clauser, Horne, Shimony, and Holt [35], leading to an analysis of possible experiments to test if quantum theory could, in fact, violate local realism [36, 37].

One of the first experimental breakthroughs came in the 1980s when Alain Aspect conducted a collection of experiments using photons emitted from a radiative atomic cascade in calcium in several experimental schemes [38–40]. Each of these experiments violated Bell's inequality and thus showed that entanglement was a purely quantum interaction. With the demonstration of entanglement, quantum information was able to develop past the ability of classical information processing with protocols for quantum key distribution, quantum teleportation, superdense coding, etc, [41]. In the 1990s, Kwiat and colleagues created two down-conversion sources [42, 43]. One of these sources was able to readily

produce entangled single-photon pairs at a much higher rate.

3.2 Qubits and Gate Operations

The building blocks of a quantum computer and quantum information processing are quantum bits. To understand a quantum bit, it is probably best to first understand its classical counterpart, the bit. In classical computing, the bit is a single piece of information. It can have one of two possible values, 0 or 1, which can be represented in the matrix form as

$$|0\rangle = \begin{bmatrix} 1 \\ 0 \end{bmatrix} \text{ and } |1\rangle = \begin{bmatrix} 0 \\ 1 \end{bmatrix}. \tag{3.1}$$

Since these are two mathematically orthogonal states, it is a clear definition of a bit. In the classical world, a bit is either in the $|0\rangle$ or $|1\rangle$ state. However, this is insufficient for the quantum world because there are cases where the bit can be in both states simultaneously [44].

This provides a clear demand for the quantum bit, or more commonly known as the qubit [45]. The qubit can be represented in matrix form with complex numbers.

$$\begin{bmatrix} c_0 \\ c_1 \end{bmatrix} \tag{3.2}$$

However, this can be easily rewritten in the form

$$\begin{bmatrix} c_0 \\ c_1 \end{bmatrix} = c_0 \begin{bmatrix} 1 \\ 0 \end{bmatrix} + c_1 \begin{bmatrix} 0 \\ 1 \end{bmatrix} = c_0 |0\rangle + c_1 |1\rangle, \tag{3.3}$$

with the condition that $|c_0|^2 + |c_1|^2 = 1$.

Next, consider the case of two qubits, q_1 and q_2. In this system, there are four simple separable states,

$$|0\rangle \otimes |0\rangle \ , \ |0\rangle \otimes |1\rangle \ , \ |1\rangle \otimes |0\rangle \ , \text{and } |1\rangle \otimes |1\rangle \tag{3.4}$$

which can be written in the following form for simplicity.

$$|0\rangle |0\rangle \ , \ |0\rangle |1\rangle \ , \ |1\rangle |0\rangle \ , \text{and } |1\rangle |1\rangle \tag{3.5}$$

or,

$$|0,0\rangle \ , \ |0,1\rangle \ , \ |1,0\rangle \ , \text{and } |1,1\rangle \tag{3.6}$$

These states are considered to be separable because they can be written in the form $|q_1, q_2\rangle = |q_1\rangle \otimes |q_2\rangle$. Same for the state

$$\frac{1}{\sqrt{2}}(|0,0\rangle + |0,1\rangle) = |0\rangle \otimes \frac{1}{\sqrt{2}}(|0\rangle + |1\rangle) \quad \text{where} \quad |q_1\rangle = |0\rangle \quad \text{and} \quad |q_2\rangle = \frac{1}{\sqrt{2}}(|0\rangle + |1\rangle). \tag{3.7}$$

The difference with these states is that one of them ($|q_2\rangle$) is now in a superposition. Meaning that it has a certain probability of being measured in the $|0\rangle$ or a certain probability of being measured in the $|1\rangle$ state. In this specific case, both have a probability of 0.5.

Next, consider the Bell states [34, 46, 47],

$$\begin{aligned}
|\Phi^+\rangle &= \frac{1}{\sqrt{2}}(|0,0\rangle + |1,1\rangle) \\
|\Phi^-\rangle &= \frac{1}{\sqrt{2}}(|0,0\rangle - |1,1\rangle) \\
|\Psi^+\rangle &= \frac{1}{\sqrt{2}}(|0,1\rangle + |1,0\rangle) \\
|\Psi^-\rangle &= \frac{1}{\sqrt{2}}(|0,1\rangle - |1,0\rangle).
\end{aligned} \tag{3.8}$$

Notice how none of these states are separable, meaning that they cannot be written in the form $|q_1, q_2\rangle = |q_1\rangle \otimes |q_2\rangle$. This makes them entangled. In fact, the Bell states are maximally entangled, which means that the quantum state has maximum Von Neumann entropy for each bipartition [48] [1,2]. These two particles are correlated, and they can not be described independently. The qubit is a single bit of information, but entanglement is what separates it from its classical counterpart. Entanglement is the basis of quantum information protocols[3]. It should also be noted that the Bell states form a complete basis for a 2-qubit Hilbert space[4] [53].

Now that the quantum bit has been established, it is important to do something with it. Much like classical information processing has gate operations that act on classical bits to perform calculations, quantum information processing has quantum gates. [54]. One of the most impactful gates is the quantum version of the exclusive-OR (XCOR) gate, known as the controlled-NOT (CNOT) gate [55]. In matrix form, it is represented as:

$$CNOT = \begin{bmatrix} 1 & 0 & 0 & 0 \\ 0 & 1 & 0 & 0 \\ 0 & 0 & 0 & 1 \\ 0 & 0 & 1 & 0 \end{bmatrix} \tag{3.9}$$

The function of the CNOT gate is that it flips the value of the second qubit based on the value of the first qubit.

$$\begin{aligned}
CNOT\,|0,0\rangle &= \begin{bmatrix} 1 & 0 & 0 & 0 \\ 0 & 1 & 0 & 0 \\ 0 & 0 & 0 & 1 \\ 0 & 0 & 1 & 0 \end{bmatrix} \begin{bmatrix} 1 \\ 0 \\ 0 \\ 0 \end{bmatrix} = \begin{bmatrix} 1 \\ 0 \\ 0 \\ 0 \end{bmatrix} = |0,0\rangle \\
CNOT\,|1,0\rangle &= \begin{bmatrix} 1 & 0 & 0 & 0 \\ 0 & 1 & 0 & 0 \\ 0 & 0 & 0 & 1 \\ 0 & 0 & 1 & 0 \end{bmatrix} \begin{bmatrix} 0 \\ 0 \\ 1 \\ 0 \end{bmatrix} = \begin{bmatrix} 0 \\ 0 \\ 0 \\ 1 \end{bmatrix} = |1,1\rangle
\end{aligned} \tag{3.10}$$

[1]The Von Neumann entropy is a way of characterizing the mixedness of a quantum state. For a certain density matrix ρ, the Von Neumann entropy, S, is mathematically defined as $S(\rho) = -Tr[\rho \log(\rho)]$ [28].

[2]The bipartition refers to the splitting up of a system into two subsystems. In the case of Bell state, which includes only two photons, each photon would be a bipartite state.

[3]Quantum information protocols include, but are not limited to; Quantum Teleportation [47], Superdense Coding [49], Quantum Key Distribution [50], Grover's Search Algorithm [51], Shor's Algorithm [52]

[4]A Hilbert space is a complete mathematical vector space with an inner product that fully encompasses all possible quantum states.

Next, consider an example where the control qubit [5] is in a superposition, and a CNOT gate is applied.

$$CNOT\left(\frac{1}{\sqrt{2}}(|0\rangle+|1\rangle)|0\rangle\right) = CNOT\left(\frac{1}{\sqrt{2}}(|0,0\rangle+|1,0\rangle)\right)$$
$$= \frac{1}{\sqrt{2}}\begin{bmatrix}1&0&0&0\\0&1&0&0\\0&0&0&1\\0&0&1&0\end{bmatrix}\begin{bmatrix}1\\0\\1\\0\end{bmatrix} = \frac{1}{\sqrt{2}}\begin{bmatrix}1\\0\\0\\1\end{bmatrix} = |\Phi^+\rangle \quad (3.11)$$

Notice that the outcome is an entangled state.

If one were to continue to apply more gated operations to the simple example given, then one would need to multiply the corresponding matrices on the left. As an example, say that the goal was to transform the Φ^+ state to the Ψ^- state. In order to do this, one would first apply a Pauli X gate to the first qubit, followed by a Pauli Z gate to the first qubit [6].

$$(\sigma_z \otimes I_2)\cdot(\sigma_x \otimes I_2)|\Phi^+\rangle = \frac{1}{\sqrt{2}}\begin{bmatrix}1&0&0&0\\0&1&0&0\\0&0&-1&0\\0&0&0&-1\end{bmatrix}\begin{bmatrix}0&0&1&0\\0&0&0&1\\1&0&0&0\\0&1&0&0\end{bmatrix}\begin{bmatrix}1\\0\\0\\1\end{bmatrix} = \frac{1}{\sqrt{2}}\begin{bmatrix}0\\1\\-1\\0\end{bmatrix} = |\Psi^-\rangle \quad (3.12)$$

While the matrix representation of state evolution is relatively simple, it is not the only way to mathematically represent state evolution. Another way is to evolve the density matrix[7] of the system, which is defined as follows. But first, it may be helpful to understand the Kronecker product, $\otimes$ [56]. If one considers two matrices, A (size $m \times n$) and B (size $p \times q$), then

$$A \otimes B \equiv \begin{bmatrix}a_{11}B & a_{12}B & \cdots & a_{1n}B\\ a_{21}B & a_{22}B & \cdots & a_{2n}B\\ \vdots & \vdots & \ddots & \vdots\\ a_{m1}B & a_{m2}B & \cdots & a_{mn}B\end{bmatrix}. \quad (3.13)$$

Following this, the density matrix of a state is defined as

$$\rho \equiv \sum_i p_i |\psi_i\rangle \otimes \langle\psi_i| \quad \text{with} \quad Tr(\rho) = 1. \quad (3.14)$$

For instance,

$$\rho(\Phi^+) = \frac{1}{2}\begin{bmatrix}1&0&0&1\\0&0&0&0\\0&0&0&0\\1&0&0&1\end{bmatrix} \quad (3.15)$$

[5] The control qubit is the qubit that decides how a gate operation is applied based on its value. It is usually chosen to be the first qubit, but not always.

[6] The Pauli gates are single-qubit gates in the form $\sigma_x = \begin{bmatrix}0&1\\1&0\end{bmatrix}$, $\sigma_y = \begin{bmatrix}0&-i\\i&0\end{bmatrix}$, and $\sigma_z = \begin{bmatrix}1&0\\0&-1\end{bmatrix}$. $\sigma_x \otimes I_2$ would apply a Pauli X gate to the first qubit, and $I_2 \otimes \sigma_x$ would apply a Pauli X gate to the second qubit. The notation I_2 signifies an Identity matrix of size 2×2.

[7] A density matrix is a mathematical object with encoded information about both pure and mixed states. It is a general description of a quantum system.

Next, say that in a certain system there is an initial state with density matrix ρ_{init}, and it is acted upon by a series of gates. Each gate has a Unitary Operator, U, associated with it, with the condition that

$$U^\dagger U = I \tag{3.16}$$

Then the final density matrix of the system ρ_{final} is calculated as follows.

$$\rho_{final} = U_k \cdots U_2 U_1 \rho_{init} U_1^\dagger U_2^\dagger \cdots U_k^\dagger \tag{3.17}$$

As an example, consider again two of the Bell states and their density operators.

$$\rho(\Phi^+) = |\Phi^+\rangle \otimes \langle\Phi^+| = \frac{1}{2}\begin{bmatrix} 1 & 0 & 0 & 1 \\ 0 & 0 & 0 & 0 \\ 0 & 0 & 0 & 0 \\ 1 & 0 & 0 & 1 \end{bmatrix} \tag{3.18}$$

$$\rho(\Psi^+) = |\Psi^+\rangle \otimes \langle\Psi^+| = \frac{1}{2}\begin{bmatrix} 0 & 0 & 0 & 0 \\ 0 & 1 & 1 & 0 \\ 0 & 1 & 1 & 0 \\ 0 & 0 & 0 & 0 \end{bmatrix} \tag{3.19}$$

In order to convert one to the other, the following unitary (U) is used.

$$U = \sigma_x \otimes I_2 = \begin{bmatrix} 0 & 0 & 1 & 0 \\ 0 & 0 & 0 & 1 \\ 1 & 0 & 0 & 0 \\ 0 & 1 & 0 & 0 \end{bmatrix} \tag{3.20}$$

$$U \cdot \rho(\Phi^+) \cdot U^\dagger = \frac{1}{2}\begin{bmatrix} 0 & 0 & 1 & 0 \\ 0 & 0 & 0 & 1 \\ 1 & 0 & 0 & 0 \\ 0 & 1 & 0 & 0 \end{bmatrix}\begin{bmatrix} 1 & 0 & 0 & 1 \\ 0 & 0 & 0 & 0 \\ 0 & 0 & 0 & 0 \\ 1 & 0 & 0 & 1 \end{bmatrix}\begin{bmatrix} 0 & 0 & 1 & 0 \\ 0 & 0 & 0 & 1 \\ 1 & 0 & 0 & 0 \\ 0 & 1 & 0 & 0 \end{bmatrix} = \frac{1}{2}\begin{bmatrix} 0 & 0 & 0 & 0 \\ 0 & 1 & 1 & 0 \\ 0 & 1 & 1 & 0 \\ 0 & 0 & 0 & 0 \end{bmatrix} = \rho(\Psi^+) \tag{3.21}$$

Once the final density matrix is calculated, the final population distribution of any state ϕ_i within the Hilbert space can be determined [28].

$$\langle\phi_i\rangle = \langle\phi_i|\,\rho_{final}\,|\phi_i\rangle \tag{3.22}$$

3.3 Kraus Representation Theorem

Another way to represent a series of quantum gate operations is in the operator-sum representation. This theory was pioneered in the 1970s [57, 58] and is based around the density matrix ρ. The density matrix of a quantum state changes as gate operations are applied to it, and Kraus was able to neatly describe the evolution of the density matrix mathematically.

To begin, consider a Hilbert space, H [53], of dimension n, and let $gl(H)$ denote the general linear vector space of all linear transformations in that space. A map, ε $(gl(H) \to gl(H))$, is completely

positive if it is linear, and if $\varepsilon \otimes I$ is positive on $H \otimes H'$ for all H'. The map is also trace-preserving if $Tr[\varepsilon(A)] = Tr[A]$ for all $\varepsilon \in gl(H)$ [59]. Kraus' Theorem states that for any quantum channel ε, there exists a finite set of operators,

$$K_0, K_1, K_2, ..., K_k \quad \text{where} \quad k \leq (dim(H))^2, \tag{3.23}$$

and

$$\varepsilon(\rho) = \sum_i K_i \rho K_i^\dagger \quad \text{with} \quad \sum_i K_i K_i^\dagger = 1. \tag{3.24}$$

It should be noted that this theorem is also known as the Operator-Sum representation[8]

3.4 Photons as Qubits

While there are several conduits for the physical qubit, such as superconducting qubits [60–62] or trapped ions [63, 64], this work focuses on the use of single photons as qubits. A qubit in the physical world can be any quantum particle with two clearly distinguishable and relatively stable quantum states. For a single photon, these two states are often vertical and horizontal polarizations; others include time-bin and spatial mode. However, this is not the full list of qualities for a viable quantum computer. DiVincenzo came up with the now-famous five (plus two) criteria for the physical implementation of a quantum computer [65].

1. A scalable physical system with well-characterized qubits.
2. The ability to initialize the state of qubits to a simple fiducial state.
3. Long relative decoherence times, much longer than gate operation time.
4. A universal set of quantum gates.
5. A qubit-specific measurement capability.
6. The ability to interconvert stationary to flying qubits.
7. The ability to faithfully transmit flying qubits between specified locations.

Going down the list, and starting from the top. How scalable is a system of photonic qubits? Single photons are produced at a high rate and with relatively good single-photon quality [66, 67]. The limitation with photonic quantum information comes from the need for these photons to be separated into different spatial modes or time bins. As of this writing, the largest collection of functioning photonic qubits is at 216 [68], implemented via time domain multiplexing. Photons have the added benefit of simple initialization, as their polarization can be easily set with minimal loss.

When it comes to coherence times, photons are good up to 15 billion years in free space—consider the partially-polarised cosmic microwave background—whereas for neutral atoms it is on order $10s$ [69], and for trapped ions it exceeds 10 minutes [70]. However, one must consider that the coherence times of the qubits only need to be long when compared to gate times and overall processing times. For quantum photonic circuits, this happens to be rather fast.

[8] For a more in-depth description of the Kraus (Operator-Sum) representation, refer to [28].

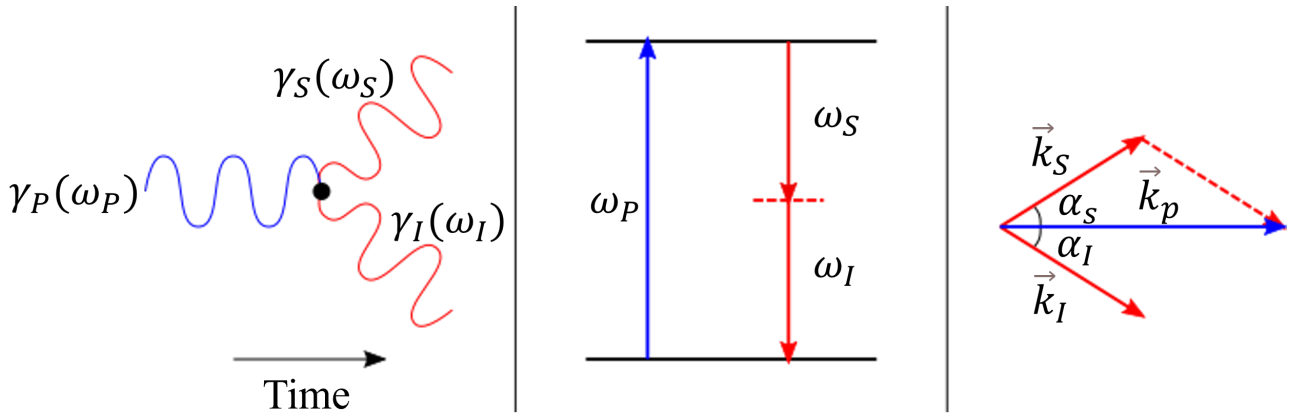


Figure 3.1: (Left) Feynman Diagram of a spontaneous parametric downconversion (SPDC) source when one photon at energy $\hbar\omega_P$ is split into two photons of energy $\hbar\omega_I$ and $\hbar\omega_S$. (Middle) Representation of the energy conservation scheme of the SPDC source. (Right) Representation of the momentum conservation scheme of the SPDC source [76].

The KLM scheme of linear optical quantum computing [71] showed that linear optics, single-photon measurement, and feedforward were the only things necessary to complete a universal set of quantum gates. Transit times of optical elements is very fast—femtosecond to nanosecond range [71, 72]—and detector deadtimes are typically $40-50\ ns$. The recovery time—aka deadtime—of a single-photon detector is the period right after it has measured a single-photon event and cannot register any following event. After this time has elapsed, meaning the detector has recovered, it can once again register a single-photon event. The limiting factor when it comes to computation time with photonic qubits is detector recovery time. Single-photon measurement also addresses the qubit-specific measurement needs, with several industry solutions existing for detecting single photons.

The last two items on the list have already been partially addressed due to existing infrastructure. Part of what makes photonic quantum information so appealing is its ability to take advantage of current telecom communication systems. We already have the means to transport light information great distances through fibers. The challenge will be to address the issue of decoherence over these long distances.

3.5 Spontaneous Parametric Down Conversion

Spontaneous Parametric Down Conversion source (SPDC) has been a tool for generating pairs of single photons for half a century [73, 74]. The process in which this happens includes two key elements: a pumping electromagnetic field and a nonlinear crystal. The photons in the pump laser interact with the nonlinearities in the crystal, causing the destruction of the pump photon and the production of two photons, the idler and signal photons. By conservation of energy, the energy of this pair of photons must equal that of the incident pump photon, and thus $\omega_I + \omega_S = \omega_P$ [75].

The production of the signal and idler photons from a single pump photon is an entirely quantum process, and thus, the photons produced by this interaction have some strong quantum properties. The full mathematical explanation of the SPDC process is outside the scope of the work presented in this document, and so a heuristic explanation will be given (see [77] for full mathematical derivation).

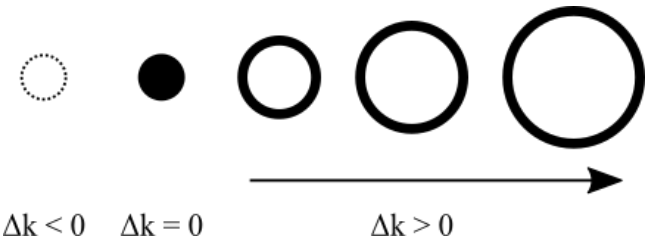


Figure 3.2: Crossectional view of the downconverted light emitted by a SPDC type 1 source negative uniaxial crystal as a function of the wave vector mismatch. From left to right: $\Delta k < 0$, the phase matching condition is not met, and thus no emission is observed. $\Delta k = 0$, exact phase matching is met, and downconverted light is observed along the axis of the pump light. $\Delta k > 0$, phase matching is observed under noncollinear conditions and the downconverted light is emitted in a cone coaxial with the pump light [79].

SPDC sources can be categorized into three distinct types: Type 0, Type 1, and Type 2 phase matching. A Type 0 SPDC source produces photons with the same polarization as the pump laser, but it is not within the scope of this thesis. The remaining two types are related to the phase matching of the nonlinear crystal. Type 1 phase matching is the case in which the electromagnetic waves produced by the process (signal and idler photon) have the same polarization. Type 2 phase matching is the case in which these photons have orthogonal polarizations [78].

First consider the process of a type 1 SPDC source with a negative uniaxial crystal, for the simple case of degenerate downconversion, i.e. $\omega_I = \omega_S$. When the angle of the pump beam is rotated with respect to the crystal, usually by physically rotating the crystal. As the angle changes, the effective indices of refraction seen by the pump beam and two photon beams changes. At the proper angle, momentum is conserved, and the phase matching condition is met [79]. At angles where this condition is not met, when $\Delta k < 0$, where

$$\Delta k = k_I + k_S - k_P, \tag{3.25}$$

no down-converted light is observed. As the angle changes and exact phase matching occurs, $\Delta k = 0$, down-converted light is observed on the axis of the pump beam. As this angle continues to increase, phase matching occurs under noncollinear conditions, and the light produced by the downconversion process is emitted in a cone around the axis of the pump beam [79].

For type 2 downconversion in the case of a negative uniaxial crystal, both the signal and idler photons can be emitted in a cone similar to that of a type 1 SPDC source [42]. However, due to the two photons experiencing different refractive indices, these two cones are centered on different propagation directions as seen in Figure 3.3.

The crucial aspect of the type 2 SPDC source is that the two photons produced can be entangled with the correct phase-matching conditions. This condition occurs when the two emission cones of the signal and idler photons overlap, creating two intersection points. While one cone carries a photon of a certain polarization, the other cone carries a photon of the orthogonal polarization. This creates a situation at the intersection point where the photon has a 50% chance of having one polarization and a 50% chance of having the other polarization. Regardless of the first photon's polarization, the second will always have the orthogonal polarization. If the photons are categorized by having horizontal or

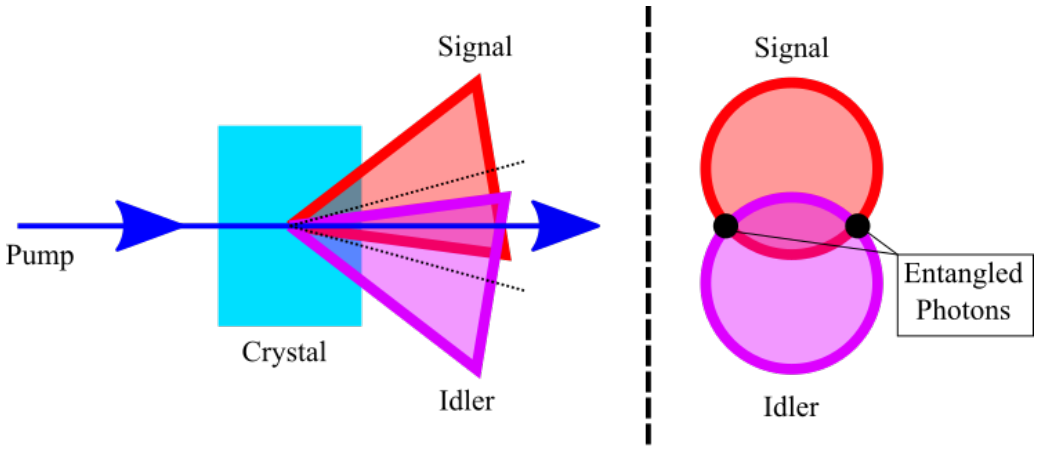


Figure 3.3: Diagram of a type 2 SPDC source. (Left) Simplistic representation of the pump beam passing through a type 2 nonlinear crystal with the emission cones of the signal and idler photons propagating in different directions. (Right) Cross-section view of the signal and idler emission cones. The overlap of the two cones makes the regions where an entangled pair of photons is produced.

vertical polarization (H or V), then in the polarization basis, the state of the two photons becomes

$$|\psi\rangle = \frac{1}{\sqrt{2}}(|H,V\rangle + |V,H\rangle). \tag{3.26}$$

Which is an entangled state [79].

While the ability to produce entangled photons is a useful tool in the area of quantum photonics, it is also useful to have a source that produces photons that are completely separable, but in the same time bin as seen in Chapter 4.

The final point to be made here about SPDC sources is that they are classified as probabilistic single-photon sources. This means, in the case of the SPDC source, that whenever a pulse of laser light is sent to the crystal, photon pair production is not guaranteed[9]. In other words, the photons are produced at arbitrary times. The production of the photon is not known until the signal photon is measured. Only then can the production of the idler photon be guaranteed [80].

3.6 Quantum Dots

Quantum dots have become a great source for single photons since their first experimental realization in the 1980s [81], with epitaxial quantum dots coming just over a decade later [82]. Since their initial conception, quantum dots have taken a number of different forms based on their fabrication methods. These include colloidal quantum dots, epitaxial quantum dots, and lithographically defined quantum dots. This section will focus on lithographically defined quantum dots formed in epitaxially grown semiconductor layers, which have been used experimentally in this work (see Chapter 5).

If one is familiar with photon absorption and emission in an atom [83], then the concept of a quantum dot may be easy to comprehend. Electrons in an atom can either be excited to higher energy levels or fall to lower energy levels by absorbing or emitting a single photon. A quantum dot (QD) acts in a

[9]As explained by Alan Migdall of the US National Institute of Standards and Technology `https://spie.org/news/photonics-focus/janfeb-2025/hunting-for-the-perfect-single-photon-source`.

similar way, as it is a two-level system with a ground state, an excited state, and one electron.

The growth of self-assembled quantum dots starts with a semiconductor substrate layer, typically GaAs (Gallium Arsenide), and then material is deposited on top of the substrate, typically InAs (Indium Arsenide)—chosen because it has a smaller bandgap than the substrate material. The deposited layer of InAs has a small lattice mismatch when compared to GaAs, which causes surface strain. As the layers of InAs build up, epitaxial islands are formed to relieve the strain in the system. These islands are then covered with another semiconductor layer of a larger bandgap material, e.g., GaAs again, to create the quantum dot [84, 85].

Once the quantum dots have been grown, they usually undergo lithography. This process carves out and shapes the material around the quantum dot into various favorable structures. The main lithography techniques include, but are not limited to, electron beam, X-ray, ion beam, and nanoimprint lithography [86]. Each of these techniques comes with different advantages and applications, such as etching resolution. Many of these techniques include the process of depositing a resist as a mask. This mask is deposited onto the InAs layer and acts as a stencil. Meaning that the resist protects the InAs layers under it, while the various lithography techniques carve away the areas not protected by the resist. However, there are exceptions to this, as electron beam lithography can be a maskless technique. In addition, lithography techniques can be classified as near ($< 100\ nm$) or far-field (microns) depending on their operating distances.

The lithography technique most prevalent the this work is called in-situ Lithography [87, 88]. This process is executed by first scanning the substrate to identify the positions of the randomly scattered quantum dots. The quantum dots can be located to within an accuracy of 50 nm. This particular process is executed with a three-color confocal microscope (attocube attoCFM1), and an optical microscopy insert cooled down to 4.2 K. Three fiber-based optical lines are collimated and sent to a microscope objective through the optical insert in free space. The sample, which includes the randomly grown quantum dots, is placed on a piezo-actuator stack to precisely control the positioning of the sample with respect to the microscope objective. Two of the fibers are used for quantum dot excitation, and one for quantum dot emission collection. By scanning the sample, the location of the quantum dots can be registered by the amount of quantum dot emission being measured. Once the viable quantum dots are located, the supporting structures can be etched around them.

This type of in-situ semiconductor quantum dot, along with other semiconductor quantum dots, makes a great candidate for high-performing single photon sources. There are three properties of the ideal single photon source. The first of these is that there must be a high degree of single-photon purity. This is to say that a single photon must be just that, single. This is not so simple to achieve as photons like to bunch together. A light pulse can be decomposed into a group of plane wave modes. Each of these modes is a quantized harmonic oscillator with defined polarization ε, spatial frequency $\boldsymbol{k}$, and frequency ω. This is shown mathematically by

$$|\psi\rangle = \sum_{\boldsymbol{k},\varepsilon,n} c_{\boldsymbol{k},\varepsilon} |n\rangle_{\boldsymbol{k},\varepsilon} \tag{3.27}$$

where c is the speed of light. In contrast, a single photon light field is composed of a single Fock state $|1\rangle_{\boldsymbol{k},\varepsilon}$. The purity of a single photon is characterized by the second-order intensity correlation function $g^{(2)}(t)$. This function states the probability of measuring a second photon after a certain amount of

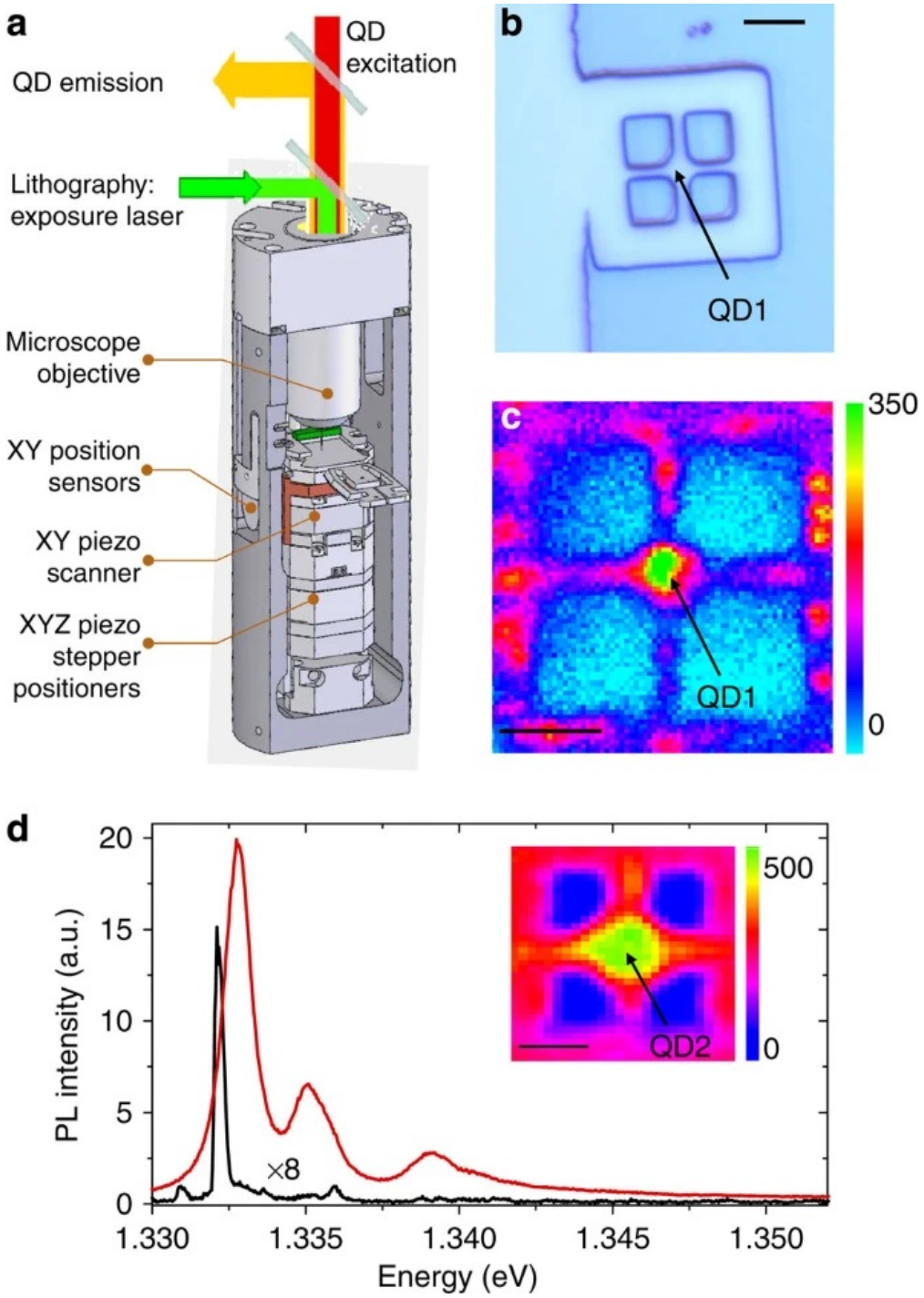


Figure 3.4: (a) Schematic of the in-situ setup used for locating and etching patterns around quantum dots. (b) Image of an in-situ lithography pattern centered on a quantum dot. Scale bar, 10 μm (c) Emission intensity map selecting a 5 nm wavelength range around the fundamental mode of the connected pillar. Scale bar, 5 μm. (d) Photoluminescence (PL) spectrum measured on a second connected pillar device at high excitation power (red) and low excitation power (black) with inserted emission intensity map. Scale bar, 3 μm [88].

time t has elapsed from measuring the first photon. So, in the ideal case, $g^{(0)}(0) = 0$. In other words, right as the first photon is measured, at time $t = 0$, a second photon is not measured. This means that there is a 0% chance of measuring a second photon at the same time as the first, so the first photon is indeed single. The second-order intensity correlation function of a single photon source is measured by the Hanbury-Brown-Twiss experiment [89].

The second attribute of an ideal single-photon source is high indistinguishability. This means that one photon can not be identifiably different from any other photon by any measurable quality. One of the central components of quantum information processing is two-photon gates (like the CNOT gate shown in Chapter 3.2), but these gates only work if the two photons entering them are indistinguishable. The indistinguishability of a single photon system is measured by the Hong-Ou-Mandel experiment [22] (see Chapter 2.5). In short, the Hong-Ou-Mandel experiment consists of sending two single photons to a 50:50 beamsplitter with one photon in each input mode. If the photons arrive at the beamsplitter at the same time and are completely indistinguishable, they will bunch together and both exit through the same output mode. If they are not perfectly indistinguishable, there is a non-zero probability that they will leave via separate output modes, leading to measurable coincidence.

Lastly, the ideal single-photon source must have a high level of brightness. The source should deliver photons with no vacuum component $|0\rangle$, meaning that there should be no loss in the system. In reality, achieving this is nearly impossible in quantum photonic systems. However, certain measures can be taken to mitigate some of the loss. The overall brightness of a single-photon source is quantified by the probability of measuring a single photon at the output of the source when compared to the maximum output. As an example, if one has an 80 MHz source, and photons are measured at the output at 20 MHz, then the source has a brightness of 25% [90].

The science and the ability of semiconductor quantum dots are constantly evolving and growing, showing a slow approach to the ideal single-photon source. Single photon purities of $> 99\%$ are now routinely achieved, and even available commercially (see e.g. products from Sparrow Quantum). The indistinguishability of quantum dots has achieved the high mark of 91.7%, which is the first time a quantum dot source has exceeded 90% visibility [91]. Additionally, quantum dot sources have been shown to achieve a brightness well above 60% [92]. Brightness will become one of the key focuses of this thesis as it is the main objective of Chapter 6.

In contrast to an SPDC source, a quantum dot is classified as a deterministic single-photon source. Photons of a deterministic source are produced at a fixed time. In an ideal quantum dot source, a single photon is produced every time a pulse of light from the laser source excites the quantum dot. This can be referred to as a “push button” source; whenever a button is pushed (laser pulse), a photon is produced. The common challenge with deterministic sources is that they become more probabilistic as extraction and coupling efficiencies decrease [80].

The following publication has been incorporated as Chapter 4.

1. [1] **Sebastian Malewicz**, Dr Marcelo de Almeida, and Prof. Andrew White, Asymmetric Quantum Interference, *Journal* Issue, Number, Year

Contributor	Statement of contribution	%
Sebastian Malewicz	writing of text	40
	proof-reading	20
	theoretical derivations	40
	numerical calculations	40
	preparation of figures	60
	initial concept	10
Dr Marcelo de Almeida	writing of text	40
	proof-reading	20
	supervision, guidance	50
	theoretical derivations	50
	preparation of figures	40
	initial concept	10
Prof. Andrew White	writing of text	20
	proof-reading	60
	supervision, guidance	50
	theoretical derivations	10
	preparation of figures	0
	initial concept	80

Most of the experimental and theoretical work was done by Sebastian Malewicz and Dr Marcelo de Almeida. The tasks were divided such that Mr Malewicz constructed most of the experimental setup while Dr de Almeida performed most of the theoretical calculations. However, this was a close collaborative effort, and thus Mr Malewicz and Dr de Almeida worked closely on both aspects of the experiment. Professor Andrew White provided guidance.

Chapter 4

Asymmetric Quantum Interference

This Chapter introduces the idea of asymmetric quantum interference. Here, I explain the theoretical background, how I adapted the theory to better model laboratory conditions, and the steps undertaken to experimentally demonstrate it. I discuss the results and their significance in the field of quantum information.

4.1 Two-Photon Interference: Theory

In 2015, Lund introduced a linear-optical method [6] to vary the Hong-Ou-Mandel effect—introduced in Chapter 2.5—to allow for selective destructive interference of any term in the beamsplitter output, i.e., to selectively remove $|2,0\rangle$, $|0,2\rangle$, or $|1,1\rangle$.

Typically, the HOM effect completely destroys the $|1,1\rangle$ and creates the NOON state of $\frac{1}{\sqrt{2}}(|2,0\rangle - |0,2\rangle)$. This is achieved by sending two photons to interact on a 50:50 beamsplitter, with one photon going to each input mode. These two photons must be indistinguishable and arrive at the same time. From here, photon bunching takes effect and the photons bunch—or group—together, so that both leave from one output port or the other. In order to further influence the output of these modes, more needs to be added to the optical circuit after the 50:50 beamsplitter. To get an idea of what is needed, let us do some mathematics.

Remember that the creation and annihilation operators, $a^\dagger$ and a, function as follows,

$$a^\dagger |N\rangle = \sqrt{N+1}\ |N+1\rangle\,,\ \ a\,|N\rangle = \sqrt{N}\ |N-1\rangle\,. \tag{4.1}$$

If we consider the polynomial form of two photons in two modes, we can see that it can be written as,

$$\frac{1}{\sqrt{2}}(|2,0\rangle + |0,2\rangle) = \frac{1}{2}(a_1^{\dagger 2} + a_2^{\dagger 2})\,|0,0\rangle\,, \tag{4.2}$$

where the subscripts 1 and 2 indicate which mode the operators act upon.

The significance of Lund's work is that it shows, under the proper conditions, that two-photon states can be transformed into each other only using linear optics. That is, two states are equivalent under linear optical transformation if the polynomial representation of these two states is the same

when subjected to a unitary change of variables. To start with this proof, first take the following polynomials in quadratic.

$$\sum_{i,j} T_{i,j} a_i, a_j \tag{4.3}$$

Next, if one considers a general unitary transformation

$$U^\dagger a_i U = \sum_{l=1}^{m} u_{i,l} a_l \tag{4.4}$$

where m is the number of modes in the system, and apply it to the polynomial.

$$\begin{aligned} \sum_{i,j} T_{i,j} \sum_k u_{i,k} a_k \sum_l u_{j,l} a_l &= \sum_{k,l} \sum_{i,j} u_{i,k} T_{i,j} u_{j,l} a_k a_l \\ &= \sum_{k,l} T'_{k,l} a_k a_l \end{aligned} \tag{4.5}$$

In this context, T' and T as matrix equation are related by

$$T' = U^t T U \tag{4.6}$$

where t denotes a matrix transpose. Generally, the matrix T will be an $m \times m$ matrix where m is the number of modes (2 in this case). So if T is symmetric, then so is T'. Notice that u_i and u_l are coefficients of the unitary matrix U, and not the unitary matrix itself.

Next, what is needed is to find some special state for T which is unique and identifies the classes of states that are accessible under all possibilities of U, which is a unitary matrix. This will satisfy the requirement that the two states are the same when subjected to a unitary change of variables.

The first step in finding T is to think about it in the following decomposition.

$$T = U^t D U \tag{4.7}$$

where U is a unitary matrix and D represents a set of variables that are related by a unitary change of variables. [6] uses Takagi factorization [93] to create the diagonal matrix of D. The importance of the Takagi factorization is that U is the same matrix that achieves both the decomposition and diagonalizes the positive definite matrix $T^\dagger T$. This then leads to a diagonal matrix D' that consists of only positive eigenvalues. These eigenvalues along the diagonal are then related to those in D by the modulus squared. The values in D will be complex; however, one can apply two procedures that can be absorbed into U. This will make D unique. The first is ordering each component in D from smallest to largest amplitude by conjugating by permutation matrices. The second is that all phase angles can be removed. The entries in D can then all be turned into non-negative values by including a diagonal matrix, which is then also incorporated into U. This can make the phase angle of D equal to zero. This method will work for a finite matrix of D of size $m \times m$.

Taking a moment to understand this deconstruction, the matrix D can be thought of as a generating state, and U can be thought of as the unitary matrix that dictates the required linear interaction needed to achieve the target state. However, if there exists some other state that shares the same decomposed D, then a unitary matrix, and therefore a linear interaction, can be found that will act as a

transformation between the two states [6].

Being that D is a diagonal matrix, the values along the diagonal will have some form that contains only the squares of the creation operators. This means that this state is a superposition of states with two photons in a single mode. Now, if some other state has the same D matrix when decomposed, then a unitary that transforms one to the other can be found. Take the following example of two states and their decompositions.

$$\begin{aligned} T_A &= U_B^t D U_B \\ T_B &= U_B^t D U_B \end{aligned} \tag{4.8}$$

D is the common matrix and can be written as

$$D = (U_B^\dagger)^t T_B U_B^\dagger \tag{4.9}$$

which gives that

$$T_A = U_A^t (U_B^\dagger)^t T_B U_B^\dagger U_A = (U_B^\dagger U_A)^t T_B U_B^\dagger U_A \tag{4.10}$$

This is all to say that the unitary required to transform from T_A to T_B is $U_B^\dagger U_A$.
In the two-photon case, the size of all matrices is 2×2 ($m = 2$). Factorizing T into the form $T = U_0^t D_0 U_0$ where

$$D_0 = \begin{bmatrix} \frac{1}{2\sqrt{2}} & 0 \\ 0 & -\frac{\sqrt{3}}{2\sqrt{2}} \end{bmatrix} \tag{4.11}$$

Reordering the matrix such that the values are in ascending amplitude using the following.

$$U_1 = \begin{bmatrix} 0 & 1 \\ 1 & 0 \end{bmatrix} U_0 \tag{4.12}$$

So then the diagonal matrix becomes,

$$D_1 = \begin{bmatrix} -\frac{\sqrt{3}}{2\sqrt{2}} & 0 \\ 0 & \frac{1}{2\sqrt{2}} \end{bmatrix} \tag{4.13}$$

Next, the negative needs to be taken care of using

$$U_2 = \begin{bmatrix} i & 0 \\ 0 & 1 \end{bmatrix} U_1 \tag{4.14}$$

Which finally gives the diagonal matrix

$$D_2 = \begin{bmatrix} \frac{\sqrt{3}}{2\sqrt{2}} & 0 \\ 0 & \frac{1}{2\sqrt{2}} \end{bmatrix} \tag{4.15}$$

Using a more concrete example with two photons in two modes. The state is

$$\frac{1}{2}|2,0\rangle + \frac{i}{\sqrt{2}}|1,1\rangle - \frac{1}{2}|0,2\rangle \tag{4.16}$$

This has the following polynomial representation of

$$T_{1,1} = -T_{2,2} = \frac{1}{2\sqrt{2}}, T_{1,2} = T_{2,1} = \frac{i}{2\sqrt{2}} \tag{4.17}$$

or,

$$T = \begin{bmatrix} T_{1,1} & T_{1,2} \\ T_{2,1} & T_{2,2} \end{bmatrix} = \frac{1}{2\sqrt{2}} \begin{bmatrix} 1 & i \\ i & -1 \end{bmatrix} \tag{4.18}$$

Given that

$$T^\dagger T = U^\dagger D^2 T \tag{4.19}$$

then $T^\dagger T$ needs to be diagonalized.

$$T^\dagger T = \frac{1}{4} \begin{bmatrix} 1 & i \\ -i & 1 \end{bmatrix} = \frac{1}{\sqrt{2}} \begin{bmatrix} 1 & -i \\ -i & 1 \end{bmatrix} \begin{bmatrix} \frac{1}{2} & 0 \\ 0 & 0 \end{bmatrix} \frac{1}{\sqrt{2}} \begin{bmatrix} 1 & i \\ i & 1 \end{bmatrix} \tag{4.20}$$

This means that

$$D^2 = \begin{bmatrix} \frac{1}{2} & 0 \\ 0 & 0 \end{bmatrix} \tag{4.21}$$

$$D = \begin{bmatrix} \frac{1}{\sqrt{2}} & 0 \\ 0 & 0 \end{bmatrix} \tag{4.22}$$

$$U = \frac{1}{\sqrt{2}} \begin{bmatrix} 1 & i \\ i & 1 \end{bmatrix} \tag{4.23}$$

In this particular case, the matrix D does not need to be reordered or corrected for any relative phase, as the eigenvalues are already positive and in descending order. Now that all the components of the decomposition are accounted for, T can be written as

$$T = U^t D U = \frac{1}{\sqrt{2}} \begin{bmatrix} 1 & i \\ i & 1 \end{bmatrix} \begin{bmatrix} \frac{1}{\sqrt{2}} & 0 \\ 0 & 0 \end{bmatrix} \frac{1}{\sqrt{2}} \begin{bmatrix} 1 & i \\ i & 1 \end{bmatrix} = \frac{1}{2\sqrt{2}} \begin{bmatrix} 1 & i \\ i & -1 \end{bmatrix} \tag{4.24}$$

Looking at the solution here, it can be used to generate the state in equation 4.16. The way of doing this using linear optics is to start with the two-photon state $|2,0\rangle$ in a single mode and have it pass through a 50:50 beamsplitter that has a $\pi/2$ phase shift applied to the transmission output of the beamsplitter for each input mode.

The second example is to start with the state

$$\frac{1}{\sqrt{2}} |2,0\rangle + \frac{i}{\sqrt{2}} |1,1\rangle \tag{4.25}$$

which has the polynomial representation of

$$T = \begin{bmatrix} \frac{1}{2} & \frac{i}{2\sqrt{2}} \\ \frac{i}{2\sqrt{2}} & 0 \end{bmatrix} \tag{4.26}$$

Using the same procedure as above, this matrix can be decomposed into the form $U^t D U$.

$$D = \begin{bmatrix} \frac{\sqrt{3}+1}{4} & 0 \\ 0 & \frac{\sqrt{3}-1}{4} \end{bmatrix} \tag{4.27}$$

$$U = \begin{bmatrix} \frac{\sqrt{3}+1}{\sqrt{2}\sqrt{3+\sqrt{3}}} & \frac{i}{\sqrt{3+\sqrt{3}}} \\ \frac{i(\sqrt{3}-1)}{\sqrt{2}\sqrt{3-\sqrt{3}}} & \frac{1}{\sqrt{3-\sqrt{3}}} \end{bmatrix} \tag{4.28}$$

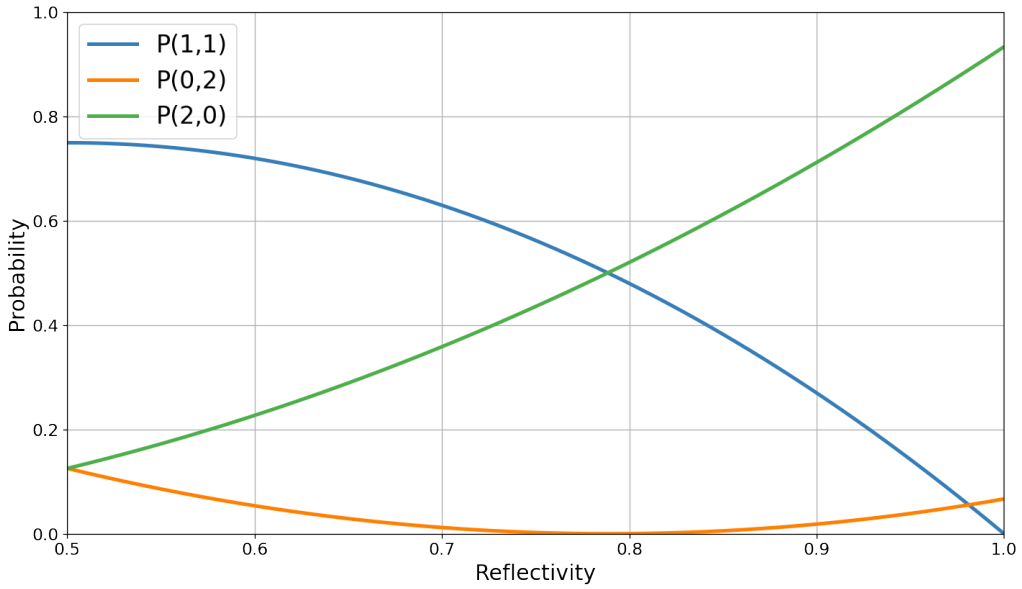


Figure 4.1: Output probability distributions of the state 4.30 incident on a variable beamsplitter. Magenta is the probability of producing the $|1,1\rangle$ component, yellow the $|2,0\rangle$, and blue the $|0,2\rangle$. The beamsplitter's reflectivity is varied from 0.5 to 1 and is defined to have a phase shift of $\pi/2$ for the transmission output for each input mode. In this example, at a reflectivity of $1/(3-\sqrt{3}\,) \approx 0.7887$, $P(1,1) = P(2,0) \neq 0$, and $P(0,2) = 0$. Figure recreated from [6].

The result for U can also be written as

$$U = e^{i \arctan(\sqrt{2-\sqrt{3}}\,)} \begin{bmatrix} 0 & 1 \\ 1 & 0 \end{bmatrix} \tag{4.29}$$

This example is the basis of the theoretical work, and describes a beamsplitter with a reflectivity of $1/(3-\sqrt{3}\,)$, which is approximately 78.9%, and a $\pi/2$ phase shift on the transmission modes. Given that the D matrices from these two examples are different, they are unique, and thus one state cannot be transformed into the other with only the use of linear optics.

It starts with a two-photon state and uses linear optical interactions to deterministically remove one of the two-photon components from the state with destructive interference. Similar to how an HOM interaction removes the $|1,1\rangle$ component, this example removes the $|0,2\rangle$ component. This interference comes from interacting the state

$$a\,|2,0\rangle + \sqrt{1-a^2}\;|0,2\rangle \quad , \quad a = \frac{\sqrt{3}+1}{2\sqrt{2}} \tag{4.30}$$

on a variable beamsplitter. The output from the variable beamsplitter consists of the $|1,1\rangle$, $|2,0\rangle$, and $|0,2\rangle$ components. The probability distribution of these components varies as the beamsplitter reflectivity varies from 0.5 to 1 (50% to 100%). At a reflectivity of $1/(3-\sqrt{3}\,)$, the $|1,1\rangle$ and $|2,0\rangle$ probabilities are equal, while the $|0,2\rangle$ is completely extinguished (see Figure 4.1).

Up until this point, all the theoretical calculations assume perfect conditions. This means that there is no loss, noise, or any other form of decoherence. HOM experiments are most effective when there is a high overlap between the two input modes.

Moving further away from the ideal theoretical case, Lund [6] notes that there are a few things that will impact the effectiveness of the measurements in an experimental setting. The first of these considerations is the level of number-resolving detection. For example, if the detector is unable to resolve the number of photons, then it would be unable to tell the difference between a two-photon event (signal) and a one-photon event (noise). This means that noise events would be counted as signal events, degrading the signature. These imperfections, along with others, are later accounted for in an updated model and noticed experimentally.

4.2 Experimental Data: Quantum Processor

We decided to conduct an experimental run using Quandela's fully programmable Ascella quantum processor [94]. This system includes a quantum dot as a single-photon source, which is then passed through a demultiplexer and a universal interferometer. The readout of the data is performed by superconducting nanowire single-photon detectors (SNSPD), which do not have photon number resolving capabilities. However, it is not necessary, as the device is using n-photon coincidence. That is, if photons are input into n modes of the m-mode processor, only n-photon events are registered. The information is then uploaded to the Quandela cloud. The universal interferometer is a 12-mode photonic chip with a reconfigurable photonic integrated circuit produced by QuiX [95]. The reconfigurability is achieved by using resistive heating of 1 *mm* long platinum phase shifters to produce π phase shift. The processor is composed of 66 unit cells, with each cell containing a tunable beamsplitter and a phase shifter. The processor has 12 input and output modes and has a circuit depth of 12, which is the maximum number of unit cells that an input mode can encounter. Additional phase shifters are included in the input and output modes for sub-wavelength delay compensation and external phase tuning. Each tunable beamsplitter is a Mach-Zehnder interferometer [96, 97], each consisting of two 50:50 directional couplers, an internal phase shifter, and an external phase shifter (see Figure 4.2).

This on-chip configuration allows for the implementation of all 12×12 unitary matrices with an average fidelity of $F = 99.7 \pm 0.08\%$. The system efficiency of the optical setup, including the single-photon source brightness, is $\sim 8\%$. The source is measured to have a single-photon purity of $> 99\%$, and indistinguishability of $\sim 94\%$. The overall system four-photon coincidence rate is on order 10^2 Hz [94].

For this particular experiment, only a portion of the quantum processor was used, specifically 5 modes, see Figure 4.4, and the circuit depth required was 5. Figure 4.3 displays the entire quantum processor with an inset, while Figure 4.4 shows the diagram of the experimental settings that were programmed into a subsection of the quantum processor. The value for the "attenuator" beamsplitter ("R3" in Figure 4.4) is chosen[1] to be $1-\gamma = 0.2673$, with $\gamma = 0.7327$ as calculated by the theoretical model under ideal conditions, see Section 4.1. An important thing to note is that while a given circuit design can be passed to Quandela's quantum processor, we do not know[2] the exact arrangements and values of heater settings after Quandela's clear-box optimisation process [98].

Prior to running any experiment on the quantum processor, simulations are calculated using Quandela's open-source framework for Photonic Quantum Programming, Perceval [99]. It is an operator-based quantum optical simulation platform in Python, and it is used for composing circuits using linear

[1] The attenuation is γ, so the reflectivity, or amount of light that remains in the mode is $1-\gamma$.

[2] For commercial reasons, Quandela chooses not to provide this information to end-users.

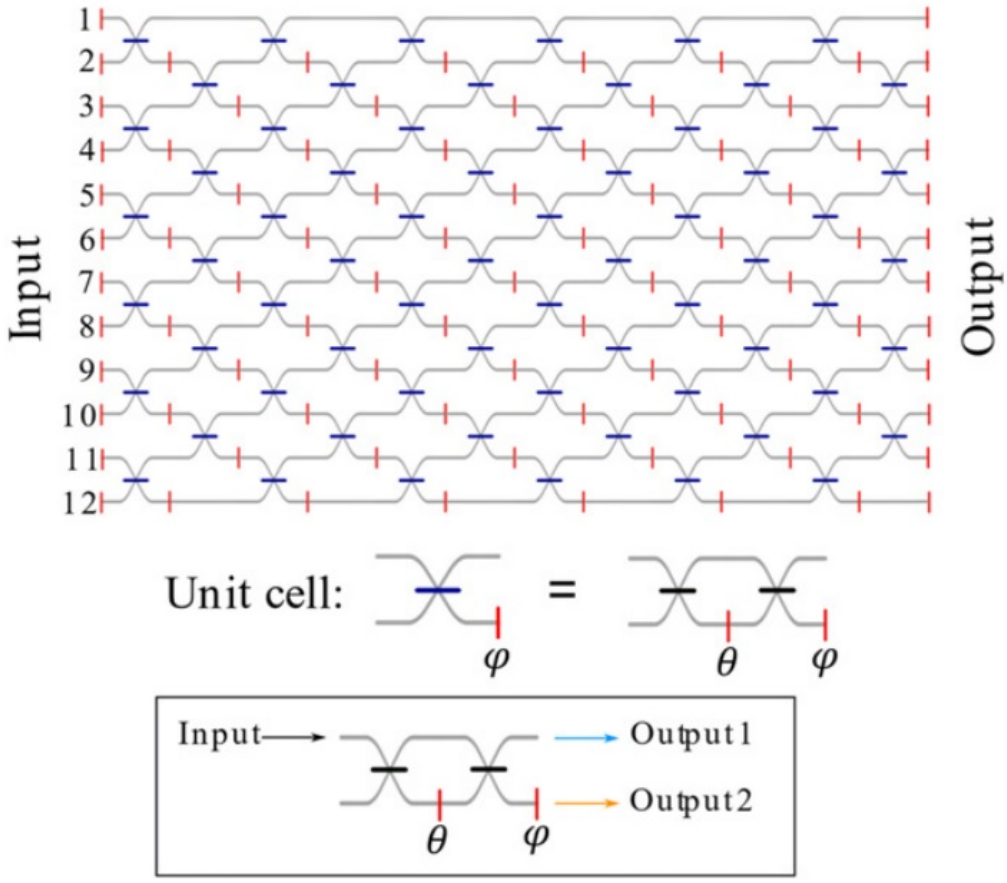


Figure 4.2: Functional diagram of 12-mode photonic processor produced by QuiX. Each blue line is a tunable beamsplitter that is a Mach-Zehnder interferometer with two 50:50 directional couplers (black lines), an internal phase shifter (θ), and an external phase shifter (φ). Phase shifters are also placed at each input and output for sub-wavelength delay compensation and external phase tuning [95].

optical materials[3]. While theoretical calculations were already made for the bulk optics experiment (Figure 4.19), the simulations run on Quandela's cloud system with Perceval are adjusted to the QPU's specific characterization (which, at this point, are not available to the public). The simulation runs are meant to test the code and work through the debugging process without submitting jobs to the QPU, which costs money. Once the simulation runs successfully, the job is then run on the QPU.

When running the experiment on the quantum processor, it calls a job for each circuit. A total of 20 jobs are sent to the processor, each having a different reflectivity value for R2. The matrix representation for each beamsplitter in the circuit is given by the unitary matrix

$$U = \begin{bmatrix} \cos(\theta) & i\sin(\theta) \\ i\sin(\theta) & \cos(\theta) \end{bmatrix} \tag{4.31}$$

Each job is run until a total of 500,000 counts have been registered across all 4 detectors. The data produced by the quantum processor shows a strong correlation to the theoretical calculations under ideal conditions. The first run, seen in Figure 4.5, uses $\gamma = 0.7327$, which is the condition that gives $P_{11} = P_{20}$ coinciding with the minimum of P_{02}. Two additional experiments were conducted using the quantum processor with $\gamma = 0.5327$ and $\gamma = 0.9327$ (see Figure 4.6). These two additional graphs

[3] See `https://perceval.quandela.net/` for a full description of Perceval.

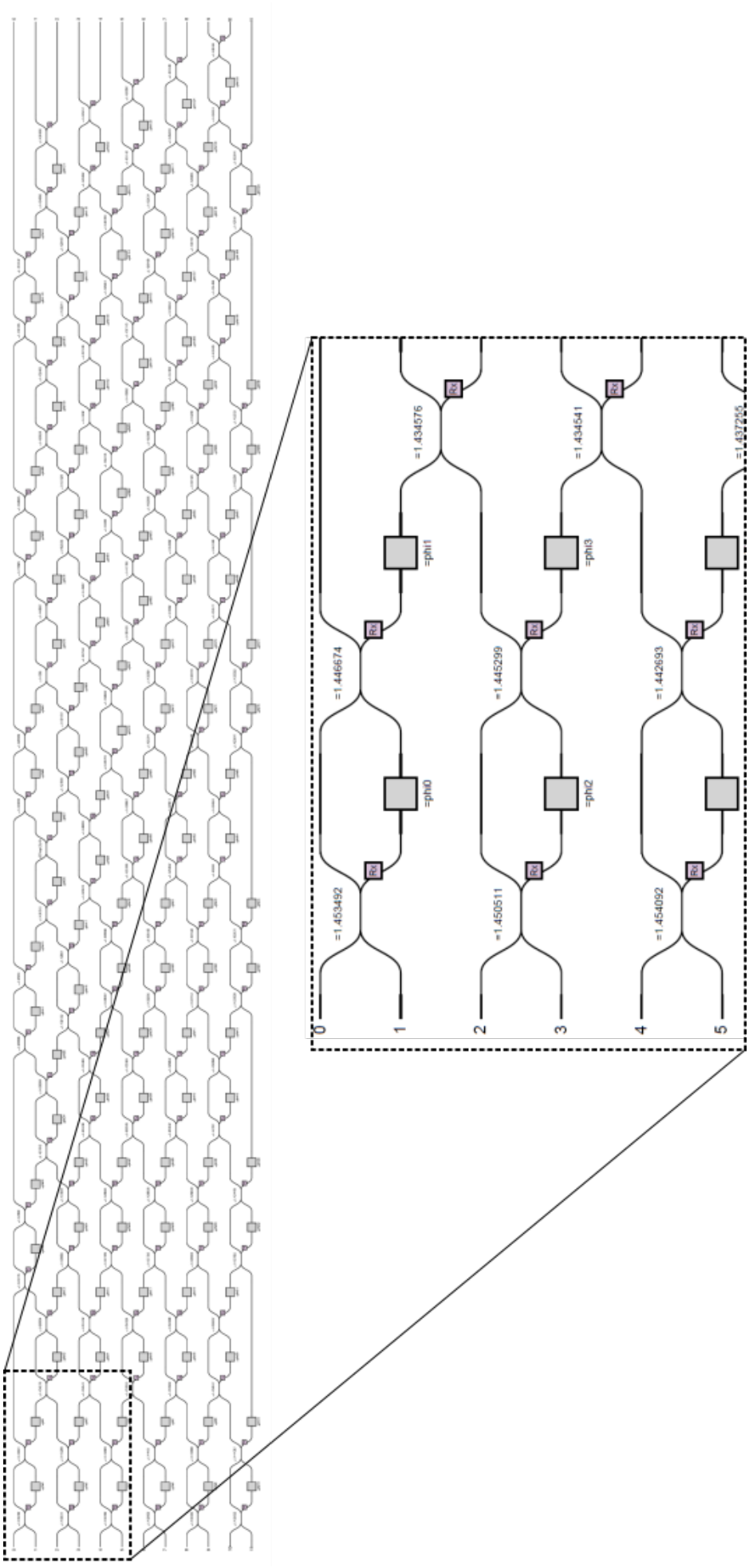


Figure 4.3: Diagram of full quantum processor with inset. The values displayed for the beamsplitters are placeholders.

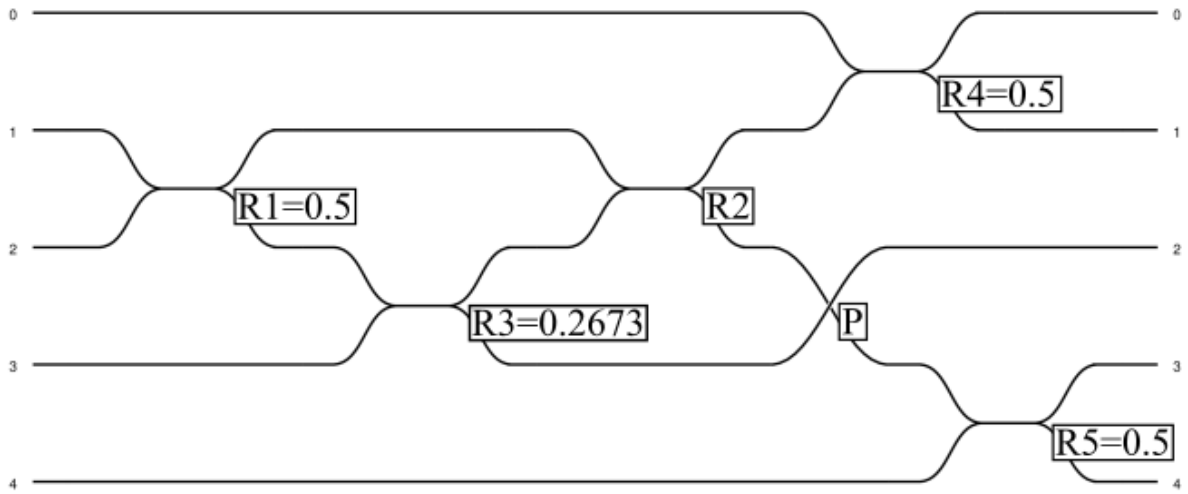


Figure 4.4: Diagram of a subsection of the quantum processor and the setting used to conduct asymmetric quantum interference. The values of R1, R3, R4, and R5 correspond to the reflectivities of the adjacent beamsplitters and are all constant. R3 functions as the attenuator, coupling mode 2 into the loss mode. The value of R2 varies from 0.5 to 1. The label "P" indicates a permutation, or a swapping of modes without interaction. Photons are counted at the output of modes 0,1,3, and 4.

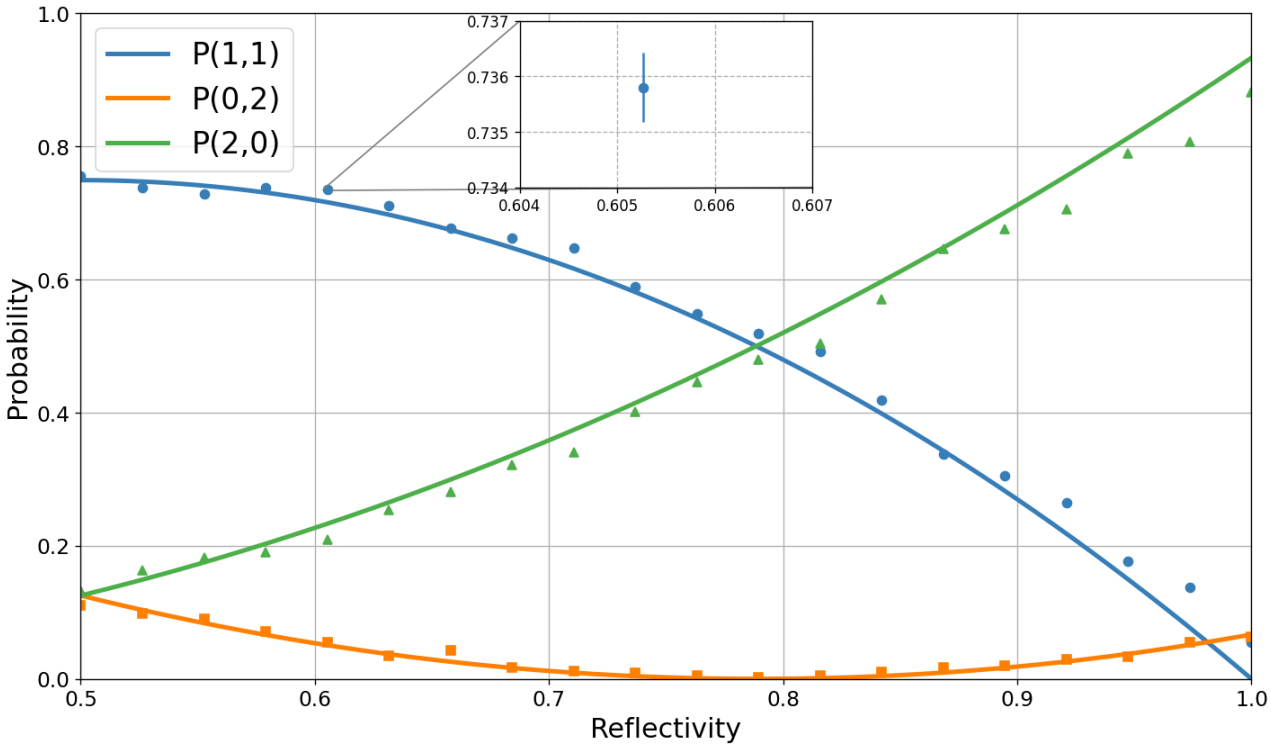


Figure 4.5: Probability distribution of the $|1,1\rangle$, $|2,0\rangle$, and $|0,2\rangle$ states as a function of beamsplitter reflectivity using Quandela's quantum processor with $\gamma = 0.7327$. The data points are compared with the theoretical calculations under ideal conditions (lines). Error bars are confined within points.

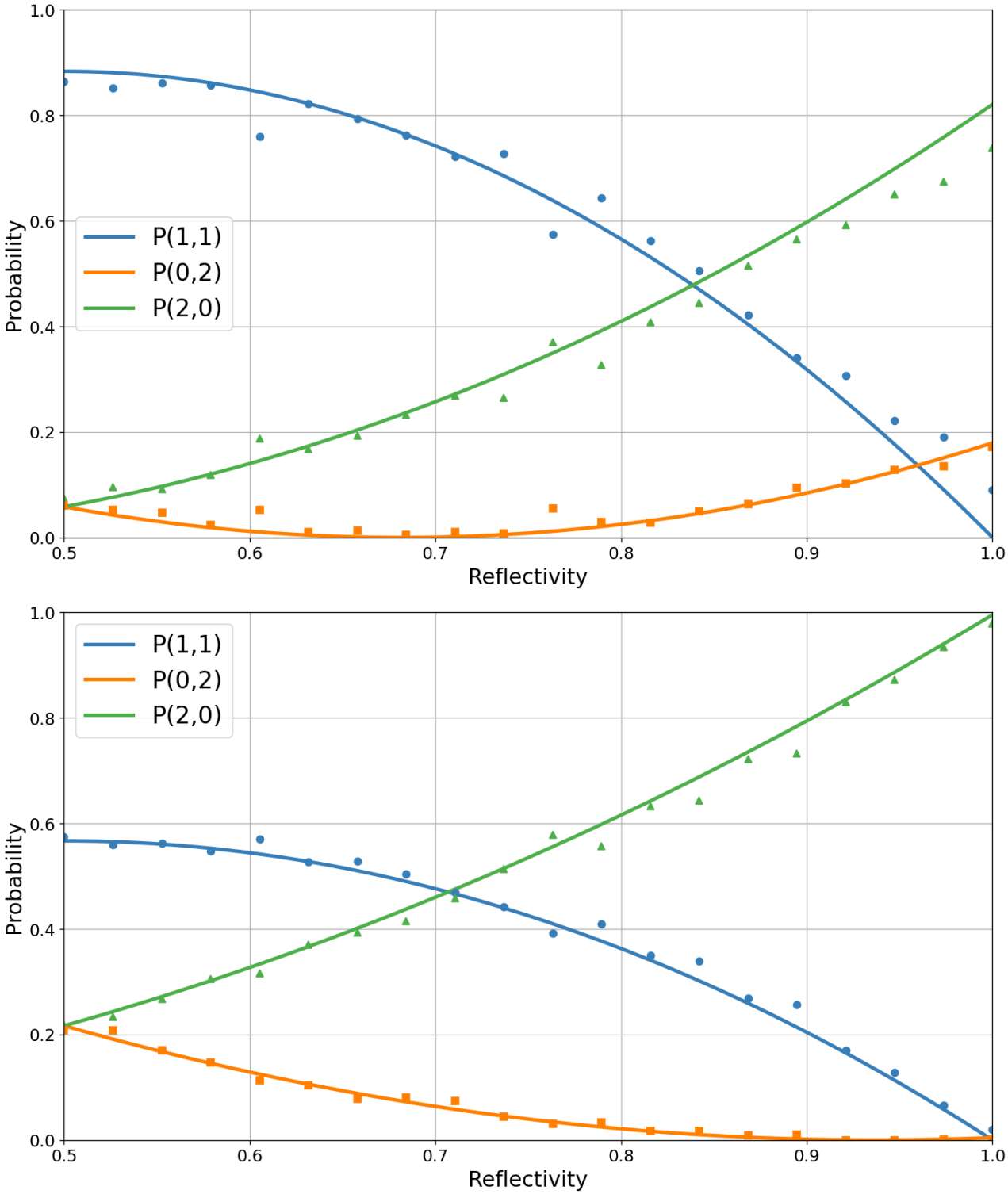


Figure 4.6: Probability distribution of the $|1,1\rangle$, $|2,0\rangle$, and $|0,2\rangle$ states as a function of beamsplitter reflectivity using Quandela's quantum processor for both (Top) $\gamma = 0.5327$, and (Bottom) $\gamma = 0.9327$. The data points are compared with the theoretical calculations under ideal conditions (lines). Error bars are confined within the points.

demonstrate the tunability of the system, allowing for control over the probability distribution of the three states.

The Lund result [6] shows that it is possible to engineer a variety of two-photon entangled states beyond the typical NOON state generated by the usual HOM experiment. Furthermore, this result is produced by linear optical interactions in addition to a controlled amount of loss. This genuine quantum effect can only be detected if using photon-number-resolving detection. In this section, we have been able to demonstrate this concept experimentally on a fully programmable quantum processor chip. This result is being written up for publication.

4.3 Bulk Optics Experimental Construction

We also decided to conduct the experiment locally using bulk optics to compare with the Quandela QPU result. In principle, the experimental construction is quite simple—a variable beamsplitter and a few number-resolving detectors—in practice, quite a bit more is required. While the theoretical model requires the initial state shown in equation 4.30, this state first has to be prepared. This is done by using a Spontaneous Parametric Down Conversion (SPDC) source, a 50:50 beamsplitter, and a variable attenuator.

The SPDC source used in this experiment is a long-established source in the Quantum Technology Laboratory [100]. It is driven by a coherent MIRA 900 mode-locked Ti:Sapphire laser tuned to 820 *nm* emitting at a rate of 76 *MHz*. The pulse is frequency doubled to 410 *nm* by a bismuth borate, BiB_3O_6 (BiBO) crystal, which produces blue light of approximately 900 *mW* power. This is then incident on a type-I phase-matched β-barium-borate (BBO) crystal. The crystal is cut to produce photons when the pump laser has normal incidence with respect to the face of the crystal. The pair of photons exit the crystal with a $\approx 3^{\circ}$ opening angle at a wavelength of 820 *nm*, and are then sent through bandpass interference filters centered at 820 *nm* with a FWHM of 5 *nm*, and coupled into their respective single-mode fibers.

The SPDC source is used to create the state $|1,1\rangle$. Note that in reality, both vacuum and higher-order terms are also created, as we discuss later. The two identical photons created are sent to a 50:50 beamsplitter. This creates the familiar NOON state of

$$\frac{1}{\sqrt{2}}(|2,0\rangle - |0,2\rangle) \tag{4.32}$$

produced by the traditional HOM. Now the question becomes, how does one make the following transformation?

$$\frac{1}{\sqrt{2}}(|2,0\rangle + |0,2\rangle) \rightarrow a\,|2,0\rangle + \sqrt{1-a^2}\;|0,2\rangle \tag{4.33}$$

At a quick glance, these two states are mathematically similar, with the only difference being the probability distributions. Given that

$$a = \frac{\sqrt{3}\;+1}{2\sqrt{2}} \approx 0.966, \tag{4.34}$$

then,

$$P(0,2) = (\sqrt{1-a^2}\;)^2 = 1-a^2 \approx 0.067 \tag{4.35}$$

This means that the $|0,2\rangle$ mode needs to be heavily attenuated by a factor of $(1-0.067)$, i.e., by 93.3%. This can be achieved by placing an attenuator in one of the spatial modes. As mentioned above, it is important to have number-resolving detection. So, the last thing to add is a pair of number-resolving detectors, one for each output arm (Figure 4.7).

The first construction of the experimental setup used two variable fiber beamsplitters with a portion of free space optics between the two. The advantage of using two variable fiber beamsplitters, as opposed to one variable and the other fixed at 50:50, is that it allows for an HOM measurement to be taken at both beamsplitters. This is essential as it assures that the path lengths of the two modes are identical up until the second beamsplitter. The process of setting identical path lengths goes as

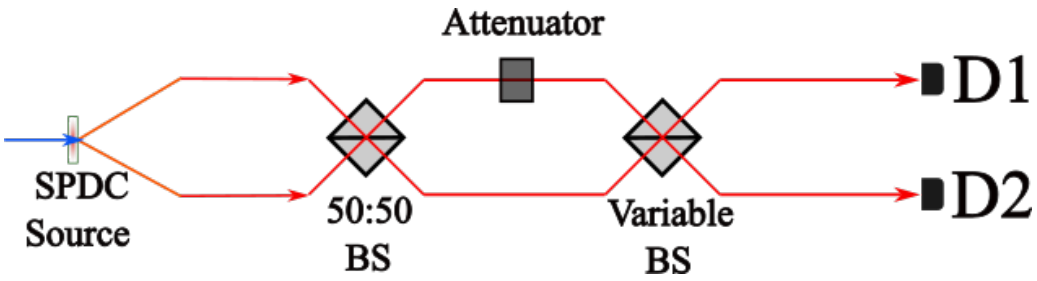


Figure 4.7: Conceptual experimental diagram for asymmetric two-photon interference. Starting with the SPDC source, both signal and idler photons are used as signal photons. Both photons arrive at the 50:50 beamsplitter simultaneously, interacting in a traditional HOM. An attenuator is placed in one of the modes to attenuate the signal by 93.3%. The remaining photons in each mode then arrive simultaneously at a variable beamsplitter. The reflectivity of the variable beamsplitter varies from 0.5 to 1. Finally, photons in each mode are detected by photon number-resolving detectors.

follows. The first fiber beamsplitter is set to 50:50, while the second is set to 0:100 (no interaction). Then, an HOM measurement is taken on the first beamsplitter. This measurement was referred to as HOM1. One of the two fiber couplers was placed just after the SPDC source was mounted on a translation stage. As the translation stage moves back and forth, it changes the free space distance between the SPDC source and the fiber coupler, which changes the overall path length of one of the two modes. The HOM measurement is taken as the path length is varied. The bottom of the HOM dip signifies when two input path lengths are equal up until the first beamsplitter. For the second HOM measurement, known as HOM2, which takes place on the second beamsplitter, the values for the variable beamsplitters were swapped. The first variable beamsplitter was set to 0:100, and the second was set to 50:50. Similar to above, one of the fiber couplers for the second beamsplitters was placed on a translation stage. Again, the HOM was measured as the translation stage moved to find the HOM dip, which signifies equal path lengths. At this point, the path lengths of the two modes are matched from the SPDC source to the first beamsplitter and from the first beamsplitter to the second. It is important to note that no attenuation has been implemented for each HOM measurement. Once completed, the first beamsplitter would be set to and held at 50:50, and the second would be varied from 50:50 to 100:0, which are the experimental testing parameters. The HOM data for this experiment can be seen in Figure 4.17.

The first iteration of the experimental setup included the use of two Newport F-CPL-830-N-FA Variable Ratio Couplers (variable beamsplitters), which use a single knob mechanism to adjust the reflectivity. Both variable beamsplitters were individually characterized to determine the reflectivity as a function of the knob's position, measured using a linear scale. However, during the data collection process, some discrepancies were noticed, which prompted a further investigation into the variable beamsplitters. It was discovered that the variable beamsplitters had mechanical backlash. A calibration curve was taken for these devices, but what was later noticed through a quick sanity check using a power meter was that turning the knob of these devices to and from the same setting yielded vastly different results. This was essentially a quick check to see if a piece of equipment was working properly, and it was easy to determine that it was not without doing a full diagnosis. This very well could also be attributed to the imprecise nature of the manual knob and human error. This now meant that the reflectivity of the variable beamsplitters could not be accurately set. This required a redesign of the experimental setup.

The decision was made to keep the first variable beamsplitter as is. As it was only moved between two settings, 50:50 while running the experiment, and 0:100 for the purpose of measuring

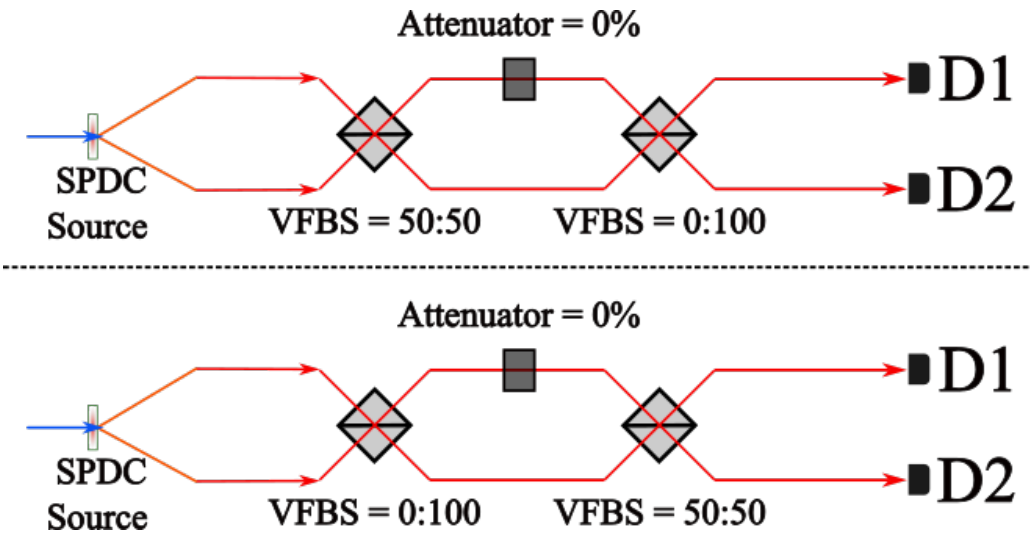


Figure 4.8: Experimental setup for measuring the HOM of the first and second beamsplitter. (Top) The first beamsplitter is set to 50:50, while the second is set to 0:100. A HOM measurement is taken on the first beamsplitter to match the path lengths of the two modes between the SPDC source and the first beamsplitter. (Bottom) The second beamsplitter is set to 50:50, while the first is set to 0:100. An HOM measurement is taken on the second beamsplitter to match the path lengths of the two modes between the first and second beamsplitters.

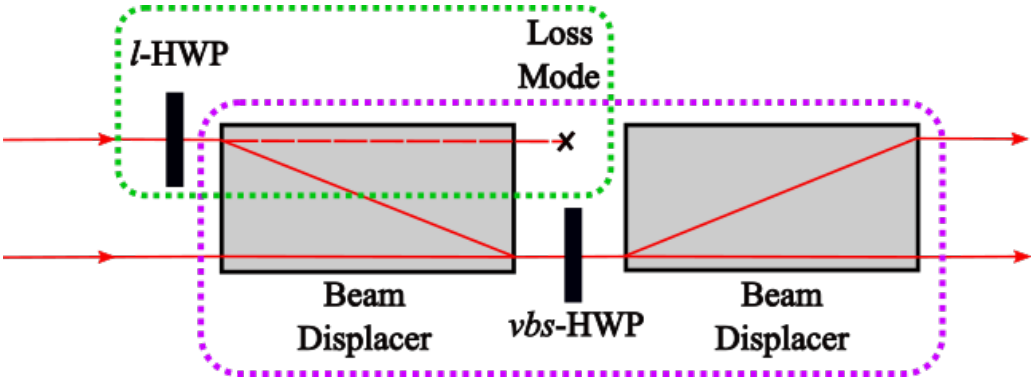


Figure 4.9: Experimental construction of the variable beamsplitter (Purple) and the variable attenuator (Green). Light in the top (bottom) mode is horizontally (vertically) polarized. The top mode passes through an adjustable half-waveplate, ℓ-HWP, which rotates the polarization to any linear polarization. The first beam displacer then splits this light: the vertically polarised component is lost (x) while the horizontally polarized component is deflected to become coaxial with the bottom mode. Since the bottom mode is vertically polarized, it passes through the first beam displacer without any effect. Both the horizontal and vertical components pass through a second half-waveplate, *vbs*-HWP, which rotates both components to any linear orientation. As the rotated beams enter the second beam displacer, the horizontal component of each is deflected, and the vertical component of each passes straight through: the combination of half-waveplate and beam displacer acts as the variable beamsplitter.

HOM2. In addition, the reflectivity of 50% can always be verified before executing experimental runs. In contrast, the second variable beamsplitter was removed and replaced with a more complex, but more advantageous design. The first of these advantages is repeatability, which was the main issue. The second is that the variable attenuator was incorporated into the design of the new variable beamsplitter. Lastly, the new variable beamsplitter was electronically automated.

The new design for the second variable beamsplitter consisted of a total of four components, a pair of calcite beam displacers and a pair of half-waveplates. The calcite beam displacer is polarization-

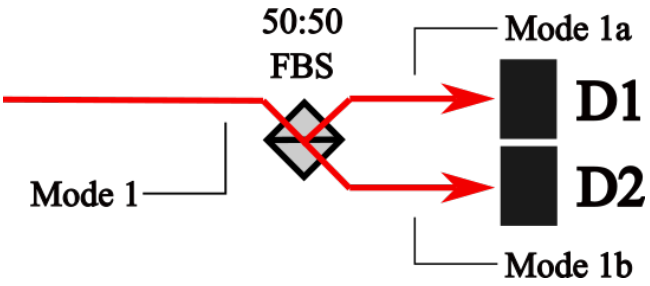


Figure 4.10: Pseudo-number-resolving photon detection. When a number-resolving detection is unavailable, the single detector is replaced by a 50:50 beamsplitter (splitting the mode into two sub-modes, 1a and 1b) and two non-number-resolving detectors. If only one detector registers a photon event, it signifies a single photon in the mode. If both detectors register photon events simultaneously, it signifies two photons in the mode. As two photons pass through the beamsplitter, there is a 50% chance that one photon will pass into each output channel of the beamsplitter. This means that two-photon events are being recorded half of the time, while the other half of the time, they are being falsely registered as single-photon events.

dependent: vertically polarized light travels straight through the crystal, while horizontally polarized light is deflected to a parallel path, as shown in Fig. 4.9. The variable beamsplitter was constructed as two calcite beam displacers with an HWP in between them. Two beams are incident on the first calcite beam displacer. The top beam is linearly polarized, the vertical component passing through the displacer as loss (so acting as the variable loss element), the horizontal component is displaced to act as input to the variable half-waveplate, *vbs*-HWP. The bottom beam is vertically polarized and passes straight to this waveplate. The polarization of the coaxial beams are adjusted with *vbs*-HWP, and the beams are input to the second calcite displacer. The beams then enter the second displacer: the horizontal component of each is deflected, and the vertical component of each passes straight through, thus forming the variable beamsplitter. If *vbs*-HWP is set to 0°, the polarizations do not change, and VBS acts as a beamsplitter with 100% transmission. If the axis is set to 45°, then the vertical (horizontal) component is rotated to horizontal (vertical), and the VBS acts as a beamsplitter with 100% reflection. If the axis is set to 22.5°, then the vertical (horizontal) component becomes diagonal (anti-diagonal), and both are split 50:50 by the calcite crystal: the VBS acts as 50:50 beamsplitter. These are just three examples, but the axis of the HWP (with respect to the vertical) can be set anywhere from 0° to 45°, which covers the full spectrum of reflectivity.

The next major component of the system is the detection scheme. As mentioned above, it is important to have number-resolving detection to distinguish between single-photon and multi-photon events. The solution is to construct a pseudo-photon-number-resolving detection scheme with avalanche photodiodes (APD). These APDs are non-number-resolving photon detectors, meaning that they are unable to differentiate between a single-photon event and a multi-photon event. However, instead of using one detector per mode, each mode was fitted with a 50:50 beamsplitter and two APDs. The mode hits the beamsplitter, which splits up the mode into mode 1a and mode 1b (see Figures 4.10 and 4.11). Each of these sub-modes is then measured by an APD. This system is essentially a four-photon detection tree similar to those described in [101, 102] with the first beamsplitter being a variable beamsplitter.

This system can now differentiate between single-photon and multi-photon events, as illustrated by the following example. As one photon enters the system, it will either be transferred into mode 1a or mode 1b, and thus only triggering one of the APDs. If two photons enter the system, one will be

transferred into mode 1a and the other into mode 2b. In this case, both APDs will be triggered at the same time. So, a single APD triggering registers a single-photon event, while both APDs triggering registers a two-photon event. However, this scheme is not a true photon number-resolving detection scheme but a pseudo-photon-number-resolving detection scheme. The first reason is that this system cannot compensate for events of more than two photons. The second reason has to do with the nature of the beamsplitter. In the case of a photon incident on a 50:50 beamsplitter, the photon has a 50% chance of exiting through each output. This probability distribution is unaffected by any photons that pass through the beamsplitter before or after, much like the flipping of a coin. No matter how often a coin has been flipped, the next flip will have an equal probability of showing heads or tails. This also holds true for two photons arriving at the beamsplitter at the same time. The output one photon takes is completely independent of the other photon. This means that in the case of a two-photon event, both photons will be transferred to the same output sub-mode and only trigger one of the APDs. This would falsely register a single-photon event. To fully break down the probability, consider two photons entering the system as depicted in Figure 4.10, the probability distribution of the photons being transferred into the sub-modes 1a and 1b is as follows.

The first photon enters sub-mode **1a** with a probability of 0.5, and the second photon enters sub-mode **1a** with a probability of 0.5. This gives an overall probability of $0.5 \times 0.5 = 0.25$.

The first photon enters sub-mode **1b** with a probability of 0.5, and the second photon enters sub-mode **1b** with a probability of 0.5. This gives an overall probability of $0.5 \times 0.5 = 0.25$.

The first photon enters sub-mode **1a** with a probability of 0.5, and the second photon enters sub-mode **1b** with a probability of 0.5. This gives an overall probability of $0.5 \times 0.5 = 0.25$.

The first photon enters sub-mode **1b** with a probability of 0.5, and the second photon enters sub-mode **1a** with a probability of 0.5. This gives an overall probability of $0.5 \times 0.5 = 0.25$.

It can be seen that the four possible outcomes are all equally likely at 25%. However, two of the possible outcomes are cases where both photons are transferred into the same sub-mode (both photons in 1a or 1b). This means that half the time, two-photon events are being registered as one-photon events, which is considered a loss, as there is no way to distinguish this from the case in which one mode loses a photon. In other words, two-photon events are only being detected half the time. This is not ideal and thus leaves room for improvement in any future experiments by using photon-number-resolving detectors, which would allow flagging and ignoring the three-or-more photon events while accurately recording the $|2,0\rangle$ and $|0,2\rangle$ states (currently recorded 50% of the time). This will need to be accounted for in the theoretical model.

The last thing to consider for this detection scheme is when higher order terms are present. Take the case of the $|2,2\rangle$ state being produced by the SPDC source. This would result in a possibility of a total of three or four photons reaching the detectors. While the cases of triple or quadruple coincidences could be removed by post-selection, there are cases where photons end up in the same detection outputs. This results in some three or four-photon states being registered as a two-photon state. This would result in a false count.

Running the experiment and analyzing the data, as seen in Figure 4.12, uncovered a large discrepancy

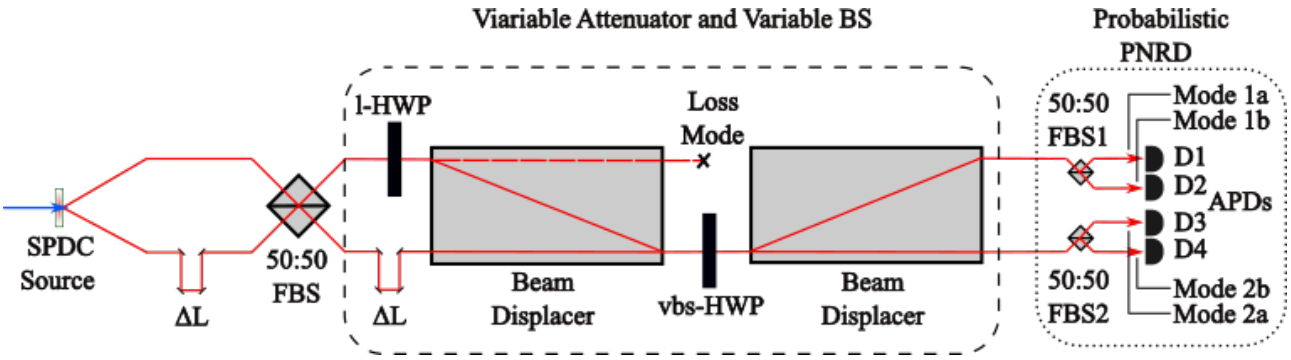


Figure 4.11: Full experimental diagram for asymmetric two-photon interference in a single mode. Two photons are produced by a SPDC source and sent into two spatial modes. First passing through a single 50:50 fiber beamsplitter and then a series of half-waveplates and beam displacers, which construct a variable beamsplitter and variable attenuator, as described in figure 4.9. Finally, photons in the two modes are detected by the probabilistic photon-number-resolving detection scheme as described in figure 4.10. The detectors are each connected to a time tagger that records the time of detection to ps accuracy, and a PC for data collection.

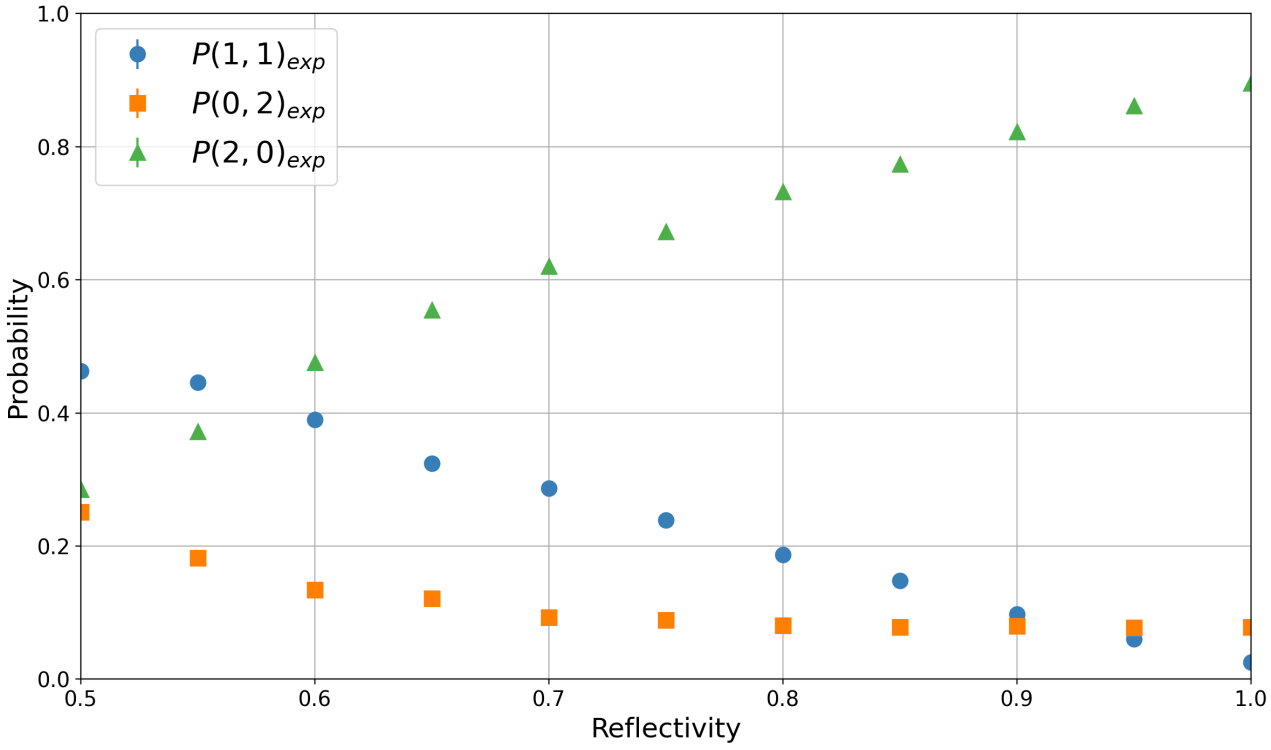


Figure 4.12: Probability distribution of the $|1,1\rangle$, $|0,2\rangle$, and $|2,0\rangle$ states using a bulk optics experimental setup with $\gamma = 0.933$. Error bars confined within points.

when compared to the theoretical calculations shown in Figure 4.1. While the trends of the $|1,1\rangle$, $|0,2\rangle$, and $|2,0\rangle$ states showed a general resemblance to the theory, it was clear that the model did not match the experimental conditions. This led us to revisit the theoretical model.

4.4 Improving the Bulk Optics Theoretical Model

Before continuing, a very important distinction must be made. While constructing the bulk optics experiment, it was understood that the attenuation to the first mode should be set to 93.3%, or $\gamma = 0.933$. However, when reconstructing the theoretical model under ideal conditions and reproducing the results

shown by Lund [6] (Figure 4.1), we calculated that the attenuation of the first mode should be 73.27%, or $\gamma = 0.7327$. This is one of the reasons the results of Figure 4.12 differ from the ideal theory. Lund was contacted for an explanation of how their result was obtained, but no response was received. By the time this discrepancy was realized, the experiment had been cannibalized to provide components for other experiments, and thus, it was not possible to take new data. Because of this, moving forward, the value of $\gamma = 0.7327$ will be used for any theoretical calculations, while the value of $\gamma = 0.933$ will be used when fitting the bulk optics experimental data.

With the updates to the experimental construction, the theoretical model needed to be updated to match. The first thing to consider is that the SPDC source is not a perfect single-photon source. Oftentimes, an SPDC source will produce multiple photons in each mode. These are known as the higher-order terms. They do not occur as frequently compared to the single two-fold events [103] (one photon in each mode), but are significant enough to disrupt the statistics. While some techniques can be implemented to reduce the rate at which higher-order terms are produced [104], the simplest fix is to reduce the power of the pumping laser. The other two main components to consider are background noise and loss. Two other factors are present in nearly every optical experiment. The main reasons for this include mirrors not having perfect reflectivity, imperfect coupling from free space into optical fibers, and light scattering. All of these things can be grouped into system loss. A final addition was made to the theoretical model to account for imperfect photon indistinguishability at the two beamsplitters.

4.4.1 Higher-Order Terms in Down Conversion

Starting at the beginning to understand how higher-order terms are produced in an SPDC source, the interaction between the pump beam and the nonlinear crystal is described by the Hamiltonian [105]

$$\hat{H}_{SPDC} = i\hbar\chi a_1^\dagger a_2^\dagger + H.c. \tag{4.36}$$

where, similar to above, $a_1^\dagger$ and $a_2^\dagger$ are the creation operators for modes 1 and 2, respectively. χ is the efficiency parameter, which in this case represents the interaction strength between the pump laser and the nonlinear crystal. χ is also linearly proportional to the amplitude of the electric field of the pump laser. Now the output state of the SPDC source can be written as [106]

$$\Psi_{SPDC} = \sqrt{1-|\varepsilon|^2}\sum_{n=0}^{\infty}\varepsilon^n |n,n\rangle . \tag{4.37}$$

Here, $\varepsilon = \chi\tau$ where τ is the interaction time of the pump pulse inside the nonlinear crystal. Now, the probability of producing n photons in each mode is given by

$$P(n) = (1-|\varepsilon|^2)|\varepsilon|^{2n}. \tag{4.38}$$

The probability of witnessing higher-order terms ($n \geq 2$) is directly related to ε, which is in turn related to χ. This gives that as the strength of the electromagnetic field of the pump laser is increased, so will the probability of producing higher-order terms. While reducing the power of the pumping laser does reduce the probability distribution of these terms, it does not completely eliminate them, and thus, must still be considered in the theoretical model. Furthermore, reducing the power also reduces the single-photon production rate and leads to longer experiment times to accumulate sufficient statistics.

4.4.2 System Loss and Noise

In every physical photonic experiment, there is inherent loss. These losses arise in almost every component of the experimental setup. A notable source of loss in our experiment is due to detector inefficiencies, which are about 58% at 820 nm[4]. Since this is a two-photon experiment, we estimate the overall detector efficiency as η_{det}=0.58^2∼0.33. Mirrors, lenses, half-wave plates, and the calcite beam displacers are all anti-reflection coated, with per-coating losses on the order of 1% or less [5]. Considering each beam path encounters 4 mirrors, 4 HWP surfaces (2 surfaces per HWP), 4 calcite beam displacer surfaces (2 surfaces per beam displacer), and 4 lens surfaces (2 surfaces per lens), the efficiency for the combined optical elements is η_{opt}=0.85.

Our experiment has four fiber-coupling points: 1) two modes from the SPDC into the fibers that go to the free-space optics; and 2) after the free-space optics, two modes into each detector fiber. Fiber-coupling efficiencies can vary from 20% to 90% [108–110], in our experiment the we estimated the efficiences to be of order 50%, yielding an overall efficiency of η_{fib}=0.5^4∼0.0625. Thus the overall system efficiency is η_{tot}=$\eta_{det}\eta_{opt}\eta_{fib}$∼1.7%.

In our experiment, the primary source of noise is dark counts from the detectors and background counts from environmental light coupled into the detection fibers. When coincidence counting, if no deliberate signal is being put onto the detectors, then we label the measured coincidences as *accidentals*. In practice, dark counts add little to accidentals: our detectors typically have <400 dark counts per second, and we have a coincidence window of a few *ns*, so we expect accidental dark counts of $3ns\times(400cps)^2$=4.8×10^{-4} per second [111]. We observe an accidental rate of a few counts per second: the majority of these are due to environmental light.

4.4.3 Imperfect Indistinguishability

It is well known that imperfect indistinguishability between photons has an effect on the quantum interference occurring in an HOM experiment [112, 113] and other multi-photon interference [114]. That is, two photons that are even slightly distinguishable interacting on a 50:50 beamsplitter will not produce a pure $\frac{1}{\sqrt{2}}(|2,0\rangle+|0,2\rangle)$ state. To model indistinguishability in the system, we use phase averaging [105, 115].

Phase averaging consists of applying a random phase to one mode before interfering on the beamsplitter and averaging. The phase operator in this basis ($|0\rangle$, $|1\rangle$, $|2\rangle$) is defined as

$$U_\phi = diag(1, e^{i\phi}, e^{2i\phi}) \tag{4.39}$$

and acts as a phase rotation on one mode. Given a density operator of a perfectly indistinguishable state, ρ_{ind}, the simulated distinguishable density operator is

$$\rho_{dist} = \frac{1}{2\pi}\int_0^{2\pi} U_\phi \rho_{ind} U_\phi^\dagger d\phi. \tag{4.40}$$

[4]Taken from Single Photon Counting Module SPCM-AQR Series datasheet [107]

[5]Mirror coatings: `https://www.thorlabs.com/newgrouppage9.cfm?objectgroup_id=139&pn=BB1-E03`; Lens transmission: `https://www.thorlabs.com/newgrouppage9.cfm?objectgroup_id=3811`; HWP transmission: `https://www.thorlabs.com/newgrouppage9.cfm?objectgroup_id=711`; Calcite Polarizer used as proxy: `https://www.thorlabs.com/newgrouppage9.cfm?objectgroup_id=815`

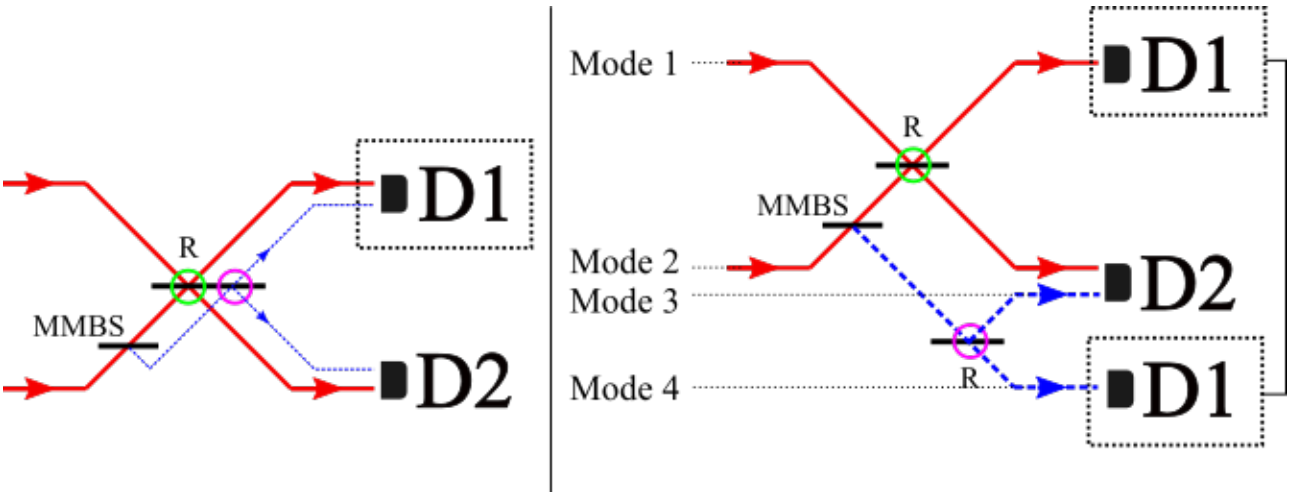


Figure 4.13: Diagram of mode mismatch calculation. (Left) Prior to the interaction on the variable beamsplitter or reflectivity "R", a portion of the light from one mode is picked off by the "mode mismatch beamsplitter" (MMBS). This portion of picked-off light is sent through the variable beamsplitter as well, but without interacting with other modes. (Right) This is modeled by sending the picked-off portion to a separate pair of modes that mimic the remainder of the original circuit.

Now, in practice, it is not possible to integrate over an infinite continuum of phases. So we approximate by summing over discrete phase values.

$$\rho_{dist} \approx \frac{1}{N_\phi} \sum_{k=1}^{N_\phi} U_{\phi_k} \rho_{ind} U_{\phi_k}^\dagger, \quad \phi_k = \frac{2\pi k}{N_\phi}. \tag{4.41}$$

Now, the imperfectly indistinguishable state is modeled as a convex mixture of the two cases.

$$\rho = \xi \rho_{ind} + (1-\xi)\rho_{dist} \tag{4.42}$$

where ξ is the indistinguishability coefficient.

4.4.4 Mode Mismatch

In free space optics, misalignment of the two beams on a beamsplitter can cause a degradation of the HOM measurement [116,117]. While we do not consider this to be a factor for the first 50:50 beamsplitter, as it is a fiber beamsplitter and thus can be assumed to have near perfect mode overlap, it must be considered for the variable beamsplitter for the following reason. Because the variable beamsplitter is a free space beamsplitter, the alignment of the two modes is the subject of human alignment capabilities.

When the two beam modes do not overlap perfectly on the beamsplitter, the portions of the modes that are not overlapping do not interact quantum mechanically. The way in which we modeled this is by picking off a portion of one mode prior to the beamsplitter interaction. The portion that is picked off then runs through the rest of the circuit without interacting with the other mode. This is done by introducing two additional modes to the system that mimic the remainder of the circuit, but with the picked-off portion of the mode (see Figure 4.13). The mode-mismatched light is recorded by the same detectors (D1 and D2), simulating photon counts that did not experience interference on the variable beamsplitter.

4.4.5 Bulk Optics Theoretical Model

First, it is important to define some of the key elements used in the system. The unitary operator of a beamsplitter between two modes is

$$U_{BS}(\theta) = e^{-i\theta(a_1^\dagger a_2 + a_1 a_2^\dagger)}, \tag{4.43}$$

where θ determines the reflectivity of the beamsplitter. Next, the operator for the SPDC source, which includes the production of higher-order terms, is as follows.

$$U_{SPDC}(\eta) = e^{-i\eta(a_1^\dagger a_2^\dagger + a_1 a_2)} \tag{4.44}$$

Here, η determines the distribution of the higher-order term production [118].

However, it is important to note that this is no longer a two-mode system. In the process of modeling loss, one cannot simply remove photons from either mode without having anywhere for these photons to go. Hence, a third mode is needed, which is a place for the lost or attenuated photons to go. This additional mode was creatively labeled as the loss mode. Loss or attenuation for each of the two original modes can be modeled by using the same beamsplitter operator as seen in equation 4.43, but between the respective mode and the loss mode. The loss or attenuation operator from the first mode is

$$U_{L1}(\theta) = e^{-i\theta(a_1^\dagger a_L + a_1 a_L^\dagger)}, \tag{4.45}$$

and similarly for loss and attenuation from the second mode

$$U_{L2}(\theta) = e^{-i\theta(a_2^\dagger a_L + a_2 a_L^\dagger)}. \tag{4.46}$$

Starting from the beginning, the initial state of the system produced by the SPDC source is

$$\psi_i = U_{SPDC}(\eta)\psi_0, \tag{4.47}$$

where η is adjusted to approximate how frequently higher-order terms are produced and ψ_0 is the vacuum state. The density matrix of the initial state is

$$\rho_i = \psi_i \psi_i^\dagger. \tag{4.48}$$

As the system progresses through the first beamsplitter, the indistinguishable density matrix becomes

$$\rho_{BS,ind} = U_{BS}(\frac{\pi}{4})\psi_i \psi_i^\dagger U_{BS}^\dagger(\frac{\pi}{4}) \tag{4.49}$$

This gives the imperfect indistinguishable density matrix of

$$\rho_{BS} = \xi_1 \rho_{BS,ind} + (1-\xi_1)\rho_{BS,dist} \tag{4.50}$$

where ξ_1 is the measured indistinguishability coefficient at the first beamsplitter and $\rho_{BS,dist}$ is calculated as dictated by Equation 4.41.

Applying the attenuation to the first mode.

$$\rho att = U_{L1}(\theta)\rho_{BS} U_{L1}^\dagger(\theta) \tag{4.51}$$

In this situation, the value of θ is dependent on how much attenuation, γ, is desired. The value of θ is calculated as

$$\theta = \arcsin\sqrt{\gamma} \tag{4.52}$$

Up until this point, no dephasing (noise and loss) has been introduced into the model. To do so, the Kraus representation theorem [119] was introduced (see Chapter 3.3). As mentioned previously, the system has become a three-mode system with the inclusion of the loss mode. The approach in modeling the dephasing of the system is to treat it like a qutrit. The dephasing of the qutrit state is as follows [120]. The presence of noise in a system can be written as the following sum of Kraus operators.

$$\kappa(\rho) = \sum_j K_j \rho K_j^\dagger \tag{4.53}$$

Where the Kraus operators, K_j, are subjected to the condition

$$\sum_j K_j K_j^\dagger = \mathbf{I}. \tag{4.54}$$

and the index j labels the different Kraus operators.

Now, the Kraus operators for qutrits are as follows. Say that dephasing noise causes the qutrit state to become completely mixed with probability p, then

$$K_0 = \sqrt{1-p}\,\mathbf{I}, \quad K_1 = \sqrt{\frac{p}{8}}\,\mathbf{Y}, \quad K_2 = \sqrt{\frac{p}{8}}\,\mathbf{Z}, \quad K_3 = \sqrt{\frac{p}{8}}\,\mathbf{Y}^2, \quad K_4 = \sqrt{\frac{p}{8}}\,\mathbf{YZ}, \tag{4.55}$$

$$K_5 = \sqrt{\frac{p}{8}}\,\mathbf{Y}^2\mathbf{Z}, \quad k_6 = \sqrt{\frac{p}{8}}\,\mathbf{YZ}^2, \quad K_7 = \sqrt{\frac{p}{8}}\,\mathbf{Y}^2\mathbf{Z}^2, \quad K_8 = \sqrt{\frac{p}{8}}\,\mathbf{Z}^2 \tag{4.56}$$

$$\mathbf{I} = \begin{bmatrix} 1 & 0 & 0 \\ 0 & 1 & 0 \\ 0 & 0 & 1 \end{bmatrix} \quad , \quad \mathbf{Y} = \begin{bmatrix} 0 & 1 & 0 \\ 1 & 0 & 0 \\ 0 & 0 & 1 \end{bmatrix} \quad , \quad \mathbf{Z} = \begin{bmatrix} 1 & 0 & 0 \\ 0 & \omega & 0 \\ 0 & 0 & \omega^2 \end{bmatrix} \quad , \quad \omega = e^{i\frac{2\pi}{3}} \tag{4.57}$$

The value of $p = 0.3$ was used in these calculations to demonstrate the effect of an arbitrary decoherence.

Now, to put it all together. Similar to above, the photons in the model interact on the first 50:50 beamsplitter and the variable attenuator. At this point, the density matrix is as shown in equation 4.51. Here is where the global dephasing is introduced, and thus the density matrix becomes

$$\rho_D = \sum_{k=0}^{8} \sum_{j=0}^{8} K_k K_j \rho_{att} K_j^\dagger K_k^\dagger. \tag{4.58}$$

The reasoning for the double sum is that the dephasing must be applied to both modes. So, K_k applies to mode 1, while K_j applies to mode 2.

Moving further through the optical circuit, this is where the mode mismatching is implemented. In order to do that, a beamsplitter unitary is implemented between modes 2 and 3. This models light being picked off from mode 2 and sent into mode 3.

$$\rho_{mm} = U_{BS23}(\theta_{mm})\rho_D U_{BS23}^\dagger(\theta_{mm}) \tag{4.59}$$

Here, θ_{mm} determines how much light is picked off from mode 2 and sent to mode 3.

For the final step, the variable beamsplitter is applied. However, because the light in mode 3 is the mode-mismatched light, it also needs to be subjected to the same operation. So, the same variable beamsplitter operation is applied between modes 1 and 2, and modes 3 and 4 (mode 4 is only necessary because a beamsplitter needs two out modes). Modes 1 and 2 interact quantum mechanically, while light in mode 3 interacts classically, as there is no light in mode 4.

$$\rho_{vbs} = U_{BS34}(\theta_{vbs})U_{BS12}(\theta_{vbs})\rho_{att}U^{\dagger}_{BS12}(\theta_{vbs})U^{\dagger}_{BS34}(\theta_{vbs}) \tag{4.60}$$

Here, U_{BS12} is a beamsplitter unitary between modes 1 and 2, while U_{BS34} is a beamsplitter unitary between modes 3 and 4. The value of θ_{vbs} is varied from $\pi/4$ to $\pi/2$. This is equivalent to varying the beamsplitter transmission-reflection ratio from 50:50 to 100:0.

Several theoretical calculations were made, each introducing one component at a time to show the evolution of the plots. First, the theoretical calculations of the state when accounting for the higher-order terms can be seen in Figure 4.14. Calculations accounting for SPDC higher-order terms and decoherence can be seen in Figure 4.15. Calculations accounting for SPDC higher-order terms, decoherence, indistinguishability on the first beamsplitter, and mode mismatch on the varaible beamsplitter can be seen in Figure 4.16. For all of these calculations, $\gamma = 0.7327$, $\eta = 0.4$, and $p = 0.3$ (for both modes). The values of η and p are arbitrary choices to demonstrate the effect of higher-order terms and decoherence on the system. In this specific case, the modeled probability distribution of the states produced by the SPDC source is

$$P_{SPDC|00\rangle} = 0.8327, \quad P_{SPDC|11\rangle} = 0.1466, \quad P_{SPDC|22\rangle} = 0.0207. \tag{4.61}$$

Terms of even higher order ($|3,3\rangle$, $|4,4\rangle$, etc.) were not included as they are produced at diminishingly smaller rates.

There are two things of note. The first being that the $|0,2\rangle$ state no longer experiences complete destructive interference. The second is that the reflectivity at which the $|1,1\rangle$ and $|2,0\rangle$ probabilities are equal has been slightly shifted when compared to the ideal case in Figure 4.1. Already, this shows the impact of including higher-order terms in the model in that they can be registered as two-photon events ($|1,1\rangle$, $|2,0\rangle$, and $|0,2\rangle$ states) without the ability of photon-number-resolving post selection.

The effect of including system decoherence and decoherence with higher order terms can be seen in figures 4.15. Notice that the decoherence and higher-order terms have a small but noticeable effect on the system. However, when implementing the effect of imperfect indistinguishability and mode mismatch, a much more noticeable effect takes place, as seen in Figure 4.16.

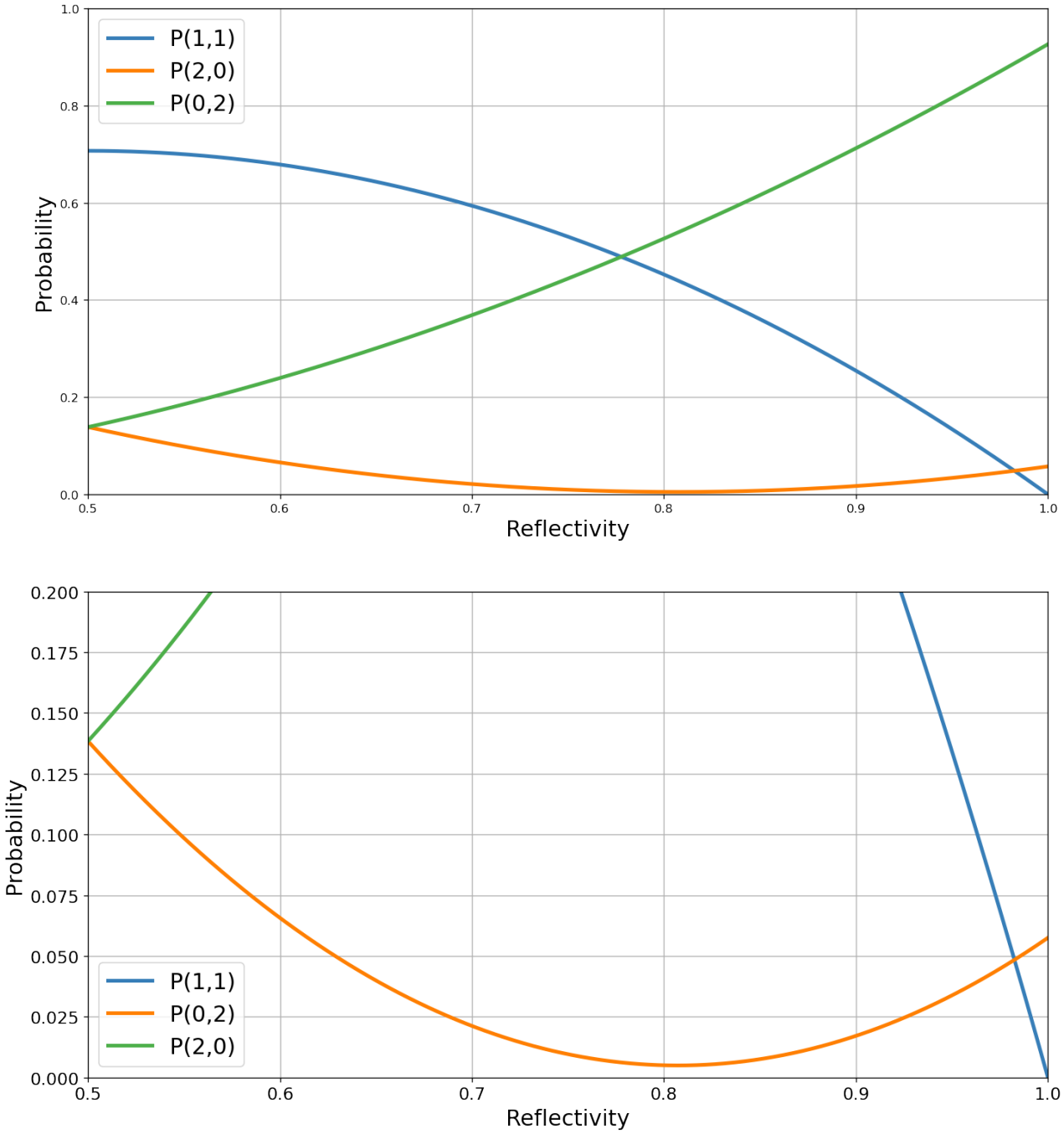


Figure 4.14: (Top) Theoretical probability distribution of the state with the production of higher-order terms from the SPDC source with $\gamma = 0.7327$, and $\eta = 0.4$. (Bottom) Zoomed in view of the $|0,2\rangle$ state showing imperfect destructive interference.

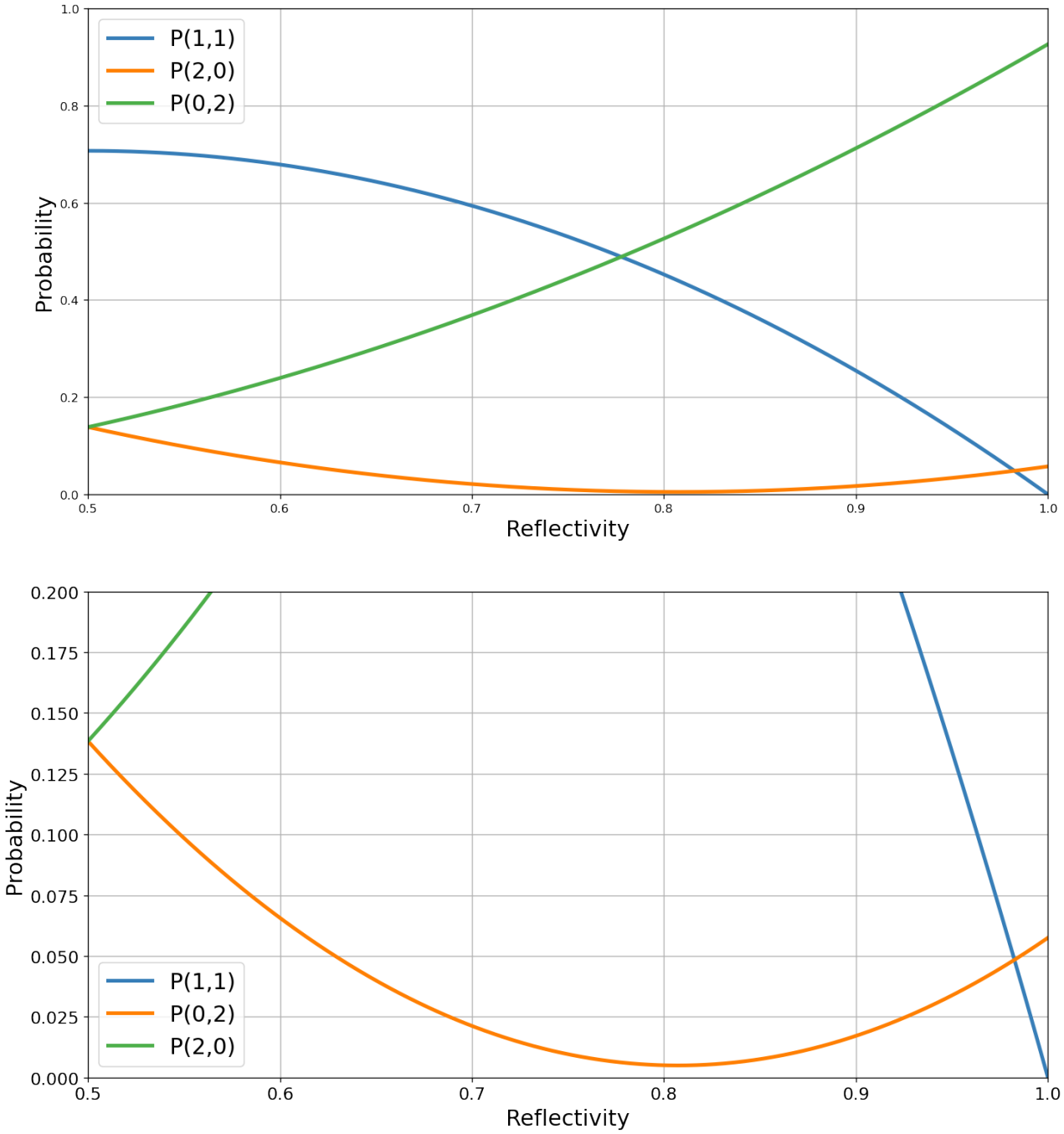


Figure 4.15: The output state probability distribution as a function of variable beamsplitter reflectivity with decoherence and higher-order terms. In this case, $\gamma = 0.7327$, $\eta = 0.4$, and $p = 0.3$ (for both modes).

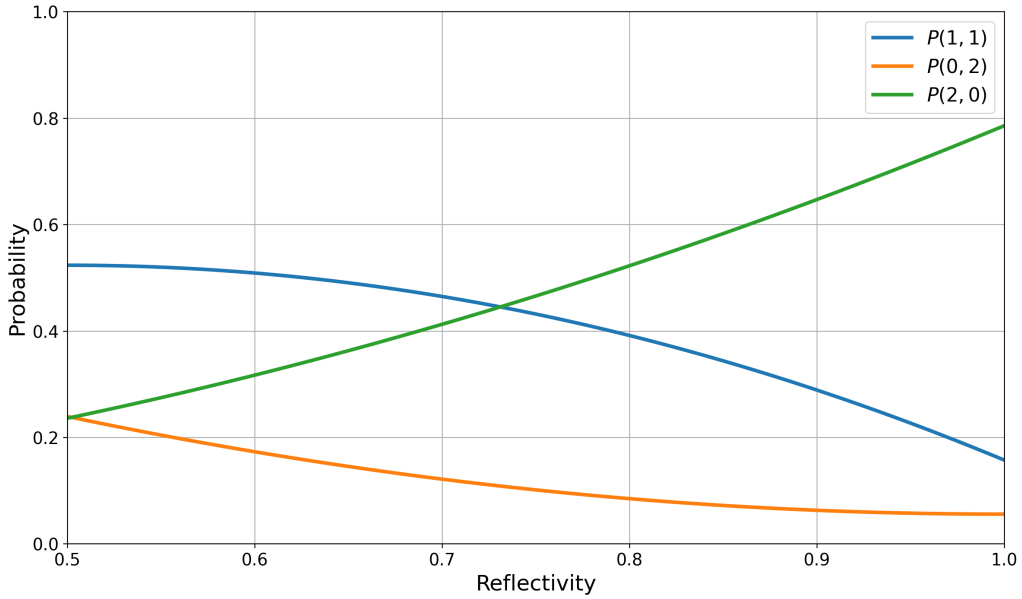


Figure 4.16: The output state probability distribution as a function of variable beamsplitter reflectivity with decoherence, higher-order terms, and imperfect indistinguishability. In this case, $\gamma = 0.7327$, $\eta = 0.4$, $p = 0.3$ (for both modes), $\xi_1 = 0.997$, and a 5% mode mismatch.

4.5 Experimental Data: Bulk Optics

As a reminder, when conducting the experiments using bulk optics, it was misunderstood that the intentional attenuation used in the first mode was to be 93.3%, and therefore $\gamma = 0.933$ was used. It was only after recreating the theoretical model that it was understood that this was not the correct value, and it instead should have been set to $\gamma = 0.7327$. By the time this was realized, the bulk optics setup was deconstructed so that parts could be used in other experiments, thus preventing further data collection. However, this does not prevent the theoretical model from accommodating this discrepancy. In this subsection, $\gamma = 0.933$ was used, and therefore, the model (fitting) used the same value.

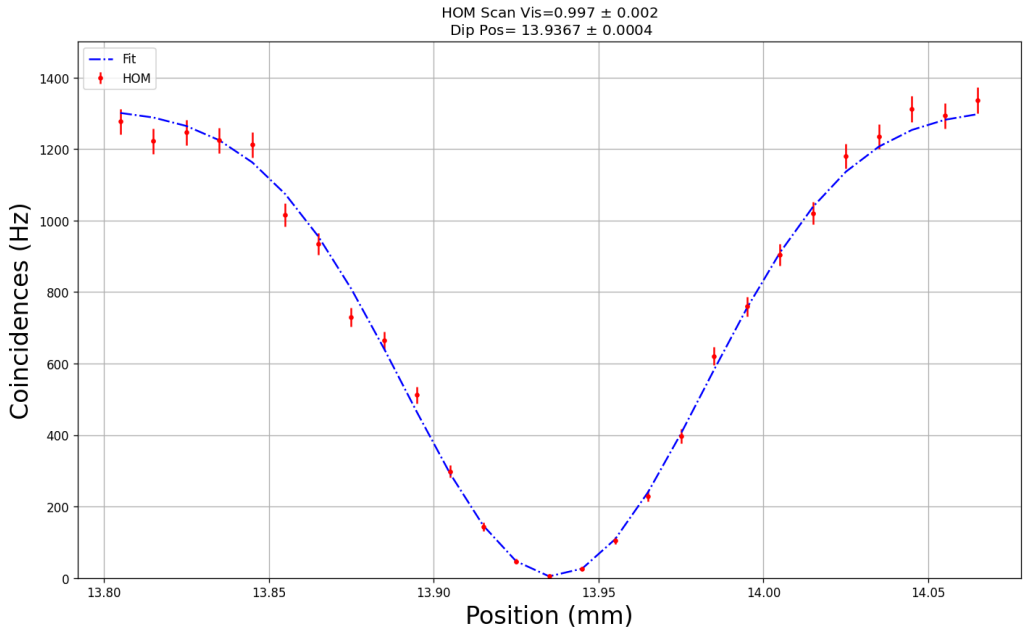
The experiment was run at a low laser power, producing approximately 1.2 $cc/MHz/nm$, to reduce the production of higher-order terms. This measurement does not account for coupling or detection efficiencies and is measured at the end of the circuit. The control of the variable beamsplitter was automated to ensure repeatability. The first step was to match the path lengths by following the procedure described in Section 4.3 and Figure 4.8. The HOM1 and HOM2 measurements can be seen in Figures 4.17 showing an indistinguishability of 0.997 ± 0.002 and 0.947 ± 0.010 for HOM1 and HOM2, respectively. The power was consistent across the two measurements, but the scan of HOM2 was subjected to additional attenuation caused by photons being launched into free space. The attenuation from Mode 1 and the variable beamsplitter reflectivity were calculated from calibration curves seen in Figure 4.18. The experimental results of the run can be seen in Figure 4.19. Data for each data point was accumulated for 12 separate 5-minute windows, resulting in an experimental run time of 11 hours.

Retrieving the bulk optics experimental data, a hybrid maximum likelihood estimation fit [121] was calculated using the updated theoretical model, the results of which can be seen in Figure 4.19. The parameters of fitting were calculated to be as follow; $\eta = 0.299986$, $p_1 = 0.299986$, $p_2 = 0.223053$, and a mode matching of 0.999997 (1 being perfect mode matching and 0 being complete mismatching).

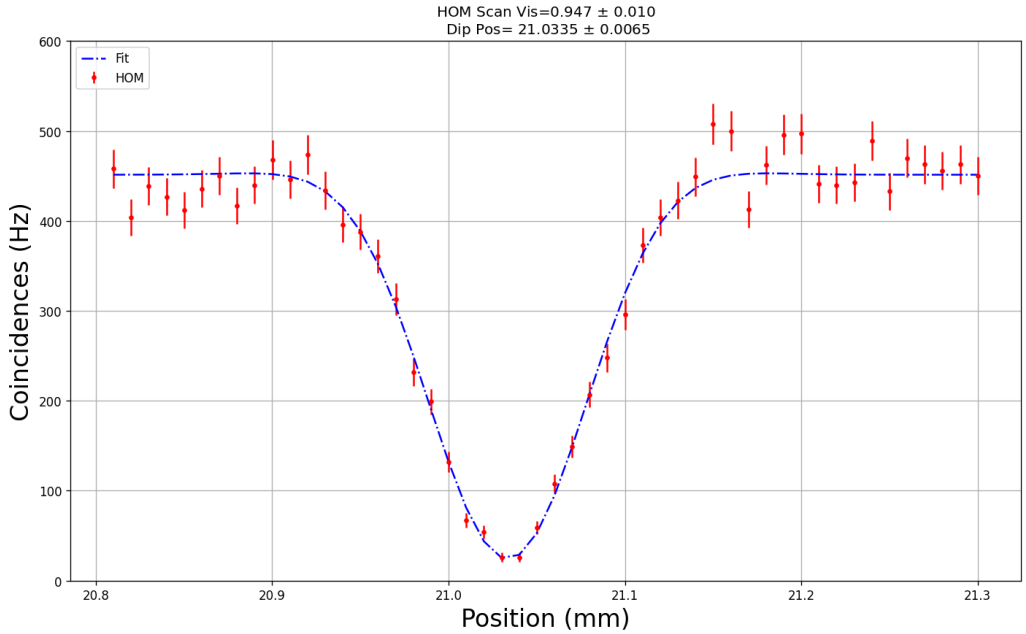
Here, p_1 and p_2 are the Kraus decoherence parameters "p" for modes 1 and 2, respectively. This value of η estimates the production of the $|1,1\rangle$ state at a probability of 0.0773, and the $|2,2\rangle$ state at a probability of 0.0075.

While the experimental data does follow the trend dictated by the theoretical model, there are some large deviations, most notably, the trend of the $|0,2\rangle$ does not experience complete extinction at any point. The theoretical calculations are exhaustive in what they consider; there is still one possible factor not included: SPDC frequency entanglement. This can be determined via a joint spectral amplitude measurement. While the joint spectral amplitude of the SPDC source used in this experiment has never been measured, it is understood that SPDC sources do have inherent frequency entanglement between the two photons produced. This effect can be mitigated by introducing a frequency filter (5 *nm* in this case), but does not completely negate the frequency entanglement and the effect it has on the HOM indistinguishability [122].

The values of η, p_1, and p_2 calculated by the least squares fit model were then passed back to the theoretical model to predict how the probability distributions as a function of both variable beamsplitter reflectivity and attenuation (see Figures 4.20 and 4.21), as well as finding the estimated conditions to produce the optimal result for bulk optics experiment. This optimal result is when $P_{11} = P_{20} \neq 0$ coincides with the minimum of P_{02}. This was found to occur when $\gamma \approx 0.5123$ and the reflectivity of the variable beamsplitter is $R = 0.8025$ (see Figure 4.22).

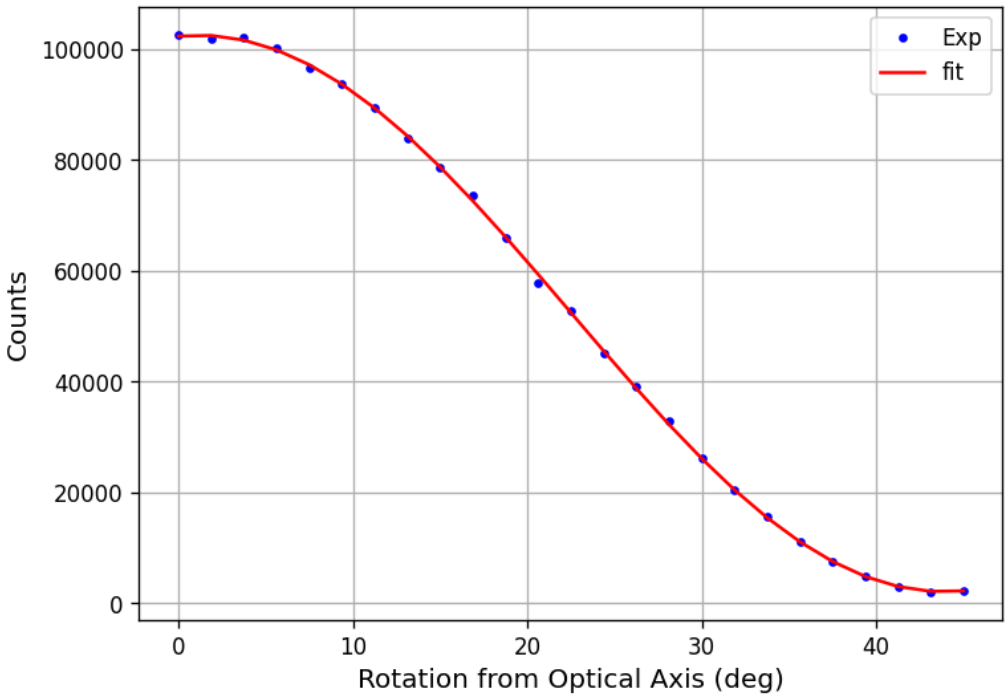


(a) HOM1

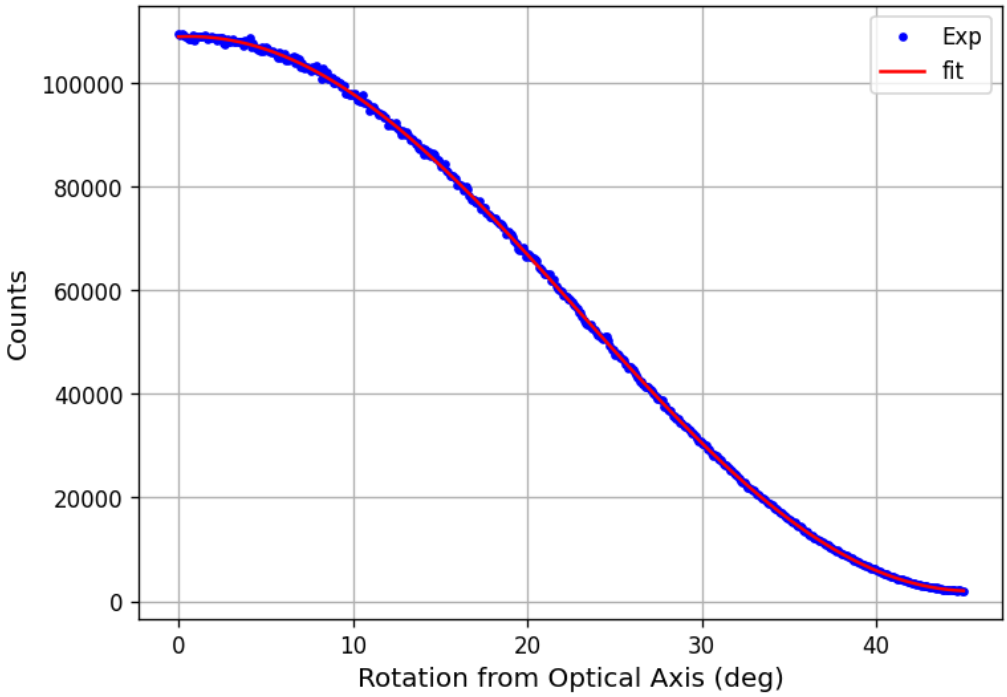


(b) HOM2

Figure 4.17: (a) HOM1 and (b) HOM2 measurements for bulk optical asymmetric quantum interference experiment.The indistinguishability of HOM1 is 0.997 ± 0.002, and 0.947 ± 0.010 for HOM2.



(a) vbs-HWP.



(b) l-HWP.

Figure 4.18: Calibration curves for the variable beamsplitter HWP, and the loss HWP determining the attenuation to Mode 1. The transmission into one output mode was measured as a function of HWP from the optical axis (degrees). The respective optical axes were determined by maximal transmission. Error bars confined within points.

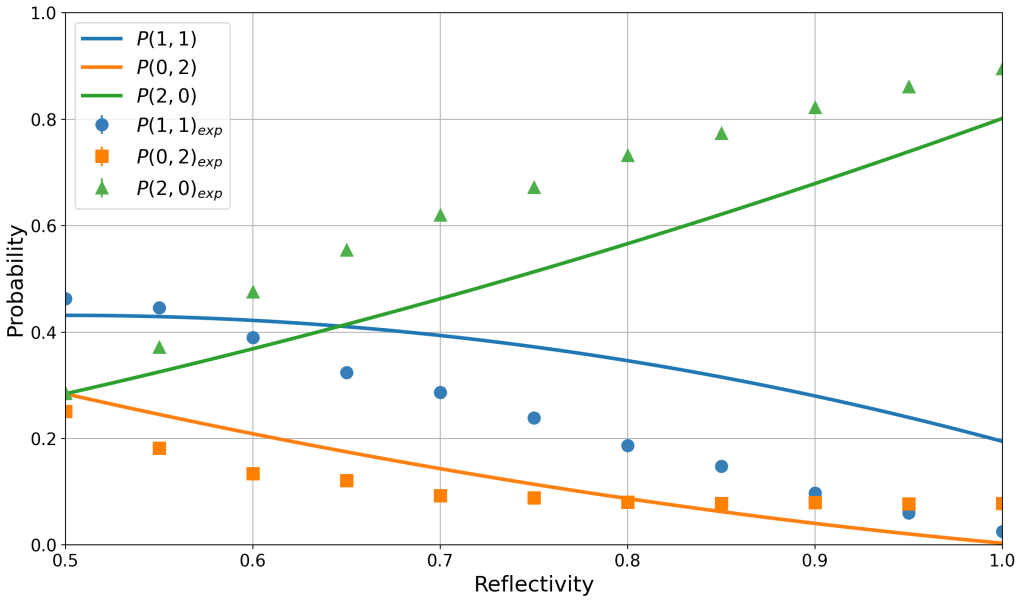


Figure 4.19: Experimental data collected using bulk optics. The $|0,2\rangle$ state experiences a minimum, but not complete extinction. All states follow the same trend as the theory indicates. Error bars are confined within the data points. $\gamma = 0.933$, $\eta = 0.299986$, $p_1 = 0.299986$, $p_2 = 0.223053$, and a mode matching of 0.999997. Error bars confined within points.

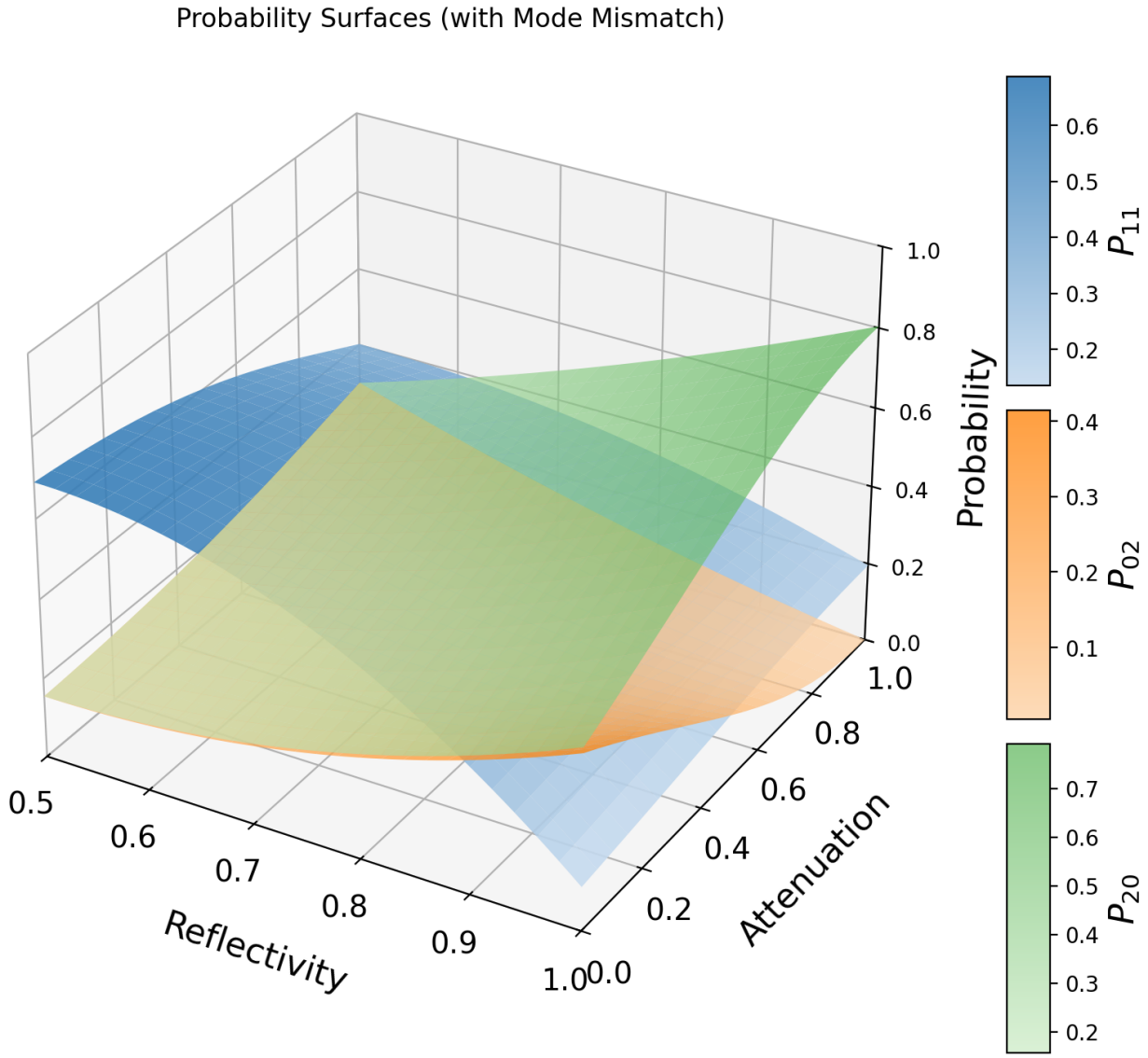


Figure 4.20: Probability distribution surface plots of the $|1,1\rangle$, $|0,2\rangle$, and $|2,0\rangle$ states as a function of variable beamsplitter reflectivity and attenuation to the first mode.

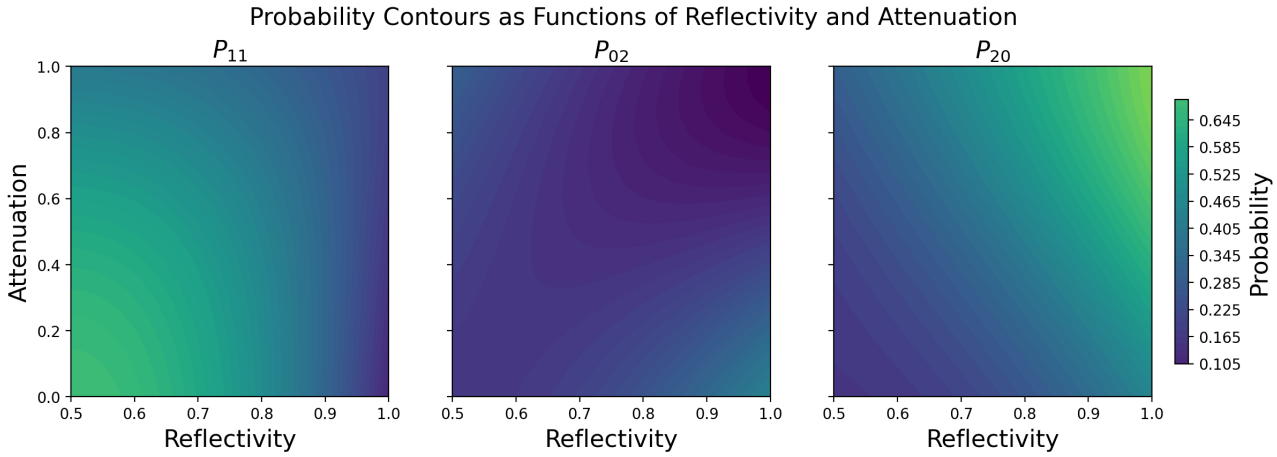


Figure 4.21: Probability distribution contour plots of the $|1,1\rangle$, $|0,2\rangle$, and $|2,0\rangle$ states as a function of variable beamsplitter reflectivity and attenuation to the first mode.

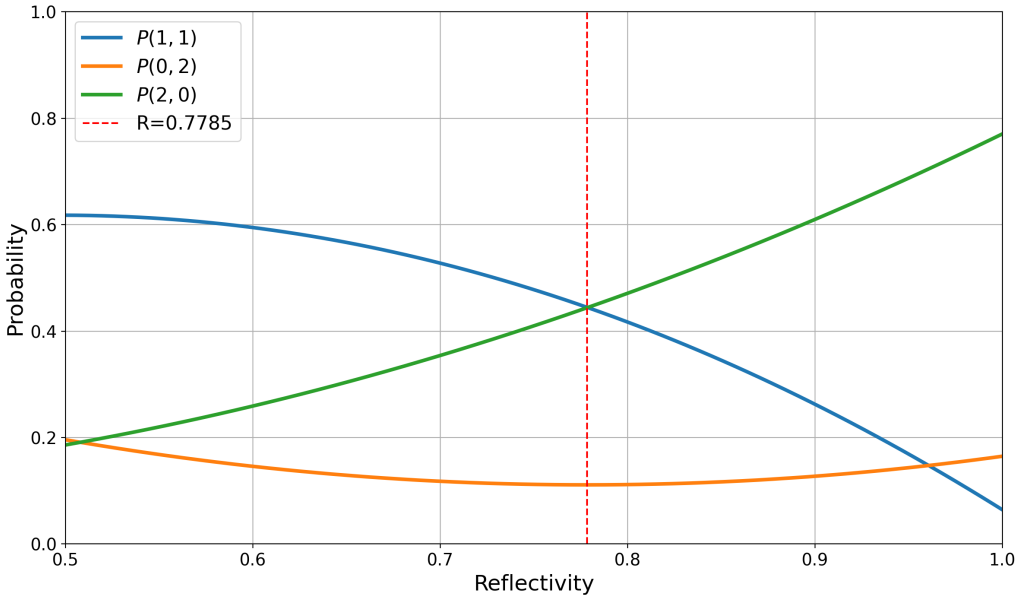


Figure 4.22: Optimal output state probability distribution of the bulk optics experiment. The optimal output state is defined by the $P_{11} = P_{20}$ coinciding with the minimum of P_{02}. The parameters used in this calculation are identical to those used in the fitting of the bulk optics experimental data (see Figure 4.19). In this case, the attenuation value differs and is calculated to be $\gamma \approx 0.5123$, which gives the optimal point a variable beamsplitter reflectivity of $R = 0.8025$.

Chapter 5

Improving Stability of the Micropillar Quantum Dot Single Photon Source

The quantum dot single photon source has already been the subject of two Ph.D. theses in the Quantum Technology Lab [123, 124]. A key issue noted in both works was the poor stability of the photon source; it could not be reliably used for multi-day experiments. In this chapter, I identify the sources of this insability and discuss the design and implementation of improvements that now allow the quantum dot single photon source to be used for long-run experiments. Indeed, my source is now being used in two Ph.D. theses: on Grover's Algorithm [125] and on Bohmian mechanics [126].

In this chapter, I describe the original and optimized excitation and collection experimental setups. I briefly discuss the strengths and weaknesses of the original setup, and how it inhibited the execution of physics experiments we wanted to do. I discuss the thinking behind my redesign, the improvements over the original, as well as new additions. The latter part of the chapter will take the reader through a step-by-step process of exciting the quantum dot and collecting the single photons that are produced. It finishes with an introduction to four-photon demultiplexing and the requirements for future development.

5.1 Basics of the Excitation and Collection Scheme

In describing the experimental setup, I can break it down into three categories. The first is the quantum dot itself, and the necessary environment to produce pure and indistinguishable single photons. Second, the optical components needed to direct an excitation laser to the quantum dot so that it can stimulate single-photon emission. I refer to this as the excitation arm of the experiment. Lastly, the collection arm of the experiment, which is the group of optics required to direct the single photons to a single-mode fiber so that they can be measured or used elsewhere. Keep in mind that the following is a big-picture overview of the experiment, and I will later describe each component of the setup in great detail in the latter part of this chapter.

5.1.1 Exciting the Quantum Dot

One of the ways that semiconductor quantum dots can be excited is by resonant excitation (see Figure 5.1), which is what the Quantum Technologies Lab has been using exclusively until this point. This

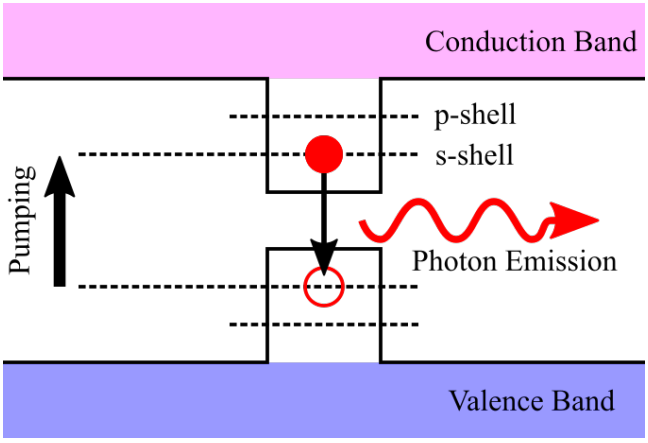


Figure 5.1: Resonant excitation pump scheme. The pump laser frequency is tuned to be resonant with the band gap frequency.

is done by tuning the laser wavelength (optical pump) to the s-shell resonant frequency of the band gap in gallium-arsenide (GaAs). This process creates a single electron-hole pair. This process also improves single-photon indistinguishability by reducing the time jitter of photon emission down to the radiative lifetime [127–130].

The quantum dot that is used in this experiment is one developed by Quandela. The quantum dot is surrounded by a supporting micro-pillar structure. This structure also includes two electric contacts to control the electric field applied to the cavity [131].

The quantum dot is fabricated by embedding an $InGaAs$ (indium gallium arsenide) layer in the center of alternating layers of $GaAs$ (gallium arsenide) and $Al_{0.9}Ga_{0.1}As$ (aluminum gallium arsenide), which act as distributed Bragg mirrors. The cavity was then doped to achieve an effective n-i-p diode structure, which was then optimized to define the Fermi level around the quantum dot and minimize the free carrier losses in the mirrors. The quantum dot and stack of Bragg mirrors are supported by four thin wires (1.5 μm thick) to a surrounding micro-pillar structure. The micro-pillar makes physical contact with an adjacent large mesa. A positive electrical contact is deposited on the top of the mesa, and a negative electrical contact is on the back of the entire sample. Applying a voltage across these two nodes allows for complete control over the electrical field passing through the quantum dot. This is important as no two quantum dots are perfectly identical. This means that even though the intended transition of the quantum dot is 925 nm, it is never exactly that. Being able to have variable control over the electric field passing through the quantum dot means that the Stark shift [132] of the quantum dot can be adjusted so that the transition of the quantum dot matches the excitation laser.

The quantum dot's operating temperature is 4 K. What this means is that the quantum dot has to be placed inside a cryostat. I used a CryoAdvance produced by Montana Instruments Corporation, which has variable temperature control between $< 3.2 - 350$ K. Within the cryostat, there is an Attocube piezo stack to position the quantum dot. The piezo stack has three degrees of freedom, and this allows for the quantum dot to be moved in three dimensions in very discreet steps. This enables me to make small adjustments to the alignment of the quantum dot with respect to the excitation laser. Placed directly above the QD is a large lens with a high numerical aperture (NA) (Olympus LCPLN20XIR with NA = 0.45, distance 8.3 mm), and a quarter- and half-waveplate (QWP & HWP). The lens is used to focus the excitation light onto the quantum dot and collimate the emitted single photons, while the

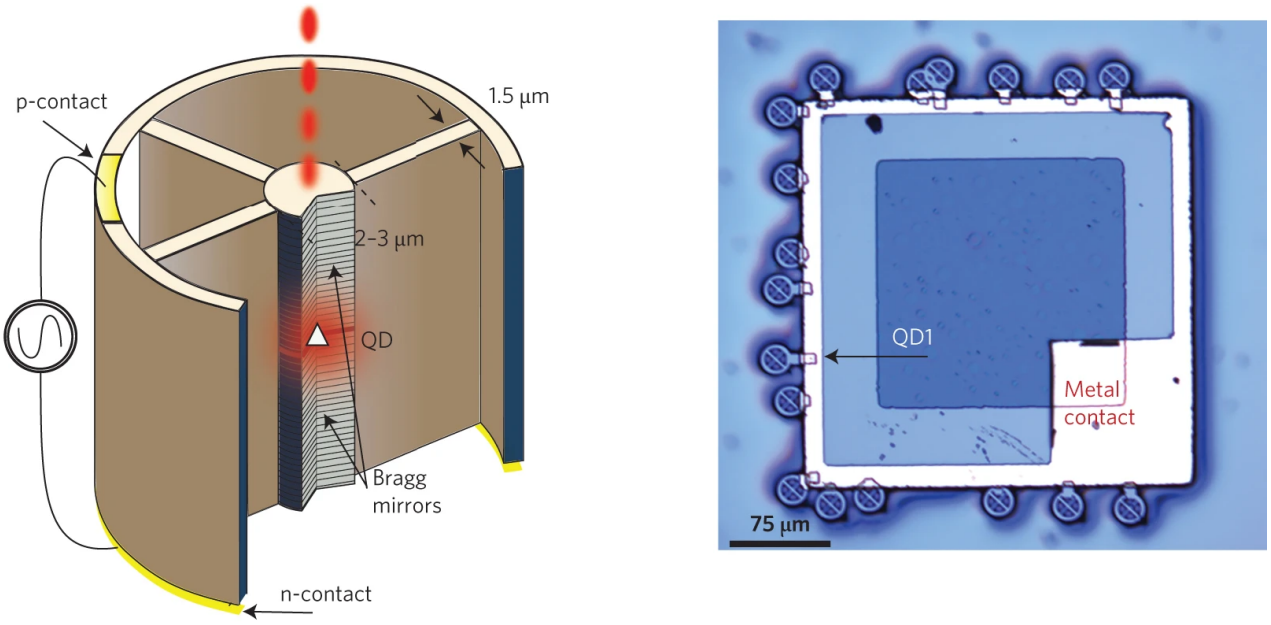


Figure 5.2: Quantum dot and surrounding structure. (Left) The InGaAa quantum dot layer is placed at the center of a stack of Bragg mirrors made up of alternating layers of GaAs and $Al_{0.9}Ga_{0.1}As$. The stack of Bragg mirrors is supported by four wires of 1.5 μm thickness to a surrounding micro-pillar structure. (Right) This micro-pillar overlaps an adjacent mesa, which has a metal diode deposited on top acting as a positive electrical node. The negative electrical node is deposited on the back of the sample. The technique used in fabrication is in situ lithography [131].

QWP and HWP are used to separate the reflected excitation light from the single photons.

While resonant pumping is designed to produce one single photon per pulse, multi-photon events can occur. The most common ways for this to occur while resonantly pumping is by overdriving the system. This happens when the laser pulses are too long in time or have an excess of power, causing the QD to re-excite immediately after decay [133, 134]. However, it is less common to use too much pump power, as it is more favorable to use lower pump power to reduce background noise.

5.1.2 Excitation Arm

The excitation arm starts with a Ti:Sapphire laser, which produces light at 925nm. The laser is pulsed, meaning that it emits a short burst of light lasting a few picoseconds every 12.5 ns. A portion of the emitted light is picked off and sent to an autocorrelator, which is used to determine that the laser is pulsing and the duration of the pulses. The remainder of the light is coupled into a single-mode fiber and sent through a pulse shaper that alters the frequency spectrum of the laser. This allows for the frequency spectrum of the laser pulse to be altered before reaching the QD. The light then continues to the quantum dot through a pair of lenses to resize the beam before reaching the focusing lens.

5.1.3 Collection Arm

Once the single photons are emitted from the QD, their beam is collimated by the same objective lens used to initially focus the excitation laser onto the QD. The single photons then travel down the collection arm of the experimental setup. The beam is resized using a pair of lenses before being coupled into a single-mode fiber. At this point, the photons can be sent to single-photon detectors for measurement or passed on to other experimental applications. This is expanded upon in Section 5.1.3.

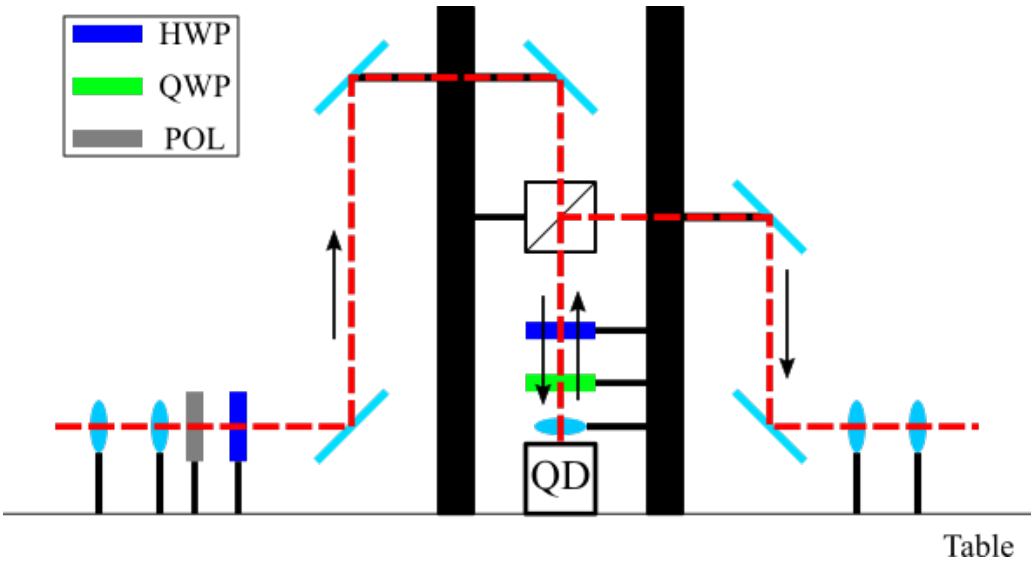


Figure 5.3: Diagram of original collection and excitation setup depicting long lever arms supporting optical elements above the optical access point of the quantum dot. The long lever arms contributed to mechanical instability.

5.2 Original Excitation and Collection Setup

When the original Quantum Dot setup was built, the aim was for the system to be functional as soon as possible. While this did yield quicker results by producing a viable source of single photons, the overall design of the system suffered.

The main design criterion for the original excitation and collection setup was speed of implementation. As can be seen from (reference fig here), the optical path is taken up from the plane of the table, and then directed down through a series of optics and a microscope objective, to the cryostat. The reason for this is that the optical entrance to the cryostat is well above the standard beam height. The layout is conceptually clean, and relatively easy to add or subtract optics, e.g., waveplates or filters, as various excitation schemes were trialed [123, 124]. The drawback, as can be seen from Figure 5.3, is that many of the optics were on long lever arms and thus had issues with stability. A common thread to the two previous theses conducted with this setup was issues of optical stability, limiting run time, and experimental use of the quantum dot photon source. One of the key goals for my thesis was to make the quantum dot single photon source system reliable, so that it could be used for a variety of physics experiments that require long run time, e.g., Grover's Algorithm (the focus of Fatemeh Mohit's thesis) or Bohmian mechanics (the focus of Sayantan Das' thesis).

5.3 Optimized Excitation and Collection Setup

While the old setup had its limitations and aspects that could be improved, it was still a quality single-photon source. When most of the experimental science being conducted in the lab is dependent on this source, it is easy to understand why my colleagues did not want to rebuild it and not have access to single photons for an extended period of time. As the old saying goes;"if it ain't broke, don't fix it".

Well, sometimes life has a way of presenting a silver lining. My silver lining came as a result of a complete lab relocation. My research group was fortunate to have the opportunity to move into a new lab space that is better able to accommodate our needs. This meant that the optical table that housed the quantum dot setup had to be cleared off for it to be moved. There is no better time to redesign an experiment than when you are forced to completely disassemble it, so that is exactly what I did.

In the following, I will describe the full redesign that I did for the quantum dot setup. While some of the experimental concepts have carried over from the old setup, such as the manner in which the reflected pump light is filtered from the single photons, the design of the system is completely different. Additionally, my colleagues and I have been able to implement different experimental techniques to improve the laser power stability and mechanical stability of the system, and thus improve the quality of the single photons produced by the quantum dot. Starting with the excitation laser, I will discuss each component in the same order in which the light passes through the system.

The main component of the optimized system is an elevated platform that holds all the optical components for the excitation and collection arms. This platform is supported by five 2-inch-diameter steel posts and is placed directly adjacent to the cryostat housing the quantum dot, as seen in Figure 5.14. This provides greater mechanical stability.

5.3.1 Excitation Laser for Quantum Dot

Starting at the beginning with the tool that is essential to all quantum optics experiments, the laser. In my case, I use a Millennia eV High Power CW DPSS laser to pump a Tsunami Ti:Sapphire Oscillator from Spectra-Physics. The Tsunami is tuned to output light at 925 *nm*.

The first optical element that the light passes through is a Faraday Isolator. This component is the new addition that was introduced to this section of the setup. To understand why this was implemented, it is first easier to understand the problem it fixes. When light passes through an optical component, such as an appropriately coated lens, most of the light passes through. However, a small portion is reflected. This reflected light is sent back into the laser cavity, causing interference. In this particular case, this interference caused instability in the power output of the laser. The issue then became how to prevent the back reflection from reaching the laser cavity.

The Faraday Isolator is the perfect tool for the job. Michael Faraday first discovered in 1845 that when a magnetic field is applied to certain materials—now known as magneto-optical materials—it becomes optically active. When linearly polarized light passes through the material and a magnetic field, the polarization rotates [135] [136]. This section of optically active material is known as a Faraday Rotator. The length of the rotator is manufactured to achieve a certain amount of rotation,

$$\theta = vBd \tag{5.1}$$

where v is the Verdet constant of the material, B is the magnetic flux density, and d is the length of the rotator. The Verdet constant of a material is defined as the rotation per length per field strength [136]. In the case of a Faraday Isolator, the desired angle of rotation is 45° as described below.

A Faraday Isolator uses this effect by first establishing a linear polarization of the light with a

linear polarizer, and as the light passes through the rotator, it is rotated by 45°. The light that is reflected back from optical elements travels back through the rotator and is rotated by a further 45° in the same direction as before. Next, the reflected light is orthogonally polarized to the incoming light and the original linear polarizer, and does not pass back through the polarizer. This new addition was useful as it was able to noticeably stabilize the power output of the laser.

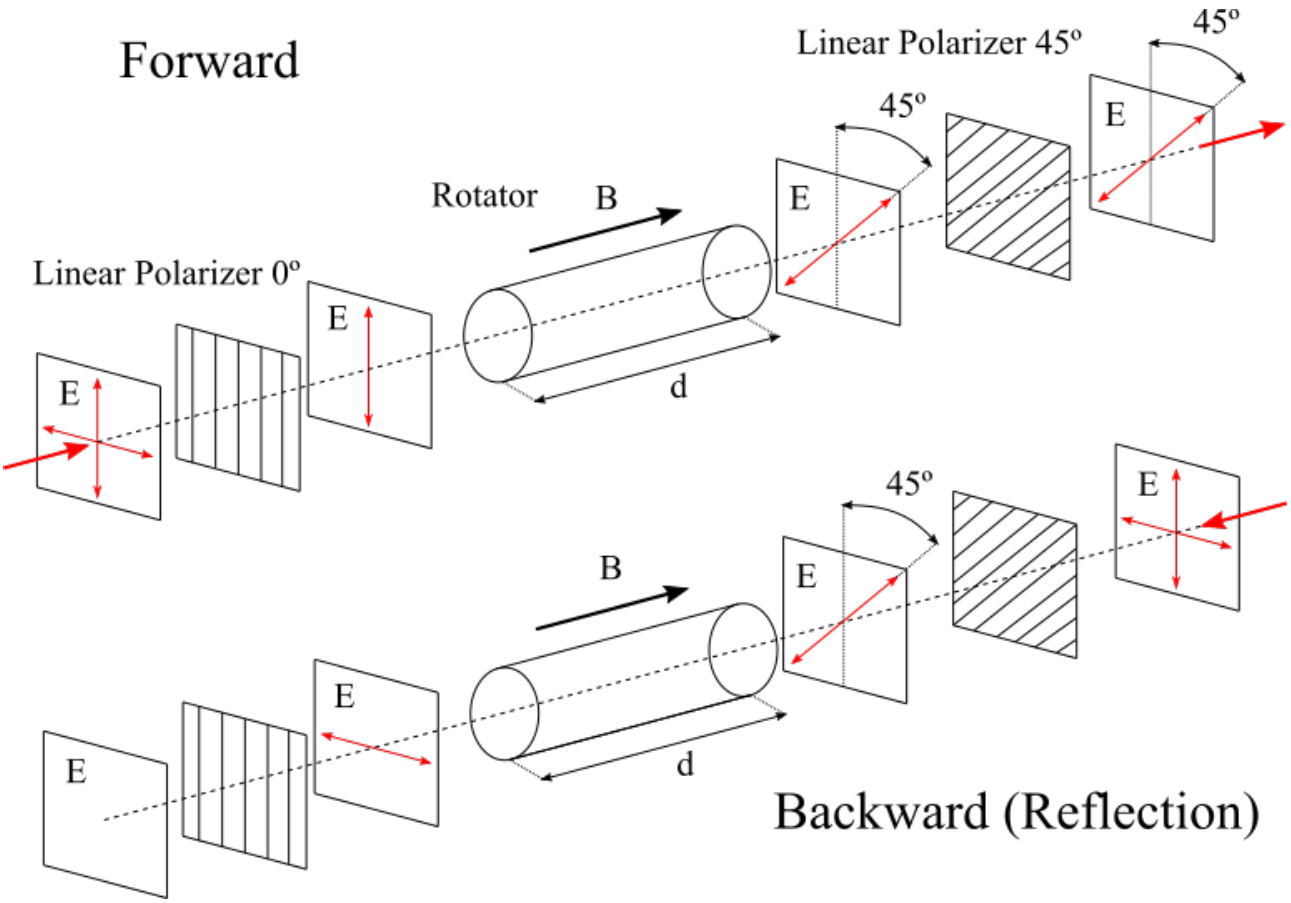


Figure 5.4: Faraday Isolator. As the light enters the isolator, it is polarized by a built-in linear polarizer, which is set to the vertical in this example. As the polarized light passes through the full length of the Rotator, it becomes rotated by 45°. It is then able to pass through the second linear polarizer set at 45° and out the other end of the Isolator. Light traveling backward through the Isolator becomes polarized at 45° and is rotated an additional 45° by the Rotator to become horizontally polarized. This polarization is orthogonal to the linear polarizer set to the vertical. Thus, the light does not pass through in the backward direction.

Immediately after the Faraday Isolator, 10% of the beam is picked off and sent to an autocorrelator (APE PulseCheck 150 by APE). The purpose of an autocorrelator is to monitor the pulse duration of the laser. It does this by splitting the incoming laser light into two paths. It then superimposes the two signals with a variable time delay between them. A non-linear interaction then determines the overlap between the two pulses [137]. It is important to monitor the pulse duration of the laser output, as it is something that can be adjusted. In the case of this experiment, it is found that a pulse duration of $4-6$ *ps* is optimal for pure single photon production.

The other 90% of the light passes through a linear polarizer, followed by a half-waveplate and a polarizing beamsplitter. These three components are used to moderate the power that is being coupled into the single-mode fiber. The linear polarizer sets the polarization of the light, and depending on the angle of this polarization with respect to the PBS, a certain percentage of light passes through the PBS

while the rest is sent to a beam dump. Rotating the HWP allows for the angle of polarization to be changed, and thus gives variable control over how much light passes through the PBS. It is important to have this in place to limit the intensity of light entering the single-mode fiber, as too high an intensity burns the fiber tip. It is not possible to do this by reducing the laser power output, as the laser achieves greater stability at high power output. The light that is coupled to the fiber is then transported to the next stage of the experimental setup.

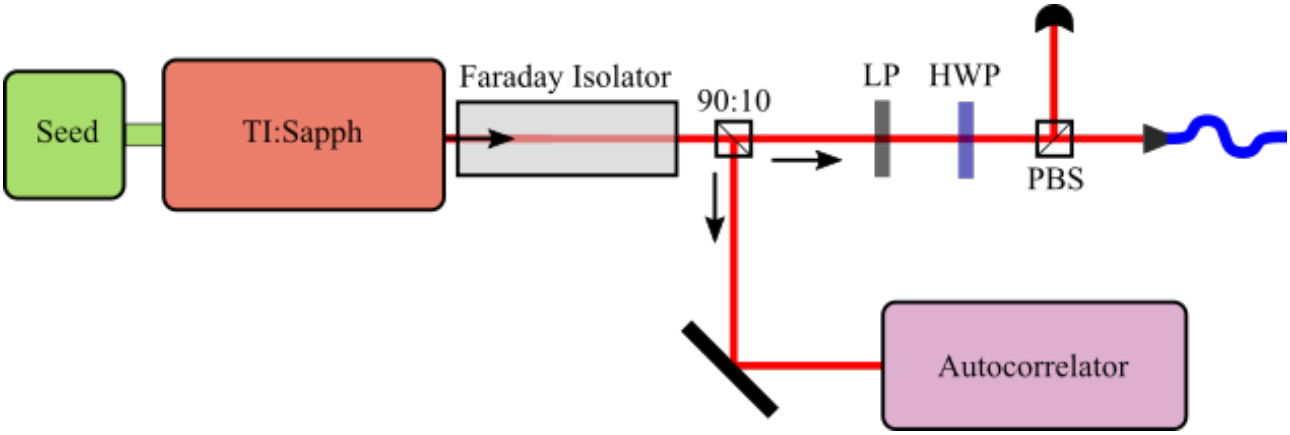


Figure 5.5: Seed laser and Ti:Sapphire laser produce an emission of 925 *nm* light, which passes through a Faraday Isolator. A portion of the beam is picked off by a beamsplitter with 10% reflection and sent to an autocorrelator to monitor the pulse duration. The remaining 90% of the beam power is transmitted through the BS and sent through a linear polarizer, a half-waveplate, and a polarizing beamsplitter so that the amount of power being coupled into the single-mode fiber can be adjusted.

5.3.2 Pulse Shaping

The quantum dot has a distinct difference in potential energy between the ground and the excited state. For the electron to complete this transition, it needs to absorb a photon with the correct energy. In this case, a photon at approximately 925.2 *nm*. While the excitation laser is centered around this wavelength, it has a finite spectrum, meaning that light at slightly longer and shorter wavelengths is also being produced in the pulse. This becomes an issue as the QD does not absorb these slightly different wavelengths, and instead, they get reflected and add to the background noise.

Before the excitation light reaches the QD, it passes through a 4F pulse shaper, Fig. 5.6 [21, 138, 139]. This is used to remove the unwanted frequencies of the excitation laser. It does this by using an optical grating to separate the different frequencies within the laser pulse into separate spatial modes. A lens then focuses the modes into individual points, while a mechanical slit allows only one of these modes to pass through. In this particular case, a single slit is used to trim the edges of the laser's spectrum, making it more narrow in frequency. In other words, the pulse becomes shaped. The slit can be moved to focus on different modes, and its width can be adjusted to let more or fewer modes pass through. These two variables can be used to optimize the QD emission and the signal-to-noise ratio.

It is also interesting to note that this experiment only uses a single slit. As mentioned above, the QD requires a pump light of a specific wavelength in order to be excited via resonant excitation. Therefore, only a single slit is needed to trim away the wavelengths that are not well absorbed by the QD and cause an increase in background noise, which worsens the signal-to-noise ratio and single-photon

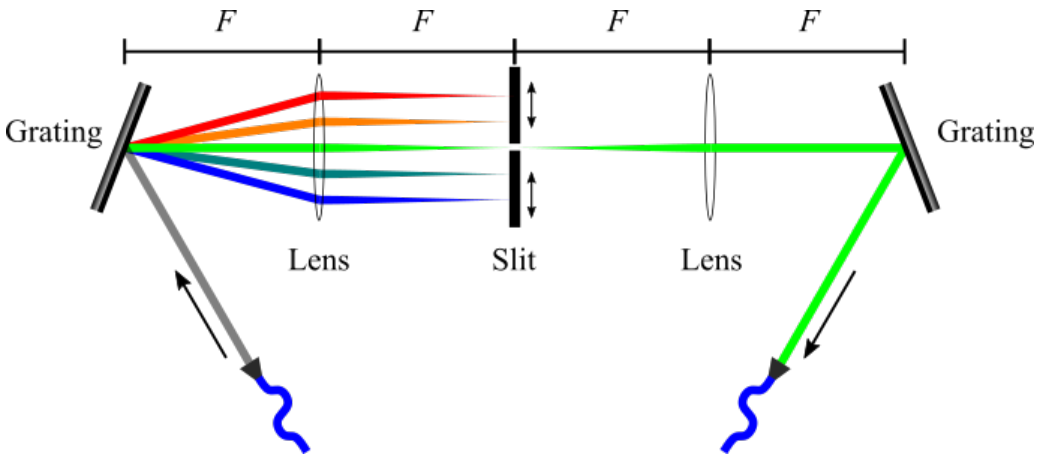


Figure 5.6: Conceptual visual representation of a 4F pulse shaper. The beam is incident on an optical grating, which provides an angular separation between the different frequency modes (these different modes are depicted by different colors). Each beam is then focused by a lens of focal length F. This lens is positioned a distance F from the grating. A mechanical slit is placed at a distance F after the lens. The slits' function is to allow the desired frequency mode to pass through while blocking the others. The mode is then collimated by another lens identical to the first and recombined on a second grating. In this case, a single slit is used. The position of the slit can be adjusted to center on a specific frequency, and the width can be adjusted to block more or fewer of the adjacent modes.

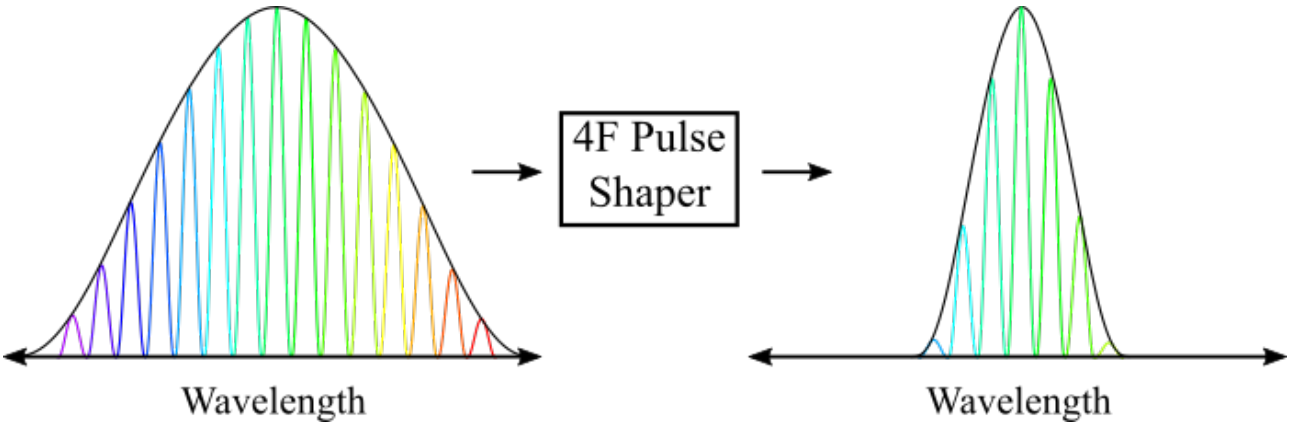


Figure 5.7: Diagram to show the basic concept of what a 4f pulse shaper achieves. In this simple example, the pulse shaper has been able to trim off the edges of the pulse, making it narrower. Note that the different colors are meant to signify red and blue detuning, while in practice, these peaks are separated by a fraction of a nanometer.

purity. However, this single slit can be replaced by a double slit to implement different excitation schemes, such as the super scheme [140].

The 4F filter was built using two Thorlabs GR25-1208 gratings and lenses with focal length $F = 1000\ mm$. The specific gratings were chosen as they provided a greater angular separation of wavelengths. The use of lenses with long focal lengths allowed more distance and time for wavelengths to separate spatially before reaching the slit. All of this is to provide more greater resolution in filtering. The mechanical slit used had an adjustable slit width and was placed on a translation stage, allowing the slit to move perpendicular to the beam path.

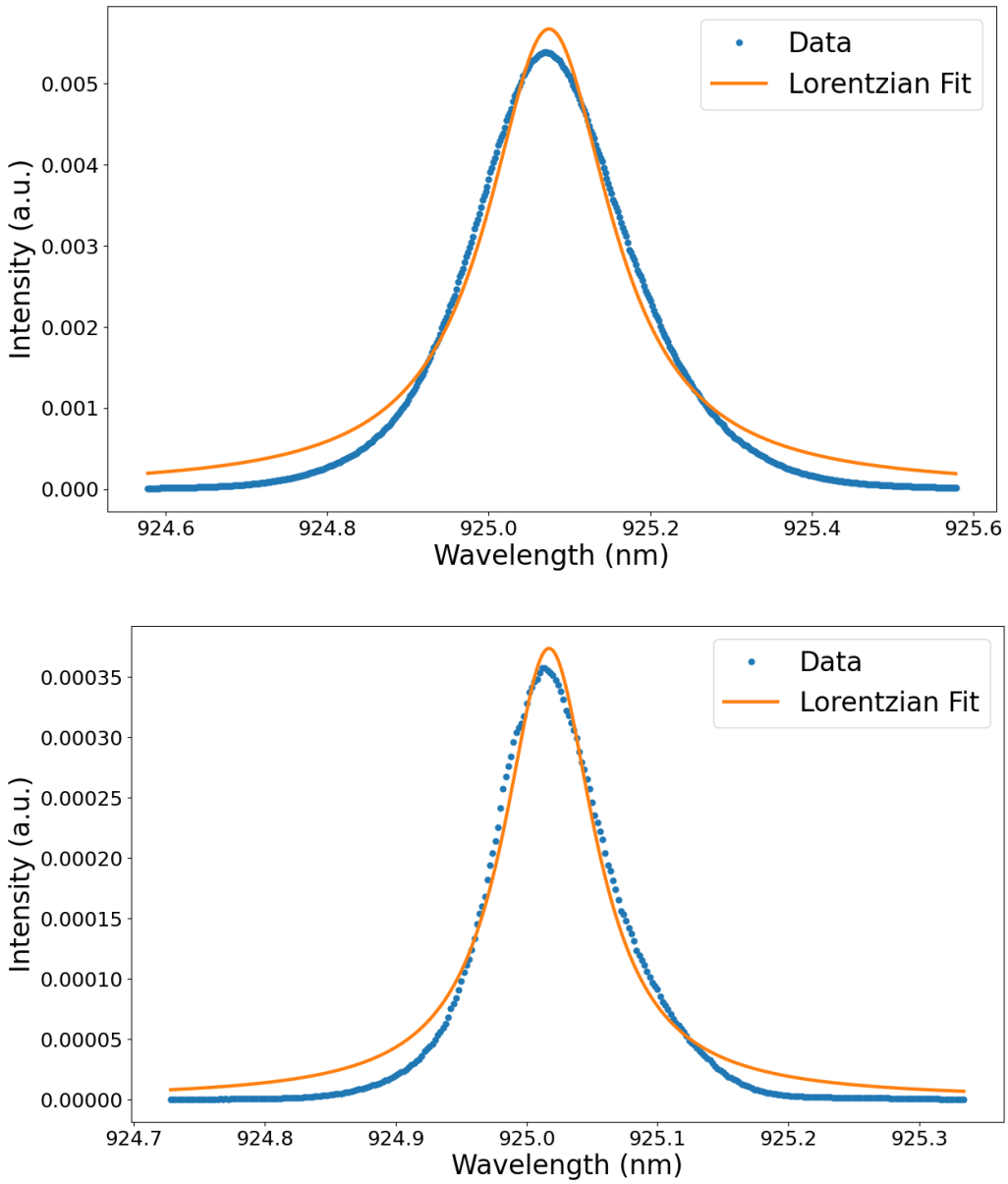


Figure 5.8: Spectrum of the pump laser (Top) before the 4F filter and (Bottom) after the 4F filter. Before filtering, the laser spectrum is centered at 925.068 *nm* with a full width at half maximum of 0.187 *nm* measured from a Lorentzian fit with reduced Chi-Squared of 5.733×10^{-8}. After filtering, the spectrum is centered at 925.012 *nm* with a full width at half maximum of 0.085 *nm* measured from a Lorentzian fit with reduced Chi-Squared of 2.373×10^{-10}.

The laser is producing a mode-locked, transform-limited pulses of $3-6$ *ps* in length, which is narrower than the typical 150 *fs* pulses usually produced by Ti:Sapphire lasers. These picosecond pulses are narrow enough (in frequency) such that no significant dispersion occurs after passing through optical elements on their way to the 4F setup. The 4F setup itself is intrinsically low dispersion, letting us adjust the amplitude of the frequency components while leaving the phase unaffected. Therefore, the pulses produced by the 4F setup are transform-limited.

The data for the spectrum of the pump light taken before and after the 4F filter was taken by Abhishek Roy and seen in Figure 5.8. Analyzing the data, it was calculated that the spectrum had a full width at half-max (FWHM) of 0.187 *nm* before the filter and 0.085 *nm* after the filter. This result shows a reduction of the FWHM by over a factor of 2. It is also suspected that this could be a conservative number, given the resolution of the spectrometer. The next steps are to measure the impact that this frequency filtering has on a HOM indistinguishability measurement.

5.3.3 Optimized Excitation Arm

Once the beam has been shaped, it continues to the final stage before reaching the quantum dot, which is referred to as the excitation arm. The excitation and collection arms (see below) are constructed on an elevated optical breadboard that sits over the quantum dot. This elevated platform is one of the major changes introduced in the new setup. The breadboard is supported by five steel rods, each 1.5 inches in diameter. This provides greater stability to the system, along with allowing the majority of the optics to be in the same two-dimensional plane.

As light passes through the excitation arm, the first thing that it encounters is a $2\times$ telescope that resizes the beam so that it can later completely fill the objective lens in front of the QD (see below). This is followed by a linear polarizer and an HWP to introduce polarization control. The LP and HWP also work with the joining PBS sitting above the QD (see below) to implement power control. The other component of the excitation arm is the LED light that is used for imaging. This path combines with the main path on a $50/50$ beamsplitter (Figure 5.9). This beamsplitter is removable as it is only needed for imaging purposes, often to provide a visual during the alignment process.

5.3.4 Quantum Dot Setup and Filtering

The excitation light is focused down onto the quantum dot through the top of the stack of Bragg mirrors. The focusing of the excitation beam is achieved by a single objective lens (Olympus LCPLN20XIR with NA = 0.45). The quantum dot produces a single photon, which is emitted through the same optical path the excitation light came in, and the beam of single photons is collimated by the same objective lens.

Above the large objective lens are an HWP and a QWP, which serve two purposes. The first is that the excitation laser's polarization must match the quantum dot's dipole so that the light is more efficiently absorbed. The second purpose is filtering the excitation light that is reflected from the top of the quantum dot cavity. This process is depicted in Figure 5.11. The excitation light reflected from the joining PBS is linearly polarized. It then passes through an HWP, which rotates the linear polarization. The QWP converts the linear polarization into circular polarization. This polarization becomes inverted (left-hand circular to right-hand circular or vice versa) once reflected from a surface

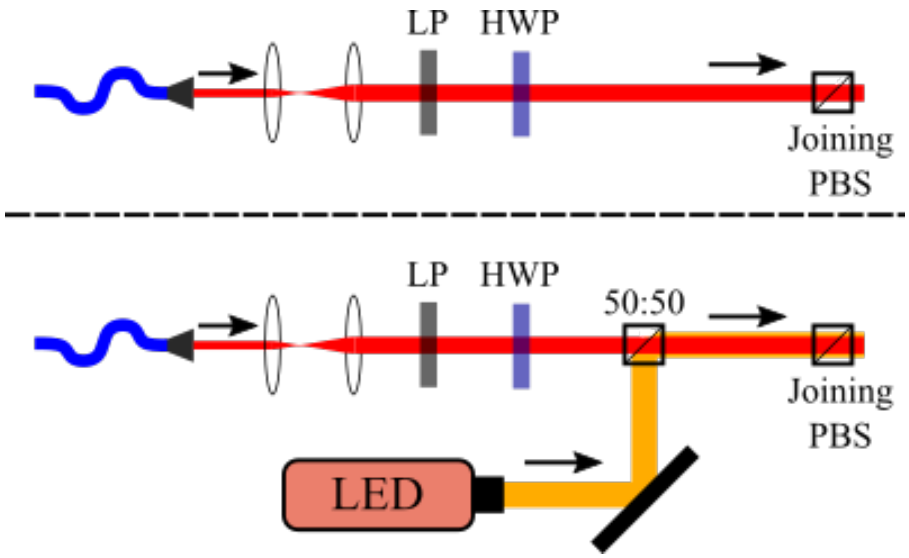


Figure 5.9: Excitation arm. The laser exiting the fiber is collimated and then resized by a 2× telescope. The light then passes through a linear polarizer and a half-waveplate to set the polarization and implement power control with the joining PBS. The joining PBS is the intersection of the excitation arm, quantum dot, and collection arm.

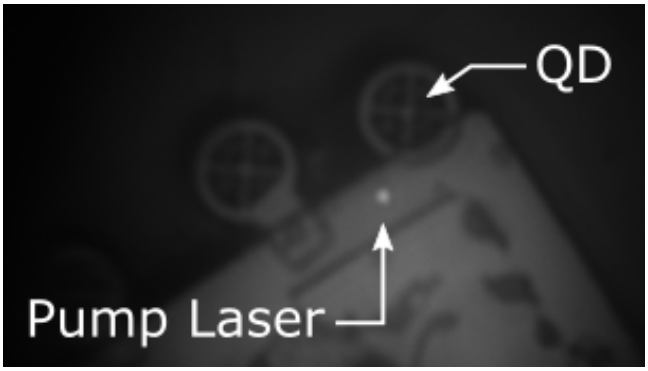


Figure 5.10: Photograph of pump laser light being reflected from the surface of the diode adjacent to the quantum dot micropillar structure. Photograph taken by Abhishek Roy.

(top of the quantum dot cavity). The reflected light travels back through the two waveplates, becoming orthogonally polarized to the joining PBS.

The alignment of the pump light to the quantum dot is broken down into three steps. First, the focused pump light is reflected from the surface of the adjacent diode and aligned such that the reflected mode is Gaussian (see Figure 5.10). This is determined by visually symmetric airy rings as the diode moves up and down, through the focus waist of the beam. Optical elements in the collection arm (see Section 5.3.5) are then adjusted to couple the reflected pump light into a single-mode fiber. Secondly, the quantum dot is positioned under the focused pump light. This allows the pump light to be reflected from the quantum dot cavity, and the coupling of the reflected pump light is optimized through manual optical alignment. Lastly, the pump light power is reduced and filtered away as described above and in Figure 5.11. The coupling of single photons into the single-mode fiber is then optimized manually and later electronically by the deformable mirror (more information on the deformable mirror alignment optimization is found in Chapter 6).

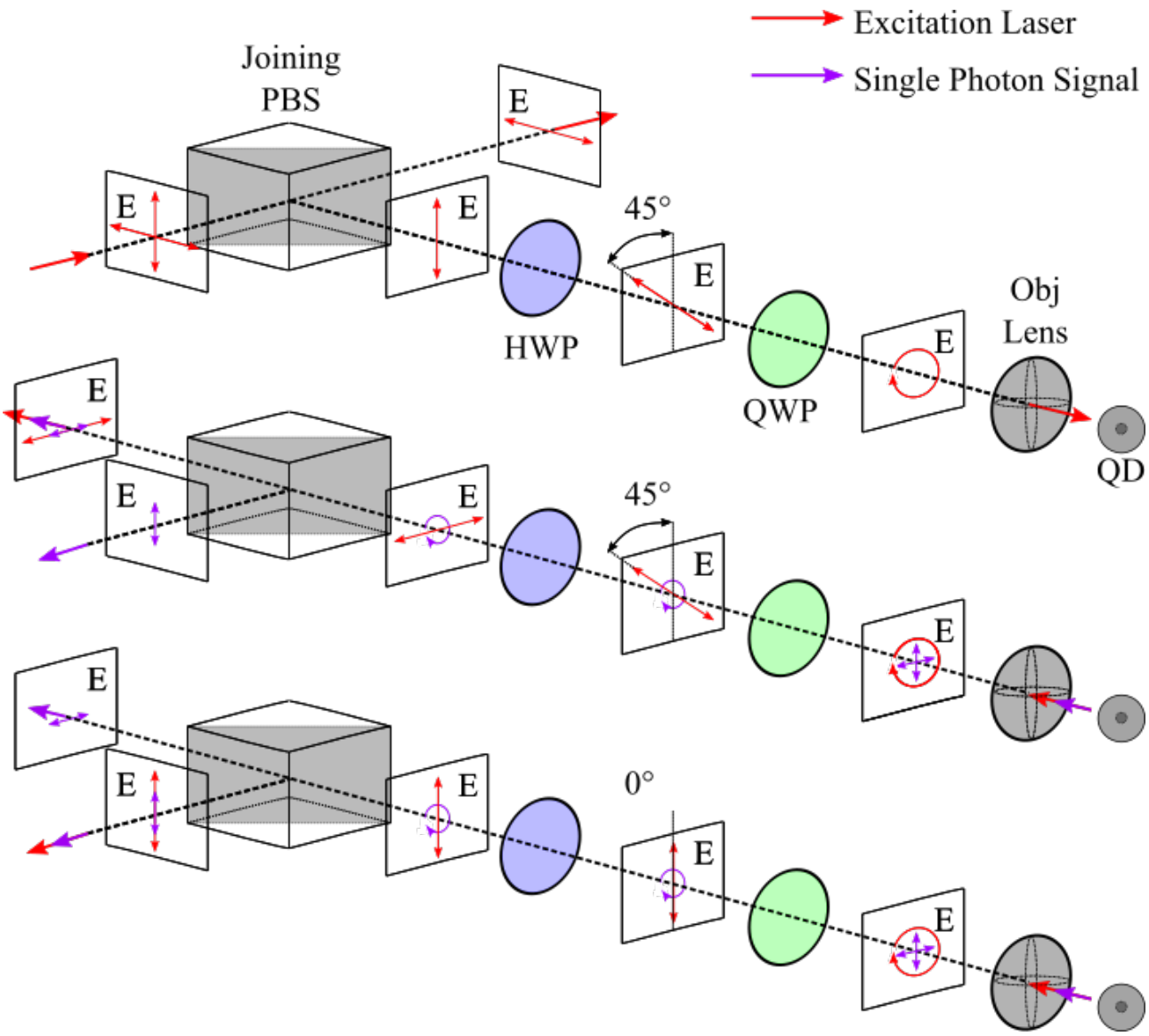


Figure 5.11: Filtering of the reflected excitation light. (Top) The incident light polarization is set in the vertical orientation by the joining PBS. It is then converted into circular polarization by an HWP and a QWP. The objective lens focuses the beam onto the quantum dot. (Middle) The reflected excitation light and the single photon produced by the quantum dot are collimated by the objective lens. While the reflected light has inverted its circular polarization due to the reflection, the single photons are unpolarized. Passing back through the QWP and HWP, the reflected excitation light is converted to a horizontal polarization and passes through the joining PBS. Allowing the reflected excitation light to pass through the PBS allows for easier alignment of optical components in the collection arm, as it is much more intense (making it easier to see on an infrared viewing card) compared to the single photons. Aligning the reflected excitation light is the first step in aligning the single-photon beam, as they have nearly identical modes. The single photons remain unpolarized and only become polarized after 50% pass through the joining PBS to the collection arm. (Bottom) The HWP is adjusted such 0° such that it does not rotate the vertically polarized light. It is then converted to LHP light and the RHP light due to the reflection from the quantum dot cavity. Finally, back to vertical and reflected by the joining PBS, preventing it from reaching the collection arm.

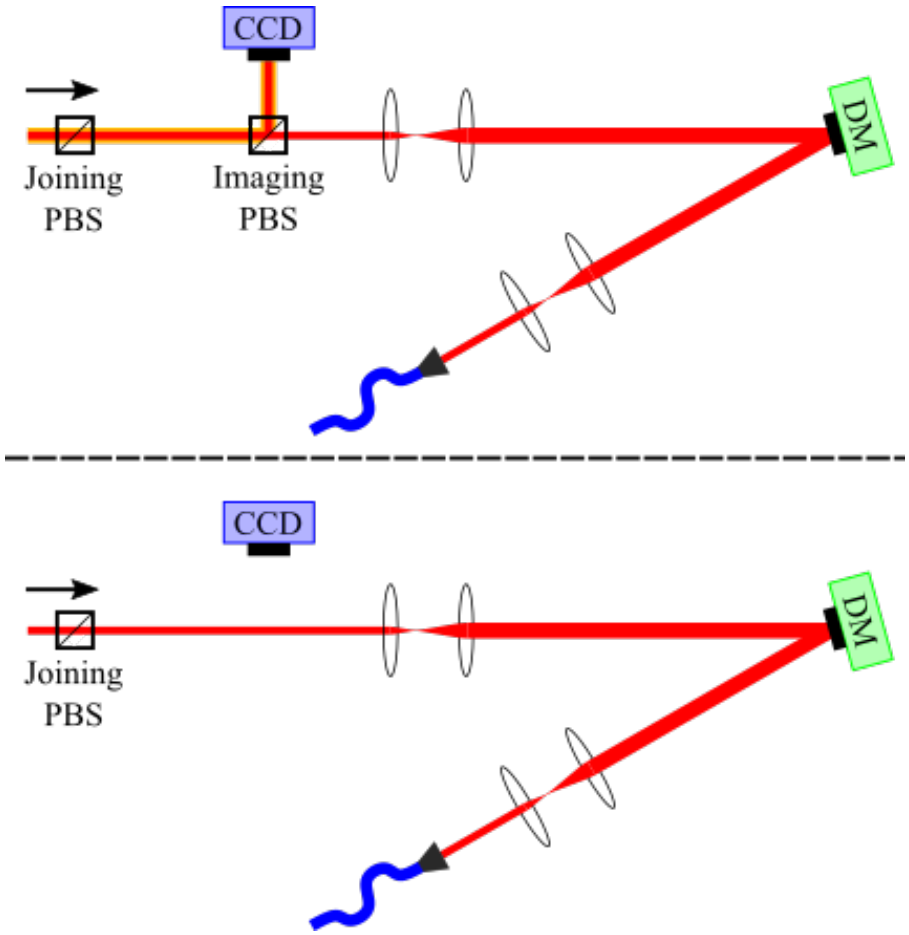


Figure 5.12: Diagram of collection arm when imaging the sample (Top) and when measuring single-photon output (Bottom).

5.3.5 Optimized Collection Arm

The collection arm of the new setup is very much the same as its predecessor, with the addition of one new key element. Following the path to the light through the collection arm, the first element that is encountered is a beamsplitter, which immediately filters off half of the single photons. This particular beamsplitter is removable, as it is only used to image the quantum dot sample. While in place, the beamsplitter sends both the LED light (used to illuminate the entire sample) and the unfiltered reflected excitation light to be captured by a CCD camera. As mentioned above, the reflected excitation light can be allowed to pass through the joining beamsplitter and down the collection arm. By doing so, the location of the focused excitation laser spot can be seen on the sample. This is an important tool in the process of alignment, as it gives the ability to determine how close the focused excitation laser spot is to the center of the micropillar structure surrounding the quantum dot. It also allows for the visual inspection of the spatial mode of the beam. A Gaussian spatial mode indicates that the incident beam is normal to the surface of the micropillar structure. Under experimental measurement conditions, the LED light is turned off, the reflected excitation light is filtered away from the collection arm, and the beamsplitter is removed.

Beyond the imaging portion of the collection arm is the actual collection. The largest update to this portion of the system is the introduction of the deformable mirror. A deformable mirror is an optical tool that consists of a highly reflective membrane that rests upon a bed of actuators. Each actuator can be individually controlled and can either push up or pull down on the membrane to deform it. The deformable mirror was implemented to increase single-photon production efficiency by optimizing

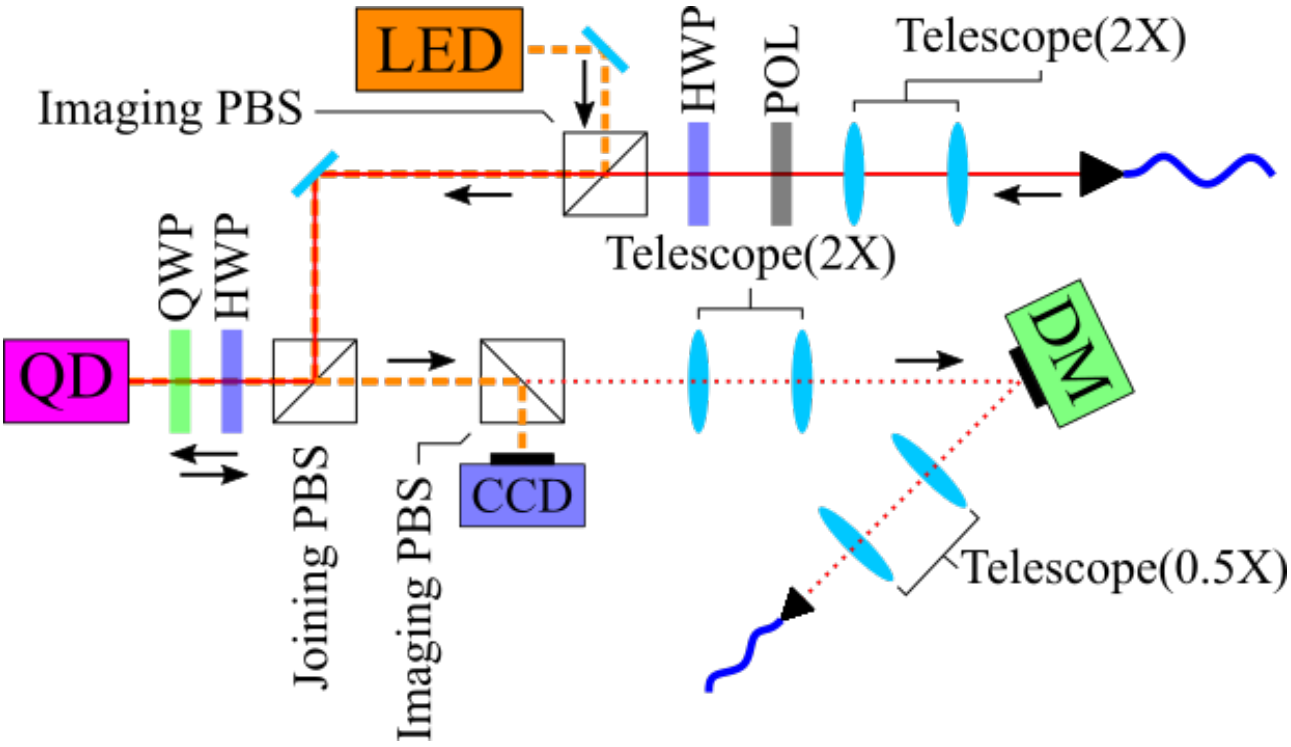


Figure 5.13: Diagram of full excitation, filtering, and collection system of the quantum dot. All components are joined by a Polarizing Beamsplitter (PBS), which is referred to as the joining PBS. The Excitation beam (red solid line) passes down the excitation arm through the joining PBS, through the filtering optics to the quantum dot (QD). The single photons (red dotted line) that are produced by the quantum dot, along with the reflected excitation laser light, pass back through the excitation filtering optics. The excitation optics are paired with the joining PBS to filter out the reflected excitation light. The single photons are then left to continue towards the collection arm. The LED (orange dashed line) illuminates the QD, and the image is captured by the CCD camera. The two imaging PBSs are implemented when imaging the QD sample, and removed when measuring single photons.

single-photon collection into a single-mode fiber. The specific deformable mirror used is the DM69-15 produced by ALPAO, which consists of a circular reflective membrane 10.5 *mm* in diameter on a bed of 69 actuators. The complexity of the deformable mirror implementation warrants its own chapter, and thus all information on this topic can be found in Chapter 6.

Telescopes are placed both before and after the deformable mirror. The purpose is to first increase the size of the single photon beam that is incident on the deformable mirror. A larger beam covers more of the surface area of the mirror, and therefore, more of the deformable mirror's actuators come into use. The system has more degrees of freedom when more actuators can affect the mode of the beam. The second telescope is to reduce the size of the beam to couple into a single-mode fiber at the end of the collection arm (see Figure 5.12).

With the optimized excitation and collection setup fully built, and with the addition of the 4F filter, a single photon purity ($g^{(2)}(0) = 0.0063 \pm 0.0016$ was obtained (measurement taken by Abhishek Roy). This exceeds previous values from this system [141] and is significantly lower than that achieved in the Quandela system, typically 2–3% [142]. The typical maximum count rate of the system is approximately 1 MHz, leaving room for further improvement. Figure 5.15 shows the single photon coincidence counts as a function of time delay. Additionally, this optimized setup now provides longer alignment times (on the order of days) due to improved mechanical stability. The quantum dot coupled

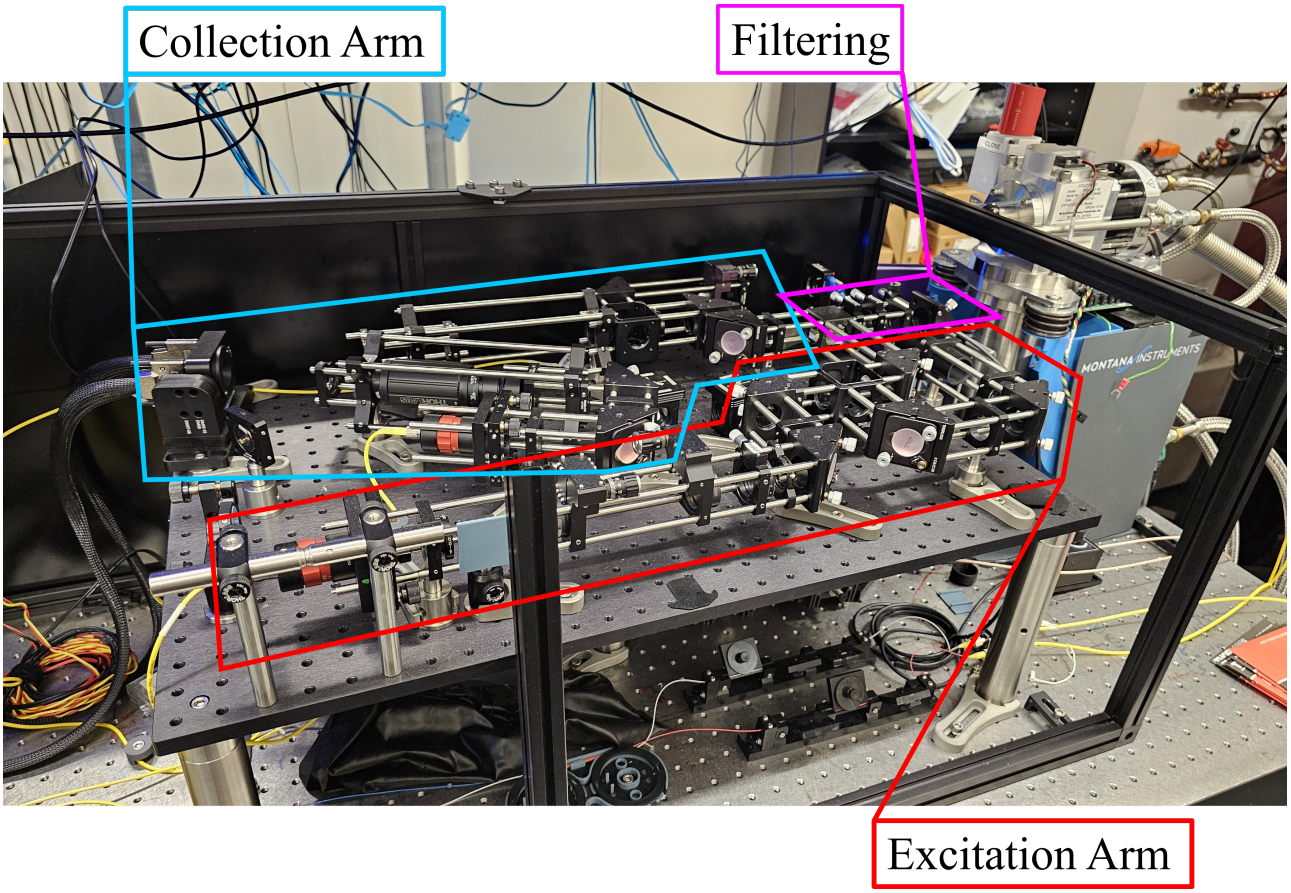


Figure 5.14: Photograph of the quantum dot excitation and collection setup. All optical components pictured are mounted atop a raised optical platform, providing mechanical stability. The quantum dot sits just below the filtering optics. What is not pictured is the 4F setup (Section 5.3.2), which is connected upstream of the excitation arm via optical fiber, and the demultiplexer (Section 5.3.6), which is connected downstream of the collection arm via optical fiber.

to the micropillar cavity has a quality factor, Q, of approximately $12,000$ [131], thus giving a full width at half maximum line width of

$$\Delta\omega = \frac{\omega_0}{Q}. \tag{5.2}$$

With $\lambda_0 = 925\ nm$, then $\omega_0 \approx 3.24\text{e}{-14}\ Hz$. This gives

$$\Delta\omega \approx \frac{3.24 \times 10^{14}}{12000} = 27\ GHz \tag{5.3}$$

So, the full width at half maximum in terms of wavelength is

$$\Delta\lambda = \frac{\lambda_0}{c}\Delta\omega \approx 0.077\ nm \tag{5.4}$$

While this is close to the FWHM achieved by the 4F filter (0.085 nm, see Figure 5.8), it suggests that there is still room for improvement. This improvement would come from a large rebuild of the 4F setup. With the current $F = 1000\ mm$, the light propagates at least 4 meters, so having lenses with larger focal lengths would allow for greater spatial separation of the frequency modes, but at the cost of an already large propagation distance. Alternatively, different gratings could be used to increase the angular separation between the frequency modes. This would most likely require the implementation of 2-inch diameter optics instead of 1-inch diameter optics to avoid clipping.

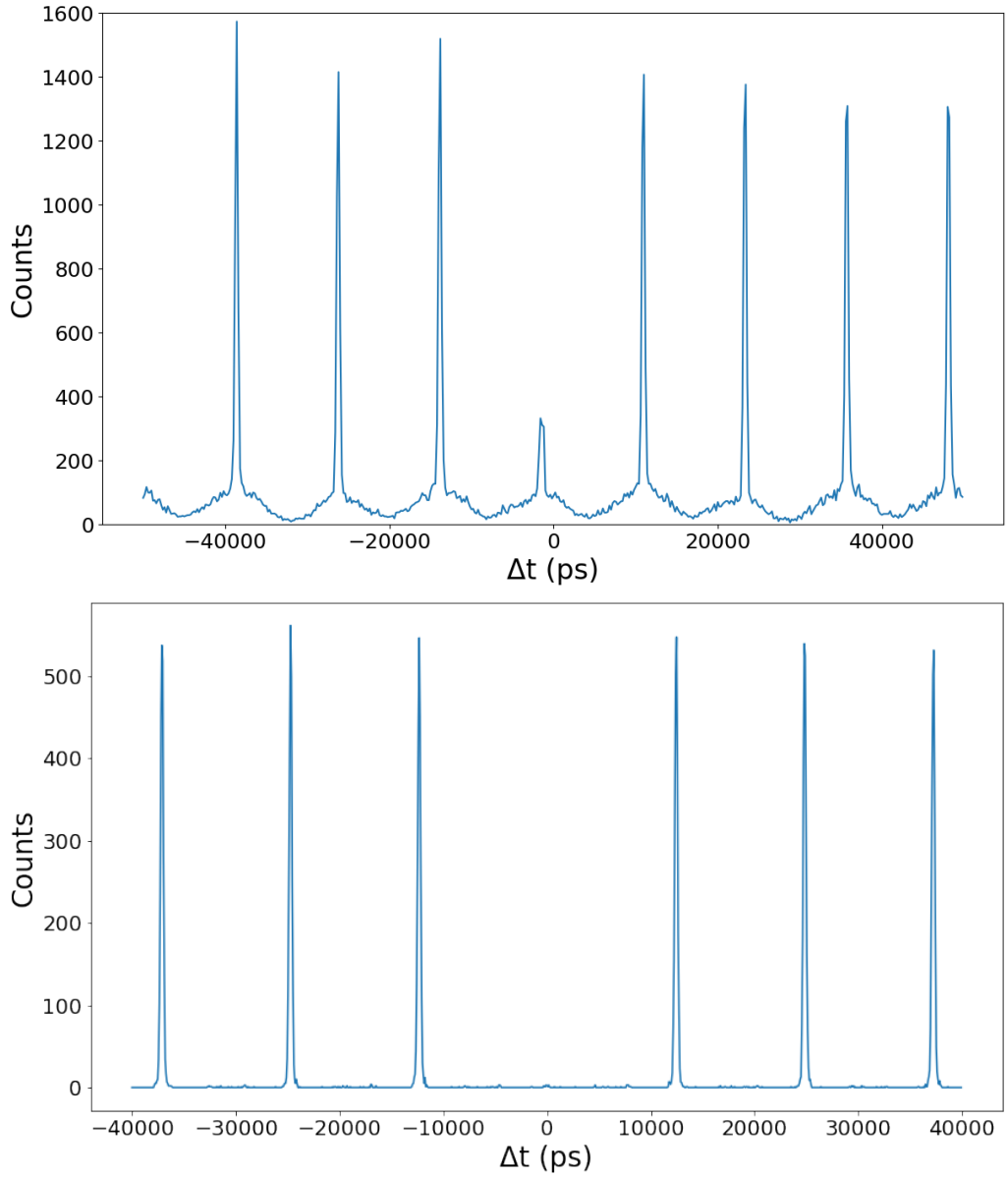


Figure 5.15: Second order correlation measurement (Top) prior to, and (Bottom) after implementing 4F frequency filtering. Accumulated counts of a second photon measured at time Δt after the first photon was recorded. A small peak at $\Delta t = 0$ signifies a low probability of measuring a second photon at the same time as the first, and thus showing high single-photon purity. $g^{(2)}(0) = 0.0063 \pm 0.0016$. This is a substantial improvement when compared to not using the 4F filter as that resulted in a non-viable single-photon source with $g^{(2)}(0) = 0.47 \pm 0.01$.

5.3.6 Four Photon Demultiplexing

At this point, the single photons have been collected into a single-mode fiber and are ready to be measured and characterized. For example, measuring their purity, $g^{(2)}(\tau)$. At this point, they are also ready to be used in single-photon optical experiments. Alternatively, there are experiments that require more than one photon running in parallel. In this case, it is necessary to separate successive photons into separate spatial modes and impose various time delays such that the photons are no longer separated in time.

To achieve this, the last component of the experimental setup is a demultiplexer. The purpose of a demultiplexer is to take a stream of single photons that are separated in time (in this case 12.5 *ns* between consecutive photons) and convert them so that they are instead separated spatially, but in the same time bin. In the case of this experiment, a four-photon demultiplexer was built. As the name suggests, it sends the first photon into one spatial mode, the second photon into a separate spatial mode, and similarly for the third and fourth spatial modes. Each path of the separate spatial modes has a different length to induce different time delays. The first path causes a delay of 37.5 *ns*, the second causes a 25 *ns* delay, and a 12.5 *ns* delay for the third. The fourth spatial mode has no delay.

The demultiplexer consists of three electro-optic modulators (EOM). These EOMs can take incoming light and quickly modulate the polarization of the light in the output. When using the EOM paired with a polarization element, such as a calcite crystal, one can split the stream of photons into two paths depending on the polarization. Vertically polarized photons will pass straight through the crystal, while horizontally polarized photons will be deflected. These two paths then each pass through another EOM that splits them again, creating a total of four paths, or spatial modes.

The construction of the demultiplexer began at the very tail end of my candidature, and thus it was passed on to the other students in the Quantum Technologies Lab. The next steps are to complete the construction of the demultiplexer and characterize the system. The aim is to achieve four-photon coincidences. This is a key step to being able to execute multi-photon experiments in the future, e.g., Grover's Algorithm [51].

Currently, the quantum dot collection efficiency is 1.25% (1 MHz photon count rate with 80 MHz driving rate). The largest form of loss comes from the unpolarized single-photons being filtered by the polarizing beamsplitter, which causes an immediate loss of half of the photons. The rest comes from losses at optical elements en route, notably coupling into the single-mode fiber. The four-photon efficiency of the system is 2.44e$=8$. Given that our demultiplexing changes the clock rate from 80 MHz to 20 MHz, this gives a ceiling to the four-photon rate of $2.44\text{e}{-8} \times 20\ MHz \approx 0.5$ four-photon counts per second. This photon count rate is similar to that previously produced by the quantum dot system [141].

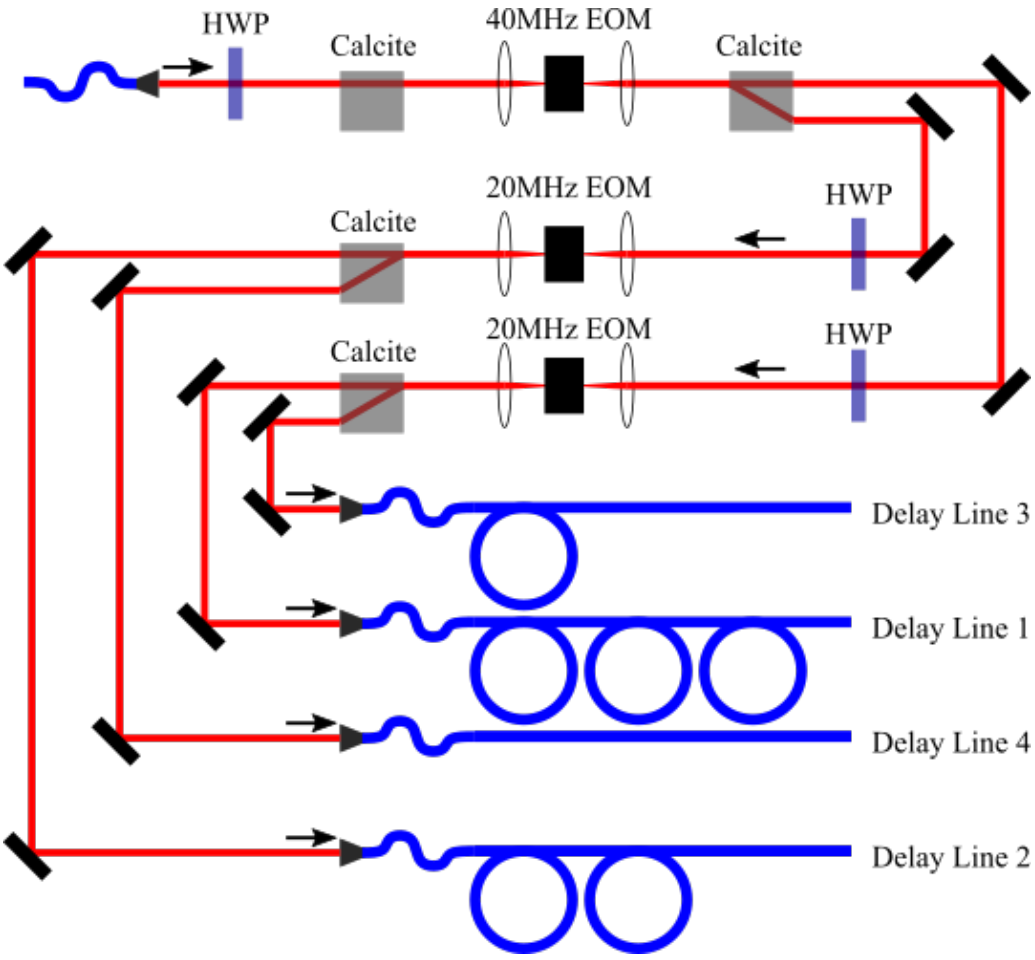


Figure 5.16: Diagram of demultiplexer. Entering the demultiplexer, the photons first pass through a half-waveplate and a calcite crystal to set the polarization passing through the system. The beam is then focused down through the first Electro-Optic Modulator (EOM) from QUBIG, which operates at 40 MHz (actual is 39.84 MHz), and recollimated on the other side. In this particular setup, the lenses used on both ends of the EOMs have a focal length of 100 mm. The beam then passes through a second calcite, which splits the path into two. The photons will either pass through the calcite or be deflected in the calcite, depending on the polarization of the photons, which is determined by the cycle of the EOM. The two split paths become nearly identical at this point, both passing through additional Half-waveplates, 20 MHz (actual is 20.04 MHz and 20.00 MHz) EOMs, and calcite crystals that split each path once again. At this point, there are a total of four independent spatial modes. Each mode is coupled into a single-mode fiber of varying lengths to introduce delays. The repetition rate of the single-photon source is 80 MHz, so the photons are produced 12.5 ns apart. The difference in delays between each spatial mode matches this time interval, such that four consecutive photons exit the demultiplexer at the same time.

Click pattern (1H, 1V, 4H, 4V)	Projected state on (2,3) $\lvert\psi\rangle_{(1H,1V,4H,4V)}$	Probability P(1H, 1V, 4H, 4V)
(1,0,1,0)	$\frac{1}{8}(\lvert V\rangle_2\lvert V\rangle_3+\lvert H\rangle_2\lvert H\rangle_3)$	1/32
(1,1,0,0)	$\frac{1}{8}(\lvert 0\rangle_2\lvert HV\rangle_3+\lvert HV\rangle_2\lvert 0\rangle_3)$	1/32
(1,0,0,1)	$\frac{1}{8}(\lvert V\rangle_2\lvert H\rangle_3+\lvert H\rangle_2\lvert V\rangle_3)$	1/32
(0,1,1,0)	$\frac{1}{8}(\lvert V\rangle_2\lvert H\rangle_3+\lvert H\rangle_2\lvert V\rangle_3)$	1/32
(0,0,1,1)	$\frac{1}{8}(\lvert 0\rangle_2\lvert HV\rangle_3+\lvert HV\rangle_2\lvert 0\rangle_3)$	1/32
(0,1,0,1)	$\frac{1}{8}(\lvert V\rangle_2\lvert V\rangle_3+\lvert H\rangle_2\lvert H\rangle_3)$	1/32

Table 5.1: Detector click patterns in modes 1 and 4 that can generate maximally entangled projected states in modes 2 and 3, and their probabilities. Adapted from [5].

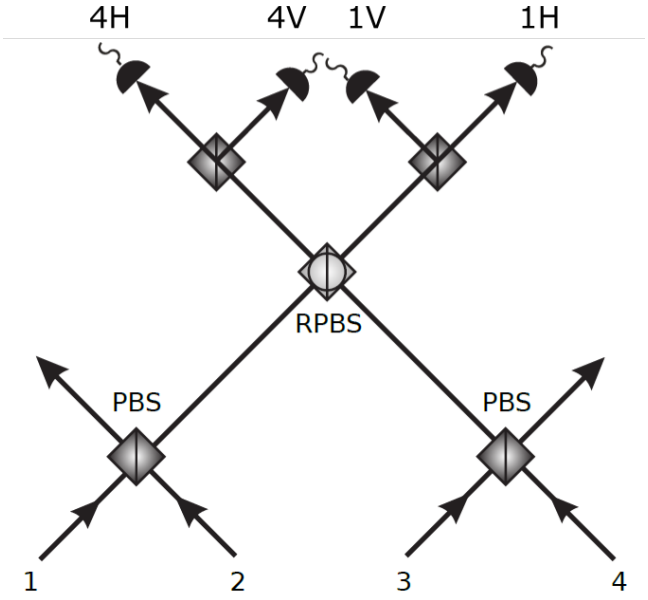


Figure 5.17: Scheme for creating event-ready heralded entanglement. Adapted from [4, 5].

5.4 Future Project: Heralded Entanglement

Generally, in photonics, the measurement of a photon is a destructive process achieved by the absorption of the photon by a material. State entanglement can be classified into two categories. The first of these is postselected entanglement, in which all photons are measured, and therefore the state is created and destroyed in the same moment and can't be used for further processing. The second is heralded entanglement, which uses ancilla photons to determine the success of the remaining, or target photons being entangled. More importantly, because the remaining photons are not measured, the state is not destroyed in this manner and can be used for further computation [143].

The scheme that is intended to be used is adapted from Zhang [4], and consists of four spatial modes. The modes are paired such that the pairs interact on polarizing beamsplitters. A photon (1, 2, 3, and 4) is placed in each input mode, having been prepared in the state $\lvert H\rangle+\lvert V\rangle$, corresponding to a linear polarization at 45°. Photons 1 and 2 interfere on one polarizing beamsplitter, while 3 and 4 interfere on the other polarizing beamsplitter. One output from each beamsplitter is then subjected to type-II fusion [144]. This essentially means they are interfered on a rotating polarizing beamsplitter (RPBS), which is a PBS with HWPs on both input modes and both output modes. This is followed by polarization-sensitive detection (see Figure 5.17). Coincidence events recorded between detectors 1H

or 1V, and 4H and 4V indicate that photons 2 and 3 have collapsed to a Bell state (maximally entangled state). The probabilistic outcome of the entangled state is calculated in [5] (see Table 5.1), determining that a maximally entangled Bell state occurs with $1/8$ probability. The full calculations can be found in Appendix B.

The intent is to use the quantum dot and demultiplexer as a four-photon source to execute Heralded entanglement on a photonic integrated circuit produced by the Institute for Photonics and Nanotechnologies in Milano, Italy. The fabrication of the device starts from a thin Corning Eagle XG alumino-borosilicate glass substrate. Multi-scan irradiation and thermal annealing inscribe waveguides into the material [145]. A series of Mach-Zehnder interferometers is inscribed into the material with thermal isolation trenches in a custom mesh to perform a certain task: Heralded Entanglement, in our case.

Chapter 6

Adaptive Optics and Machine Learning

This chapter is an expansion of previous work [7], where the aim was to improve single photon collection efficiency through the use of adaptive optics and machine learning. Since then, the technique has been applied to the new quantum dot setup as seen in Chapter 5, and the topology of the deformable mirror was more closely examined. This chapter will discuss in detail the two major components of this experiment, which are the deformable mirror and the genetic algorithm.

The goal of the deformable mirror and machine learning is to improve coupling into a single-mode fiber by improving mode matching. The mode produced by the quantum dot differs from the mode of the single-mode fiber. The quantum dot has a hard edged refractive index profile with a large step — vacuum ($n = 1$) to gallium arsenide ($n \approx 3.56$) to vacuum ($n = 1$) — whereas the fiber optic is much smaller — flourine-doped silica cladding ($n \approx 1.444$) to pure-silica core ($n \approx 1.450$) to flourine-doped silica cladding ($n \approx 1.444$) — and sizes of the modes differ as well. This setup also accounts for imperfections to the transverse mode introduced by optical elements along the way.

6.1 Deformable Mirror

The deformable mirror (DM) is the adaptive optics portion of this experimental tandem. The DM was manufactured by ALPAO, and the specific model used was the DM69-15. Unlike most bulk optics used in experimental quantum photonics, the DM has the ability to change its shape and thus change the way it reflects light. The concept of how the DM changes its shape, or the topology of the mirror's surface, is as follows. A highly reflective membrane surface rests upon a grid of actuators. These actuators are confined to a single dimension, and so they can only move up or down. As they do so, they either push or pull on the membrane, locally deforming it.

The specific DM used (DM69-15) consists of a bed of 69 individually controlled actuators, which are arranged in a pseudo-circular grid pattern. Each actuator is controlled by a magnet and coil pair. The magnet sits above the coil, and the magnitude of current running through the coil determines how far the magnet is displaced. This, in turn, determines how far the actuator is displaced and how much the membrane is locally deformed. The separation between each actuator (pitch)is 1.5 *mm*. The useful size of the membrane is 10.5 *mm* in diameter. Each actuator has a range of approximately 2.3 μm and a resolution of 2.8 *nm* [146] [147]. This allows for precise adjustment of beam steering, along with the ability to explore mirror surface topologies aside from a normal flat mirror surface.

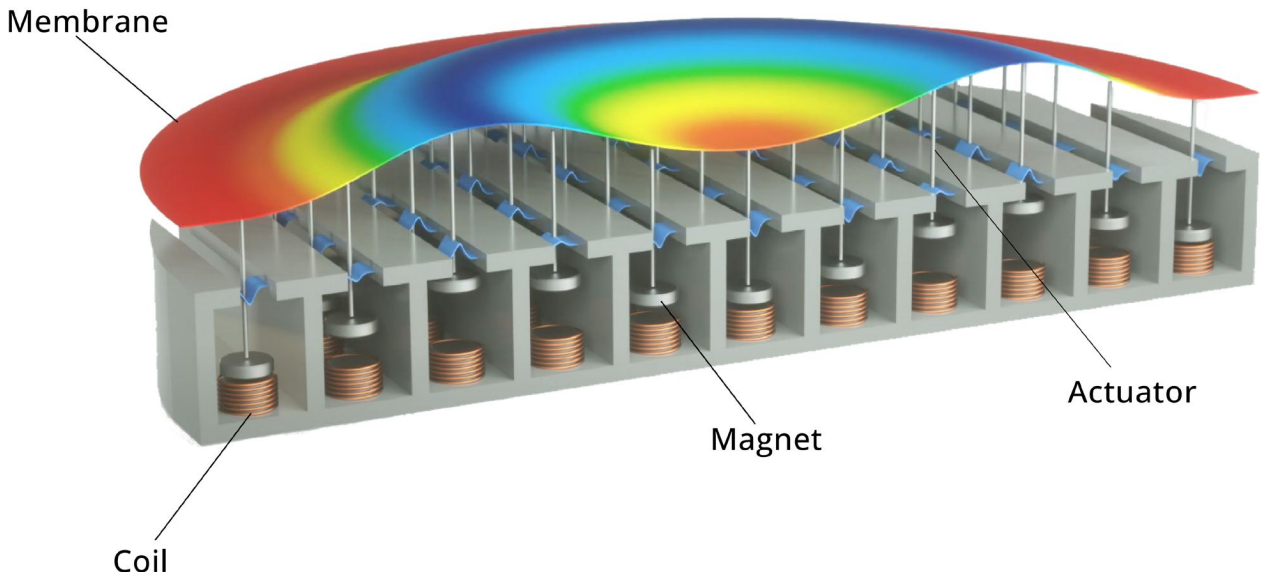


Figure 6.1: 3D rendering of deformable mirror. A flexible and highly reflective membrane rests on a bed of actuators. Each actuator is individually controlled by a single magnet and electrical coil. The displacement of the magnet is determined by the amount of current passing through the coil (Courtesy of ALPAO, accessed 10 October 2024, https://www.alpao.com/).

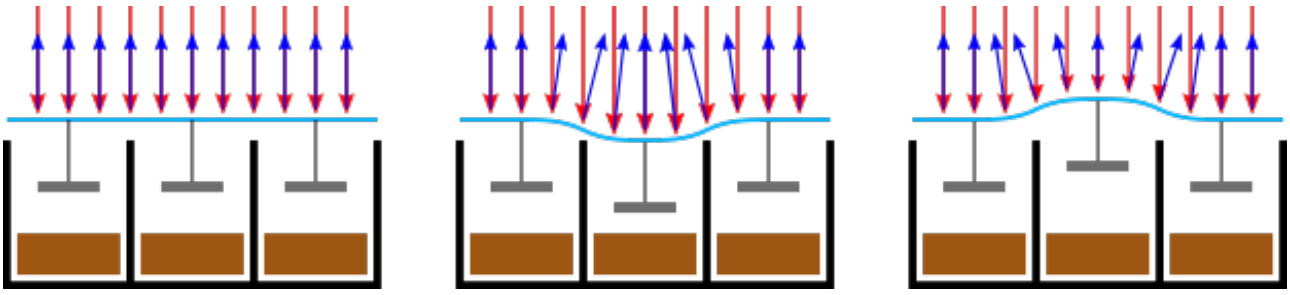


Figure 6.2: Depiction of how the movement of one actuator affects the surface of the deformable mirror and the reflection of incident light. The incident light is shown in red, the reflected light in blue. The surface of the DM, which is attached to the actuator, is shown in light blue, and a magnet is shown in gray. The magnet's position is controlled by the coil shown in brown.

Implementing the deformable mirror into the collection arm of the quantum dot setup can be seen in Figure 5.12. There are two things of note when installing the DM into the collection arm. The first is that the size of the beam should be as large as possible without clipping on the edges of the DM. This allows for more of the actuator to be useful and thus more degrees of freedom when manipulating the beam with the DM. An actuator has no effect if light is not incident on the portion of the membrane that it is responsible for. So, before the DM, a telescope is used to increase the beam diameter. At this moment, the beam diameter is too large once it has reflected from the DM to be coupled into an optical fiber. Therefore, another telescope is used to reduce the size of the beam once more. The second thing to consider is to have the beam incident at a shallow angle with respect to the normal of the DM membrane. The reason for doing so is that it allows for the beam to have a large cross-sectional view of the membrane. Ideally, this angle should be as small as the physical constraints of the experimental setup allow, without the angle being exactly normal to the membrane, as that would send the light back instead of down a new path leading into the collection fiber.

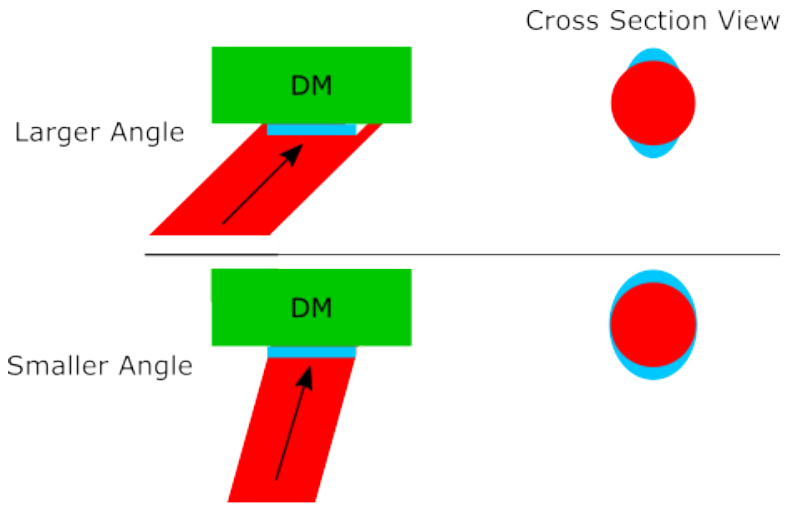


Figure 6.3: A smaller incidence angle of the laser with respect to the normal of the deformable mirror (DM) reduces the amount of clipping the laser has a large beam diameter. Green represents the deformable mirrors housing unit, while blue represents the surface of the highly reflective membrane. Red represents the incident beam. The right-hand side is from the incident laser's perspective and demonstrates how the effective area of the reflective membrane narrows as the angle of incidence becomes shallower.

6.2 Genetic Algorithm

The actuators on the DM can be individually controlled electronically, and the position of each actuator can be updated manually. The goal is to use the DM actuators to more efficiently direct light into a single-mode fiber. However, with 69 actuators and each actuator having 4,000 possible inputs, exploring each possible membrane topology manually is not feasible. The solution to this was to implement a machine learning algorithm to speed up the search for a membrane topology that more efficiently couples the incident light.

The inspiration for the algorithm came from [148], where they used a deformable mirror to couple light from a point-like source. The way they initiated their algorithm was by creating groupings of 5 actuators. In the initialization process, a single group of actuators is chosen, and each actuator is given a value of $\pm\beta$ (β is set by the user). With 5 actuators and 2 values for each actuator, there are 32 possible combinations for which the output power, our count rate, is recorded. During this time, all other actuators are set to a neutral position. The top-performing permutations from this group are chosen as "parents" for the first generation, while the variance of power output is later used as a weighting for inter-generational variances. The "children" are created from the parents by using a multivariate normal distribution N (see Figure 6.5).

$$\boldsymbol{Y}^{t+1} = \sum_{i=1}^{k} \omega_i N(\boldsymbol{Y}_i^t, a_i \boldsymbol{I}_d) \tag{6.1}$$

Here, $\boldsymbol{Y}^{t+1}$ is the child vector, $\boldsymbol{Y}^t$ is the parent vector, and k is the number of parents. The value of ω is set by

$$\omega_i = \frac{c_i}{\sum_{i=1}^{k} c_i} \tag{6.2}$$

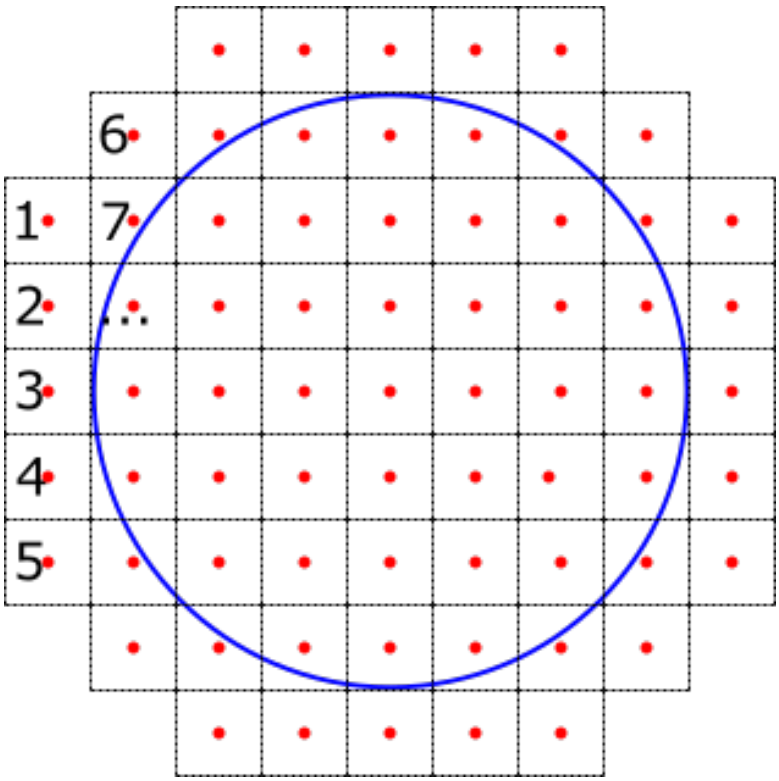


Figure 6.4: Layout of the actuators in the deformable mirror. The red dots signify the actuator placement, while the blue circle signifies the pupil diameter of 10.5 *mm*, which is the effective area of the mirror. Notice that there is a layer of actuators outside the pupil. These actuators are used to control the edge of the mirror. The rows and columns of actuators are separated by 1.5 *mm*, and the Actuators are numbered starting from the top left corner.

where c_i is the count rate ω is the count rate given by the i-th parent. Additionally, the value of a_i is given by

$$a_i = (\frac{C}{c_i})^{\gamma}\rho \tag{6.3}$$

where C is the estimated max count rate while γ and ρ are variables set by the user [148]. The γ sets the sensitivity of the search on the count rate relative to the estimated maximum, and ρ sets the extent of the search space. A full description of the algorithm used can be found in [148].

The first implementation of this method into our quantum dot setup was nearly identical to that described in [148]. However, as described in [7], there seemed to be an issue occurring after the initialization phase. Each grouping of actuators would run through the 32 different configurations, and the top-performing configurations would be selected. Once the initial measurements were taken, the actuators were then addressed as one group of 69 as opposed to groups of 5. Once this happened, the experiment experienced an almost complete loss of all coupling. The suspected reasoning for this is that the coupling from each group of 5 actuators is not completely independent from the others surrounding it, and there is a form of mechanical cross-talk between adjacent actuators. It is believed that as one actuator moves, it bends portions of the mirror surface attached to the surrounding actuators.

The approach to address this issue was to simplify the initialization process of the algorithm. Instead of initializing each group of 5 actuators individually, it was decided to initialize the entire group of 69 actuators at once. This was done by giving the entire bed of actuators a set of random configurations, typically anywhere from 50 to 100 configurations. In each random configuration, each actuator was

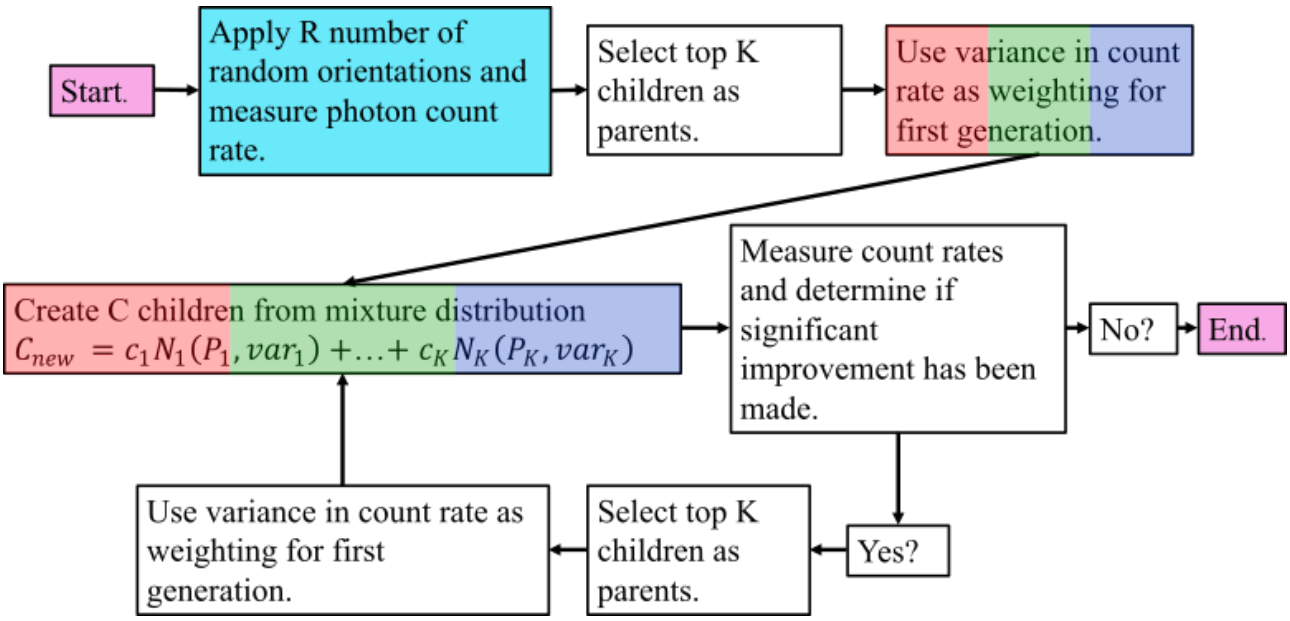


Figure 6.5: Flow chart of the genetic algorithm. The program initializes by applying a random orientation to the entire group of actuators. The user defines the number of initial random orientations as well as the range within which each actuator is initially confined. The top-performing initial random orientations are chosen as "parent" orientations for the first generation. The variance in the count rates is used as weighting for the first generation of "children" orientations. The children are created by way of a mixed, multi-variable distribution. The count rates of the new generation are taken and compared to those of the previous generations. If a significant increase is measured, the top-performing children are used as parents for the next generation. This cycle continues until the count rates of new generations plateau and no significant increase is measured. The coloring of the different stages matches those found in figure 6.6 for visual reference.

given a random value within a user-determined range of values. This range was typically a subset of the 4000 possible values. This range was narrowed down over multiple test runs as larger actuator displacements caused decoupling. The top-performing configurations of the initialization phase were then used as the parents for the first generation. From this point, the subsequent generations of mirror configurations were created using the weighting method described above. The algorithm would then continue to run until it detected no significant increase in the running average in count rate over the most recent three generations. At this point, the best-performing configuration for the entire run was then selected as the final configuration, and the final measurements of this configuration were taken to calculate the increase in average count rate.

While preliminary data was taken in [7] for this project, there was an issue with the stability of the laser frequency at the time, leading to considerable variation in the single-photon count rate, see the bottom panel of Figure 5.2 in [7]. The quantum-dot microcavity system is highly sensitive to fluctuations in laser frequency, leading to fluctuations in output brightness. The reason this is an issue is because of the following. Say that the genetic algorithm is in the middle of measuring the relative coupling efficiency of one of the children it has produced for one of the generations, and records a relatively higher count rate compared to the other children in the same generation. However, at that same moment, the output of the pump laser has spiked and thus produced a higher rate of single photons. So, is the higher count rate due to a more efficient deformable mirror orientation, or is it due to a higher photon production rate? Similarly, when a child's orientation performed poorly, was it

because it was inefficiently coupling into the fiber, or was the pump power low during that moment in time? For this particular setup, there was no way to tell.

The solution to help mitigate this issue was to install a Faraday isolator as described in Chapter 5.3.1. Generally speaking, it is also favorable to have a controlled and stable output for most quantum photonic experiments. Along with the Faraday isolator, new data was taken on the fully rebuilt quantum dot setup where the deformable mirror is permanently installed (see Figure 6.6) as opposed to previous experimental runs where the deformable mirror setup was tacked onto the old quantum dot experimental setup.

Three different measurements were taken to quantify the deformable mirrors' performance. These measurements follow the same steps that are taken in the alignment procedure of the quantum dot experiment. First, the pump light is reflected from a blank surface on the diode that is adjacent to the micropillar supporting the quantum dot. Coupling into the collection fiber is then achieved by hand and maximized. From here, the genetic algorithm is executed, and the improvement in the count rate is recorded. Next, the sample is moved so that the pump laser is incident on the quantum dot cavity. The rotated light is the light that reflects from the cavity and is used to get an initial alignment of the source. The mode of the rotated light is similar to that of the single photon stream. The intensity of the reflected light is much greater than the single photon stream, and so it is much easier to detect visually with the assistance of infrared cards, and thus easier to align. Once manual alignment has been maximized, the algorithm is executed. Finally, the rotated light is filtered out as described in Figure 5.11. Doing this allows only the single photons to reach the collection fiber. Once again, coupling is maximized manually, and the algorithm is executed. A single avalanche photodiode (APD) was used to record the count rates in each run for both manual alignment and machine learning optimization. In addition, when recording the light reflected from the top of the diode and the rotated light, the beams had to be heavily attenuated so as not to damage the APD. Using the deformable mirror and executing the genetic algorithm showed significant improvement in count rate for all three cases. For the reflected pump light, there was a 46% increase in counts, 173% increase for the rotated light, and 226% increase for the single photon count rate (multipliers of $\times 1.46, \times 2.73, \times 3.26$). The results can be seen in Figure 6.6.

The final orientations of each run were recorded and plotted as a topological map, as shown in Figure 6.7. In each run, there is a clear directional shift for all the actuators. This leads to the belief that the alignment of the different beams into the single-mode fiber was not initially perfectly aligned along one axis, and the algorithm corrected for this. However, looking at how the actuators are displaced with respect to one another, no clear pattern can be seen. This leads to the belief that the mirror and algorithm were attempting to correct for random noise in the mode of each beam.

Let us reflect—pardon the pun—on the elegance of this scheme. The deformable mirror replaces one of the steering mirrors that we would have used to couple light into the cavity-dot fiber: since it is replacing an existing element, it does not add additional loss. Next, looking at Figure 6.6, we can see that the magenta points on the left of the plots are the intrinsic coupling from the cavity-dot output into the fiber when reflected from a flat mirror. Deforming the mirror clearly improves the coupling, so we can conclude that the initial mode was not optimally shaped for coupling into the fiber. This may be due to irregularities in the interposing optics, or a result of the hard-edge in the refractive index of the pillar, and so on. The beauty of this scheme is that we don't have to identify the sources of the beam

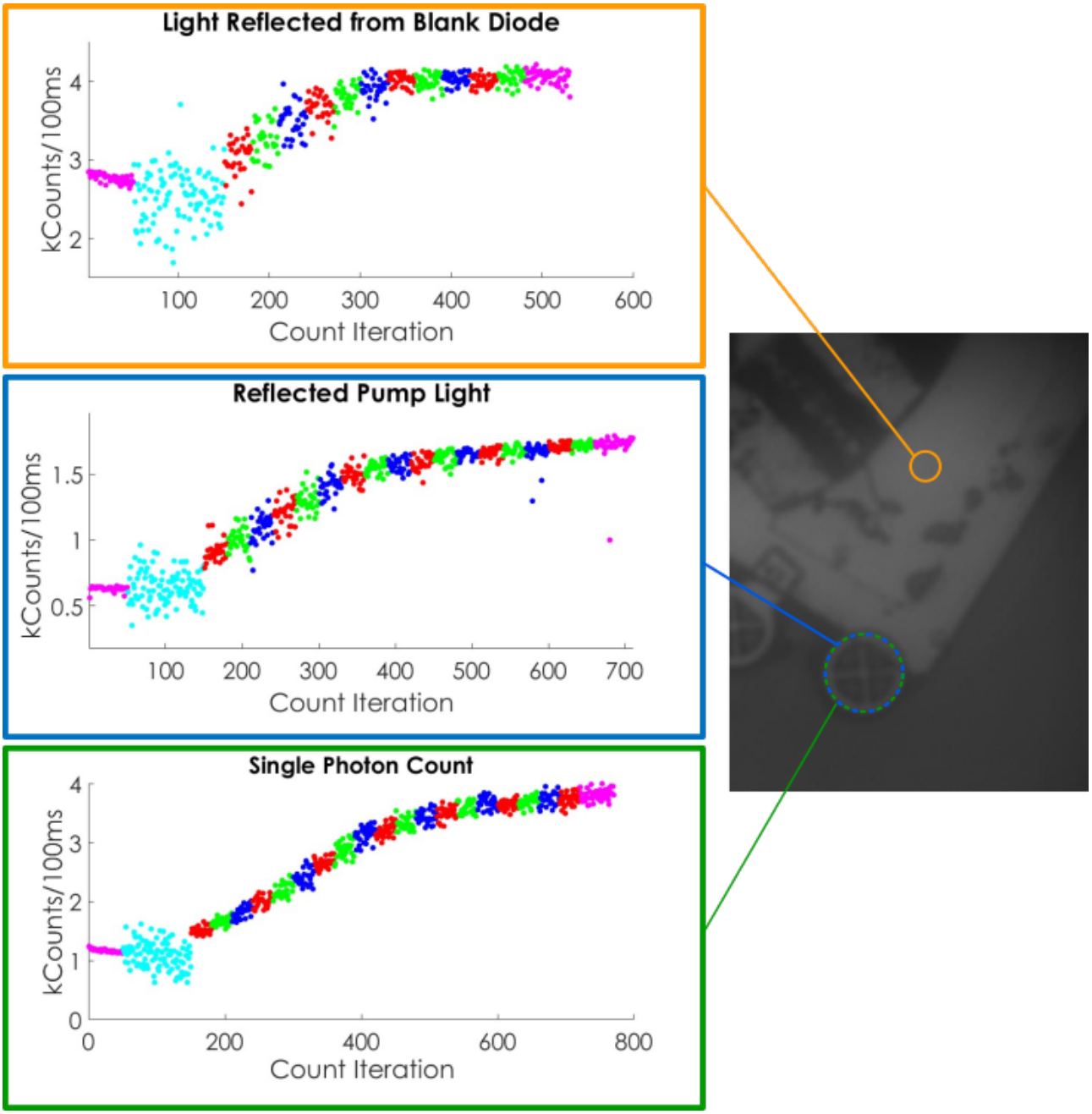


Figure 6.6: Experimental data of count rates measured during the execution of the genetic algorithm on three separate runs. The coloring of the points corresponds to the similarly colored boxes in the flow chart of Figure 6.5. Magenta signifies the initial and final measurements, and cyan indicates the initialization phase of the algorithm, while the red/green/blue identifies each successive generation. (Top) Pump light is reflected from a blank space on the diode. The count rate is increased by $\times 1.46$. (Middle) Pump light is reflected from the quantum dot cavity (rotated light). The count rate is increased by $\times 2.73$. (Bottom) Reflected pump light is filtered out, leaving a stream of single photons to be collected. The count rate is increased by $\times 3.26$. (Right) Photo of the sample indicating where the pump light was incident for each run.

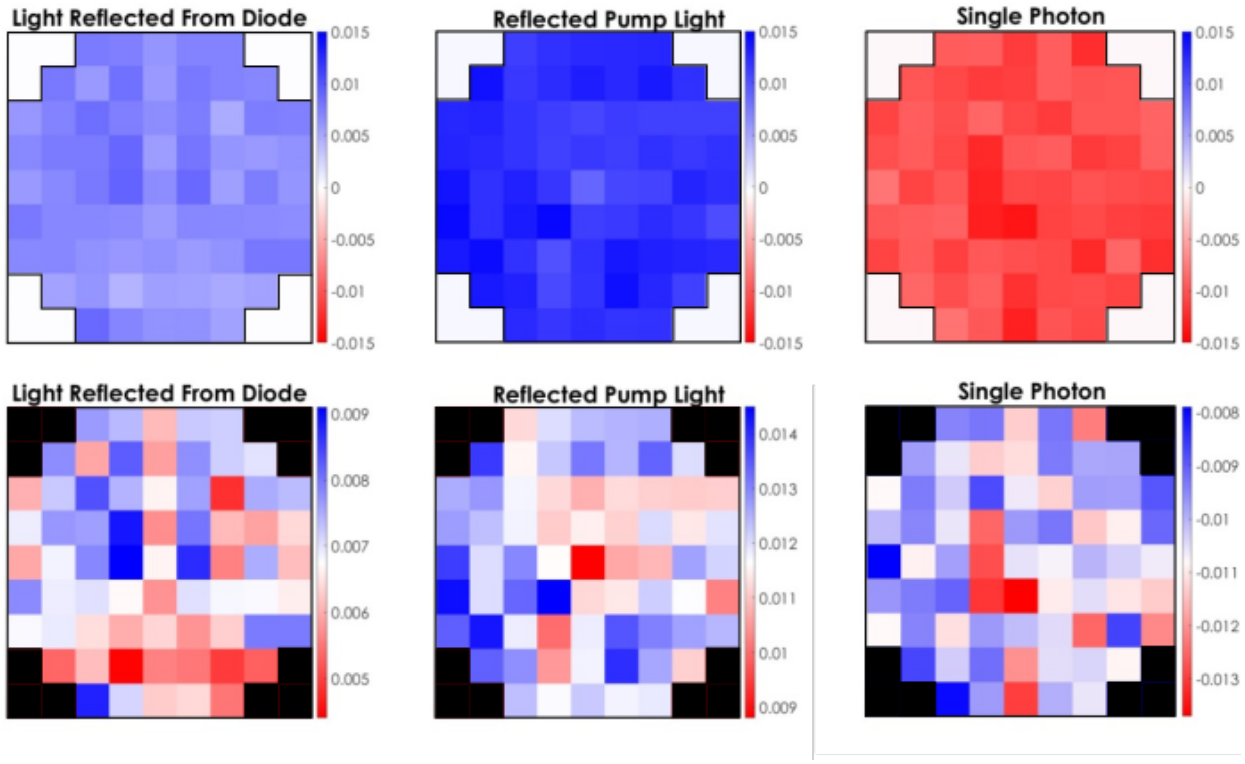


Figure 6.7: Topological depiction of the final orientation of the deformable mirror at the end of the experimental runs, where the light reflected from the diode, the reflected light (rotated light), and single photons were collected into a single-mode fiber, and the genetic algorithm was used to optimize coupling. The top row shows the final position of each actuator on a global scale, while the bottom row shows the topological maps with colors adjusted for the minimum and maximum values. On this scale, 0.00012 corresponds to a physical distance of 2.8 *nm* [146] [147]. Note that there is no discernible overlap in the topographical positions of the DM for the three different scenarios.

irregularities to correct them.

Subsequent to this work, my colleague and visiting PhD student Abhishek Roy has been implementing different algorithms to see if the coupling can be further improved. While the current genetic algorithm does save time when it comes to finding optimal coupling, the new experimental processes being tested implements the Nelder-Mead algorithm [149]. This shows promise with respect to speed, and we plan to submit a publication based on it, combined with the work presented in this thesis.

Chapter 7

Conclusion

The work presented in this thesis is all aimed at the development and understanding of quantum photonics and quantum information. This was addressed in multiple ways, first by interpreting a theoretical concept of asymmetric quantum interference and realizing it under experimental conditions. Secondly, creating a viable and stable single-photon source to be used in further experimentation. Lastly, the application of machine learning and experimental equipment to improve the efficiency of laboratory work.

The ability to selectively adjust the population distribution of the output state is a theoretical concept that was proven in this work. By interfering two photons on a 50:50 beamsplitter to produce the state $(|2,0\rangle + |0,2\rangle)/\sqrt{2}$ and passing one spatial mode through a variable attenuator and interfering both modes on a variable beamsplitter. While the theory shows a complete destructive interference of one of the states, the experimental data was unable to demonstrate the same complete destructive interference. A great effort was made to explain this behavior by updating the theoretical model to account for laboratory experimental conditions. This included introducing higher-order terms produced by the SPDC source, decoherence, imperfect indistinguishability, and spatial mode mismatch. While this significantly altered the probability distributions, this new model was still unable to justify the experimental data.

However, when running the experiment with a fully integrated quantum dot and programmable photonic chip, the results showed a strong correlation to the theoretical model calculated under ideal conditions. This result experimentally demonstrates the production of asymmetric quantum entanglement, which is able to generate a variety of two-photon entangled states beyond the typical NOON state of HOM interference.

The most time-consuming of the tasks was the complete reconstruction of the quantum dot excitation and collection setup. This was brought on by the quantum dot laboratory's physical relocation. While many concepts of the original experimental setup remain, many improvements and additions have been made. Starting from the excitation side, a Faraday isolator was inserted at the output of the excitation laser, significantly improving the laser power output stability while pulsing. Additionally, frequency filtering was applied to the excitation laser light prior to reaching the quantum dot. This came in the form of a 4F filter, which reduced the width of the spectrum by just over a factor of 2, from a FWHM of 0.229 *nm* to 0.106 *nm*, which more closely aligns with the frequency mode of the quantum dot micropillar cavity (≈ 0.077 *nm*). This reduces the amount of light passing to the

quantum dot that is not closely centered on the wavelength of 925 *nm*. This is effective in improving the single photon purity, as light not at this wavelength cannot be absorbed by the quantum dot during resonant excitation. As a result, the single-photon purity of the quantum dot system was improved from $g^{(2)}(0) = 0.47$ (not viable as a single-photon source) to $g^{(2)}(0) = 0.0063$.

Additionally, the redesigned quantum dot excitation and collection setup provides more mechanical stability. This allows for alignment to hold for longer periods of time when compared to the previous setup. In turn, this creates the opportunity to explore experiments that require longer run times and avoids the need for daily realignment.

Furthermore, on the collection side of the quantum dot, a demultiplexer was installed. This particular demultiplexer transferred a single stream of photons into four spatial modes. Each mode was given various delay lines, such that the photons in each mode were then allocated to the same time bin. The next steps are to completely characterize the system so that it can be used for future experiments involving multi-photon quantum circuits.

Lastly, incorporating adaptive optics and machine learning shows an improvement in both laser and single photon coupling into a single-mode fiber. This technique achieves improved results when compared to manual alignment for this particular system. Additionally, this program is executed in a relatively short amount of time (typically 10-20 minutes), quickly increasing the brightness of the system. This system also allows for daily automated readjustments to the alignment, reducing the need for manual alignment. The next step is to implement a different algorithm to further improve the efficiency of the coupling and the time expended.

Bibliography

[1] S. Malewicz, M. de Almeida, A. White, Asymmetric Quantum Interference, Manuscript in Preparation. (Cited on pages iv and 30.)

[2] S. Malewicz, Tunable Quantum Interference (2023). (Cited on page iv.)

[3] S. Malewicz, Bending Mirrors to Collect More Photons (2024). (Cited on page iv.)

[4] Q. Zhang, X.-H. Bao, C.-Y. Lu, X.-Q. Zhou, T. Yang, T. Rudolph, J.-W. Pan, Demonstration of a scheme for the generation of "event-ready" entangled photon pairs from a single-photon source, Physical Review A 77 (6) (2008) 062316. doi:10.1103/PhysRevA.77.062316.
URL https://link.aps.org/doi/10.1103/PhysRevA.77.062316 (Cited on pages xiii, 81, 111, and 112.)

[5] N. Quesada, Fusion Gates with Partially Distinguishable PhotonsIn Preparation (2025). (Cited on pages xiii, 81, 82, and 111.)

[6] A. P. Lund, Classes of two-photon states defined by linear interactions and destructive two-photon quantum interference in a single mode, Physical Review A 92 (5) (2015) 053844. doi:10.1103/PhysRevA.92.053844.
URL https://link.aps.org/doi/10.1103/PhysRevA.92.053844 (Cited on pages 1, 31, 32, 33, 35, 36, 41, and 48.)

[7] S. Malewicz, Masters of Science Thesis: Implementation of Adaptive Optics to Maximize Single-Photon Collection Efficiency, Ph.D. thesis, The University of Queensland, Brisbane, Australia (2021). (Cited on pages 1, 83, 86, and 87.)

[8] A. Einstein, On the Quantum Theory of Radiation, in: Concepts of Quantum Optics, Elsevier, 1983, pp. 93–104. doi:10.1016/B978-0-08-029160-4.50016-6.
URL https://linkinghub.elsevier.com/retrieve/pii/B9780080291604500166 (Cited on page 4.)

[9] M. Planck, The Theory of Heat Radiation, P. Blakiston's Son & Co, Philadelphia, 1914. (Cited on page 4.)

[10] A. Einstein, Zur Quantentheorie der Strahlung, Physikalische Zeitschrift 18 (1917) 121–128, aDS Bibcode: 1917PhyZ...18..121E.
URL https://ui.adsabs.harvard.edu/abs/1917PhyZ...18..121E (Cited on page 4.)

[11] J.-i. Nishizawa, Extension of frequencies from maser to laser: How the laser evolved and was extended to terahertz during my research life A personal review, Proceedings of the Japan

Academy, Series B 85 (10) (2009) 454–465. doi:10.2183/pjab.85.454.
URL https://www.jstage.jst.go.jp/article/pjab/85/10/85_10_454/_article (Cited on page 4.)

[12] T. H. Maiman, Stimulated Optical Radiation in Ruby, Nature 187 (4736) (1960) 493–494. doi:10.1038/187493a0.
URL https://www.nature.com/articles/187493a0 (Cited on pages 4 and 5.)

[13] A. Javan, Possibility of Production of Negative Temperature in Gas Discharges, Physical Review Letters 3 (2) (1959) 87–89. doi:10.1103/PhysRevLett.3.87.
URL https://link.aps.org/doi/10.1103/PhysRevLett.3.87 (Cited on page 5.)

[14] A. Javan, W. R. Bennett, D. R. Herriott, Population Inversion and Continuous Optical Maser Oscillation in a Gas Discharge Containing a He-Ne Mixture, Physical Review Letters 6 (3) (1961) 106–110. doi:10.1103/PhysRevLett.6.106.
URL https://link.aps.org/doi/10.1103/PhysRevLett.6.106 (Cited on page 5.)

[15] C. K. N. Patel, CW HIGH POWER N2–CO2 LASER, Applied Physics Letters 7 (1) (1965) 15–17. doi:10.1063/1.1754233.
URL https://pubs.aip.org/apl/article/7/1/15/65434/CW-HIGH-POWER-N2-CO2-LASER (Cited on page 5.)

[16] J. C. Polanyi, Proposal for an Infrared Maser Dependent on Vibrational Excitation, The Journal of Chemical Physics 34 (1) (1961) 347–348. doi:10.1063/1.1731608.
URL https://pubs.aip.org/jcp/article/34/1/347/207190/Proposal-for-an-Infrared-Maser-Dependent-on (Cited on page 5.)

[17] J. V. V. Kasper, G. C. Pimentel, HCl Chemical Laser, Physical Review Letters 14 (10) (1965) 352–354. doi:10.1103/PhysRevLett.14.352.
URL https://link.aps.org/doi/10.1103/PhysRevLett.14.352 (Cited on page 5.)

[18] D. J. Spencer, T. A. Jacobs, H. Mirels, R. W. F. Gross, Continuous-wave chemical laser, International Journal of Chemical Kinetics 1 (5) (1969) 493–494. doi:10.1002/kin.550010510.
URL https://onlinelibrary.wiley.com/doi/10.1002/kin.550010510 (Cited on page 5.)

[19] P. P. Sorokin, J. R. Lankard, Stimulated Emission Observed from an Organic Dye, Chloroaluminum Phthalocyanine, IBM Journal of Research and Development 10 (2) (1966) 162–163. doi:10.1147/rd.102.0162.
URL http://ieeexplore.ieee.org/document/5392065/ (Cited on page 5.)

[20] F. P. Schäfer, W. Schmidt, J. Volze, ORGANIC DYE SOLUTION LASER, Applied Physics Letters 9 (8) (1966) 306–309. doi:10.1063/1.1754762.
URL https://pubs.aip.org/apl/article/9/8/306/116904/ORGANIC-DYE-SOLUTION-LASER (Cited on page 5.)

[21] A. M. Weiner, Ultrafast Optics, 1st Edition, Wiley, 2009. doi:10.1002/9780470473467.
URL https://onlinelibrary.wiley.com/doi/book/10.1002/9780470473467 (Cited on pages 7, 8, and 69.)

[22] C. K. Hong, Z. Y. Ou, L. Mandel, Measurement of subpicosecond time intervals between two photons by interference, Physical Review Letters 59 (18) (1987) 2044–2046. doi:10.1103/PhysRevLett.59.2044.
URL https://link.aps.org/doi/10.1103/PhysRevLett.59.2044 (Cited on pages 10, 15, and 28.)

[23] M. S. Kim, W. Son, V. Bužek, P. L. Knight, Entanglement by a beam splitter: Nonclassicality as a prerequisite for entanglement, Physical Review A 65 (3) (2002) 032323. doi:10.1103/PhysRevA.65.032323.
URL https://link.aps.org/doi/10.1103/PhysRevA.65.032323 (Cited on page 10.)

[24] W. Xiang-bin, Theorem for the beam-splitter entangler, Physical Review A 66 (2) (2002) 024303. doi:10.1103/PhysRevA.66.024303.
URL https://link.aps.org/doi/10.1103/PhysRevA.66.024303 (Cited on page 10.)

[25] Z. Y. Ou, Quantum multi-particle interference due to a single-photon state, Quantum and Semiclassical Optics: Journal of the European Optical Society Part B 8 (2) (1996) 315–322. doi:10.1088/1355-5111/8/2/001.
URL https://iopscience.iop.org/article/10.1088/1355-5111/8/2/001 (Cited on pages 10 and 11.)

[26] R. Paschotta, Beam Splitters - an encyclopedia article, in: RP Photonics Encyclopedia, RP Photonics AG, 2008. doi:10.61835/mjw.
URL https://www.rp-photonics.com/beam_splitters.html (Cited on page 12.)

[27] D. F. Vanderwerf, Applied Prismatic and Reflective Optics, SPIE, 1000 20th Street, Bellingham, WA 98227-0010 USA, 2010. doi:10.1117/3.867634.
URL http://link.aip.org/link/doi/10.1117/3.867634 (Cited on pages 12, 13, and 14.)

[28] M. A. Nielsen, I. L. Chuang, Quantum computation and quantum information, 10th Edition, Cambridge university press, Cambridge, 2010. (Cited on pages 14, 19, 21, and 22.)

[29] A. M. Brańczyk, Hong-Ou-Mandel Interference, version Number: 1 (2017). doi:10.48550/ARXIV.1711.00080.
URL https://arxiv.org/abs/1711.00080 (Cited on page 16.)

[30] O. Passon, Kelvin's clouds, American Journal of Physics 89 (11) (2021) 1037–1041. doi:10.1119/10.0005620.
URL https://pubs.aip.org/ajp/article/89/11/1037/859801/Kelvin-s-clouds (Cited on page 17.)

[31] D. O. Soares-Pinto, Quantum Information Science: From foundations to new technologies, Physica B: Condensed Matter 653 (2023) 414510. doi:https://doi.org/10.1016/j.physb.2022.414510.
URL https://www.sciencedirect.com/science/article/pii/S0921452622007955 (Cited on page 17.)

[32] G. Adesso, R. L. Franco, V. Parigi, Foundations of quantum mechanics and their impact on contemporary society, Philosophical Transactions of the Royal Society A: Mathematical,

Physical and Engineering Sciences 376 (2123) (2018) 20180112. doi:10.1098/rsta.2018.0112.
URL https://royalsocietypublishing.org/doi/10.1098/rsta.2018.0112 (Cited on page 17.)

[33] A. Einstein, B. Podolsky, N. Rosen, Can Quantum-Mechanical Description of Physical Reality Be Considered Complete?, Physical Review 47 (10) (1935) 777–780. doi:10.1103/PhysRev.47.777.
URL https://link.aps.org/doi/10.1103/PhysRev.47.777 (Cited on page 17.)

[34] J. S. Bell, On the Einstein Podolsky Rosen paradox, Physics Physique Fizika 1 (3) (1964) 195–200. doi:10.1103/PhysicsPhysiqueFizika.1.195.
URL https://link.aps.org/doi/10.1103/PhysicsPhysiqueFizika.1.195 (Cited on pages 17 and 19.)

[35] J. F. Clauser, M. A. Horne, A. Shimony, R. A. Holt, Proposed Experiment to Test Local Hidden-Variable Theories, Physical Review Letters 23 (15) (1969) 880–884. doi:10.1103/PhysRevLett.23.880.
URL https://link.aps.org/doi/10.1103/PhysRevLett.23.880 (Cited on page 17.)

[36] J. F. Clauser, A. Shimony, Bell's theorem. Experimental tests and implications, Reports on Progress in Physics 41 (12) (1978) 1881–1927. doi:10.1088/0034-4885/41/12/002.
URL https://iopscience.iop.org/article/10.1088/0034-4885/41/12/002 (Cited on page 17.)

[37] J. F. Clauser, M. A. Horne, Experimental consequences of objective local theories, Physical Review D 10 (2) (1974) 526–535. doi:10.1103/PhysRevD.10.526.
URL https://link.aps.org/doi/10.1103/PhysRevD.10.526 (Cited on page 17.)

[38] A. Aspect, P. Grangier, G. Roger, Experimental Tests of Realistic Local Theories via Bell's Theorem, Physical Review Letters 47 (7) (1981) 460–463. doi:10.1103/PhysRevLett.47.460.
URL https://link.aps.org/doi/10.1103/PhysRevLett.47.460 (Cited on page 17.)

[39] A. Aspect, J. Dalibard, G. Roger, Experimental Test of Bell's Inequalities Using Time- Varying Analyzers, Physical Review Letters 49 (25) (1982) 1804–1807. doi:10.1103/PhysRevLett.49.1804.
URL https://link.aps.org/doi/10.1103/PhysRevLett.49.1804 (Cited on page 17.)

[40] A. Aspect, P. Grangier, G. Roger, Experimental Realization of Einstein-Podolsky-Rosen-Bohm *Gedankenexperiment* : A New Violation of Bell's Inequalities, Physical Review Letters 49 (2) (1982) 91–94. doi:10.1103/PhysRevLett.49.91.
URL https://link.aps.org/doi/10.1103/PhysRevLett.49.91 (Cited on page 17.)

[41] A. Slaoui, N. Ikken, L. Btissam Drissi, R. Ahl Laamara, Quantum communication protocols: From theory to implementation in the quantum computer, in: B. Carpentieri (Ed.), Quantum Computing - Innovations and Applications in Modern Research, IntechOpen, 2023. doi:10.5772/intechopen.1002792.
URL https://www.intechopen.com/chapters/1160897 (Cited on page 17.)

[42] P. G. Kwiat, K. Mattle, H. Weinfurter, A. Zeilinger, A. V. Sergienko, Y. Shih, New High-Intensity Source of Polarization-Entangled Photon Pairs, Physical Review Letters 75 (24) (1995) 4337–4341. doi:10.1103/PhysRevLett.75.4337.
URL https://link.aps.org/doi/10.1103/PhysRevLett.75.4337 (Cited on pages 17 and 24.)

[43] P. G. Kwiat, E. Waks, A. G. White, I. Appelbaum, P. H. Eberhard, Ultrabright source of polarization-entangled photons, Physical Review A 60 (2) (1999) R773–R776. doi:10.1103/PhysRevA.60.R773.
URL https://link.aps.org/doi/10.1103/PhysRevA.60.R773 (Cited on page 17.)

[44] N. S. Yanofsky, An Introduction to Quantum Computing, version Number: 1 (2007). doi:10.48550/ARXIV.0708.0261.
URL https://arxiv.org/abs/0708.0261 (Cited on page 18.)

[45] B. Schumacher, Quantum coding, Physical Review A 51 (4) (1995) 2738–2747. doi:10.1103/PhysRevA.51.2738.
URL https://link.aps.org/doi/10.1103/PhysRevA.51.2738 (Cited on page 18.)

[46] A. Peres, Incompatible results of quantum measurements, Physics Letters A 151 (3-4) (1990) 107–108. doi:10.1016/0375-9601(90)90172-K.
URL https://linkinghub.elsevier.com/retrieve/pii/037596019090172K (Cited on page 19.)

[47] C. H. Bennett, G. Brassard, C. Crépeau, R. Jozsa, A. Peres, W. K. Wootters, Teleporting an unknown quantum state via dual classical and Einstein-Podolsky-Rosen channels, Physical Review Letters 70 (13) (1993) 1895–1899. doi:10.1103/PhysRevLett.70.1895.
URL https://link.aps.org/doi/10.1103/PhysRevLett.70.1895 (Cited on page 19.)

[48] S.-K. Chu, C.-T. Ma, R.-X. Miao, C.-H. Wu, Maximally Entangled State and Bell's Inequality in QubitsPublisher: arXiv Version Number: 1 (2017). doi:10.48550/ARXIV.1711.04415.
URL https://arxiv.org/abs/1711.04415 (Cited on page 19.)

[49] C. H. Bennett, S. J. Wiesner, Communication via one- and two-particle operators on Einstein-Podolsky-Rosen states, Physical Review Letters 69 (20) (1992) 2881–2884. doi:10.1103/PhysRevLett.69.2881.
URL https://link.aps.org/doi/10.1103/PhysRevLett.69.2881 (Cited on page 19.)

[50] C. H. Bennett, G. Brassard, Quantum cryptography: Public key distribution and coin tossingPublisher: arXiv Version Number: 1 (2020). doi:10.48550/ARXIV.2003.06557.
URL https://arxiv.org/abs/2003.06557 (Cited on page 19.)

[51] L. K. Grover, A fast quantum mechanical algorithm for database search, in: Proceedings of the twenty-eighth annual ACM symposium on Theory of computing - STOC '96, ACM Press, Philadelphia, Pennsylvania, United States, 1996, pp. 212–219. doi:10.1145/237814.237866.
URL http://portal.acm.org/citation.cfm?doid=237814.237866 (Cited on pages 19 and 79.)

[52] P. Shor, Algorithms for quantum computation: discrete logarithms and factoring, in: Proceedings 35th Annual Symposium on Foundations of Computer Science, IEEE Comput. Soc. Press, Santa

Fe, NM, USA, 1994, pp. 124–134. doi:10.1109/SFCS.1994.365700.
URL http://ieeexplore.ieee.org/document/365700/ (Cited on page 19.)

[53] G. Botelho, D. Pellegrino, E. Teixeira, Hilbert Spaces, in: Introduction to Functional Analysis, Springer Nature Switzerland, Cham, 2025, pp. 85–116, series Title: Universitext. doi:10.1007/978-3-031-81791-5_5.
URL https://link.springer.com/10.1007/978-3-031-81791-5_5 (Cited on pages 19 and 21.)

[54] C. H. Bennett, Logical Reversibility of Computation, IBM Journal of Research and Development 17 (6) (1973) 525–532, publisher: IBM. doi:10.1147/rd.176.0525.
URL http://ieeexplore.ieee.org/document/5391327/ (Cited on page 19.)

[55] J. W. d. Bakker, J. v. Leeuwen, Automata, Languages and Programming: Seventh Colloquium, Noordwijkerhout, The Netherlands, July 14-18, 1980. Proceedings, no. 85 in Lecture Notes in Computer Science, Springer Berlin Heidelberg, Berlin, Heidelberg, 1980. doi:10.1007/3-540-10003-2. (Cited on page 19.)

[56] S. Axler, Linear Algebra Done Right, Undergraduate Texts in Mathematics, Springer International Publishing, Cham, 2024. doi:10.1007/978-3-031-41026-0.
URL https://link.springer.com/10.1007/978-3-031-41026-0 (Cited on page 20.)

[57] K. Kraus, General state changes in quantum theory, Annals of Physics 64 (2) (1971) 311–335. doi:10.1016/0003-4916(71)90108-4.
URL https://linkinghub.elsevier.com/retrieve/pii/0003491671901084 (Cited on page 21.)

[58] M.-D. Choi, Completely positive linear maps on complex matrices, Linear Algebra and its Applications 10 (3) (1975) 285–290. doi:10.1016/0024-3795(75)90075-0.
URL https://linkinghub.elsevier.com/retrieve/pii/0024379575900750 (Cited on page 21.)

[59] W. G. Ritter, Quantum Channels and Representation TheoryPublisher: arXiv Version Number: 1 (2005). doi:10.48550/ARXIV.QUANT-PH/0502153.
URL https://arxiv.org/abs/quant-ph/0502153 (Cited on page 22.)

[60] O. Ezratty, Perspective on superconducting qubit quantum computing, The European Physical Journal A 59 (5) (2023) 94. doi:10.1140/epja/s10050-023-01006-7.
URL https://link.springer.com/10.1140/epja/s10050-023-01006-7 (Cited on page 22.)

[61] M. Kjaergaard, M. E. Schwartz, J. Braumüller, P. Krantz, J. I.-J. Wang, S. Gustavsson, W. D. Oliver, Superconducting Qubits: Current State of Play, Annual Review of Condensed Matter Physics 11 (1) (2020) 369–395. doi:10.1146/annurev-conmatphys-031119-050605.
URL https://www.annualreviews.org/doi/10.1146/annurev-conmatphys-031119-050605 (Cited on page 22.)

[62] H.-L. Huang, D. Wu, D. Fan, X. Zhu, Superconducting quantum computing: a review, Science China Information Sciences 63 (8) (2020) 180501. doi:10.1007/s11432-020-2881-9.
URL https://link.springer.com/10.1007/s11432-020-2881-9 (Cited on page 22.)

[63] T. Strohm, K. Wintersperger, F. Dommert, D. Basilewitsch, G. Reuber, A. Hoursanov, T. Ehmer, D. Vodola, S. Luber, Ion-Based Quantum Computing Hardware: Performance and End-User Perspective, version Number: 1 (2024). doi:10.48550/ARXIV.2405.11450.
URL https://arxiv.org/abs/2405.11450 (Cited on page 22.)

[64] C. D. Bruzewicz, J. Chiaverini, R. McConnell, J. M. Sage, Trapped-ion quantum computing: Progress and challenges, Applied Physics Reviews 6 (2) (2019) 021314. doi:10.1063/1.5088164.
URL https://pubs.aip.org/apr/article/6/2/021314/570103/Trapped-ion-quantum-computing-Progress-and (Cited on page 22.)

[65] D. P. DiVincenzo, The Physical Implementation of Quantum Computation, Fortschritte der Physik 48 (9-11) (2000) 771–783. doi:10.1002/1521-3978(200009)48:9/11<771::AID-PROP771>3.0.CO;2-E.
URL https://onlinelibrary.wiley.com/doi/10.1002/1521-3978(200009)48:9/11<771::AID-PROP771>3.0.CO;2-E (Cited on page 22.)

[66] K. M. Shafi, R. Yalla, K. P. Nayak, Bright and polarized fiber in-line single photon source based on plasmon-enhanced emission into nanofiber guided modes, version Number: 1 (2022). doi:10.48550/ARXIV.2206.13029.
URL https://arxiv.org/abs/2206.13029 (Cited on page 22.)

[67] H. Wang, H. Yuan, Q. Zeng, L. Zhou, H. Ma, Z. Yuan, Bright Heralded Single-Photon Source Saturating Theoretical Single-photon PurityPublisher: arXiv Version Number: 3 (2024). doi:10.48550/ARXIV.2404.03236.
URL https://arxiv.org/abs/2404.03236 (Cited on page 22.)

[68] L. S. Madsen, F. Laudenbach, M. F. Askarani, F. Rortais, T. Vincent, J. F. F. Bulmer, F. M. Miatto, L. Neuhaus, L. G. Helt, M. J. Collins, A. E. Lita, T. Gerrits, S. W. Nam, V. D. Vaidya, M. Menotti, I. Dhand, Z. Vernon, N. Quesada, J. Lavoie, Quantum computational advantage with a programmable photonic processor, Nature 606 (7912) (2022) 75–81. doi:10.1038/s41586-022-04725-x.
URL https://www.nature.com/articles/s41586-022-04725-x (Cited on page 22.)

[69] H. J. Manetsch, G. Nomura, E. Bataille, K. H. Leung, X. Lv, M. Endres, A tweezer array with 6100 highly coherent atomic qubits, version Number: 3 (2024). doi:10.48550/ARXIV.2403.12021.
URL https://arxiv.org/abs/2403.12021 (Cited on page 22.)

[70] H. Wang, Y. He, Y.-H. Li, Z.-E. Su, B. Li, H.-L. Huang, X. Ding, M.-C. Chen, C. Liu, J. Qin, J.-P. Li, Y.-M. He, C. Schneider, M. Kamp, C.-Z. Peng, S. Höfling, C.-Y. Lu, J.-W. Pan, High-efficiency multiphoton boson sampling, Nature Photonics 11 (6) (2017) 361–365. doi:10.1038/nphoton.2017.63.
URL https://www.nature.com/articles/nphoton.2017.63 (Cited on page 22.)

[71] E. Knill, R. Laflamme, G. J. Milburn, A scheme for efficient quantum computation with linear optics, Nature 409 (6816) (2001) 46–52. doi:10.1038/35051009.
URL https://www.nature.com/articles/35051009 (Cited on page 23.)

[72] X. Qiang, X. Zhou, J. Wang, C. M. Wilkes, T. Loke, S. O'Gara, L. Kling, G. D. Marshall, R. Santagati, T. C. Ralph, J. B. Wang, J. L. O'Brien, M. G. Thompson, J. C. F. Matthews, Large-scale silicon quantum photonics implementing arbitrary two-qubit processing, Nature Photonics 12 (9) (2018) 534–539. doi:10.1038/s41566-018-0236-y.
URL https://www.nature.com/articles/s41566-018-0236-y (Cited on page 23.)

[73] D. N. Klyshko, Parametric luminescence and parametric scattering in crystals, JETP Letters 6 (1967) 23–25. (Cited on page 23.)

[74] D. C. Burnham, D. L. Weinberg, Observation of Simultaneity in Parametric Production of Optical Photon Pairs, Physical Review Letters 25 (2) (1970) 84–87. doi:10.1103/PhysRevLett.25.84.
URL https://link.aps.org/doi/10.1103/PhysRevLett.25.84 (Cited on page 23.)

[75] O. Slattery, L. Ma, K. Zong, X. Tang, Background and Review of Cavity-Enhanced Spontaneous Parametric Down-Conversion, Journal of Research of the National Institute of Standards and Technology 124 (2019) 124019. doi:10.6028/jres.124.019.
URL https://nvlpubs.nist.gov/nistpubs/jres/124/jres.124.019.pdf (Cited on page 23.)

[76] C. Couteau, Spontaneous parametric down-conversion, Contemporary Physics 59 (3) (2018) 291–304. doi:10.1080/00107514.2018.1488463.
URL https://www.tandfonline.com/doi/full/10.1080/00107514.2018.1488463 (Cited on page 23.)

[77] L. Mandel, E. Wolf, Optical Coherence and Quantum Optics, 1st Edition, Cambridge University Press, 1995. doi:10.1017/CBO9781139644105.
URL https://www.cambridge.org/core/product/identifier/9781139644105/type/book (Cited on page 23.)

[78] J. E. Midwinter, J. Warner, The effects of phase matching method and of uniaxial crystal symmetry on the polar distribution of second-order non-linear optical polarization, British Journal of Applied Physics 16 (8) (1965) 1135–1142. doi:10.1088/0508-3443/16/8/312.
URL https://iopscience.iop.org/article/10.1088/0508-3443/16/8/312 (Cited on page 24.)

[79] R. W. Boyd, Nonlinear optics, fourth edition Edition, Elsevier, AP Academic Press, London, 2020. doi:10.1016/C2015-0-05510-1. (Cited on pages 24 and 25.)

[80] E. Meyer-Scott, C. Silberhorn, A. Migdall, Single-photon sources: Approaching the ideal through multiplexing, Review of Scientific Instruments 91 (4) (2020) 041101. doi:10.1063/5.0003320.
URL https://pubs.aip.org/rsi/article/91/4/041101/1030773/Single-photon-sources-Approaching-the-ideal (Cited on pages 25 and 28.)

[81] A. I. Ekimov, A. A. Onushchenko, Quantum Size Effect in Three-Dimensional Microscopic Semiconductor Crystals, JETP Letters 118 (S1) (2023) S15–S17. doi:10.1134/S0021364023130040.
URL https://link.springer.com/10.1134/S0021364023130040 (Cited on page 25.)

[82] D. Leonard, M. Krishnamurthy, C. M. Reaves, S. P. Denbaars, P. M. Petroff, Direct formation of quantum-sized dots from uniform coherent islands of InGaAs on GaAs surfaces, Applied Physics Letters 63 (23) (1993) 3203–3205. doi:10.1063/1.110199.
URL https://pubs.aip.org/apl/article/63/23/3203/62454/Direct-formation-of-quantum-sized-dots-from (Cited on page 25.)

[83] H. Friedrich, Theoretical Atomic Physics, second revised and enlarged edition Edition, Advanced Texts in Physics, Springer, Berlin Heidelberg, 1998. doi:10.1007/978-3-662-03704-1. (Cited on page 25.)

[84] P. Ramasamy, Unidirectional growth of benzophenone single crystals from solution, Journal of Crystal Growth 310 (7-9) (2008) 1501–1504. doi:10.1016/j.jcrysgro.2007.11.070.
URL https://linkinghub.elsevier.com/retrieve/pii/S0022024807010561 (Cited on page 26.)

[85] D. Leonard, K. Pond, P. M. Petroff, Critical layer thickness for self-assembled InAs islands on GaAs, Physical Review B 50 (16) (1994) 11687–11692. doi:10.1103/PhysRevB.50.11687.
URL https://link.aps.org/doi/10.1103/PhysRevB.50.11687 (Cited on page 26.)

[86] P. Basu, J. Verma, V. Abhinav, R. K. Ratnesh, Y. K. Singla, V. Kumar, Advancements in Lithography Techniques and Emerging Molecular Strategies for Nanostructure Fabrication, International Journal of Molecular Sciences 26 (7) (2025) 3027. doi:10.3390/ijms26073027.
URL https://www.mdpi.com/1422-0067/26/7/3027 (Cited on page 26.)

[87] A. Dousse, L. Lanco, J. Suffczyński, E. Semenova, A. Miard, A. Lemaître, I. Sagnes, C. Roblin, J. Bloch, P. Senellart, Controlled Light-Matter Coupling for a Single Quantum Dot Embedded in a Pillar Microcavity Using Far-Field Optical Lithography, Physical Review Letters 101 (26) (2008) 267404. doi:10.1103/PhysRevLett.101.267404.
URL https://link.aps.org/doi/10.1103/PhysRevLett.101.267404 (Cited on page 26.)

[88] A. K. Nowak, S. L. Portalupi, V. Giesz, O. Gazzano, C. Dal Savio, P.-F. Braun, K. Karrai, C. Arnold, L. Lanco, I. Sagnes, A. Lemaître, P. Senellart, Deterministic and electrically tunable bright single-photon source, Nature Communications 5 (1) (2014) 3240. doi:10.1038/ncomms4240.
URL https://www.nature.com/articles/ncomms4240 (Cited on pages 26 and 27.)

[89] R. H. Brown, R. Q. Twiss, Correlation between Photons in two Coherent Beams of Light, Nature 177 (4497) (1956) 27–29. doi:10.1038/177027a0.
URL https://www.nature.com/articles/177027a0 (Cited on page 28.)

[90] P. Senellart, G. Solomon, A. White, High-performance semiconductor quantum-dot single-photon sources, Nature Nanotechnology 12 (11) (2017) 1026–1039. doi:10.1038/nnano.2017.218.
URL https://www.nature.com/articles/nnano.2017.218 (Cited on page 28.)

[91] N. Hauser, M. Bayerbach, J. Kaupp, Y. Reum, G. Peniakov, J. Michl, M. Kamp, T. Huber-Loyola, A. T. Pfenning, S. Höfling, S. Barz, Deterministic and highly indistinguishable single photons in the telecom C-band, version Number: 1 (2025). doi:10.48550/ARXIV.2505.09695.
URL https://arxiv.org/abs/2505.09695 (Cited on page 28.)

[92] O. Gazzano, S. Michaelis De Vasconcellos, C. Arnold, A. Nowak, E. Galopin, I. Sagnes, L. Lanco, A. Lemaître, P. Senellart, Bright solid-state sources of indistinguishable single photons, Nature Communications 4 (1) (2013) 1425. doi:10.1038/ncomms2434.
URL https://www.nature.com/articles/ncomms2434 (Cited on page 28.)

[93] T. Takagi, On an Algebraic Problem Reluted to an Analytic Theorem of Carathéodory and Fejér and on an Allied Theorem of Landau, Japanese journal of mathematics :transactions and abstracts 1 (0) (1924) 83–93. doi:10.4099/jjm1924.1.0_83.
URL https://www.jstage.jst.go.jp/article/jjm1924/1/0/1_0_83/_article (Cited on page 32.)

[94] N. Maring, A. Fyrillas, M. Pont, E. Ivanov, P. Stepanov, N. Margaria, W. Hease, A. Pishchagin, A. Lemaître, I. Sagnes, T. H. Au, S. Boissier, E. Bertasi, A. Baert, M. Valdivia, M. Billard, O. Acar, A. Brieussel, R. Mezher, S. C. Wein, A. Salavrakos, P. Sinnott, D. A. Fioretto, P.-E. Emeriau, N. Belabas, S. Mansfield, P. Senellart, J. Senellart, N. Somaschi, A versatile single-photon-based quantum computing platform, Nature Photonics 18 (6) (2024) 603–609. doi:10.1038/s41566-024-01403-4.
URL https://www.nature.com/articles/s41566-024-01403-4 (Cited on page 36.)

[95] C. Taballione, R. Van Der Meer, H. J. Snijders, P. Hooijschuur, J. P. Epping, M. De Goede, B. Kassenberg, P. Venderbosch, C. Toebes, H. Van Den Vlekkert, P. W. H. Pinkse, J. J. Renema, A universal fully reconfigurable 12-mode quantum photonic processor, Materials for Quantum Technology 1 (3) (2021) 035002. doi:10.1088/2633-4356/ac168c.
URL https://iopscience.iop.org/article/10.1088/2633-4356/ac168c (Cited on pages 36 and 37.)

[96] V. Vedral, Introduction to quantum information science, Oxford graduate texts, Oxford University Press, Oxford, 2006, oCLC: ocm70173203. (Cited on page 36.)

[97] R. Paschotta, Interferometers - an encyclopedia article, in: RP Photonics Encyclopedia, RP Photonics AG, 2005. doi:10.61835/kva.
URL https://www.rp-photonics.com/interferometers.html (Cited on page 36.)

[98] A. Fyrillas, O. Faure, N. Maring, J. Senellart, N. Belabas, Scalable machine learning-assisted clear-box characterization for optimally controlled photonic circuits, Optica 11 (3) (2024) 427. doi:10.1364/OPTICA.512148.
URL https://opg.optica.org/abstract.cfm?URI=optica-11-3-427 (Cited on page 36.)

[99] N. Heurtel, A. Fyrillas, G. D. Gliniasty, R. Le Bihan, S. Malherbe, M. Pailhas, E. Bertasi, B. Bourdoncle, P.-E. Emeriau, R. Mezher, L. Music, N. Belabas, B. Valiron, P. Senellart, S. Mansfield, J. Senellart, Perceval: A Software Platform for Discrete Variable Photonic Quantum Computing, Quantum 7 (2023) 931. doi:10.22331/q-2023-02-21-931.
URL https://quantum-journal.org/papers/q-2023-02-21-931/ (Cited on page 36.)

[100] N. K. Langford, Encoding, manipulating and measuring quantum information in optics, PhD Thesis, The University of Queensland (Jan. 2007). doi:10.14264/136626.
URL https://espace.library.uq.edu.au/view/UQ:136626 (Cited on page 42.)

[101] F. Piacentini, M. P. Levi, A. Avella, M. López, S. Kück, S. V. Polyakov, I. P. Degiovanni, G. Brida, M. Genovese, Positive operator-valued measure reconstruction of a beam-splitter tree-based photon-number-resolving detector, Optics Letters 40 (7) (2015) 1548. doi:10.1364/OL.40.001548.
URL https://opg.optica.org/abstract.cfm?URI=ol-40-7-1548 (Cited on page 45.)

[102] E. A. Goldschmidt, F. Piacentini, I. R. Berchera, S. V. Polyakov, S. Peters, S. Kück, G. Brida, I. P. Degiovanni, A. Migdall, M. Genovese, Mode reconstruction of a light field by multiphoton statistics, Physical Review A 88 (1) (2013) 013822. doi:10.1103/PhysRevA.88.013822.
URL https://link.aps.org/doi/10.1103/PhysRevA.88.013822 (Cited on page 45.)

[103] J. Tiedau, T. J. Bartley, G. Harder, A. E. Lita, S. W. Nam, T. Gerrits, C. Silberhorn, Scalability of parametric down-conversion for generating higher-order Fock states, Physical Review A 100 (4) (2019) 041802. doi:10.1103/PhysRevA.100.041802.
URL https://link.aps.org/doi/10.1103/PhysRevA.100.041802 (Cited on page 48.)

[104] M. A. Broome, M. P. Almeida, A. Fedrizzi, A. G. White, Reducing multi-photon rates in pulsed down-conversion by temporal multiplexing, Optics Express 19 (23) (2011) 22698. doi:10.1364/OE.19.022698.
URL https://opg.optica.org/oe/abstract.cfm?uri=oe-19-23-22698 (Cited on page 48.)

[105] Z.-Y. J. Ou, Multi-photon quantum interference, Springer, New York, NY, 2007. (Cited on pages 48 and 49.)

[106] P. Kok, W. J. Munro, K. Nemoto, T. C. Ralph, J. P. Dowling, G. J. Milburn, Linear optical quantum computing with photonic qubits, Reviews of Modern Physics 79 (1) (2007) 135–174. doi:10.1103/RevModPhys.79.135.
URL https://link.aps.org/doi/10.1103/RevModPhys.79.135 (Cited on page 48.)

[107] E. Optoelectronics, Single Photon Counting Module: {SPCM-AQR} Series, technical datasheet (Jul. 1999).
URL https://www.egginc.com/opto (Cited on page 49.)

[108] N. Schwaller, G. Park, R. Okamoto, S. Takeuchi, Optimizing the coupling efficiency of spontaneous parametric down-conversion photon pairs into single-mode fibers, Physical Review A 106 (4) (2022) 043719. doi:10.1103/PhysRevA.106.043719.
URL https://link.aps.org/doi/10.1103/PhysRevA.106.043719 (Cited on page 49.)

[109] P. B. Dixon, D. Rosenberg, V. Stelmakh, M. E. Grein, R. S. Bennink, E. A. Dauler, A. J. Kerman, R. J. Molnar, F. N. C. Wong, Heralding efficiency and correlated-mode coupling of near-IR fiber-coupled photon pairs, Physical Review A 90 (4) (2014) 043804. doi:10.1103/PhysRevA.90.043804.
URL https://link.aps.org/doi/10.1103/PhysRevA.90.043804 (Cited on page 49.)

[110] O. Kwon, Y.-W. Cho, Y.-H. Kim, Single-mode coupling efficiencies of type-II spontaneous parametric down-conversion: Collinear, noncollinear, and beamlike phase matching, Physical Review A 78 (5) (2008) 053825. doi:10.1103/PhysRevA.78.053825.
URL https://link.aps.org/doi/10.1103/PhysRevA.78.053825 (Cited on page 49.)

[111] C. Dutsov, P. Cassette, B. Sabot, K. Mitev, Evaluation of the accidental coincidence counting rates in TDCR counting, Nuclear Instruments and Methods in Physics Research Section A: Accelerators, Spectrometers, Detectors and Associated Equipment 977 (2020) 164292. doi:10.1016/j.nima.2020.164292.
URL https://linkinghub.elsevier.com/retrieve/pii/S0168900220306884 (Cited on page 49.)

[112] S. Wang, C.-X. Liu, J. Li, Q. Wang, Research on the Hong-Ou-Mandel interference with two independent sources, Scientific Reports 9 (1) (2019) 3854. doi:10.1038/s41598-019-40720-5.
URL https://www.nature.com/articles/s41598-019-40720-5 (Cited on page 49.)

[113] L. Mandel, Quantum effects in one-photon and two-photon interference, Reviews of Modern Physics 71 (2) (1999) S274–S282. doi:10.1103/RevModPhys.71.S274.
URL https://link.aps.org/doi/10.1103/RevModPhys.71.S274 (Cited on page 49.)

[114] A. Hochrainer, M. Lahiri, M. Erhard, M. Krenn, A. Zeilinger, Quantum indistinguishability by path identity and with undetected photons, Reviews of Modern Physics 94 (2) (2022) 025007. doi:10.1103/RevModPhys.94.025007.
URL https://link.aps.org/doi/10.1103/RevModPhys.94.025007 (Cited on page 49.)

[115] T. Legero, T. Wilk, A. Kuhn, G. Rempe, Time-resolved two-photon quantum interference, Applied Physics B 77 (8) (2003) 797–802. doi:10.1007/s00340-003-1337-x.
URL http://link.springer.com/10.1007/s00340-003-1337-x (Cited on page 49.)

[116] P. S. K. Lee, M. P. Van Exter, Spatial labeling in a two-photon interferometer, Physical Review A 73 (6) (2006) 063827. doi:10.1103/PhysRevA.73.063827.
URL https://link.aps.org/doi/10.1103/PhysRevA.73.063827 (Cited on page 50.)

[117] L.-P. Deng, G.-F. Dang, K. Wang, Spatial-mode two-photon interference at a beam splitter, Physical Review A 74 (6) (2006) 063819. doi:10.1103/PhysRevA.74.063819.
URL https://link.aps.org/doi/10.1103/PhysRevA.74.063819 (Cited on page 50.)

[118] T. Jennewein, M. Barbieri, A. G. White, Single-photon device requirements for operating linear optics quantum computing outside the post-selection basis, Journal of Modern Optics 58 (3-4) (2011) 276–287. doi:10.1080/09500340.2010.546894.
URL http://www.tandfonline.com/doi/abs/10.1080/09500340.2010.546894 (Cited on page 51.)

[119] K. Kraus, A. Böhm, J. D. Dollard, W. H. Wootters (Eds.), States, Effects, and Operations Fundamental Notions of Quantum Theory: Lectures in Mathematical Physics at the University of Texas at Austin, no. 190 in Lecture Notes in Physics, Springer Berlin Heidelberg, Berlin, Heidelberg, 1983. doi:10.1007/3-540-12732-1. (Cited on page 52.)

[120] A. Sebastian, A. N. Mansar, N. C. Randeep, Beyond Qubits: An Extensive Noise Analysis for Qutrit Quantum Teleportation, International Journal of Theoretical Physics 62 (12) (2023) 258. doi:10.1007/s10773-023-05515-5.
URL https://link.springer.com/10.1007/s10773-023-05515-5 (Cited on page 52.)

[121] R. B. Millar, Maximum likelihood estimation and inference: with examples in R, SAS, and ADMB, no. v. 111 in Statistics in Practice, Wiley, Hoboken, N.J, 2011. doi:10.1002/9780470094846. (Cited on page 56.)

[122] P. J. Mosley, J. S. Lundeen, B. J. Smith, P. Wasylczyk, A. B. U'Ren, C. Silberhorn, I. A. Walmsley, Heralded Generation of Ultrafast Single Photons in Pure Quantum States, Physical Review Letters 100 (13) (2008) 133601. doi:10.1103/PhysRevLett.100.133601.
URL https://link.aps.org/doi/10.1103/PhysRevLett.100.133601 (Cited on page 57.)

[123] N. A. Zakaria, Exploring engineered solid-state single-photon emitters as multi-photon sources, PhD Thesis, The University of Queensland (Jun. 2022). doi:10.14264/f1db6c1.
URL https://espace.library.uq.edu.au/view/UQ:f1db6c1 (Cited on pages 63 and 66.)

[124] J. C. Loredo Rosillo, Enabling multi-photon experiments with solid-state emitters: a farewell to downconversion, PhD Thesis, The University of Queensland (Aug. 2016). doi:10.14264/uql.2016.595.
URL http://espace.library.uq.edu.au/view/UQ:399491 (Cited on pages 63 and 66.)

[125] F. Mohit, Quantum Technologies: From Integration to Foundations, Ph.D. thesis, The University of Queensland, in preparation. (Cited on page 63.)

[126] S. Das, Experimental Demonstration of Relativistic Bomean Trajectories of a Single Photon, Ph.D. thesis, The University of Queensland, in preparation. (Cited on page 63.)

[127] A. Kiraz, M. Atatüre, A. Imamoğlu, Quantum-dot single-photon sources: Prospects for applications in linear optics quantum-information processing, Physical Review A 69 (3) (2004) 032305. doi:10.1103/PhysRevA.69.032305.
URL https://link.aps.org/doi/10.1103/PhysRevA.69.032305 (Cited on page 64.)

[128] E. B. Flagg, S. V. Polyakov, T. Thomay, G. S. Solomon, Dynamics of Nonclassical Light from a Single Solid-State Quantum Emitter, Physical Review Letters 109 (16) (2012) 163601. doi:10.1103/PhysRevLett.109.163601.
URL https://link.aps.org/doi/10.1103/PhysRevLett.109.163601 (Cited on page 64.)

[129] T. Huber, A. Predojević, G. S. Solomon, G. Weihs, Effects of photo-neutralization on the emission properties of quantum dots, Optics Express 24 (19) (2016) 21794. doi:10.1364/OE.24.021794.
URL https://opg.optica.org/abstract.cfm?URI=oe-24-19-21794 (Cited on page 64.)

[130] O. Gazzano, T. Huber, V. Loo, S. Polyakov, E. B. Flagg, G. S. Solomon, Effects of resonant-laser excitation on the emission properties in a single quantum dot, Optica 5 (4) (2018) 354. doi:10.1364/OPTICA.5.000354.
URL https://opg.optica.org/abstract.cfm?URI=optica-5-4-354 (Cited on page 64.)

[131] N. Somaschi, V. Giesz, L. De Santis, J. C. Loredo, M. P. Almeida, G. Hornecker, S. L. Portalupi, T. Grange, C. Antón, J. Demory, C. Gómez, I. Sagnes, N. D. Lanzillotti-Kimura, A. Lemaítre, A. Auffeves, A. G. White, L. Lanco, P. Senellart, Near-optimal single-photon sources in the solid state, Nature Photonics 10 (5) (2016) 340–345. doi:10.1038/nphoton.2016.23.
URL https://www.nature.com/articles/nphoton.2016.23 (Cited on pages 64, 65, and 77.)

[132] J. Stark, Beobachtungen über den Effekt des elektrischen Feldes auf Spektrallinien. I. Quereffekt, Annalen der Physik 348 (7) (1914) 965–982. doi:10.1002/andp.19143480702.
URL https://onlinelibrary.wiley.com/doi/10.1002/andp.19143480702 (Cited on page 64.)

[133] C. Matthiesen, A. N. Vamivakas, M. Atatüre, Subnatural Linewidth Single Photons from a Quantum Dot, Physical Review Letters 108 (9) (2012) 093602. doi:10.1103/PhysRevLett.108.093602.
URL https://link.aps.org/doi/10.1103/PhysRevLett.108.093602 (Cited on page 65.)

[134] A. Nick Vamivakas, Y. Zhao, C.-Y. Lu, M. Atatüre, Spin-resolved quantum-dot resonance fluorescence, Nature Physics 5 (3) (2009) 198–202. doi:10.1038/nphys1182.
URL https://www.nature.com/articles/nphys1182 (Cited on page 65.)

[135] M. Faraday, T. Martin, Faraday's diary : being the various philosophical notes of experimental investigation, G. Bell, Lodon, 1932. (Cited on page 67.)

[136] A. Zvezdin, V. Kotov, Modern Magnetooptics and Magnetooptical Materials, 0th Edition, CRC Press, 1997. doi:10.1201/9780367802608.
URL https://www.taylorfrancis.com/books/9781420050844 (Cited on page 67.)

[137] R. Paschotta, Field guide to laser pulse generation, no. FG14 in SPIE field guides, SPIE Press, Bellingham, Wash, 2008. (Cited on page 68.)

[138] A. M. Weiner, Femtosecond pulse shaping using spatial light modulators, Review of Scientific Instruments 71 (5) (2000) 1929–1960. doi:10.1063/1.1150614.
URL https://pubs.aip.org/rsi/article/71/5/1929/436146/Femtosecond-pulse-shaping-using-spatial-light (Cited on page 69.)

[139] A. M. Weiner, Ultrafast optical pulse shaping: A tutorial review, Optics Communications 284 (15) (2011) 3669–3692. doi:https://doi.org/10.1016/j.optcom.2011.03.084.
URL https://www.sciencedirect.com/science/article/pii/S0030401811003750 (Cited on page 69.)

[140] Y. Karli, F. Kappe, V. Remesh, T. K. Bracht, J. Münzberg, S. Covre Da Silva, T. Seidelmann, V. M. Axt, A. Rastelli, D. E. Reiter, G. Weihs, SUPER Scheme in Action: Experimental Demonstration of Red-Detuned Excitation of a Quantum Emitter, Nano Letters 22 (16) (2022) 6567–6572. doi:10.1021/acs.nanolett.2c01783.
URL https://pubs.acs.org/doi/10.1021/acs.nanolett.2c01783 (Cited on page 70.)

[141] J. C. Loredo, N. A. Zakaria, N. Somaschi, C. Anton, L. De Santis, V. Giesz, T. Grange, M. A. Broome, O. Gazzano, G. Coppola, I. Sagnes, A. Lemaitre, A. Auffeves, P. Senellart, M. P.

Almeida, A. G. White, Scalable performance in solid-state single-photon sources, Optica 3 (4) (2016) 433. doi:10.1364/OPTICA.3.000433.
URL https://opg.optica.org/abstract.cfm?URI=optica-3-4-433 (Cited on pages 76 and 79.)

[142] Quandela | Leading Photonic Quantum Computing Solutions.
URL https://www.quandela.com/ (Cited on page 76.)

[143] I. Forbes, F. Ghafari, E. C. R. Deacon, S. P. Singh, E. Lavie, P. Yard, R. D. Shaw, A. Laing, N. Tischler, Heralded generation of entanglement with photons, version Number: 1 (2025). doi:10.48550/ARXIV.2502.00982.
URL https://arxiv.org/abs/2502.00982 (Cited on page 81.)

[144] D. E. Browne, T. Rudolph, Resource-Efficient Linear Optical Quantum Computation, Physical Review Letters 95 (1) (2005) 010501. doi:10.1103/PhysRevLett.95.010501.
URL https://link.aps.org/doi/10.1103/PhysRevLett.95.010501 (Cited on page 81.)

[145] C. Pentangelo, N. Di Giano, S. Piacentini, R. Arpe, F. Ceccarelli, A. Crespi, R. Osellame, High-fidelity and polarization-insensitive universal photonic processors fabricated by femtosecond laser writing, Nanophotonics 13 (12) (2024) 2259–2270. doi:10.1515/nanoph-2023-0636.
URL https://www.degruyter.com/document/doi/10.1515/nanoph-2023-0636/html (Cited on page 82.)

[146] Correspondence with Alpao Support. (Cited on pages 83 and 90.)

[147] Actuator Patterns for ALPAO DMs (2020). (Cited on pages 83 and 90.)

[148] A. D. Hill, D. Hervas, J. Nash, M. Graham, A. Burgers, U. Paudel, D. Steel, C. Schneider, M. Kamp, S. Höfling, J. Wang, J. Lin, W. Zhao, P. G. Kwiat, Optimizing single-mode collection from pointlike sources of single photons with adaptive optics, Optics Express 25 (16) (2017) 18629. doi:10.1364/OE.25.018629.
URL https://opg.optica.org/abstract.cfm?URI=oe-25-16-18629 (Cited on pages 85 and 86.)

[149] J. A. Nelder, R. Mead, A Simplex Method for Function Minimization, The Computer Journal 7 (4) (1965) 308–313. doi:10.1093/comjnl/7.4.308.
URL https://academic.oup.com/comjnl/article-lookup/doi/10.1093/comjnl/7.4.308 (Cited on page 90.)

[150] J. C. Maxwell, XXV. *On physical lines of force*: Part I.– *The Theory of Molecular Vortices applied to Magnetic Phenomena*, The London, Edinburgh, and Dublin Philosophical Magazine and Journal of Science 21 (139) (1861) 161–175. doi:10.1080/14786446108643033.
URL https://www.tandfonline.com/doi/full/10.1080/14786446108643033 (Cited on page 109.)

[151] J. C. Maxwell, VIII. A dynamical theory of the electromagnetic field, Philosophical Transactions of the Royal Society of London 155 (1865) 459–512. doi:10.1098/rstl.1865.0008.
URL https://royalsocietypublishing.org/doi/10.1098/rstl.1865.0008 (Cited on page 109.)

[152] C. F. Gauss, Theoria attractionis corporum sphaeroidicorum ellipticorum homogeneorum, methodo nova tractata, in: Werke, Springer Berlin Heidelberg, Berlin, Heidelberg, 1877, pp. 279–286. doi:10.1007/978-3-642-49319-5_8.
URL http://link.springer.com/10.1007/978-3-642-49319-5_8 (Cited on page 109.)

[153] T. C. Ralph, N. K. Langford, T. B. Bell, A. G. White, Linear optical controlled-NOT gate in the coincidence basis, Physical Review A 65 (6) (2002) 062324. doi:10.1103/PhysRevA.65.062324.
URL https://link.aps.org/doi/10.1103/PhysRevA.65.062324 (Cited on page 111.)

Appendix A

Maxwell's Equations

A.1 Maxwell's Equations

Light is the common term for what is scientifically known as electromagnetic radiation or electromagnetic waves. As the name suggests, light has an electric and a magnetic component, both working together by oscillating synchronously. To understand light, it is important to understand how the electric and magnetic fields of light relate to each other and behave. A great place to start is with Maxwell's equations [150] [151].

$$\nabla \cdot \boldsymbol{E} = \frac{\rho}{\varepsilon_0} \tag{A.1}$$

$$\nabla \cdot \boldsymbol{B} = 0 \tag{A.2}$$

$$\nabla \times \boldsymbol{E} = -\frac{\partial \boldsymbol{B}}{\partial t} \tag{A.3}$$

$$\nabla \times \frac{\boldsymbol{B}}{\mu_0} = \varepsilon_0 \frac{\partial \boldsymbol{E}}{\partial t} + \boldsymbol{J} \tag{A.4}$$

In these equations, $\boldsymbol{E}$ and $\boldsymbol{B}$ represent the electric and magnetic fields, respectively. The charge density ρ is the charge per unit volume, and the current density $\boldsymbol{J}$ describes the motion of charge density. The permittivity, ε_0, and permeability, μ_0, are both constants.

The first of these equations (A.1), is Gauss's Law [152]. It describes the flux of the electric field that emanates from a closed surface and shows that it is proportional to the net charge contained within it. This can be more apparent if you consider the integral form of Gauss's Law.

$$\oint_S \boldsymbol{E}(\boldsymbol{r}) \cdot \hat{\boldsymbol{n}}\, da = \frac{1}{\varepsilon_0} \int_V \rho(\boldsymbol{r})\, dv \tag{A.5}$$

The second equation (A.2), is Gauss's Law for magnetic fields. Similar to the previous Gauss's Law, it describes the magnetic flux extruding from a closed surface. However, notice that it is equal to zero. This means that the total magnetic flux extruding from a surface is perfectly balanced. For those who are familiar with magnetic field lines, this is represented by the same number of lines pointing inwards as there are pointing outwards.

The third equation (A.3, is Faraday's Law. Michael Faraday discovered that if one changes magnetic

fields, it creates an electric field. This was later known as induction. One of the most simple ways to observe induction is to move a magnet around in the vicinity of a loop of wire and measure the current passing through the wire. So if we look at the integral for of equation A.3

$$\oint_C \boldsymbol{E} \cdot dl = -\frac{\partial}{\partial t} \int_S \boldsymbol{B} \cdot \hat{\boldsymbol{n}} \, da, \tag{A.6}$$

it can be seen that the change in magnetic field through a surface (right side) is related to the voltage around the loop that contains that surface (left side).

Lastly, Ampere's Law. To talk about this law, it can be nice to first talk about the Biot-Savart Law, which goes as follows.

$$\boldsymbol{B}(\boldsymbol{r}) = \frac{\mu_0}{4\pi} \int_V \boldsymbol{J}(\boldsymbol{r}') \times \frac{(\boldsymbol{r} - \boldsymbol{r}')}{|\boldsymbol{r} - \boldsymbol{r}'|^3} \, dv' \tag{A.7}$$

Here, $\boldsymbol{r}$ is the position of the source, and $\boldsymbol{r}'$ is a point on a line. Now, taking the curl of the Biot-Savart Law, one gets

$$\nabla \times \boldsymbol{B}(\boldsymbol{r}) = \frac{\mu_0}{4\pi} \int_V \nabla_{\boldsymbol{r}} \times \left(\boldsymbol{J}(\boldsymbol{r}') \times \frac{(\boldsymbol{r} - \boldsymbol{r}')}{|\boldsymbol{r} - \boldsymbol{r}'|^3} \right) dv' \tag{A.8}$$

Eleminating some terms because $\boldsymbol{J}$ does not depend on $\boldsymbol{r}$, also assuming that $\boldsymbol{J}$ is completely confined within the volume V such that it is zero at the surface S, and performing the integrations leaves the equation in the form

$$\nabla \times \boldsymbol{B} = \mu_o \boldsymbol{J}. \tag{A.9}$$

This is similar to the final Maxwell equation, but it's not quite there. Ampere's Law only applies to quasi-steady-state situations. To fix this, Maxwell came up with his correction to Ampere's Law. Ampere's Law assumes that $\nabla \cdot \boldsymbol{J} = 0$, however, there exists situations where this is not the case. Maxwell concluded that instead,

$$\nabla \cdot \boldsymbol{J} = -\frac{\partial \rho}{\partial t}, \tag{A.10}$$

which is called the continuity equation for charge and current densities. This states that the charge must be piling up inside a volume to which the current flows.

So, now taking the curl of the magnetic field as was done to derive Ampere's Law, but now taking into account Maxwell's correction, one finds that

$$\nabla \times \boldsymbol{B} = \mu_0 \boldsymbol{J} + \frac{\mu_0}{4\pi} \frac{\partial}{\partial t} \int_V \rho(\boldsymbol{r}') \frac{\boldsymbol{r} - \boldsymbol{r}'}{|\boldsymbol{r} - \boldsymbol{r}'|^3} \, dv' \tag{A.11}$$

Realizing that the integral in this equation is nearly the definition of the net electric field produced by a charge density in a volume, a substitution can be made.

$$\nabla \times \frac{\boldsymbol{B}}{\mu_0} = \boldsymbol{J} + \varepsilon_0 \frac{\partial \boldsymbol{E}}{\partial t} \tag{A.12}$$

This is the fourth Maxwell equation (A.4).

While this is not the most mathematically rigorous explanation of Maxwell's Equations, it is important to understand their significance

Appendix B

Heralded Entanglement: Full Calculations

Work done is this appendix is taken directly from [5].

B.1 Notation and Optical Elements

We use $a_{i,\sigma,k}$ for the annihilation operator of a photon in path i, polarization σ (1 = H, 2 = V), and frequency mode k, with canonical commutation relations

$$[a_{i,\sigma,k}, a^\dagger_{i',\sigma',k'}] = \delta_{i,i'}\delta_{\sigma,\sigma'}\delta_{k,k'}, \tag{B.1}$$

$$[a_{i,\sigma,k}, a_{i',\sigma',k'}] = 0, \qquad [a^\dagger_{i,\sigma,k}, a^\dagger_{i',\sigma',k'}] = 0. \tag{B.2}$$

A PBS between paths i and j implements U_{ij}, and an HWP in path k implements V_k:

$$U_{ij}a_{i,1,k}U^\dagger_{ij} = a_{i,1,k}, \qquad U_{ij}a_{i,2,k}U^\dagger_{ij} = a_{j,2,k}, \tag{B.3}$$

$$V_k a_{k,1,l}V^\dagger_k = \frac{a_{k,1,l}+a_{k,2,l}}{\sqrt{2}} = d_{k,1,l}, \qquad V_k a_{k,1,l}V^\dagger_k = \frac{a_{k,1,l}-a_{k,2,l}}{\sqrt{2}} = d_{k,2,l}, \tag{B.4}$$

so that $d_{k,\sigma,l}$ are diagonal and anti-diagonal polarization modes. PBSs and HWPs do not change the frequency index.

B.2 Event-Ready Pair Generation

Following the event-ready entanglement scheme proposed by Zhang *et al.* [4] and based on the linear-optical CNOT principle of Ralph *et al.* [153], we prepare four single photons (paths 1–4) in diagonal polarization:

$$|\psi_A\rangle = d^\dagger_{1,1}d^\dagger_{2,1}d^\dagger_{3,1}d^\dagger_{4,1}|\text{vac}\rangle = |D\rangle_1|D\rangle_2|D\rangle_3|D\rangle_4. \tag{B.5}$$

Send (1,2) and (3,4) through PBSs:

$$\begin{aligned}|\psi_B\rangle &= U_{12}U_{34}|\psi_A\rangle, &\text{(B.6)}\\ &= \tfrac{1}{4}(a^\dagger_{2,2}a^\dagger_{2,1} + a^\dagger_{1,1}a^\dagger_{1,2} + a^\dagger_{1,1}a^\dagger_{2,1} + a^\dagger_{2,2}a^\dagger_{1,2})\\ &\quad\times(a^\dagger_{4,2}a^\dagger_{4,1} + a^\dagger_{3,1}a^\dagger_{3,2} + a^\dagger_{3,1}a^\dagger_{4,1} + a^\dagger_{4,2}a^\dagger_{3,2})|\text{vac}\rangle\\ &= \tfrac{1}{4}\big(|0\rangle_1|HV\rangle_2 + |HV\rangle_1|0\rangle_2 + |H\rangle_1|H\rangle_2 + |V\rangle_1|V\rangle_2\big)\\ &\quad\times\big(|0\rangle_3|HV\rangle_4 + |HV\rangle_3|0\rangle_4 + |H\rangle_3|H\rangle_4 + |V\rangle_3|V\rangle_4\big) = |\phi_{12}\rangle|\phi_{34}\rangle. &\text{(B.7)}\end{aligned}$$

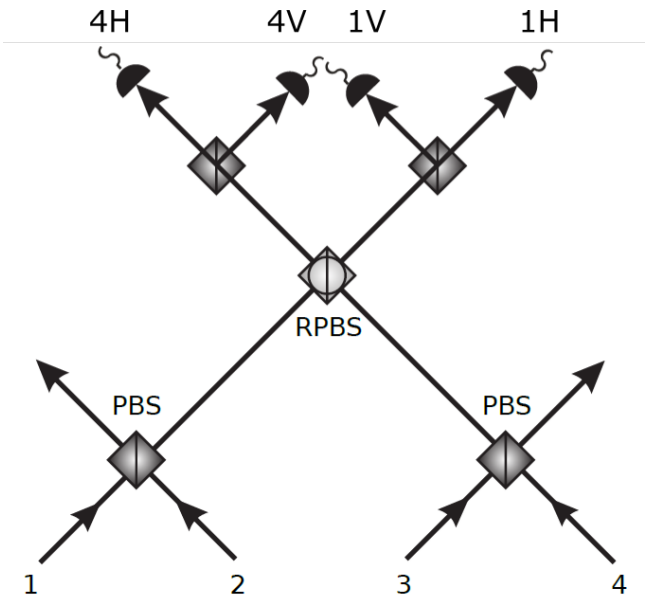


Figure B.1: Scheme for creating event ready heralded entanglement. Adapted from [4].

This state is then sent to a rotated PBS (RPBS: a PBS with HWPs on inputs and outputs). We condition on two polarization-resolving detector clicks in paths 1 and 4.

B.2.1 Sector I: At least one vacuum mode

Project the component with a vacuum in either (1,2) or (3,4):

$$\begin{aligned}\Pi_0|\psi_B\rangle = \tfrac{1}{4}\Big[&(|0\rangle_1|HV\rangle_2+|HV\rangle_1|0\rangle_2)(|0\rangle_3|HV\rangle_4+|HV\rangle_3|0\rangle_4)\\&+(|0\rangle_1|HV\rangle_2+|HV\rangle_1|0\rangle_2)(|H\rangle_3|H\rangle_4+|V\rangle_3|V\rangle_4)\\&+(|H\rangle_1|H\rangle_2+|V\rangle_1|V\rangle_2)(|0\rangle_3|HV\rangle_4+|HV\rangle_3|0\rangle_4)\Big].\end{aligned} \tag{B.8}$$

Conditioning on two photons in (1,4) and two in (2,3) gives

$$|\psi_C^{(0)}\rangle = \Pi_0|\psi_B\rangle|_{2,2} = \tfrac{1}{4}\big(|0\rangle_1|HV\rangle_2|0\rangle_3|HV\rangle_4+|HV\rangle_1|0\rangle_2|HV\rangle_3|0\rangle_4\big), \tag{B.9}$$

with probability $1/8$.

The RPBS acts as

$$\begin{aligned}U_{\mathrm{RPBS}}|0\rangle_1|HV\rangle_4 = \tfrac{1}{4}\Big[&\sqrt{2}\,(|0\rangle_1|2H\rangle_4-|2H\rangle_1|0\rangle_4-|2V\rangle_1|0\rangle_4+|0\rangle_1|2V\rangle_4)\\&+2|HV\rangle_1|0\rangle_4+2|0\rangle_1|HV\rangle_4\Big],\end{aligned} \tag{B.10}$$

$$\begin{aligned}U_{\mathrm{RPBS}}|HV\rangle_1|0\rangle_4 = \tfrac{1}{4}\Big[&-\sqrt{2}\,(|0\rangle_1|2H\rangle_4-|2H\rangle_1|0\rangle_4-|2V\rangle_1|0\rangle_4+|0\rangle_1|2V\rangle_4)\\&+2|HV\rangle_1|0\rangle_4+2|0\rangle_1|HV\rangle_4\Big].\end{aligned} \tag{B.11}$$

The only way to observe two coincident clicks is with orthogonal polarizations in the same output path (1 or 4). The conditional probability for two clicks given $|\psi_C^{(0)}\rangle$ is $1/2$, so this sector contributes $1/8\times 1/2 = 1/16$. The post-selected state on (2,3) is

$$|\psi_D\rangle = \frac{1}{\sqrt{2}}\big(|HV\rangle_2|0\rangle_3+|0\rangle_2|HV\rangle_3\big), \qquad |\psi_E\rangle = U_{2,3}|\psi_D\rangle = \frac{1}{\sqrt{2}}\big(|H\rangle_2|V\rangle_3+|V\rangle_2|H\rangle_3\big). \tag{B.12}$$

B.2.2 Sector II: One photon in each path

The component with one photon in each of (1,2,3,4) is

$$|\psi_3^{(1)}\rangle = (I-\Pi_0)|\psi_B\rangle = \tfrac{1}{4}(|H\rangle_1|H\rangle_2 + |V\rangle_1|V\rangle_2)(|H\rangle_3|H\rangle_4 + |V\rangle_3|V\rangle_4), \tag{B.13}$$

with probability $1/4$. Introduce the Bell states

$$|\phi^{\pm}\rangle = \tfrac{1}{\sqrt{2}}\big(|H\rangle|H\rangle \pm |V\rangle|V\rangle\big), \qquad |\psi^{\pm}\rangle = \tfrac{1}{\sqrt{2}}\big(|H\rangle|V\rangle \pm |V\rangle|H\rangle\big), \tag{B.14}$$

so that

$$|\psi_3^{(1)}\rangle = \tfrac{1}{4}\big(|\psi^+\rangle_{1,4}|\psi^+\rangle_{2,3} + |\psi^-\rangle_{1,4}|\psi^-\rangle_{2,3} + |\phi^+\rangle_{1,4}|\phi^+\rangle_{2,3} + |\phi^-\rangle_{1,4}|\phi^-\rangle_{2,3}\big). \tag{B.15}$$

The RPBS and detectors discriminate only the two symmetric Bell states, i.e. they succeed with probability $1/2$, giving a contribution $1/2 \times 1/4 = 1/8$.

Total success probability. Adding both sectors yields $1/16 + 1/8 = 3/16$ for preparing a maximally entangled state in modes (2,3).

B.3 Click Patterns Leading to Entanglement

The successful detection patterns and projected states (each occurring with probability $1/32$) are summarized below:

Click pattern (1H, 1V, 4H, 4V)	Projected state on (2,3) $\lvert\psi\rangle_{(1H,1V,4H,4V)}$	Probability P(1H, 1V, 4H, 4V)
(1,0,1,0)	$\frac{1}{8}(\lvert V\rangle_2\lvert V\rangle_3 + \lvert H\rangle_2\lvert H\rangle_3)$	$1/32$
(1,1,0,0)	$\frac{1}{8}(\lvert 0\rangle_2\lvert HV\rangle_3 + \lvert HV\rangle_2\lvert 0\rangle_3)$	$1/32$
(1,0,0,1)	$\frac{1}{8}(\lvert V\rangle_2\lvert H\rangle_3 + \lvert H\rangle_2\lvert V\rangle_3)$	$1/32$
(0,1,1,0)	$\frac{1}{8}(\lvert V\rangle_2\lvert H\rangle_3 + \lvert H\rangle_2\lvert V\rangle_3)$	$1/32$
(0,0,1,1)	$\frac{1}{8}(\lvert 0\rangle_2\lvert HV\rangle_3 + \lvert HV\rangle_2\lvert 0\rangle_3)$	$1/32$
(0,1,0,1)	$\frac{1}{8}(\lvert V\rangle_2\lvert V\rangle_3 + \lvert H\rangle_2\lvert H\rangle_3)$	$1/32$

Appendix C

Jupyter Notebook: Asymmetric Quantum Interference Modeling and Fitting

```
#!/usr/bin/env python

# coding: utf-8


# In[ ]:




from qutip import *


import numpy as np


import matplotlib.pyplot as plt


from mpl_toolkits.mplot3d import Axes3D


import plotly.graph_objects as go


```

```
import matplotlib.ticker as ticker


import matplotlib.colors


from matplotlib import cm


from scipy.optimize import curve_fit


import pandas as pd


from scipy.stats import chi2


from scipy.optimize import *


from matplotlib.colors import LinearSegmentedColormap


from mpl_toolkits.axes_grid1.inset_locator import inset_axes,
    mark_inset




# # Load Experimental Data


# In[ ]:
```

```
#Experimental values of tunable reflectivity values.


r_exp=[0.5,0.55,0.6,0.65,0.7,0.75,0.8,0.85,0.9,0.95,1]


#Importing experimental data


raw_data=pd.read_csv("full_run_.csv",sep='\t')


#Processing detection probabilities


C12 = np.zeros(len(raw_data))

C34 = np.zeros(len(raw_data))

C13 = np.zeros(len(raw_data))

C14 = np.zeros(len(raw_data))

C23 = np.zeros(len(raw_data))

C24 = np.zeros(len(raw_data))

norm = np.zeros(len(raw_data))

exp_P11 = np.zeros(len(raw_data))

exp_P20 = np.zeros(len(raw_data))

exp_P02 = np.zeros(len(raw_data))

HWP3 = np.zeros(len(raw_data))

e_norm = np.zeros(len(raw_data))

Sum = np.zeros(len(raw_data))

e_Sum = np.zeros(len(raw_data))

err_P11 = np.zeros(len(raw_data))
```

```
130
131 err_P20 = np.zeros(len(raw_data))
132
133 err_P02 = np.zeros(len(raw_data))
134
135
136
137 for i in range(len(raw_data)):
138
139     C12[i] = float(raw_data["Var2"][i])
140
141     C34[i] = float(raw_data["Var3"][i])
142
143     C13[i] = float(raw_data["Var4"][i])
144
145     C14[i] = float(raw_data["Var5"][i])
146
147     C23[i] = float(raw_data["Var6"][i])
148
149     C24[i] = float(raw_data["Var7"][i])
150
151     HWP3[i] = float(raw_data["Var1"][i])
152
153     norm[i] = (C12[i] + C34[i]) * 2 + C13[i] + C14[i] + C23[i] + C24[i
        ]
154
155     c11_counts = C13[i] + C14[i] + C23[i] + C24[i]
156
157     c20_counts = C12[i] * 2
158
159     c02_counts = C34[i] * 2
160
161     exp_P11[i] = (C13[i] + C14[i] + C23[i] + C24[i]) / norm[i]
162
163     exp_P20[i] = (C12[i] * 2) / norm[i]
164
165     exp_P02[i] = (C34[i] * 2) / norm[i]
166
167     e_norm[i] = np.sqrt(
168
169         np.sqrt(C12[i]) ** 2
170
171         + np.sqrt(C34[i]) ** 2
172
173         + np.sqrt(C13[i]) ** 2
174
175         + np.sqrt(C14[i]) ** 2
176
177         + np.sqrt(C23[i]) ** 2
```

```
178
179         + np.sqrt(C24[i]) ** 2
180
181     )
182
183     Sum[i] = C13[i] + C14[i] + C23[i] + C24[i]
184
185     e_Sum[i] = np.sqrt(
186
187         np.sqrt(C13[i]) ** 2
188
189         + np.sqrt(C14[i]) ** 2
190
191         + np.sqrt(C23[i]) ** 2
192
193         + np.sqrt(C24[i]) ** 2
194
195     )
196
197     err_P11[i] = exp_P11[i] * np.sqrt((e_Sum[i] / Sum[i]) ** 2 + (
        e_norm[i] / norm[i]) ** 2)
198
199     err_P20[i] = exp_P20[i] * np.sqrt(
200
201         (np.sqrt(C12[i]) / C12[i]) ** 2 + (e_norm[i] / norm[i]) ** 2
202
203     )
204
205     err_P02[i] = exp_P02[i] * np.sqrt(
206
207         (np.sqrt(C34[i]) / C34[i]) ** 2 + (e_norm[i] / norm[i]) ** 2
208
209     )
210
211
212
213
214
215 data=np.array([exp_P11,exp_P02,exp_P20])
216
217
218
219 error=np.array([err_P11,err_P02,err_P20])
220
221
222
223 data_flatten=data.flatten()
224
225
```

```
226
227 error_flatten=error.flatten()
228
229
230
231 print(exp_P11)
232
233 print(exp_P02)
234
235 print(exp_P20)
236
237
238
239
240
241 # ## Plot Experimental Data
242
243
244
245 # In[ ]:
246
247
248
249
250
251 fig, (ax0, ax1, ax2) = plt.subplots(nrows=1, ncols=3, sharex=True,
       sharey=True,
252
253                                     figsize=(12, 6))
254
255 ax0.set_ylabel("Probability", fontsize=20)
256
257 ax0.set_ylim([0,1])
258
259 ax0.grid(True)
260
261 ax0.set_xlabel(r'$\eta$', fontsize=12)
262
263 ax0.errorbar(r_exp,exp_P11,(err_P11),linestyle="None",marker='s',label
       ="$P(1,1)_{exp}$",c="r")
264
265 #ax0.plot(r_exp,(P11 + my_fit1.residual * e_P11), "-r", label="Fitting
        P(1,1)")
266
267 ax0.legend(loc="upper left")
268
269
270
```

```
271 ax1.errorbar(r_exp,exp_P20,(err_P20),linestyle="None",marker='s',label
    ="$P(2,0)_{exp}$",c="b")
272
273 #ax1.plot(r_exp,(P20 + my_fit2.residual * e_P20), "-b", label="Fitting
     P(2,0)")
274
275 ax1.legend(loc="best")
276
277 ax1.set_xlabel(r'$\eta$', fontsize=12)
278
279 ax1.set_ylim([0,1])
280
281 ax1.grid(True)
282
283
284
285 ax2.errorbar(r_exp,exp_P02,(err_P02),linestyle="None",marker='s',label
    ="$P(0,2)_{exp}$",c="g")
286
287 #ax2.plot(r_exp,(P02 + my_fit3.residual * e_P02), "-g", label="Fitting
     P(2,0)")
288
289 ax2.legend(loc="best")
290
291 ax2.set_xlabel(r'$\eta$', fontsize=12)
292
293 ax2.set_ylim([0,1])
294
295 ax2.grid(True)
296
297
298
299 print("P11 =", exp_P11)
300
301 print("P02 =", exp_P02)
302
303 print("P20 =", exp_P20)
304
305
306
307
308
309 # # Model
310
311
312
313 # * Beam-Splitter Operator: $\mathcal{U_{BS}}=\exp\left[-i\theta(a_1
    ^{\dagger}a_2+a_1a_2^{\dagger})\right]$
314
```

```
#

# * Loss mode: $\mathcal{U}_{loss}=\exp\left[-i\theta(a_{2}^{\dagger}
   a_{loss}+a_2a_{loss}^{\dagger})\right]$ (needs to trace out loss
   mode)

#

# * SPDC: $\mathcal{U}_{SPDC}=\exp\left[-i\eta(a_{1}^{\dagger}a_{2}^{\
   dagger}+a_1 a_{2})\right]$


# In[ ]:




# Beam splitter modes


def A(n):

    return destroy(n)


# Beam splitter operator


def BS(theta, a_sig, b_sig):

    H_bs = theta * (a_sig.dag()*b_sig + a_sig*b_sig.dag())

    return (-1j * H_bs).expm()


# Psi SPDC


def spdc(eta, a1, a2):

    H = eta * (a1.dag()*a2.dag() - a1*a2)

```

```
    return H.expm()


    return U


# def spdc(eta,A1,A2):
#     return eta*A1.dag()*A2.dag()+1/2*(eta*A1.dag()*A2.dag())**2




# ## Testing code using a 50/50 BS


# In[ ]:



n = 3  # number of photons
# mode operator
A1n = qutip.tensor(A(n), qeye(n), qeye(n))
A2n = qutip.tensor(qeye(n), A(n), qeye(n))
An_loss = qutip.tensor(qeye(n), qeye(n), A(n))



# ## Ideal Case


# In[ ]:
```

```
410
411 n = 3  # number of photons
412
413 # mode operator
414
415 A1n = qutip.tensor(A(n), qeye(n), qeye(n))
416
417 A2n = qutip.tensor(qeye(n), A(n), qeye(n))
418
419 An_loss = qutip.tensor(qeye(n), qeye(n), A(n))
420
421
422
423
424
425 # 50/50 BS
426
427 UBS1 = BS(np.pi / 4, A1n, A2n)
428
429
430
431
432
433
434
435
436
437 # ## Density Matrix evolution
438
439
440
441 # In[ ]:
442
443
444
445
446
447 # Loss
448
449 gamma = 0.7327
450
451 theta_gamma = np.arcsin(np.sqrt(gamma))
452
453
454
455 r = np.linspace(0.5, 1, 1001)
456
457 theta_r = np.arcsin(np.sqrt(r))
458
```

```
459
460
461 # Porjectors basis |11>,|20>,|02>
462
463
464
465 P11 = np.zeros(len(r))
466
467 P20 = np.zeros(len(r))
468
469 P02 = np.zeros(len(r))
470
471 P22 = np.zeros(len(r))
472
473
474
475 # 50/50 Beamsplitter (preparation)
476
477
478
479 UBS1 = BS(np.pi / 4, A1n, A2n)  # First HOM#
480
481
482
483 # Loss mode
484
485
486
487 L = BS(theta_gamma, A1n, An_loss)
488
489
490
491 psi_in = A1n.dag() * A2n.dag() * ket("000", n).unit()  # ideal single-
    photon source
492
493
494
495 # Density Matrix
496
497
498
499 rho_in = L.dag() * UBS1.dag() * psi_in * psi_in.dag() * UBS1 * L
500
501
502
503 rho_in = rho_in.unit()
504
505
506
```

```
507 for i in range(len(r)):
508
509     rho_out = (BS(theta_r[i], A1n, A2n).dag() * rho_in * BS(theta_r[i
        ], A1n, A2n))
510
511     P11[i] = expect(ket("11", n).proj(), rho_out.ptrace([0, 1]))
512
513     P20[i] = expect(ket("20", n).proj(), rho_out.ptrace([0, 1]))
514
515     P02[i] = expect(ket("02", n).proj(), rho_out.ptrace([0, 1]))
516
517     P22[i] = expect(ket("22", n).proj(), rho_out.ptrace([0, 1]))
518
519     ptotal = P11 + (P02 + P20) + P22
520
521     #normalize all values
522
523     P11[i] = P11[i]/ptotal[i]
524
525     P20[i] = P20[i]/ptotal[i]
526
527     P02[i] = P02[i]/ptotal[i]
528
529
530
531 P02Norm = (P02)
532
533 Min02 = min(P02Norm)
534
535 Min02Loc = np.argmin(P02Norm)
536
537 # Plot
538
539
540
541 fig, ax = plt.subplots()
542
543 ax.set_ylabel("Probability", fontsize=18)
544
545 ax.set_xlabel("Reflectivity", fontsize=18)
546
547 ax.grid(True)
548
549 # ax.set_xlabel(r'$\eta^{\prime\prime}$', fontsize=20)
550
551 ax.plot(r, P11, '#377eb8', linewidth=3, label="P(1,1)")
552
553 ax.plot(r, P02, '#ff7f00', linewidth=3, label="P(0,2)")
554
```

```
555 ax.plot(r, P20, '#4daf4a', linewidth=3, label="P(2,0)")
556
557 #ax.axvline(x = r[Min02Loc], color = 'r')#, label = f'R = {r[Min02Loc
    ]}')
558
559 ax.legend(loc="best",fontsize=20)
560
561 #ax.set_title("Input state = " r"$a~|20\rangle +\sqrt{1-a^2}|02\
    rangle$")
562
563 # ax.set_title('a=0.97',fontsize=16)
564
565 ax.set_ylim([0, 1])
566
567 ax.set_xlim([0.5, 1])
568
569 plt.xticks(fontsize="14")
570
571 plt.yticks(fontsize="14")
572
573 fig.set_size_inches(14, 8)
574
575 fig.set_dpi(120)
576
577 df = pd.read_csv("ascella_qpu_results1_with_errors.csv").sort_values("
    R2")
578
579 plt.errorbar(df["R2"], df["P11"], yerr=df["sigma_P11"], fmt="o", color
    ="#377eb8", label=r"$P_{11}$")
580
581 plt.errorbar(df["R2"], df["P20"], yerr=df["sigma_P20"], fmt="^", color
    ="#4daf4a", label=r"$P_{20}$")
582
583 plt.errorbar(df["R2"], df["P02"], yerr=df["sigma_P02"], fmt="s", color
    ="#ff7f00", label=r"$P_{02}$")
584
585
586
587 # Create inset axes (width=25% of main plot, height=25%)
588
589 axins = inset_axes(ax, width="25%", height="25%", loc='upper center')
590
591
592
593 # Plot the same data again inside the inset
594
595 axins.errorbar(df["R2"], df["P11"], yerr=df["sigma_P11"], fmt='o',
    color="#377eb8")
596
```

```
597 axins.errorbar(df["R2"], df["P20"], yerr=df["sigma_P20"], fmt='^',
       color="#4daf4a")
598
599 axins.errorbar(df["R2"], df["P02"], yerr=df["sigma_P02"], fmt='s',
       color="#ff7f00")
600
601
602
603 # Set zoom region (adjust these values to focus where error bars are
       relevant)
604
605 x1, x2 = 0.604, 0.607
606
607 y1, y2 = 0.734, 0.737
608
609 axins.set_xlim(x1, x2)
610
611 axins.set_ylim(y1, y2)
612
613 axins.grid(True, linestyle='--', alpha=1)
614
615
616
617 # Optionally link inset with rectangle on main plot
618
619 mark_inset(ax, axins, loc1=2, loc2=4, fc="none", ec="0.5")
620
621
622
623
624
625 plt.show()
626
627 #print(r[Min02Loc])
628
629
630
631
632
633 # ## SPDC source
634
635
636
637 # In[ ]:
638
639
640
641
642
```

```
643 # Loss
644
645 gamma = 0.7327
646
647 theta_gamma = np.arcsin(np.sqrt(gamma))
648
649
650
651 r = np.linspace(0.5, 1, 1001)
652
653 theta_r = np.arcsin(np.sqrt(r))
654
655
656
657 eta = 0.4
658
659
660
661 psi_in = spdc(eta, A1n, A2n) * ket("000", n).unit()  # single-photons
       from spdc
662
663
664
665 # Rates at which the 00, 11, and 22 terms are produced from the SPDC.
666
667 P00_SPDC = expect(ket("00",n).proj(),psi_in.ptrace([0,1]))
668
669 P11_SPDC = expect(ket("11",n).proj(),psi_in.ptrace([0,1]))
670
671 P22_SPDC = expect(ket("22",n).proj(),psi_in.ptrace([0,1]))
672
673 print(P00_SPDC/(P00_SPDC+P11_SPDC+P22_SPDC))
674
675 print(P11_SPDC/(P00_SPDC+P11_SPDC+P22_SPDC))
676
677 print(P22_SPDC/(P00_SPDC+P11_SPDC+P22_SPDC))
678
679
680
681 # Loss mode
682
683
684
685 L = BS(theta_gamma, A1n, An_loss)
686
687
688
689 # Density Matrix
690
```

```
691
692
693 rho_in = L.dag() * UBS1.dag() * psi_in * psi_in.dag() * UBS1 * L
694
695
696
697 rho_in = rho_in.unit()
698
699
700
701 for i in range(len(r)):
702
703     rho_out = (BS(theta_r[i], A1n, A2n).dag() * rho_in * BS(theta_r[i
        ], A1n, A2n))
704
705     P11[i] = expect(ket("11", n).proj(), rho_out.ptrace([0, 1]))
706
707     P20[i] = expect(ket("20", n).proj(), rho_out.ptrace([0, 1]))
708
709     P02[i] = expect(ket("02", n).proj(), rho_out.ptrace([0, 1]))
710
711     P22[i] = expect(ket("22", n).proj(), rho_out.ptrace([0, 1]))
712
713     ptotal = P11 + (P02 + P20) + P22
714
715     #normalize all values
716
717     P11[i] = P11[i]/ptotal[i]
718
719     P20[i] = P20[i]/ptotal[i]
720
721     P02[i] = P02[i]/ptotal[i]
722
723
724
725 # Plot
726
727
728
729 fig, ax = plt.subplots(2, 1)
730
731 ax[0].set_ylabel("Probability", fontsize=18)
732
733 ax[0].set_xlabel("Reflectivity", fontsize=18)
734
735 ax[0].grid(True)
736
737 # ax.set_xlabel(r'$\eta^{\prime\prime}$', fontsize=20)
738
```

```
ax[0].plot(r, P11, "#377eb8", linewidth=3, label="P(1,1)")

ax[0].plot(r, P02, "#ff7f00", linewidth=3, label="P(2,0)")

ax[0].plot(r, P20, "#4daf4a", linewidth=3, label="P(0,2)")

ax[0].legend(loc="best")

ax[0].set_title("SPDC",fontsize=24)

# ax.set_title('a=0.97',fontsize=16)

ax[0].set_ylim([0, 1])

ax[0].set_xlim([0.5, 1])

ax[1].set_ylabel("Probability", fontsize=18)

ax[1].set_xlabel("Reflectivity", fontsize=18)

ax[1].grid(True)

# ax.set_xlabel(r'$\eta^{\prime\prime}$', fontsize=20)

ax[1].plot(r, P11, "#377eb8", linewidth=3, label="P(1,1)")

ax[1].plot(r, P02, "#ff7f00", linewidth=3, label="P(0,2)")

ax[1].plot(r, P20, "#4daf4a", linewidth=3, label="P(2,0)")

ax[1].legend(loc="best")

ax[1].set_title("SPDC " r"$P(0,2)$ zoom", fontsize=24)

# ax.set_title('a=0.97',fontsize=16)

ax[1].set_ylim([0, 0.2])

ax[1].set_xlim([0.5, 1])

plt.xticks(fontsize="14")

plt.yticks(fontsize="14")

fig.set_size_inches(14, 16)

fig.set_dpi(120)

plt.show()
```

```
788
789
790
791
792
793 # ## Qutrit Noise-Channels
794
795
796
797 # #### Depol. Channel
798
799 #
800
801 # $\rho\rightarrow\mathcal{E}(\rho)=\sum_j K_j\rho K^{\dagger}_j$
      where $\sum_j K_j K^{\dagger}_j=\mathcal{1}$
802
803
804
805 # ## SPDC higher order and Q-trit decoherence
806
807
808
809 # In[ ]:
810
811
812
813
814
815 result = fit_p1_p2_eta(
816
817     r_exp,
818
819     exp_P11, exp_P02, exp_P20,
820
821     err_P11, err_P02, err_P20,
822
823     A1n=A1n, A2n=A2n, An_loss=An_loss, UBS1=UBS1, n=n,
824
825     gamma=0.933,
826
827     p0=(0.3, 0.3, 0.4)
828
829 )
830
831
832
833 p1_fit, p2_fit, eta_fit = result.x
834
835
```

```
836
837 print("Best-fit parameters:")
838
839 print(f"p1 = {p1_fit:.4f}")
840
841 print(f"p2 = {p2_fit:.4f}")
842
843 print(f"eta = {eta_fit:.4f}")
844
845 print(f" = {result.chi2:.3f}, reduced  = {result.chi2_red:.3f}")
846
847
848
849
850
851 # In[ ]:
852
853
854
855
856
857 # ---- Parameters ----
858
859
860
861 #Attenuation of mode 1
862
863 gamma = 0.7327
864
865 theta_gamma = np.arcsin(np.sqrt(gamma))
866
867
868
869 # Reflectivities for variable BS
870
871 r = np.linspace(0.5, 1, 1001)
872
873 theta_r = np.arcsin(np.sqrt(r))
874
875
876
877 # SPDC source
878
879 eta = 0.4 #eta_fit
880
881
882
883 #Noise parameters for mode 1 (p1) and mode 2 (p2).
884
```

```
#If fitting to experimental data, use the values calculated from the "Fitting" section (below),

p1 = 0.3 #p1_fit

p2 = 0.3 #p2_fit



# ---- End of Parameters ----

psi_in = spdc(eta, A1n, A2n) * ket("000", n).unit()



pp1 = np.sqrt(p1 / 8)

pp2 = np.sqrt(p2 / 8)



omega = np.exp(-1j * 2 * np.pi / 3)



ID = qeye(3)



Y = Qobj(np.asmatrix([[0, 1, 0], [1, 0, 0], [0, 0, 1]]))



Z = Qobj(np.asmatrix([[1, 0, 0], [0, omega, 0], [0, 0, omega**2]]))



##Krauss operators



Kmode1 = []



Kmode2 = []



```

```
#For mode 1.

# K0

Kmode1.append(tensor(np.sqrt(1 - p1) * ID, qeye(3), qeye(3)))

# K1

Kmode1.append(tensor(pp1 * Y, qeye(3), qeye(3)))

# K2

Kmode1.append(tensor(pp1 * Z, qeye(3), qeye(3)))

# K3

Kmode1.append(tensor(pp1 * Y**2, qeye(3), qeye(3)))

# K4

Kmode1.append(tensor(pp1 * Y * Z, qeye(3), qeye(3)))

# K5

Kmode1.append(tensor(pp1 * Y**2 * Z, qeye(3), qeye(3)))

# K6

Kmode1.append(tensor(pp1 * Y * Z**2, qeye(3), qeye(3)))

# K7

Kmode1.append(tensor(pp1 * Y**2 * Z**2, qeye(3), qeye(3)))

# K5

Kmode1.append(tensor(pp1 * Z**2, qeye(3), qeye(3)))



#For mode 2.

# K0

Kmode2.append(tensor(qeye(3), np.sqrt(1 - p2) * ID, qeye(3)))

# K1

Kmode2.append(tensor(qeye(3), pp2 * Y, qeye(3)))
```

```
982
983 # K2
984
985 Kmode2.append(tensor(qeye(3), pp2 * Z, qeye(3)))
986
987 # K3
988
989 Kmode2.append(tensor(qeye(3), pp2 * Y**2, qeye(3)))
990
991 # K4
992
993 Kmode2.append(tensor(qeye(3), pp2 * Y * Z, qeye(3)))
994
995 # K5
996
997 Kmode2.append(tensor(qeye(3), pp2 * Y**2 * Z, qeye(3)))
998
999 # K6
1000
1001 Kmode2.append(tensor(qeye(3), pp2 * Y * Z**2, qeye(3)))
1002
1003 # K7
1004
1005 Kmode2.append(tensor(qeye(3), pp2 * Y**2 * Z**2, qeye(3)))
1006
1007 # K5
1008
1009 Kmode2.append(tensor(qeye(3), pp2 * Z**2, qeye(3)))
1010
1011
1012
1013 psi_in = spdc(eta, A1n, A2n) * ket("000", n).unit()  # single-photons
     from spdc
1014
1015
1016
1017 #Attenuation unitary.
1018
1019 L = BS(theta_gamma, A1n, An_loss)
1020
1021
1022
1023 #Choose one of the following "rho_in" to uncomment:
1024
1025 #rho_in = (psi_in * psi_in.dag()).unit() #SPDC source, nothing else
     applied to state.
1026
1027 #rho_in = (UBS1.dag() * psi_in * psi_in.dag() * UBS1).unit() #SPDC
     source and first 50/50 beamsplitter.
```

```
1028
1029 rho_in = (L.dag() * UBS1.dag() * psi_in * psi_in.dag() * UBS1 * L).
        unit() #SPDC source, 50/50 beamsplitter, and attenuation.
1030
1031
1032
1033 #Apply Kraus opperators to model system decoherence.
1034
1035 rho_in_d = 0
1036
1037
1038
1039 for i in range(len(Kmode1)):
1040
1041     rho_in_d += Kmode1[i] * rho_in * Kmode1[i].dag()
1042
1043
1044
1045 for i in range(len(Kmode2)):
1046
1047     rho_in_d += Kmode2[i] * rho_in * Kmode2[i].dag()
1048
1049
1050
1051 rho_in_d.unit()
1052
1053
1054
1055 #Initialize empty matrices.
1056
1057 P11 = np.zeros(len(r))
1058
1059 P20 = np.zeros(len(r))
1060
1061 P02 = np.zeros(len(r))
1062
1063 P22 = np.zeros(len(r))
1064
1065 ptotal = np.zeros(len(r))
1066
1067
1068
1069 #Calculate probability distributions as reflectivity varies.
1070
1071 for i in range(len(r)):
1072
1073     #Choose one of the following "rho_out" to uncomment.
1074
1075     #rho_out = (rho_in_d).unit() #Without variable beamsplitter.
```

```
    rho_out = (BS(theta_r[i], A1n, A2n).dag() * rho_in * BS(theta_r[i
       ], A1n, A2n)) #With variable beamsplitter.

    P11[i] = expect(ket("11", n).proj(), rho_out.ptrace([0, 1])).real

    P20[i] = expect(ket("20", n).proj(), rho_out.ptrace([0, 1])).real

    P02[i] = expect(ket("02", n).proj(), rho_out.ptrace([0, 1])).real

    P22[i] = expect(ket("22", n).proj(), rho_out.ptrace([0, 1])).real

    ptotal[i] = P11[i] + P02[i] + P20[i] + P22[i]

    #normalize all values

    P11[i] = P11[i]/ptotal[i]

    P20[i] = P20[i]/ptotal[i]

    P02[i] = P02[i]/ptotal[i]



P02Norm = (P02)

Min02 = min(P02Norm)

Min02Loc = np.argmin(P02Norm)



# Plot



fig, ax = plt.subplots()

ax.set_ylabel("Probability", fontsize=18)

ax.set_xlabel("Reflectivity", fontsize=18)

ax.grid(True)

# ax.set_xlabel(r'$\eta^{\prime\prime}$', fontsize=20)

ax.plot(r, P11, "#377eb8", linewidth=3, linestyle='-', label="$P(1,1)_
   {fit}$")

```

```
ax.plot(r, P02, "#ff7f00", linewidth=3, linestyle='-', label="$P(0,2)_{fit}$")

ax.plot(r, P20, "#4daf4a", linewidth=3, linestyle='-', label="$P(2,0)_{fit}$")

ax.axvline(x = r[Min02Loc], color = 'r', label = f'R = {r[Min02Loc]}')

ax.errorbar(r_exp,exp_P11,(err_P11), linestyle="None",marker='.', markersize="20",c="#377eb8", label="$P(1,1)_{exp}$")#Use if wanting to plot with experimental data

ax.errorbar(r_exp,exp_P02,(err_P02), linestyle="None",marker='s', markersize="10",c="#ff7f00", label="$P(0,2)_{exp}$")#Use if wanting to plot with experimental data

ax.errorbar(r_exp,exp_P20,(err_P20), linestyle="None",marker='^', markersize="10",c="#4daf4a", label="$P(2,0)_{exp}$")#Use if wanting to plot with experimental data

ax.legend(loc="best",fontsize=20)

#ax.set_title("SPDC+Decoherence", fontsize=24)

#ax.set_title('a=0.97',fontsize=16)

ax.set_ylim([0, 1])

ax.set_xlim([0.5, 1])

plt.xticks(fontsize="14")

plt.yticks(fontsize="14")

fig.set_size_inches(14, 8)

fig.set_dpi(200)

plt.show()




# ## Varying Attenuation and Reflectivity; SPDC Higher-Order and Decoherence


```

```
# In[ ]:




#Reflectivities

r = np.linspace(0.5, 1, 11)

theta_r = np.arcsin(np.sqrt(r))



#Attenuations

atten = np.linspace(0,1,11)

theta_atten = np.arcsin(np.sqrt(atten))



R, ATTEN = np.meshgrid(r, atten)



#State from SPDC source



#eta determines how much the higher order terms are produced.

eta = 0.4 #fit_vals[2]



psi_in = spdc(eta, A1n, A2n) * ket("000", n).unit()  # single-photons
    from spdc



#Initialize empty matrices.

P11 = np.zeros((len(atten),len(r)))

P20 = np.zeros((len(atten),len(r)))

P02 = np.zeros((len(atten),len(r)))

```

```
P22 = np.zeros((len(atten),len(r)))

ptotal = np.zeros((len(atten),len(r)))


for j in range(len(atten)):



    #Attenuation unitary.

    L = BS(theta_atten[j], A1n, An_loss)



    #Choose one of the following "rho_in" to uncomment:

    #rho_in = (psi_in * psi_in.dag()).unit() #SPDC source, nothing
       else applied to state.

    #rho_in = (UBS1.dag() * psi_in * psi_in.dag() * UBS1).unit() #SPDC
        source and first 50/50 beamsplitter.

    rho_in = (L.dag() * UBS1.dag() * psi_in * psi_in.dag() * UBS1 * L)
       .unit() #SPDC source, 50/50 beamsplitter, and attenuation.



    #Apply Kraus opperators to model system decoherence.

    rho_in_d = 0



    for i in range(len(Kmode1)):

        rho_in_d += Kmode1[i] * rho_in * Kmode1[i].dag()



    for i in range(len(Kmode2)):

        rho_in_d += Kmode2[i] * rho_in * Kmode2[i].dag()



    rho_in_d.unit()

```

```
    #Calculate probability distributions as reflectivity varies.

    for i in range(len(r)):

        #Choose one of the following "rho_out" to uncomment.

        #rho_out = (rho_in_d).unit() #Without variable beamsplitter.

        rho_out = (BS(theta_r[i], A1n, A2n).dag() * rho_in * BS(
           theta_r[i], A1n, A2n)) #With variable beamsplitter.

        P11[j][i] = expect(ket("11", n).proj(), rho_out.ptrace([0, 1])
           ).real

        P02[j][i] = expect(ket("02", n).proj(), rho_out.ptrace([0, 1])
           ).real#Here the 02 and 20 states have swapped labels. Doesn
           't affect math.

        P20[j][i] = expect(ket("20", n).proj(), rho_out.ptrace([0, 1])
           ).real#Here the 02 and 20 states have swapped labels. Doesn
           't affect math.

        P22[j][i] = expect(ket("22", n).proj(), rho_out.ptrace([0, 1])
           ).real

        #ptotal is used to normalize the probabilities.

        ptotal[j][i] = P11[j][i] + P02[j][i] + P20[j][i] + P22[j][i]

        #normalize all values

        P11[j][i] = P11[j][i]/ptotal[j][i]

        P20[j][i] = P20[j][i]/ptotal[j][i]

        P02[j][i] = P02[j][i]/ptotal[j][i]


# Plot


fig = plt.figure()

ax = fig.add_subplot(111, projection='3d')

```

```
ax.grid(True)

#Plot three surfaces.

surf1 = ax.plot_surface(R, ATTEN, P11, cmap='cividis', alpha=0.85, label="P(1,1)")

surf2 = ax.plot_surface(R, ATTEN, P02, cmap='magma', alpha=0.65, label="P(0,2)")

surf3 = ax.plot_surface(R, ATTEN, P20, cmap='cool', alpha=0.5, label="P(2,0)")

#Set title and axes labels.

#ax.set_title("SPDC+Decoherence", fontsize=24)

ax.set_xlabel("Reflectivity", fontsize=16, labelpad=16)

ax.set_ylabel("Attenuation", fontsize=16, labelpad=16)

ax.set_zlabel("Probability", fontsize=16, labelpad=8)

ax.set_title("Probability Surfaces")

ax.set_ylim([0, 1])

ax.set_xlim([0.5, 1])

ax.set_zlim([0,1])

plt.xticks(fontsize="14")

plt.yticks(fontsize="14")

# Optional colorbars

# --- Correctly define manual colorbar axes ---

# Each argument is a list of four floats, not separate float args

cax1 = fig.add_axes([0.77, 0.60, 0.02, 0.25])  # top colorbar

cax2 = fig.add_axes([0.77, 0.33, 0.02, 0.25])  # middle

cax3 = fig.add_axes([0.77, 0.06, 0.02, 0.25])  # bottom
```

```
# --- Add colorbars ---

fig.colorbar(surf1, cax=cax1).set_label(r"$P_{11}$", fontsize="16")

fig.colorbar(surf2, cax=cax2).set_label(r"$P_{02}$", fontsize="16")

fig.colorbar(surf3, cax=cax3).set_label(r"$P_{20}$", fontsize="16")

#Figure size.

fig.set_size_inches(14, 8)

fig.set_dpi(200)

plt.margins(0.1)

plt.show()




# In[ ]:




fig, axes = plt.subplots(1, 3, figsize=(14, 4), sharex=True, sharey=
    True)



# --- Common color limits and colormap ---

vmin, vmax = 0, 1

cmap = "viridis"



# --- P11 subplot ---

cont1 = axes[0].contourf(R, ATTEN, P11, levels=40, cmap=cmap, vmin=
    vmin, vmax=vmax)

axes[0].set_title(r"$P_{11}$", fontsize=16)


```

```
1392
1393 # --- P02 subplot ---
1394
1395 cont2 = axes[1].contourf(R, ATTEN, P02, levels=40, cmap=cmap, vmin=
        vmin, vmax=vmax)
1396
1397 axes[1].set_title(r"$P_{02}$", fontsize=16)
1398
1399
1400
1401 # --- P20 subplot ---
1402
1403 cont3 = axes[2].contourf(R, ATTEN, P20, levels=40, cmap=cmap, vmin=
        vmin, vmax=vmax)
1404
1405 axes[2].set_title(r"$P_{20}$", fontsize=16)
1406
1407
1408
1409 # --- Shared colorbar ---
1410
1411 cbar = fig.colorbar(cont1, ax=axes, orientation='vertical', shrink
        =0.8, fraction=0.05, pad=0.02)
1412
1413 cbar.set_label("Probability", fontsize=16)
1414
1415 cbar.ax.tick_params(labelsize=10)
1416
1417
1418
1419 # --- Axis labels ---
1420
1421 for ax in axes:
1422
1423     ax.set_xlabel("Reflectivity", fontsize=16)
1424
1425 axes[0].set_ylabel("Attenuation", fontsize=16)
1426
1427
1428
1429 # --- Global title ---
1430
1431 fig.suptitle("Probability Contours as Functions of Reflectivity and
        Attenuation", fontsize=16, y=1.02)
1432
1433
1434
1435 #plt.tight_layout()
1436
```

```
fig.set_dpi(200)

plt.show()




# ## SPDC Higher-Order, Decoherence, and HOM Indistinguishabilities


# In[ ]:




r_fit = np.asarray(r_exp, dtype=float)


result = fit_eta_p1_p2(

    r_fit,

    exp_P11, exp_P02, exp_P20,

    err_P11, err_P02, err_P20,

    A1n, A2n, An_loss, UBS1, n,

    gamma=0.933,

    xi1=0.997,

    xi2=0.947,

    nphi=8

)


eta_fit_dis, p1_fit_dis, p2_fit_dis, gamma_use, xi1_use, xi2_use =
   result["params"]


```

```
print("Fit results:")

for name, val in zip(result["param_names"], result["params"]):

    print(f"{name} = {val:.6f}")

print(f"chi2 = {result['chi2']:.3f}, reduced chi2 = {result['chi2_red
    ']:.3f}")




# In[ ]:




# ---- Parameters ----


#Attenuation of mode 1

gamma = 0.933 #0.7074

theta_gamma = np.arcsin(np.sqrt(gamma))


# Reflectivities for variable BS

r = np.linspace(0.5, 1, 1001)

theta_r = np.arcsin(np.sqrt(r))


# SPDC source

eta = 0.4 #eta_fit_dis


# Indistinguishability (HOM visibility) parameters

xi1 = 0.997   # preparation (UBS1)

```

```
xi2 = 0.947   # variable beamsplitter

nphi = 8      # number of phase samples for distinguishable averaging



#Noise parameters for mode 1 (p1) and mode 2 (p2).

#If fitting to experimental data, use the values calculated from the "
   Fitting" section (below),

p1 = 0.3 #p1_fit_dis

p2 = 0.3 #p2_fit_dis



# ---- End of Parameters ----

psi_in = spdc(eta, A1n, A2n) * ket("000", n).unit()



pp1 = np.sqrt(p1 / 8)

pp2 = np.sqrt(p2 / 8)



omega = np.exp(-1j * 2 * np.pi / 3)



ID = qeye(3)



Y = Qobj(np.asmatrix([[0, 1, 0], [1, 0, 0], [0, 0, 1]]))



Z = Qobj(np.asmatrix([[1, 0, 0], [0, omega, 0], [0, 0, omega**2]]))



##Krauss operators



```

```
Kmode1 = []


Kmode2 = []


#For mode 1.
# K0
Kmode1.append(tensor(np.sqrt(1 - p1) * ID, qeye(3), qeye(3)))
# K1
Kmode1.append(tensor(pp1 * Y, qeye(3), qeye(3)))
# K2
Kmode1.append(tensor(pp1 * Z, qeye(3), qeye(3)))
# K3
Kmode1.append(tensor(pp1 * Y**2, qeye(3), qeye(3)))
# K4
Kmode1.append(tensor(pp1 * Y * Z, qeye(3), qeye(3)))
# K5
Kmode1.append(tensor(pp1 * Y**2 * Z, qeye(3), qeye(3)))
# K6
Kmode1.append(tensor(pp1 * Y * Z**2, qeye(3), qeye(3)))
# K7
Kmode1.append(tensor(pp1 * Y**2 * Z**2, qeye(3), qeye(3)))
# K5
Kmode1.append(tensor(pp1 * Z**2, qeye(3), qeye(3)))


#For mode 2.
```

```
1630
1631 # K0
1632
1633 Kmode2.append(tensor(qeye(3), np.sqrt(1 - p2) * ID, qeye(3)))
1634
1635 # K1
1636
1637 Kmode2.append(tensor(qeye(3), pp2 * Y, qeye(3)))
1638
1639 # K2
1640
1641 Kmode2.append(tensor(qeye(3), pp2 * Z, qeye(3)))
1642
1643 # K3
1644
1645 Kmode2.append(tensor(qeye(3), pp2 * Y**2, qeye(3)))
1646
1647 # K4
1648
1649 Kmode2.append(tensor(qeye(3), pp2 * Y * Z, qeye(3)))
1650
1651 # K5
1652
1653 Kmode2.append(tensor(qeye(3), pp2 * Y**2 * Z, qeye(3)))
1654
1655 # K6
1656
1657 Kmode2.append(tensor(qeye(3), pp2 * Y * Z**2, qeye(3)))
1658
1659 # K7
1660
1661 Kmode2.append(tensor(qeye(3), pp2 * Y**2 * Z**2, qeye(3)))
1662
1663 # K5
1664
1665 Kmode2.append(tensor(qeye(3), pp2 * Z**2, qeye(3)))
1666
1667
1668
1669 # Attenuation unitary
1670
1671 L = BS(theta_gamma, A1n, An_loss)
1672
1673
1674
1675 # --- Phase operator for distinguishability modeling ---
1676
1677 def phase_op(phi):
1678
```

```
    """Phase shift on mode 0: |k> -> e^{i k phi} |k>"""

    return Qobj(np.diag([1, np.exp(1j*phi), np.exp(2j*phi)]))


# ---- First Beamsplitter (UBS1) ----

# Indistinguishable case:

rho_pre_ind = UBS1.dag() * psi_in * psi_in.dag() * UBS1


# Distinguishable case (phase-averaged on one arm before UBS1)

rho_pre_dist = 0

for phi in np.linspace(0, 2*np.pi, nphi, endpoint=False):

    Uphi = tensor(phase_op(phi), qeye(3), qeye(3))

    rho_pre_dist += UBS1.dag() * (Uphi * psi_in) * (psi_in.dag() *
       Uphi.dag()) * UBS1

rho_pre_dist /= nphi


# Mix according to xi1

rho_pre = (xi1 * rho_pre_ind + (1 - xi1) * rho_pre_dist).unit()


# ---- Attenuation ----

rho_in = (L.dag() * rho_pre * L).unit()


# ---- Apply Kraus operators for decoherence ----

rho_in_d = 0

for K1 in Kmode1:

    for K2 in Kmode2:

```

```
        rho_in_d += K2 * K1 * rho_in * K1.dag() * K2.dag()

rho_in_d = rho_in_d.unit()



# ---- Initialize arrays ----

P11 = np.zeros(len(r))

P20 = np.zeros(len(r))

P02 = np.zeros(len(r))

P22 = np.zeros(len(r))

ptotal = np.zeros(len(r))



# ---- Variable beamsplitter (UBS2) ----

for i, theta in enumerate(theta_r):

    U = BS(theta, A1n, A2n)



    # --- Indistinguishable output ---

    rho_out_ind = (U.dag() * rho_in_d * U)

    rho12_ind = rho_out_ind.ptrace([0, 1])

    p11_ind = expect(ket("11", n).proj(), rho12_ind).real

    p20_ind = expect(ket("20", n).proj(), rho12_ind).real

    p02_ind = expect(ket("02", n).proj(), rho12_ind).real

    p22_ind = expect(ket("22", n).proj(), rho12_ind).real



    # --- Distinguishable output (phase-averaged) ---

    p11_d, p20_d, p02_d, p22_d = 0, 0, 0, 0

    for phi in np.linspace(0, 2*np.pi, nphi, endpoint=False):
```

```
        Uphi = tensor(phase_op(phi), qeye(3), qeye(3))

        rho_phi = Uphi * rho_in_d * Uphi.dag()

        rho_out_d = (U.dag() * rho_phi * U)

        rho12_d = rho_out_d.ptrace([0, 1])

        p11_d += expect(ket("11", n).proj(), rho12_d).real

        p20_d += expect(ket("20", n).proj(), rho12_d).real

        p02_d += expect(ket("02", n).proj(), rho12_d).real

        p22_d += expect(ket("22", n).proj(), rho12_d).real

    p11_d /= nphi; p20_d /= nphi; p02_d /= nphi; p22_d /= nphi


    # --- Mix based on xi2 ---

    p11 = xi2 * p11_ind + (1 - xi2) * p11_d

    p20 = xi2 * p20_ind + (1 - xi2) * p20_d

    p02 = xi2 * p02_ind + (1 - xi2) * p02_d

    p22 = xi2 * p22_ind + (1 - xi2) * p22_d


    # --- Normalize ---

    ptotal[i] = p11 + p20 + p02 + p22

    P11[i] = p11 / ptotal[i]

    P20[i] = p20 / ptotal[i]

    P02[i] = p02 / ptotal[i]


P02Norm = (P02)

Min02 = min(P02Norm)

```

```
Min02Loc = np.argmin(P02Norm)



# --- Done ---

print(f"HOM indistinguishabilities: xi1={xi1:.3f}, xi2={xi2:.3f}")



# Graph

fig, ax = plt.subplots()

ax.set_ylabel("Probability", fontsize=18)

ax.set_xlabel("Reflectivity", fontsize=18)

ax.grid(True)

# ax.set_xlabel(r'$\eta^{\prime\prime}$', fontsize=20)

ax.plot(r, P11, "#377eb8", linewidth=3, linestyle='-', label="$P(1,1)_{fit}$")

ax.plot(r, P02, "#ff7f00", linewidth=3, linestyle='-', label="$P(0,2)_{fit}$")

ax.plot(r, P20, "#4daf4a", linewidth=3, linestyle='-', label="$P(2,0)_{fit}$")

ax.axvline(x = r[Min02Loc], color = 'r', label = f'R = {r[Min02Loc]}')

ax.errorbar(r_exp,exp_P11,(err_P11), linestyle="None",marker='.', markersize="20",c="#377eb8", label="$P(1,1)_{exp}$")#Use if wanting to plot with experimental data

ax.errorbar(r_exp,exp_P02,(err_P02), linestyle="None",marker='s', markersize="10",c="#ff7f00", label="$P(0,2)_{exp}$")#Use if wanting to plot with experimental data

ax.errorbar(r_exp,exp_P20,(err_P20), linestyle="None",marker='^', markersize="10",c="#4daf4a", label="$P(2,0)_{exp}$")#Use if wanting to plot with experimental data

ax.legend(loc="best",fontsize=20)

#ax.set_title("SPDC+Decoherence", fontsize=24)

```

```
#ax.set_title('a=0.97',fontsize=16)

ax.set_ylim([0, 1])

ax.set_xlim([0.5, 1])

plt.xticks(fontsize="14")

plt.yticks(fontsize="14")

fig.set_size_inches(14, 8)

fig.set_dpi(200)

plt.show()




# In[ ]:




# --- User knobs ---

xi1 = 0.997   # HOM indistinguishability at the first (UBS1, 50/50)
   beamsplitter

xi2 = 0.947   # HOM indistinguishability at the variable beamsplitter

nphi = 8      # phase samples for distinguishable averaging (812 is
   reasonable)



# Reflectivities (variable BS)

r = np.linspace(0.5, 1, 11)

theta_r = np.arcsin(np.sqrt(r))   # R = sin^2(theta)



# Attenuations (loss BS)  values are POWER reflectivities

atten = np.linspace(0, 1, 11)
```

```
theta_atten = np.arcsin(np.sqrt(atten))



# Parameter grid

R, ATTEN = np.meshgrid(r, atten)



# SPDC source

eta = 0.4

psi_in = spdc(eta, A1n, A2n) * ket("000", n).unit()




# ------------------------------------------------------------

# Helper: phase operator on a single qutrit mode

# ------------------------------------------------------------

def phase_op(phi):

    vals = np.array([

        1.0,

        np.exp(1j*phi),

        np.exp(2j*phi)

    ], dtype=np.complex128)

    return Qobj(np.diag(vals), dims=[[3], [3]])




# Precompute phase operators (good speed boost)

phis = np.linspace(0.0, 2*np.pi, int(nphi), endpoint=False)

```

```
Uphi_list = [tensor(phase_op(phi), qeye(3), qeye(3)) for phi in phis]
```

```
# ------------------------------------------------------------
```

```
# Probability arrays
```

```
# ------------------------------------------------------------
```

```
P11 = np.zeros((len(atten), len(r)))
```

```
P20 = np.zeros((len(atten), len(r)))
```

```
P02 = np.zeros((len(atten), len(r)))
```

```
P22 = np.zeros((len(atten), len(r)))
```

```
# ------------------------------------------------------------
```

```
# Main loop: attenuation then reflectivity
```

```
# ------------------------------------------------------------
```

```
for j in range(len(atten)):
```

```
    # Loss BS (power reflectivity -> angle)
```

```
    L = BS(theta_atten[j], A1n, An_loss)
```

```
    # ------------------------------------------------------------
```

```
    # First BS (UBS1): Indistinguishable branch
```

```
    # ------------------------------------------------------------
```

```
    rho_pre_ind = UBS1.dag() * psi_in * psi_in.dag() * UBS1
```

```
    # ------------------------------------------------------------

    # First BS (UBS1): Distinguishable surrogate (phase averaged)

    # ------------------------------------------------------------

    rho_pre_dist = 0 * rho_pre_ind     # <-- correct dims here

    for Uphi in Uphi_list:

        rho_pre_dist += UBS1.dag() * (Uphi * psi_in) * (psi_in.dag() *
            Uphi.dag()) * UBS1

    rho_pre_dist /= nphi



    # ------------------------------------------------------------

    # Mix by xi1 & apply attenuation

    # ------------------------------------------------------------

    rho_pre = (xi1 * rho_pre_ind + (1 - xi1) * rho_pre_dist).unit()

    rho_in  = (L.dag() * rho_pre * L).unit()



    # ------------------------------------------------------------

    # Decoherence via Kraus double sum

    # ------------------------------------------------------------

    rho_in_d = 0 * rho_in          # <-- correct dims

    for K1 in Kmode1:

        for K2 in Kmode2:

            rho_in_d += K2 * K1 * rho_in * K1.dag() * K2.dag()

    rho_in_d = rho_in_d.unit()



    # Measurement operators
```

```
    P_11 = ket("11", n).proj()

    P_20 = ket("20", n).proj()

    P_02 = ket("02", n).proj()

    P_22 = ket("22", n).proj()


    # ------------------------------------------------------------

    # Loop over variable beamsplitter reflectivity

    # ------------------------------------------------------------

    for i in range(len(r)):


        U = BS(theta_r[i], A1n, A2n)


        # ------------------------------------------------------

        # Indistinguishable output

        # ------------------------------------------------------

        rho_out_i = U.dag() * rho_in_d * U

        rho12_i   = rho_out_i.ptrace([0, 1])


        p11_i = expect(P_11, rho12_i).real

        p20_i = expect(P_20, rho12_i).real

        p02_i = expect(P_02, rho12_i).real

        p22_i = expect(P_22, rho12_i).real


        ptot_i = p11_i + p20_i + p02_i + p22_i
```

```
        P11_i, P20_i, P02_i = p11_i/ptot_i, p20_i/ptot_i, p02_i/ptot_i


        # ------------------------------------------------------

        # Distinguishable surrogate (phase average)

        # ------------------------------------------------------

        p11_acc = p20_acc = p02_acc = p22_acc = 0.0


        for Uphi in Uphi_list:

            rho_phi = Uphi * rho_in_d * Uphi.dag()

            rho_out_d = U.dag() * rho_phi * U

            rho12_d   = rho_out_d.ptrace([0, 1])


            p11_acc += expect(P_11, rho12_d).real

            p20_acc += expect(P_20, rho12_d).real

            p02_acc += expect(P_02, rho12_d).real

            p22_acc += expect(P_22, rho12_d).real


        p11_d = p11_acc / nphi

        p20_d = p20_acc / nphi

        p02_d = p02_acc / nphi

        p22_d = p22_acc / nphi


        ptot_d = p11_d + p20_d + p02_d + p22_d

        P11_d, P20_d, P02_d = p11_d/ptot_d, p20_d/ptot_d, p02_d/ptot_d
```

```
2156
2157            # ------------------------------------------------------
2158
2159            # Blend by xi2 (mix normalized distributions)
2160
2161            # ------------------------------------------------------
2162
2163            P11[j, i] = xi2 * P11_i + (1 - xi2) * P11_d
2164
2165            P20[j, i] = xi2 * P20_i + (1 - xi2) * P20_d
2166
2167            P02[j, i] = xi2 * P02_i + (1 - xi2) * P02_d
2168
2169            P22[j, i] = 1 - (P11[j, i] + P20[j, i] + P02[j, i])
2170
2171
2172
2173
2174
2175    # ------------------------------------------------------------
2176
2177    # 3D Plotting (same as yours)
2178
2179    # ------------------------------------------------------------
2180
2181    fig = plt.figure()
2182
2183    ax = fig.add_subplot(111, projection='3d')
2184
2185    ax.grid(True)
2186
2187
2188
2189    surf1 = ax.plot_surface(R, ATTEN, P11, cmap='cividis', alpha=0.85)
2190
2191    surf2 = ax.plot_surface(R, ATTEN, P02, cmap='magma',  alpha=0.65)
2192
2193    surf3 = ax.plot_surface(R, ATTEN, P20, cmap='cool',   alpha=0.50)
2194
2195
2196
2197    ax.set_xlabel("Reflectivity", fontsize=16, labelpad=16)
2198
2199    ax.set_ylabel("Attenuation", fontsize=16, labelpad=16)
2200
2201    ax.set_zlabel("Probability", fontsize=16, labelpad=8)
2202
2203    ax.set_title("Probability Surfaces (with HOM indistinguishability)")
2204
```

```
2205
2206
2207 ax.set_xlim([0.5, 1])
2208
2209 ax.set_ylim([0, 1])
2210
2211 ax.set_zlim([0, 1])
2212
2213
2214
2215 fig.set_size_inches(14, 8)
2216
2217 fig.set_dpi(200)
2218
2219 plt.show()
2220
2221
2222
2223
2224
2225 # In[ ]:
2226
2227
2228
2229
2230
2231 fig, axes = plt.subplots(1, 3, figsize=(14, 4), sharex=True, sharey=
       True)
2232
2233
2234
2235 # --- Common color limits and colormap ---
2236
2237 vmin, vmax = 0, 1.0
2238
2239 cmap = "viridis"
2240
2241
2242
2243 # --- P11 subplot ---
2244
2245 cont1 = axes[0].contourf(R, ATTEN, P11, levels=40, cmap=cmap, vmin=
       vmin, vmax=vmax)
2246
2247 axes[0].set_title(r"$P_{11}$", fontsize=16)
2248
2249
2250
2251 # --- P02 subplot ---
```

```
2252
2253 cont2 = axes[1].contourf(R, ATTEN, P02, levels=40, cmap=cmap, vmin=
        vmin, vmax=vmax)
2254
2255 axes[1].set_title(r"$P_{02}$", fontsize=16)
2256
2257
2258
2259 # --- P20 subplot ---
2260
2261 cont3 = axes[2].contourf(R, ATTEN, P20, levels=40, cmap=cmap, vmin=
        vmin, vmax=vmax)
2262
2263 axes[2].set_title(r"$P_{20}$", fontsize=16)
2264
2265
2266
2267 # --- Shared colorbar ---
2268
2269 cbar = fig.colorbar(cont1, ax=axes, orientation='vertical', shrink
        =0.8, fraction=0.05, pad=0.02)
2270
2271 cbar.set_label("Probability", fontsize=16)
2272
2273 cbar.ax.tick_params(labelsize=10)
2274
2275
2276
2277 # --- Axis labels ---
2278
2279 for ax in axes:
2280
2281     ax.set_xlabel("Reflectivity", fontsize=16)
2282
2283 axes[0].set_ylabel("Attenuation", fontsize=16)
2284
2285
2286
2287 # --- Global title ---
2288
2289 fig.suptitle("Probability Contours as Functions of Reflectivity and
        Attenuation", fontsize=16, y=1.02)
2290
2291
2292
2293 #plt.tight_layout()
2294
2295 fig.set_dpi(200)
2296
```

```
plt.show()
```

```
# # Including Higher-Order, Decoherece, Mode Mismatch
```

```
# In[ ]:
```

```
fit = fit_eta_p1_p2_mu2(
    r_exp,
    exp_P11, exp_P02, exp_P20,
    err_P11, err_P02, err_P20,
    xi1=0.997,
    gamma=0.933,
    nphi=8,
    p0=(0.4, 0.3, 0.3, 0.10)  # initial , p1, p2, 2
)
```

```
print("eta  =", fit["eta"])
print("p1   =", fit["p1"])
print("p2   =", fit["p2"])
print("mu2  =", fit["mu2"])
print("chi2 =", fit["chi2"])
print("reduced chi2 =", fit["chi2_red"])
```

```
# In[ ]:



fit = fit_HOM_MLE_hybrid(
    r_exp,
    c11_counts,
    c02_counts,
    c20_counts,
    eta_max=0.3,
    p1_max=0.3,
    p2_max=0.3,
    mu2_min=0.94,   # lower bound
    mu2_max=1.0,   # upper bound
    p0_phys=(0.05, 0.05, 0.05, 0.95),
    verbose=True
)

eta_fit_MLE, p1_fit_MLE, p2_fit_MLE, mu2_fit_MLE = fit["params"]



# In[ ]:
```

```
psi_in = spdc(0.1, A0, A1) * ket("00000", d)

psi_in = psi_in.unit()

rho_spdc = psi_in * psi_in.dag()    # pure-state density matrix



P00_spdc = expect(ket("00000", d).proj(), rho_spdc).real

P11_spdc = expect(ket("11000", d).proj(), rho_spdc).real

P22_spdc = expect(ket("22000", d).proj(), rho_spdc).real

print(f"Terms produced by spdc: P00 = {P00_spdc}, P11 = {P11_spdc},
   P22 = {P22_spdc}")

print(2*P22_spdc/P11_spdc)




# In[ ]:




# ========= Helper functions =========

def embed_single(op, mode, N, d):

    ops = [qeye(d)] * N

    ops[mode] = op

    return tensor(*ops)



def build_annihilation_ops(N, d):

    from qutip import destroy

    return [embed_single(destroy(d), m, N, d) for m in range(N)]


```

```
def BS(theta, a_i, a_j):

    H_bs = theta * (a_i.dag() * a_j + a_i * a_j.dag())

    return (-1j * H_bs).expm()


def theta_from_mu(mu):

    mu = np.clip(mu, 0, 1)

    return np.arccos(np.sqrt(mu))


# ========= Dimensions and modes =========

d = 3   # Fock dimension

N = 5   # modes: 0=signal,1=idler,2=mismatch,3=extraBS,4=loss

M0, M1, MMIS, M3, MLOSS = 0, 1, 2, 3, 4


a_ops = build_annihilation_ops(N, d)

A0, A1, A2, A3, A4 = a_ops


# ========= Parameters =========

gamma = 0.5123

theta_gamma = np.arcsin(np.sqrt(gamma))


r = np.linspace(0.5, 1, 1001)

theta_r = np.arccos(np.sqrt(r))   # your chosen mapping


eta = eta_fit_MLE

p1 = p1_fit_MLE
```

```
p2 = p2_fit_MLE



xi1 = 0.997

nphi = 8

mu2 = mu2_fit_MLE  # physical mode mismatch for second BS



# ========= SPDC Input =========

psi_in = spdc(eta, A0, A1) * ket("00000", d)

psi_in = psi_in.unit()

rho_spdc = psi_in * psi_in.dag()    # pure-state density matrix



P00_spdc = expect(ket("00000", d).proj(), rho_spdc).real

P11_spdc = expect(ket("11000", d).proj(), rho_spdc).real

P22_spdc = expect(ket("22000", d).proj(), rho_spdc).real

print(f"Terms produced by spdc: P00 = {P00_spdc}, P11 = {P11_spdc},
   P22 = {P22_spdc}")



# ========= Kraus noise =========

ID = qeye(3)

omega = np.exp(-1j * 2 * np.pi / 3)

Y = Qobj(np.array([[0, 1, 0],

                   [1, 0, 0],

                   [0, 0, 1]], dtype=complex))

Z = Qobj(np.array([[1, 0, 0],

                   [0, omega, 0],
```

```
                    [0, 0, omega**2]], dtype=complex))


pp1 = np.sqrt(p1 / 8)

pp2 = np.sqrt(p2 / 8)


Kmode1 = []

Kmode2 = []


# ---- For mode 0 (signal) ----

Kmode1.append(tensor(np.sqrt(1 - p1) * ID, qeye(3), qeye(3), qeye(3),
    qeye(3)))

Kmode1.append(tensor(pp1 * Y,              qeye(3), qeye(3), qeye(3),
    qeye(3)))

Kmode1.append(tensor(pp1 * Z,              qeye(3), qeye(3), qeye(3),
    qeye(3)))

Kmode1.append(tensor(pp1 * Y**2,           qeye(3), qeye(3), qeye(3),
    qeye(3)))

Kmode1.append(tensor(pp1 * Y * Z,          qeye(3), qeye(3), qeye(3),
    qeye(3)))

Kmode1.append(tensor(pp1 * Y**2 * Z,       qeye(3), qeye(3), qeye(3),
    qeye(3)))

Kmode1.append(tensor(pp1 * Y * Z**2,       qeye(3), qeye(3), qeye(3),
    qeye(3)))

Kmode1.append(tensor(pp1 * Y**2 * Z**2,    qeye(3), qeye(3), qeye(3),
    qeye(3)))

Kmode1.append(tensor(pp1 * Z**2,           qeye(3), qeye(3), qeye(3),
    qeye(3)))


# ---- For mode 1 (idler) ----
```

```
2580
2581 Kmode2.append(tensor(qeye(3), np.sqrt(1 - p2) * ID, qeye(3), qeye(3),
        qeye(3)))
2582
2583 Kmode2.append(tensor(qeye(3), pp2 * Y,             qeye(3), qeye(3),
        qeye(3)))
2584
2585 Kmode2.append(tensor(qeye(3), pp2 * Z,             qeye(3), qeye(3),
        qeye(3)))
2586
2587 Kmode2.append(tensor(qeye(3), pp2 * Y**2,          qeye(3), qeye(3),
        qeye(3)))
2588
2589 Kmode2.append(tensor(qeye(3), pp2 * Y * Z,         qeye(3), qeye(3),
        qeye(3)))
2590
2591 Kmode2.append(tensor(qeye(3), pp2 * Y**2 * Z,      qeye(3), qeye(3),
        qeye(3)))
2592
2593 Kmode2.append(tensor(qeye(3), pp2 * Y * Z**2,      qeye(3), qeye(3),
        qeye(3)))
2594
2595 Kmode2.append(tensor(qeye(3), pp2 * Y**2 * Z**2,   qeye(3), qeye(3),
        qeye(3)))
2596
2597 Kmode2.append(tensor(qeye(3), pp2 * Z**2,          qeye(3), qeye(3),
        qeye(3)))
2598
2599
2600
2601 # ========= Optical elements =========
2602
2603 L     = BS(theta_gamma,        A1, A4)             # attenuation (
        mode1 <-> loss)
2604
2605 U_mis = BS(theta_from_mu(mu2), A1, A2)             # mismatch (mode1
        <-> mode2)
2606
2607 UBS1  = BS(np.pi/4,            A0, A1)             # first BS (HOM
        preparation)
2608
2609
2610
2611 def phase_op(phi):
2612
2613     vals = np.array([1.0,
2614
2615                      np.exp(1j*phi),
2616
```

```
                      np.exp(2j*phi)],
                     dtype=np.complex128)
    return Qobj(np.diag(vals), dims=[[3],[3]])


def phase_on_mode(phi, mode):
    return embed_single(phase_op(phi), mode, N, d)


# ========= First BS (phase-mixing indistinguishability) =========
# Indistinguishable case:
rho_pre_ind = UBS1 * rho_spdc * UBS1.dag()


# Distinguishable case (phase-averaged on one arm before UBS1)
rho_pre_dist = 0 * rho_pre_ind     # correct dims from the start
for phi in np.linspace(0, 2*np.pi, nphi, endpoint=False):
    Uphi = phase_on_mode(phi, M0)
    rho_pre_dist += UBS1 * (Uphi * psi_in) * (psi_in.dag() * Uphi.dag
       ()) * UBS1.dag()
rho_pre_dist /= nphi


# Mix according to xi1
rho_pre = (xi1 * rho_pre_ind + (1 - xi1) * rho_pre_dist).unit()


# ========= Attenuation + Noise =========
rho_in = (L * rho_pre * L.dag()).unit()


```

```
rho_in_d = 0 * rho_in

for K1 in Kmode1:

    for K2 in Kmode2:

        rho_in_d += K2 * K1 * rho_in * K1.dag() * K2.dag()

rho_in_d = rho_in_d.unit()



# ========= Variable BS stage =========

P11 = np.zeros(len(r))

P20 = np.zeros(len(r))

P02 = np.zeros(len(r))

ptotal = np.zeros(len(r))



for i, theta in enumerate(theta_r):

    U_main  = BS(theta, A0, A1)   # main variable BS (0<->1)

    U_misBS = BS(theta, A2, A3)   # mismatched branch BS (2<->3)



    # Apply mismatch coupling before BS

    rho_m = U_mis * rho_in_d * U_mis.dag()



    # Both BSs act together

    U_total = U_misBS * U_main

    rho_out = U_total * rho_m * U_total.dag()



    # --- Photon coincidences ---

```

```
2714
2715      # For p11: photons in modes (0,1) or (0,2) or (0,3)
2716
2717      p11  = expect(ket("11000", d).proj(), rho_out).real  # 0&1
2718
2719      p11 += expect(ket("10100", d).proj(), rho_out).real  # 0&2
2720
2721      p11 += expect(ket("10010", d).proj(), rho_out).real  # 0&3
2722
2723
2724
2725      # For p02: two photons away from mode 0
2726
2727      p02  = expect(ket("02000", d).proj(), rho_out).real  # 2 in 1
2728
2729      p02 += expect(ket("01100", d).proj(), rho_out).real  # 1 in 1, 1
             in 2
2730
2731      p02 += expect(ket("01010", d).proj(), rho_out).real  # 1 in 1, 1
             in 3
2732
2733      p02 += expect(ket("00200", d).proj(), rho_out).real  # 2 in 2
2734
2735      p02 += expect(ket("00110", d).proj(), rho_out).real  # 1 in 2, 1
             in 3
2736
2737      p02 += expect(ket("00020", d).proj(), rho_out).real  # 2 in 3
2738
2739
2740
2741      # For p20: 2 photons in mode 0
2742
2743      p20 = expect(ket("20000", d).proj(), rho_out).real
2744
2745
2746
2747      total = p11 + p02 + p20
2748
2749      if total == 0:
2750
2751          continue
2752
2753
2754
2755      P11[i] = p11 / total
2756
2757      P02[i] = p02 / total
2758
2759      P20[i] = p20 / total
```

```
    ptotal[i] = total



# ========= Plot =========

Min02Loc = np.argmin(P02)

print(f"xi1 (phase-mixing) = {xi1:.3f}")

print(f"mu2 (mode mismatch) = {mu2:.3f}")



fig, ax = plt.subplots()

ax.set_ylabel("Probability", fontsize=18)

ax.set_xlabel("Reflectivity", fontsize=18)

ax.grid(True)

ax.plot(r, P11, linewidth=3, label="$P(1,1)$")

ax.plot(r, P02, linewidth=3, label="$P(0,2)$")

ax.plot(r, P20, linewidth=3, label="$P(2,0)$")

ax.axvline(x=r[Min02Loc], color='r', linestyle='--', label=f'R={r[
   Min02Loc]:.4f}')

#ax.errorbar(r_exp, exp_P11, err_P11, linestyle="None", marker='.',
   markersize=20, c="#377eb8", label="$P(1,1)_{exp}$")

#ax.errorbar(r_exp, exp_P02, err_P02, linestyle="None", marker='s',
   markersize=10, c="#ff7f00", label="$P(0,2)_{exp}$")

#ax.errorbar(r_exp, exp_P20, err_P20, linestyle="None", marker='^',
   markersize=10, c="#4daf4a", label="$P(2,0)_{exp}$")

ax.legend(loc="best", fontsize=16)

ax.set_ylim([0, 1])

ax.set_xlim([0.5, 1])

plt.xticks(fontsize=14)

```

```
plt.yticks(fontsize=14)

fig.set_size_inches(14, 8)

fig.set_dpi(200)

plt.show()




# In[ ]:




# ========= Parameters =========

gamma = 0.933

eta = eta_fit_MLE

p1 = p1_fit_MLE

p2 = p2_fit_MLE



xi1 = 0.997       # phase-mixing indistinguishability at first BS

nphi = 8          # number of phase samples

mu2 = mu2_fit_MLE     # mode mismatch coupling for second BS (1 =
   perfect mode match)



# Reflectivity scan for variable BS

r = np.linspace(0.5, 1, 51)

theta_r = np.arccos(np.sqrt(r))  # R = cos(theta)



# Attenuation scan (loss BS power reflectivity)

```

```
atten = np.linspace(0, 1, 21)

theta_atten = np.arcsin(np.sqrt(atten))



R, ATTEN = np.meshgrid(r, atten)



# ========= SPDC Input =========

psi_in = spdc(eta, A0, A1) * ket("00000", d)

psi_in = psi_in.unit()



# ========= Optical elements =========

UBS1 = BS(np.pi/4, A0, A1)                    # first BS (HOM
   preparation)

U_mis = BS(theta_from_mu(mu2), A1, A2)        # mismatch coupling (
   mode1 <-> mode2)



# ========= First BS (phase-mixing indistinguishability) =========

rho_pre_ind = UBS1 * (psi_in * psi_in.dag()) * UBS1.dag()

rho_pre_dist = 0

for phi in np.linspace(0, 2*np.pi, nphi, endpoint=False):

    Uphi = phase_on_mode(phi, M0)

    rho_pre_dist += UBS1 * (Uphi * psi_in) * (psi_in.dag() * Uphi.dag
       ()) * UBS1.dag()

rho_pre_dist /= nphi



# Mix according to xi1

rho_pre = (xi1 * rho_pre_ind + (1 - xi1) * rho_pre_dist).unit()

```

```
2899
2900
2901 # ========= Initialize storage arrays =========
2902
2903 P11 = np.zeros((len(atten), len(r)))
2904
2905 P20 = np.zeros((len(atten), len(r)))
2906
2907 P02 = np.zeros((len(atten), len(r)))
2908
2909 ptotal = np.zeros((len(atten), len(r)))
2910
2911
2912
2913 # ========= Full 2D scan over attenuation and BS reflectivity
        =========
2914
2915 for j, theta_loss in enumerate(theta_atten):
2916
2917     # Attenuation (mode 1 <-> loss)
2918
2919     L = BS(theta_loss, A1, A4)
2920
2921     rho_in = (L * rho_pre * L.dag()).unit()
2922
2923
2924
2925     # --- Apply Kraus noise (already defined) ---
2926
2927     rho_in_d = 0
2928
2929     for K1 in Kmode1:
2930
2931         for K2 in Kmode2:
2932
2933             rho_in_d += K2 * K1 * rho_in * K1.dag() * K2.dag()
2934
2935     rho_in_d = rho_in_d.unit()
2936
2937
2938
2939     # --- Apply mode mismatch before variable BS ---
2940
2941     rho_in_m = U_mis * rho_in_d * U_mis.dag()
2942
2943
2944
2945     # --- Variable BS sweep ---
2946
```

```
    for i, theta in enumerate(theta_r):

        U_main = BS(theta, A0, A1)      # main variable BS (0<->1)

        U_misBS = BS(theta, A2, A3)     # mismatched branch BS (2<->3)



        # Both BSs act together

        U_total = U_misBS * U_main

        rho_out = U_total * rho_in_m * U_total.dag()



        # Projectors for relevant outcomes

        # For p11

        p11 = expect(ket("11000", d).proj(), rho_out).real # mode 0
           and 1

        p11 += expect(ket("10100", d).proj(), rho_out).real # mode 0
           and 2 (mode mismatched)

        p11 += expect(ket("10010", d).proj(), rho_out).real # mode 0
           and 3 (mode mismatched)

        # For p02

        p02 = expect(ket("02000", d).proj(), rho_out).real # 2 photons
            in mode 1

        p02 += expect(ket("01100", d).proj(), rho_out).real # mode 1
           and 2 (mode mismatched)

        p02 += expect(ket("01010", d).proj(), rho_out).real # mode 1
           and 2 (mode mismatched)

        p02 += expect(ket("00200", d).proj(), rho_out).real # 2
           photons in mode 2 (mode mismatched)

        p02 += expect(ket("00110", d).proj(), rho_out).real # mode 2
           and 3 (mode mismatched)

        p02 += expect(ket("00020", d).proj(), rho_out).real # 2
           photons in mode 3 (mode mismatched)

```

```
2987
2988
2989            # For p20
2990
2991            p20 = expect(ket("20000", d).proj(), rho_out).real # 2 photons
                    in mode 0
2992
2993
2994
2995            total = p11 + p02 + p20
2996
2997            if total == 0:
2998
2999                continue
3000
3001
3002
3003            P11[j, i] = p11 / total
3004
3005            P02[j, i] = p02 / total
3006
3007            P20[j, i] = p20 / total
3008
3009            ptotal[j, i] = total
3010
3011
3012
3013    # ========= 3D Surface Plot =========
3014
3015
3016
3017    blue_map   = LinearSegmentedColormap.from_list("blue_map",   ["#c6dbef
           ", "#377eb8"])
3018
3019    orange_map = LinearSegmentedColormap.from_list("orange_map", ["#fdd0a2
           ", "#ff7f00"])
3020
3021    green_map  = LinearSegmentedColormap.from_list("green_map",  ["#c7e9c0
           ", "#4daf4a"])
3022
3023
3024
3025    fig = plt.figure(figsize=(14,8), dpi=200)
3026
3027    ax = fig.add_subplot(111, projection='3d')
3028
3029    ax.grid(True)
3030
3031    surf1 = ax.plot_surface(R, ATTEN, P11, cmap=blue_map, alpha=0.9)
```

```
surf2 = ax.plot_surface(R, ATTEN, P02, cmap=orange_map, alpha=0.75)

surf3 = ax.plot_surface(R, ATTEN, P20, cmap=green_map, alpha=0.65)

ax.set_xlabel("Reflectivity", fontsize=16, labelpad=16)

ax.set_ylabel("Attenuation", fontsize=16, labelpad=16)

ax.set_zlabel("Probability",  fontsize=16, labelpad=8)

ax.set_title("Probability Surfaces (with Mode Mismatch)")

ax.set_ylim([0, 1])

ax.set_xlim([0.5, 1])

ax.set_zlim([0, 1])

plt.xticks(fontsize="14")

plt.yticks(fontsize="14")

cax1 = fig.add_axes([0.77, 0.60, 0.02, 0.25])

cax2 = fig.add_axes([0.77, 0.33, 0.02, 0.25])

cax3 = fig.add_axes([0.77, 0.06, 0.02, 0.25])

fig.colorbar(surf1, cax=cax1).set_label(r"$P_{11}$", fontsize="16")

fig.colorbar(surf2, cax=cax2).set_label(r"$P_{02}$", fontsize="16")

fig.colorbar(surf3, cax=cax3).set_label(r"$P_{20}$", fontsize="16")

fig.set_size_inches(14, 8)

fig.set_dpi(200)

plt.margins(0.1)

plt.show()




# In[ ]:

```

```
3081
3082
3083
3084
3085 fig, axes = plt.subplots(1, 3, figsize=(14, 4), sharex=True, sharey=
        True)
3086
3087
3088
3089 # --- Common color limits and colormap ---
3090
3091 vmin, vmax = 0, 1.0
3092
3093 cmap = "viridis"
3094
3095
3096
3097 # --- P11 subplot ---
3098
3099 cont1 = axes[0].contourf(R, ATTEN, P11, levels=40, cmap=cmap, vmin=
        vmin, vmax=vmax)
3100
3101 axes[0].set_title(r"$P_{11}$", fontsize=16)
3102
3103
3104
3105 # --- P02 subplot ---
3106
3107 cont2 = axes[1].contourf(R, ATTEN, P02, levels=40, cmap=cmap, vmin=
        vmin, vmax=vmax)
3108
3109 axes[1].set_title(r"$P_{02}$", fontsize=16)
3110
3111
3112
3113 # --- P20 subplot ---
3114
3115 cont3 = axes[2].contourf(R, ATTEN, P20, levels=40, cmap=cmap, vmin=
        vmin, vmax=vmax)
3116
3117 axes[2].set_title(r"$P_{20}$", fontsize=16)
3118
3119
3120
3121 # --- Shared colorbar ---
3122
3123 cbar = fig.colorbar(cont1, ax=axes, orientation='vertical', shrink
        =0.8, fraction=0.05, pad=0.02)
3124
```

```
cbar.set_label("Probability", fontsize=16)

cbar.ax.tick_params(labelsize=10)



# --- Axis labels ---

for ax in axes:

    ax.set_xlabel("Reflectivity", fontsize=16)

axes[0].set_ylabel("Attenuation", fontsize=16)



# --- Global title ---

fig.suptitle("Probability Contours as Functions of Reflectivity and
   Attenuation", fontsize=16, y=1.02)



#plt.tight_layout()

fig.set_dpi(200)

plt.show()







# # Fitting


# In[ ]:







def theoretical_probabilities(r, p1, p2, eta, A1n, A2n, An_loss, UBS1,
    n):

    """

    Compute theoretical P11, P20, P02 for given p1, p2, eta.
```

```
    Returns concatenated probabilities for fitting.

    """

    pp1 = np.sqrt(p1 / 8)

    pp2 = np.sqrt(p2 / 8)

    omega = np.exp(-1j * 2 * np.pi / 3)

    ID = qeye(3)

    Y = Qobj(np.array([[0, 1, 0],

                       [1, 0, 0],

                       [0, 0, 1]], dtype=complex))

    Z = Qobj(np.array([[1, 0, 0],

                       [0, omega, 0],

                       [0, 0, omega**2]], dtype=complex))


    # Kraus operators

    Kmode1, Kmode2 = [], []


    for i in range(3):

        # just placeholders to avoid repetition

        pass


    # Mode 1

    Kmode1.append(tensor(np.sqrt(1 - p1) * ID, qeye(3), qeye(3)))

    Kmode1 += [tensor(op, qeye(3), qeye(3)) for op in

               [pp1 * Y, pp1 * Z, pp1 * Y**2, pp1 * Y*Z, pp1 * Y**2*Z,
```

```
                pp1 * Y*Z**2, pp1 * Y**2*Z**2, pp1 * Z**2]]


    # Mode 2

    Kmode2.append(tensor(qeye(3), np.sqrt(1 - p2) * ID, qeye(3)))

    Kmode2 += [tensor(qeye(3), op, qeye(3)) for op in

               [pp2 * Y, pp2 * Z, pp2 * Y**2, pp2 * Y*Z, pp2 * Y**2*Z,

                pp2 * Y*Z**2, pp2 * Y**2*Z**2, pp2 * Z**2]]


    # SPDC source

    psi_in = spdc(eta, A1n, A2n) * ket("000", n).unit()


    # Attenuation

    gamma = 0.7327

    L = BS(np.arcsin(gamma), A1n, An_loss)

    rho_in = (L.dag() * UBS1.dag() * psi_in * psi_in.dag() * UBS1 * L)
       .unit()


    # Decoherence

    rho_in_d = 0

    for K1 in Kmode1:

        for K2 in Kmode2:

            rho_in_d += K2 * K1 * rho_in * K1.dag() * K2.dag()

    tr = rho_in_d.tr()

    if tr == 0 or np.isnan(tr):

        raise ValueError(f"Invalid rho_in_d at p1={p1}, p2={p2}, eta={
           eta}")
```

```
3268
3269        rho_in_d = rho_in_d / tr
3270
3271    # Output probabilities
3272
3273        P11, P20, P02 = [], [], []
3274
3275
3276
3277        for ri in r:
3278
3279            rho_out = (BS(ri, A1n, A2n).dag() * rho_in_d * BS(ri, A1n, A2n
                ))
3280
3281            p11 = expect(ket("11", n).proj(), rho_out.ptrace([0, 1]))
3282
3283            p20 = expect(ket("20", n).proj(), rho_out.ptrace([0, 1]))
3284
3285            p02 = expect(ket("02", n).proj(), rho_out.ptrace([0, 1]))
3286
3287            ptotal = p11 + p20 + p02 + expect(ket("22", n).proj(), rho_out
                .ptrace([0, 1]))
3288
3289            P11.append(p11 / ptotal)
3290
3291            P20.append(p20 / ptotal)
3292
3293            P02.append(p02 / ptotal)
3294
3295
3296
3297        return np.concatenate([P11, P02, P20])
3298
3299
3300
3301
3302
3303    # In[ ]:
3304
3305
3306
3307
3308
3309    # Combine experimental data
3310
3311    y_exp = np.concatenate([exp_P11, exp_P02, exp_P20])
3312
3313
3314
```

```
# Choose set of reflectivities

r = r_exp



# Physically reasonable bounds:

# p1, p2, eta are probabilities/efficiencies, so between 0 and 1

bounds = ([0, 0, 0], [1, 1, 1])



# Initial guess for [p1, p2, eta]

p0 = [0.3, 0.3, 0.4]



if "sigma" not in globals():

    sigma = np.ones_like(y_exp)



# IMPORTANT: when you call curve_fit, pass the same sigma and set
   absolute_sigma=True

params, cov = curve_fit(

    lambda r, p1, p2, eta: theoretical_probabilities(r, p1, p2, eta,
       A1n, A2n, An_loss, UBS1, n),

    r,

    y_exp,

    p0=p0,

    bounds=([1e-9, 1e-9, 1e-9], [1-1e-9, 1-1e-9, 1-1e-9]),

    sigma=sigma,

    absolute_sigma=True,

    maxfev=5000

)
```

```
3362
3363
3364
3365 # Model prediction at best-fit
3366
3367 y_fit = theoretical_probabilities(r, *params, A1n, A2n, An_loss, UBS1,
         n)
3368
3369
3370
3371 # Pearson chi-square
3372
3373 resid = (y_exp - y_fit) / sigma
3374
3375 chi2_val = np.sum(resid**2)
3376
3377
3378
3379 # Degrees of freedom = (#points) - (#free params)
3380
3381 dof = y_exp.size - len(params)
3382
3383 chi2_red = chi2_val / dof
3384
3385
3386
3387 # p-value: probability of obtaining chi2 >= observed if model is true
3388
3389 p = chi2.sf(chi2_val, dof)
3390
3391
3392
3393 print("Best-fit parameters:")
3394
3395 print(f"p1 = {params[0]:.4f}")
3396
3397 print(f"p2 = {params[1]:.4f}")
3398
3399 print(f"eta = {params[2]:.4f}")
3400
3401 print(f"chi^2 = {chi2_val:.3f}")
3402
3403 print(f"reduced chi^2 = {chi2_red:.3f} (dof = {dof})")
3404
3405 print(f"p-value = {p:.3g}")
3406
3407
3408
3409
```

```
# In[ ]:



from scipy.optimize import least_squares


def model_probabilities(r_points, p1, p2, eta, gamma,
                        A1n, A2n, An_loss, UBS1, n):
    """
    Compute P11(r), P02(r), P20(r) for given (p1, p2, eta, gamma)
    at the reflectivity values r_points.

    Returns:
        P11, P02, P20  (each 1D np.array of same length as r_points)
    """


    # ---- SPDC input state ----
    psi_in = spdc(eta, A1n, A2n) * ket("000", n).unit()


    # ---- Noise / decoherence Kraus operators ----
    pp1 = np.sqrt(p1 / 8.0)
    pp2 = np.sqrt(p2 / 8.0)


    omega = np.exp(-1j * 2 * np.pi / 3)
```

```
    ID = qeye(3)

    Y = Qobj(np.array([[0, 1, 0],

                       [1, 0, 0],

                       [0, 0, 1]], dtype=complex))

    Z = Qobj(np.array([[1, 0, 0],

                       [0, omega, 0],

                       [0, 0, omega**2]], dtype=complex))


    Kmode1 = []

    Kmode2 = []


    # For mode 1.

    Kmode1.append(tensor(np.sqrt(1 - p1) * ID, qeye(3), qeye(3)))

    Kmode1.append(tensor(pp1 * Y,              qeye(3), qeye(3)))

    Kmode1.append(tensor(pp1 * Z,              qeye(3), qeye(3)))

    Kmode1.append(tensor(pp1 * Y**2,           qeye(3), qeye(3)))

    Kmode1.append(tensor(pp1 * Y * Z,          qeye(3), qeye(3)))

    Kmode1.append(tensor(pp1 * Y**2 * Z,       qeye(3), qeye(3)))

    Kmode1.append(tensor(pp1 * Y * Z**2,       qeye(3), qeye(3)))

    Kmode1.append(tensor(pp1 * Y**2 * Z**2,    qeye(3), qeye(3)))

    Kmode1.append(tensor(pp1 * Z**2,           qeye(3), qeye(3)))


    # For mode 2.

    Kmode2.append(tensor(qeye(3), np.sqrt(1 - p2) * ID, qeye(3)))

    Kmode2.append(tensor(qeye(3), pp2 * Y,              qeye(3)))
```

```
    Kmode2.append(tensor(qeye(3), pp2 * Z,              qeye(3)))

    Kmode2.append(tensor(qeye(3), pp2 * Y**2,           qeye(3)))

    Kmode2.append(tensor(qeye(3), pp2 * Y * Z,          qeye(3)))

    Kmode2.append(tensor(qeye(3), pp2 * Y**2 * Z,       qeye(3)))

    Kmode2.append(tensor(qeye(3), pp2 * Y * Z**2,       qeye(3)))

    Kmode2.append(tensor(qeye(3), pp2 * Y**2 * Z**2,    qeye(3)))

    Kmode2.append(tensor(qeye(3), pp2 * Z**2,           qeye(3)))


    # ---- Attenuation unitary ----

    theta_gamma = np.arcsin(np.sqrt(gamma))

    L = BS(theta_gamma, A1n, An_loss)


    # Choose which rho_in you want (this line is your last choice):

    rho_in = (L.dag() * UBS1.dag() * psi_in * psi_in.dag() * UBS1 * L)
       .unit()


    # ---- Apply Kraus operators (decoherence) ----

    rho_in_d = 0 * rho_in  # zero Qobj with correct dims


    for K in Kmode1:

        rho_in_d += K * rho_in * K.dag()

    for K in Kmode2:

        rho_in_d += K * rho_in * K.dag()


    rho_in_d = rho_in_d.unit()
```

```
3556
3557
3558
3559      # ---- Initialize probability arrays ----
3560
3561      P11 = np.zeros(len(r_points), dtype=float)
3562
3563      P20 = np.zeros(len(r_points), dtype=float)
3564
3565      P02 = np.zeros(len(r_points), dtype=float)
3566
3567      P22 = np.zeros(len(r_points), dtype=float)
3568
3569
3570
3571      # ---- Calculate probabilities for each reflectivity ----
3572
3573      for i, r_val in enumerate(r_points):
3574
3575          theta_r = np.arcsin(np.sqrt(r_val))
3576
3577          U_BS_var = BS(theta_r, A1n, A2n)
3578
3579
3580
3581          # With variable beamsplitter after decoherence:
3582
3583          rho_out = U_BS_var.dag() * rho_in_d * U_BS_var
3584
3585
3586
3587          rho_01 = rho_out.ptrace([0, 1])   # trace out other modes
3588
3589
3590
3591          P11[i] = expect(ket("11", n).proj(), rho_01).real
3592
3593          P20[i] = expect(ket("20", n).proj(), rho_01).real
3594
3595          P02[i] = expect(ket("02", n).proj(), rho_01).real
3596
3597          P22[i] = expect(ket("22", n).proj(), rho_01).real
3598
3599
3600
3601          ptotal = P11[i] + P02[i] + P20[i] + P22[i]
3602
3603          if ptotal > 0:
3604
```

```
            P11[i] /= ptotal

            P20[i] /= ptotal

            P02[i] /= ptotal

        else:

            # if something pathological happens, set to zero

            P11[i] = P20[i] = P02[i] = 0.0


    return P11, P02, P20




def fit_p1_p2_eta(r_exp,

                  exp_P11, exp_P02, exp_P20,

                  err_P11, err_P02, err_P20,

                  A1n, A2n, An_loss, UBS1, n,

                  gamma=0.933,

                  p0=(0.3, 0.3, 0.4)):

    """

    Fit p1, p2, eta to experimental HOM data using your full model.


    Returns:

        result (scipy.optimize.OptimizeResult) with:

          - result.x = [p1_fit, p2_fit, eta_fit]

          - result.chi2

          - result.chi2_red

    """
```

```
    y_exp = np.concatenate([exp_P11, exp_P02, exp_P20])
    sigma = np.concatenate([err_P11, err_P02, err_P20])


    # Avoid zero uncertainties
    sigma_safe = np.where(sigma <= 0, 1.0, sigma)


    def residuals(theta):
        p1, p2, eta = theta


        # Hard bounds check (least_squares also enforces, but this
           prevents weird states)
        if (p1 < 0) or (p1 > 1) or (p2 < 0) or (p2 > 1) or (eta < 0)
           or (eta > 1):
            return np.ones_like(y_exp) * 1e6


        P11_mod, P02_mod, P20_mod = model_probabilities(
            r_exp, p1, p2, eta, gamma,
            A1n, A2n, An_loss, UBS1, n
        )


        y_mod = np.concatenate([P11_mod, P02_mod, P20_mod])


        return (y_mod - y_exp) / sigma_safe
```

```
    result = least_squares(

        residuals,

        x0=np.array(p0),

        bounds=([0.0, 0.0, 0.0], [1.0, 1.0, 1.0]),

        loss="soft_l1",

        f_scale=0.03,

        max_nfev=20000,

        xtol=1e-10, ftol=1e-10, gtol=1e-10

    )



    # Compute  and reduced

    res_vec = residuals(result.x)

    chi2 = np.sum(res_vec**2)

    dof = y_exp.size - 3   # 3 fit parameters

    chi2_red = chi2 / dof if dof > 0 else np.nan



    # Attach to result for convenience

    result.chi2 = chi2

    result.chi2_red = chi2_red



    return result




# # Robust Fitting (Least-Squares + Logit + Nuisance Params)

#
```

```
3750
3751 # This section adds a more **robust** fitting pipeline:
3752
3753 # - Unconstrained optimization via **logit** transform for (p1, p2,
       eta, gamma)  (0,1).
3754
3755 # - **Reflectivity calibration** parameters `a` (scale) and `b` (
       offset): `r_eff = clip(a*r + b, 0, 1)`.
3756
3757 # - **Visibility** parameter `v` to absorb mode mismatch.
3758
3759 # - **Robust loss** (`soft_l1`) with `scipy.optimize.least_squares`.
3760
3761 # - Numerical hygiene (real parts only, single trace normalization,
       clipping) and a safety fallback for NaNs.
3762
3763 #
3764
3765 # It does **not** delete your previous codethis is an additive, drop-
       in alternative.
3766
3767 #
3768
3769
3770
3771 # In[ ]:
3772
3773
3774
3775
3776
3777 # --- Logistic helpers ---
3778
3779 def inv_logit(x): return 1 / (1 + np.exp(-x))
3780
3781 def logit(p): return np.log(p / (1 - p))
3782
3783
3784
3785 def BS_from_R(R, A1n, A2n):
3786
3787     """Construct BS operator from reflectivity R."""
3788
3789     R = np.clip(R, 0.0, 1.0)
3790
3791     theta = np.arcsin(np.sqrt(R))
3792
3793     return BS(theta, A1n, A2n)
3794
```

```
3795
3796
3797 # --- Theoretical model (no indistinguishability) ---
3798
3799 def theoretical_probabilities_no_indist(
3800
3801     r, p1, p2, eta,
3802
3803     A1n, A2n, An_loss, UBS1, n,
3804
3805     *,
3806
3807     gamma=0.933
3808
3809 ):
3810
3811     """
3812
3813     Computes [P11, P02, P20] for the ideal distinguishable-photon
        model.
3814
3815     """
3816
3817     # --- Base operators ---
3818
3819     pp1 = np.sqrt(p1 / 8.0)
3820
3821     pp2 = np.sqrt(p2 / 8.0)
3822
3823     omega = np.exp(-1j * 2 * np.pi / 3)
3824
3825     ID = qeye(3)
3826
3827     Y = Qobj(np.array([[0, 1, 0], [1, 0, 0], [0, 0, 1]], dtype=complex
        ))
3828
3829     Z = Qobj(np.array([[1, 0, 0], [0, omega, 0], [0, 0, omega**2]],
        dtype=complex))
3830
3831
3832
3833     # --- Kraus operators ---
3834
3835     Kmode1 = [tensor(np.sqrt(1 - p1) * ID, qeye(3), qeye(3))]
3836
3837     Kmode1 += [tensor(op, qeye(3), qeye(3)) for op in
3838
3839                 [pp1 * Y, pp1 * Z, pp1 * Y**2, pp1 * Y * Z,
3840
```

```
                pp1 * Y**2 * Z, pp1 * Y * Z**2, pp1 * Y**2 * Z**2, pp1
                    * Z**2]]


    Kmode2 = [tensor(qeye(3), np.sqrt(1 - p2) * ID, qeye(3))]

    Kmode2 += [tensor(qeye(3), op, qeye(3)) for op in

               [pp2 * Y, pp2 * Z, pp2 * Y**2, pp2 * Y * Z,

                pp2 * Y**2 * Z, pp2 * Y * Z**2, pp2 * Y**2 * Z**2, pp2
                    * Z**2]]


    # --- SPDC source state ---

    psi_in = spdc(eta, A1n, A2n) * ket("000", n).unit()


    # --- Attenuation (loss) ---

    L = BS(np.arcsin(np.sqrt(gamma)), A1n, An_loss)


    # --- Include first beamsplitter and attenuation ---

    rho_in = (L.dag() * UBS1.dag() * psi_in * psi_in.dag() * UBS1 * L)
       .unit()


    # --- Apply Kraus noise operators (decoherence) ---

    rho_in_d = Qobj()

    for K1 in Kmode1:

        for K2 in Kmode2:

            rho_in_d += K2 * K1 * rho_in * K1.dag() * K2.dag()

    rho_in_d = rho_in_d.unit()
```

```
    # --- Measurement operators ---

    P_11 = ket("11", n).proj()

    P_20 = ket("20", n).proj()

    P_02 = ket("02", n).proj()

    P_22 = ket("22", n).proj()



    # --- Variable BS sweep ---

    P11, P20, P02 = [], [], []

    for Ri in r:

        U = BS_from_R(Ri, A1n, A2n)

        rho_out = (U.dag() * rho_in_d * U)

        rho12 = rho_out.ptrace([0, 1])

        p11 = expect(P_11, rho12).real

        p20 = expect(P_20, rho12).real

        p02 = expect(P_02, rho12).real

        p22 = expect(P_22, rho12).real

        ptotal = p11 + p20 + p02 + p22

        P11.append(p11 / ptotal)

        P20.append(p20 / ptotal)

        P02.append(p02 / ptotal)



    return np.concatenate([np.array(P11), np.array(P02), np.array(P20)
       ])
```

```
# --- Robust fitting routine (no indistinguishability) ---

def fit_robust_no_indist(

    y_exp, r, A1n, A2n, An_loss, UBS1, n,

    *, gamma=0.933, x0=None, sigma=None

):

    """

    Fit p1, p2, eta to experimental data assuming fully
       distinguishable model.

    """

    if sigma is None:

        sigma = np.ones_like(y_exp)



    def resid(theta_raw):

        p1, p2, eta = map(inv_logit, theta_raw)

        y_mod = theoretical_probabilities_no_indist(

            r, p1, p2, eta,

            A1n, A2n, An_loss, UBS1, n,

            gamma=gamma

        )

        if (not np.all(np.isfinite(y_mod))) or (y_mod.shape != y_exp.
           shape):

            return np.ones_like(y_exp) * 1e6

        return (y_mod - y_exp) / sigma



    if x0 is None:

        x0 = [logit(0.3), logit(0.3), logit(0.4)]
```

```
    res = least_squares(
        resid, x0,
        loss="soft_l1", f_scale=0.03,
        max_nfev=20000, xtol=1e-10, ftol=1e-10, gtol=1e-10
    )


    p1, p2, eta = map(inv_logit, res.x)
    y_fit = theoretical_probabilities_no_indist(
        r, p1, p2, eta,
        A1n, A2n, An_loss, UBS1, n,
        gamma=gamma
    )


    resid_vals = (y_exp - y_fit) / sigma
    chi2_val = float(np.sum(resid_vals**2))
    dof = int(y_exp.size - len(res.x))
    chi2_red = chi2_val / max(dof, 1)


    return {
        "params": np.array([p1, p2, eta, gamma]),
        "param_names": ["p1", "p2", "eta", "gamma"],
        "y_fit": y_fit,
        "chi2": chi2_val,
```

```
        "chi2_red": chi2_red,

        "dof": dof,

        "success": res.success,

        "message": res.message,

        "res": res,

    }




# ## Fitting while accounting for HOM Indistinguishability


# In[ ]:




from scipy.optimize import least_squares


def inv_logit(x):

    return 1.0 / (1.0 + np.exp(-x))


def logit(p):

    p = np.clip(p, 1e-9, 1-1e-9)

    return np.log(p / (1.0 - p))


def phase_op(phi):

    """Phase shift on a single qutrit mode |k> -> e^{i k phi} |k>."""

    vals = np.array(
```

```
        [1.0,
         np.exp(1j * phi),
         np.exp(2j * phi)],
        dtype=np.complex128
    )
    return Qobj(np.diag(vals), dims=[[3], [3]])
def theoretical_probabilities_fit(
    r_points,
    eta, p1, p2,
    A1n, A2n, An_loss, UBS1, n,
    *,
    gamma=0.933,
    xi1=0.997,
    xi2=0.947,
    nphi=8
):
    """
    Full HOM model returning concatenated [P11, P02, P20]
    for given eta, p1, p2 at reflectivities r_points.
    """

    # ---- SPDC source ----
    psi_in = spdc(eta, A1n, A2n) * ket("000", n).unit()
```

```
    # ---- Noise params ----

    pp1 = np.sqrt(p1 / 8.0)

    pp2 = np.sqrt(p2 / 8.0)

    omega = np.exp(-1j * 2 * np.pi / 3)


    ID = qeye(3)

    Y = Qobj(np.array([[0, 1, 0],

                       [1, 0, 0],

                       [0, 0, 1]], dtype=complex))

    Z = Qobj(np.array([[1, 0, 0],

                       [0, omega, 0],

                       [0, 0, omega**2]], dtype=complex))


    # ---- Kraus operators ----

    Kmode1 = []

    Kmode2 = []


    # Mode 1

    Kmode1.append(tensor(np.sqrt(1 - p1) * ID, qeye(3), qeye(3)))

    Kmode1.append(tensor(pp1 * Y,              qeye(3), qeye(3)))

    Kmode1.append(tensor(pp1 * Z,              qeye(3), qeye(3)))

    Kmode1.append(tensor(pp1 * Y**2,           qeye(3), qeye(3)))

    Kmode1.append(tensor(pp1 * Y * Z,          qeye(3), qeye(3)))

    Kmode1.append(tensor(pp1 * Y**2 * Z,       qeye(3), qeye(3)))

    Kmode1.append(tensor(pp1 * Y * Z**2,       qeye(3), qeye(3)))
```

```
    Kmode1.append(tensor(pp1 * Y**2 * Z**2,    qeye(3), qeye(3)))

    Kmode1.append(tensor(pp1 * Z**2,           qeye(3), qeye(3)))


    # Mode 2

    Kmode2.append(tensor(qeye(3), np.sqrt(1 - p2) * ID, qeye(3)))

    Kmode2.append(tensor(qeye(3), pp2 * Y,              qeye(3)))

    Kmode2.append(tensor(qeye(3), pp2 * Z,              qeye(3)))

    Kmode2.append(tensor(qeye(3), pp2 * Y**2,           qeye(3)))

    Kmode2.append(tensor(qeye(3), pp2 * Y * Z,          qeye(3)))

    Kmode2.append(tensor(qeye(3), pp2 * Y**2 * Z,       qeye(3)))

    Kmode2.append(tensor(qeye(3), pp2 * Y * Z**2,       qeye(3)))

    Kmode2.append(tensor(qeye(3), pp2 * Y**2 * Z**2,    qeye(3)))

    Kmode2.append(tensor(qeye(3), pp2 * Z**2,           qeye(3)))


    # ---- Attenuation unitary ----

    theta_gamma = np.arcsin(np.sqrt(gamma))

    L = BS(theta_gamma, A1n, An_loss)


    # ---- First BS (UBS1): distinguishability at preparation (xi1)
       ----

    rho_pre_ind = UBS1.dag() * psi_in * psi_in.dag() * UBS1


    phis = np.linspace(0, 2*np.pi, nphi, endpoint=False)

    rho_pre_dist = 0 * rho_pre_ind

    for phi in phis:
```

```
4226
4227            Uphi = tensor(phase_op(phi), qeye(3), qeye(3))
4228
4229            rho_pre_dist += UBS1.dag() * (Uphi * psi_in) * (psi_in.dag() *
                    Uphi.dag()) * UBS1
4230
4231        rho_pre_dist /= nphi
4232
4233
4234
4235        rho_pre = (xi1 * rho_pre_ind + (1 - xi1) * rho_pre_dist).unit()
4236
4237
4238
4239        # ---- Attenuation ----
4240
4241        rho_in = (L.dag() * rho_pre * L).unit()
4242
4243
4244
4245        # ---- Decoherence ----
4246
4247        rho_in_d = 0 * rho_in
4248
4249        for K1 in Kmode1:
4250
4251            for K2 in Kmode2:
4252
4253                rho_in_d += K2 * K1 * rho_in * K1.dag() * K2.dag()
4254
4255        rho_in_d = rho_in_d.unit()
4256
4257
4258
4259        # ---- Measurement projectors ----
4260
4261        P_11 = ket("11", n).proj()
4262
4263        P_20 = ket("20", n).proj()
4264
4265        P_02 = ket("02", n).proj()
4266
4267        P_22 = ket("22", n).proj()
4268
4269
4270
4271        # ---- Arrays for probabilities ----
4272
4273        P11 = np.zeros(len(r_points))
```

```
    P20 = np.zeros(len(r_points))

    P02 = np.zeros(len(r_points))



    # ---- Variable BS (UBS2, xi2 distinguishability) ----

    for i, R in enumerate(r_points):

        theta = np.arcsin(np.sqrt(R))

        U = BS(theta, A1n, A2n)



        # indistinguishable contribution

        rho_out_ind = (U.dag() * rho_in_d * U)

        rho12_ind = rho_out_ind.ptrace([0, 1])

        p11_i = expect(P_11, rho12_ind).real

        p20_i = expect(P_20, rho12_ind).real

        p02_i = expect(P_02, rho12_ind).real

        p22_i = expect(P_22, rho12_ind).real

        ptot_i = p11_i + p20_i + p02_i + p22_i

        P11i = p11_i / ptot_i

        P20i = p20_i / ptot_i

        P02i = p02_i / ptot_i



        # distinguishable surrogate (phase averaged)

        p11_d = p20_d = p02_d = p22_d = 0.0

        for phi in phis:

            Uphi = tensor(phase_op(phi), qeye(3), qeye(3))
```

```
            rho_phi = Uphi * rho_in_d * Uphi.dag()

            rho_out_d = (U.dag() * rho_phi * U)

            rho12_d = rho_out_d.ptrace([0, 1])


            p11_d += expect(P_11, rho12_d).real

            p20_d += expect(P_20, rho12_d).real

            p02_d += expect(P_02, rho12_d).real

            p22_d += expect(P_22, rho12_d).real


        p11_d /= nphi; p20_d /= nphi; p02_d /= nphi; p22_d /= nphi

        ptd = p11_d + p20_d + p02_d + p22_d

        P11d = p11_d / ptd

        P20d = p20_d / ptd

        P02d = p02_d / ptd


        # mix by xi2

        P11[i] = xi2 * P11i + (1 - xi2) * P11d

        P20[i] = xi2 * P20i + (1 - xi2) * P20d

        P02[i] = xi2 * P02i + (1 - xi2) * P02d


    # Concatenate in same order as your experimental vector

    return np.concatenate([P11, P02, P20])

def fit_eta_p1_p2(

    r_exp,

    exp_P11, exp_P02, exp_P20,
```

```
    err_P11, err_P02, err_P20,
    A1n, A2n, An_loss, UBS1, n,
    *,
    gamma=0.933,
    xi1=0.997,
    xi2=0.947,
    nphi=8,
    x0=None
):
    """
    Robust fit for eta, p1, p2 (xi1, xi2, gamma fixed).
    Returns a dict with params, chi2, chi2_red, etc.
    """

    # Build data and sigma vectors
    y_exp = np.concatenate([exp_P11, exp_P02, exp_P20])
    sigma = np.concatenate([err_P11, err_P02, err_P20])
    sigma = np.where(sigma <= 0, 1.0, sigma)

    def resid(theta_raw):
        # theta_raw = logit(eta), logit(p1), logit(p2)
        eta_, p1_, p2_ = map(inv_logit, theta_raw)

        y_mod = theoretical_probabilities_fit(
```

```
            r_exp,

            eta_, p1_, p2_,

            A1n, A2n, An_loss, UBS1, n,

            gamma=gamma,

            xi1=xi1,

            xi2=xi2,

            nphi=nphi

        )


        if (not np.all(np.isfinite(y_mod))) or (y_mod.shape != y_exp.
           shape):

            return np.ones_like(y_exp) * 1e6


        return (y_mod - y_exp) / sigma


    if x0 is None:

        # initial guesses: eta=0.4, p1=0.3, p2=0.3

        x0 = list(map(logit, [0.4, 0.3, 0.3]))


    res = least_squares(

        resid, x0,

        loss="soft_l1",

        f_scale=0.03,

        max_nfev=20000,

        xtol=1e-10,

```

```
        ftol=1e-10,

        gtol=1e-10

    )



    eta_fit, p1_fit, p2_fit = map(inv_logit, res.x)



    y_fit = theoretical_probabilities_fit(

        r_exp,

        eta_fit, p1_fit, p2_fit,

        A1n, A2n, An_loss, UBS1, n,

        gamma=gamma,

        xi1=xi1,

        xi2=xi2,

        nphi=nphi

    )



    resid_vals = (y_exp - y_fit) / sigma

    chi2_val = float(np.sum(resid_vals**2))

    dof = y_exp.size - len(res.x)

    chi2_red = chi2_val / max(dof, 1)



    return {

        "params": np.array([eta_fit, p1_fit, p2_fit, gamma, xi1, xi2])
           ,

        "param_names": ["eta", "p1", "p2", "gamma", "xi1", "xi2"],

```

```
        "y_fit": y_fit,

        "chi2": chi2_val,

        "chi2_red": chi2_red,

        "dof": dof,

        "success": res.success,

        "message": res.message,

        "res": res,

    }




## Fitting while accounting for Higher-Order Terms, Decoherence, Indistinguishability on the first beamsplitter, and Mode Mismatch on the second beamplitter.


# In[ ]:




import numpy as np

from scipy.optimize import least_squares




# ========== CHI-SQUARED WRAPPER ============================================

#
```

```
4560
4561
4562
4563 def HOM_model_chi2(
4564
4565     r, eta, p1, p2, mu2,
4566
4567     exp_P11, exp_P02, exp_P20,
4568
4569     err_P11, err_P02, err_P20,
4570
4571     *,
4572
4573     xi1=0.997,
4574
4575     gamma=0.933,
4576
4577     nphi=8
4578
4579 ):
4580
4581     """
4582
4583     Computes  and reduced  for a set of HOM model parameters.
4584
4585     Returns:
4586
4587         - model probabilities (P11, P02, P20)
4588
4589         - chi, chi_red, dof
4590
4591         - residual vector
4592
4593         - flattened model/exp/sigma arrays
4594
4595     """
4596
4597
4598
4599     # Run the optical model
4600
4601     P11, P02, P20 = HOM_model_unweighted(
4602
4603         r, eta, p1, p2, mu2,
4604
4605         xi1=xi1,
4606
4607         gamma=gamma,
```

```
        nphi=nphi
    )


    # Flatten
    y_model = np.concatenate([P11, P02, P20])
    y_exp   = np.concatenate([exp_P11, exp_P02, exp_P20])
    sigma   = np.concatenate([err_P11, err_P02, err_P20])


    sigma = np.where(sigma <= 1e-12, 1e-12, sigma)


    # Compute
    residuals = (y_model - y_exp) / sigma
    chi2 = np.sum(residuals**2)


    # Degrees of freedom
    k = 4  # eta, p1, p2, mu2
    dof = len(y_exp) - k
    chi2_red = chi2 / max(dof, 1)


    return {
        "P11": P11,
        "P02": P02,
        "P20": P20,
        "chi2": chi2,
```

```
        "chi2_red": chi2_red,

        "dof": dof,

        "residuals": residuals,

        "y_model": y_model,

        "y_exp": y_exp,

        "sigma": sigma

    }









#
    ================================================================================


# ========== ROBUST FITTING (soft L1)
    ========================================


#
    ================================================================================



def fit_eta_p1_p2_mu2(

    r_exp,

    exp_P11, exp_P02, exp_P20,

    err_P11, err_P02, err_P20,

    *,

    xi1=0.997,

    gamma=0.933,

    nphi=8,

```

```
    p0=(0.4, 0.3, 0.3, 0.1)  # initial guess: (eta, p1, p2, mu2)

):

    """

    Robust nonlinear fitting of:

        (eta, p1, p2, mu2)

    using the HOM model with mode mismatch.


    Uses soft-L1 robust loss.

    Returns full fit diagnostics including  and reduced .

    """


    # Flatten experimental arrays

    y_exp = np.concatenate([exp_P11, exp_P02, exp_P20])

    sigma = np.concatenate([err_P11, err_P02, err_P20])

    sigma = np.where(sigma <= 1e-12, 1e-12, sigma)


    # --- Parameter transforms (01 logistic) ---

    def logit(p):

        p = np.clip(p, 1e-9, 1 - 1e-9)

        return np.log(p / (1 - p))


    def inv_logit(x):

        return 1 / (1 + np.exp(-x))


    def unpack(raw):
```

```
        eta  = inv_logit(raw[0])

        p1   = inv_logit(raw[1])

        p2   = inv_logit(raw[2])

        mu2  = inv_logit(raw[3])

        return eta, p1, p2, mu2


    # --- Initial guess ---

    x0 = np.array([

        logit(p0[0]),

        logit(p0[1]),

        logit(p0[2]),

        logit(p0[3])

    ])


    # --- Residual function ---

    def residuals(raw):

        eta, p1, p2, mu2 = unpack(raw)


        # Run the optical simulation

        P11, P02, P20 = HOM_model_unweighted(

            r_exp, eta, p1, p2, mu2,

            xi1=xi1,

            gamma=gamma,

            nphi=nphi
```

```
        )


        y_model = np.concatenate([P11, P02, P20])


        # Safety
        if not np.all(np.isfinite(y_model)):
            return np.ones_like(y_exp) * 1e6


        return (y_model - y_exp) / sigma


    # --- Run nonlinear robust least squares ---
    sol = least_squares(
        residuals,
        x0,
        loss="soft_l1",
        f_scale=0.03,
        max_nfev=20000,
        xtol=1e-12,
        ftol=1e-12,
        gtol=1e-12
    )


    # --- Convert fitted parameters ---
    eta, p1, p2, mu2 = unpack(sol.x)
```

```
    # --- Compute  at optimum ---
    chi = HOM_model_chi2(
        r_exp,
        eta, p1, p2, mu2,
        exp_P11, exp_P02, exp_P20,
        err_P11, err_P02, err_P20,
        xi1=xi1,
        gamma=gamma,
        nphi=nphi
    )


    return {
        "eta": eta,
        "p1": p1,
        "p2": p2,
        "mu2": mu2,
        "raw_params": sol.x,


        # Fit statistics
        "chi2": chi["chi2"],
        "chi2_red": chi["chi2_red"],
        "dof": chi["dof"],
        "residuals": chi["residuals"],
```

```
        # Model curves

        "P11_fit": chi["P11"],

        "P02_fit": chi["P02"],

        "P20_fit": chi["P20"],


        "success": sol.success,

        "message": sol.message

    }



# ## MLE Hybrid Fit


# In[ ]:



import numpy as np

from scipy.optimize import minimize, differential_evolution


# ================================================================================

# Logistic transforms

# ================================================================================

def inv_logit(x):

    return 1 / (1 + np.exp(-x))
```

```
4942
4943
4944
4945 def logit(p):
4946
4947     p = np.clip(p, 1e-12, 1 - 1e-12)
4948
4949     return np.log(p / (1 - p))
4950
4951
4952
4953 #
    ==========================================================================
4954
4955 # Multinomial NLL using HOM_model_unweighted with parameter caps
4956
4957 #
    ==========================================================================
4958
4959 def nll_multinomial(params_raw,
4960
4961                     r_exp, c11, c02, c20,
4962
4963                     eta_max, p1_max, p2_max,
4964
4965                     mu2_min, mu2_max):
4966
4967     """
4968
4969     Negative log-likelihood for multinomial counts using the full
        optical model.
4970
4971     Parameters are logistic-mapped into (0, param_max), except mu2
        which is
4972
4973     mapped into [mu2_min, mu2_max].
4974
4975     """
4976
4977
4978
4979     # ---------- Raw  physical mapping ----------
4980
4981     eta = eta_max * inv_logit(params_raw[0])
4982
4983     p1  = p1_max  * inv_logit(params_raw[1])
4984
```

```
    p2  = p2_max  * inv_logit(params_raw[2])


    # map to [mu2_min, mu2_max]
    mu2_frac = inv_logit(params_raw[3])                # in (0,1)
    mu2      = mu2_min + (mu2_max - mu2_min) * mu2_frac


    # ---------- Optical model prediction ----------
    P11_th, P02_th, P20_th = HOM_model_unweighted(r_exp, eta, p1, p2,
       mu2)


    # Normalize (safety)
    eps = 1e-14
    P11_th = np.clip(P11_th, eps, 1)
    P02_th = np.clip(P02_th, eps, 1)
    P20_th = np.clip(P20_th, eps, 1)
    norm = P11_th + P02_th + P20_th
    P11_th /= norm
    P02_th /= norm
    P20_th /= norm


    # ---------- Log-likelihood ----------
    ll = c11 * np.log(P11_th) + c02 * np.log(P02_th) + c20 * np.log(
       P20_th)
    return -np.sum(ll)
```

```
5032
5033 # ============================================================================
5034
5035 #  and reduced  calculation
5036
5037 # ============================================================================
5038
5039 def chi2_stats(P11_th, P02_th, P20_th, exp_P11, exp_P02, exp_P20,
     err_P11, err_P02, err_P20):
5040
5041     """
5042
5043     Compute  and reduced  after a final MLE fit.
5044
5045     """
5046
5047     chi2  = np.sum(((exp_P11 - P11_th)/err_P11)**2)
5048
5049     chi2 += np.sum(((exp_P02 - P02_th)/err_P02)**2)
5050
5051     chi2 += np.sum(((exp_P20 - P20_th)/err_P20)**2)
5052
5053
5054
5055     dof = exp_P11.size*3 - 4   # 4 fitted parameters
5056
5057     chi2_red = chi2 / max(dof, 1)
5058
5059
5060
5061     return chi2, chi2_red, dof
5062
5063
5064
5065
5066
5067 # ============================================================================
5068
5069 # Hybrid Global (DE) + Local (L-BFGS) MLE fit
5070
5071 # ============================================================================
```

```
5072
5073 def fit_HOM_MLE_hybrid(
5074
5075     r_exp, c11, c02, c20,
5076
5077     *,
5078
5079     # Physical parameter caps
5080
5081     eta_max=0.3,
5082
5083     p1_max=0.3,
5084
5085     p2_max=0.3,
5086
5087     mu2_min=0.8,      #  NEW lower bound (set to whatever you like)
5088
5089     mu2_max=1.0,      # upper bound
5090
5091     # Initial guess in PHYSICAL space
5092
5093     p0_phys=(0.05, 0.05, 0.05, 0.95),
5094
5095     verbose=True
5096
5097 ):
5098
5099     """
5100
5101     Fits (eta, p1, p2, mu2) using logistic parameterization + physical
         caps,
5102
5103     with mu2 constrained to [mu2_min, mu2_max].
5104
5105     """
5106
5107
5108
5109     # ---------- Physical initial guess  raw logistic space ----------
5110
5111     eta0, p10, p20, mu20 = p0_phys
5112
5113
5114
5115     # guard against out-of-range initials
5116
5117     mu20 = np.clip(mu20, mu2_min + 1e-6, mu2_max - 1e-6)
5118
5119
```

```
    eta_frac  = eta0  / eta_max

    p1_frac   = p10   / p1_max

    p2_frac   = p20   / p2_max

    mu2_frac0 = (mu20 - mu2_min) / (mu2_max - mu2_min)


    p0_raw = np.array([

        logit(eta_frac),

        logit(p1_frac),

        logit(p2_frac),

        logit(mu2_frac0),

    ])


    # ---------- Objective in raw space ----------

    def obj_raw(raw_params):

        return nll_multinomial(

            raw_params,

            r_exp, c11, c02, c20,

            eta_max, p1_max, p2_max,

            mu2_min, mu2_max

        )


    if verbose:

        print("\n Running differential evolution global search...\n")
```

```
    raw_bounds = [(-10, 10)] * 4


    # ---------- Global search ----------
    result_global = differential_evolution(
        obj_raw,
        bounds=raw_bounds,
        polish=False,
        updating='deferred'
    )


    raw_best = result_global.x


    if verbose:
        print("Global optimum (raw parameters):", raw_best)


    # ---------- Local refinement ----------
    result_local = minimize(
        obj_raw,
        x0=raw_best,
        method="L-BFGS-B",
        bounds=raw_bounds
    )


    raw_final = result_local.x

```

```
    # ---------- Map back to physical parameters ----------

    eta_fit = eta_max * inv_logit(raw_final[0])

    p1_fit  = p1_max  * inv_logit(raw_final[1])

    p2_fit  = p2_max  * inv_logit(raw_final[2])

    mu2_frac_fit = inv_logit(raw_final[3])

    mu2_fit = mu2_min + (mu2_max - mu2_min) * mu2_frac_fit



    if verbose:

        print("\n===== Final MLE Fit Results (with mu2  [%.3f, %.3f]) ====="

            % (mu2_min, mu2_max))

        print(f"   = {eta_fit:.6f}")

        print(f"p1  = {p1_fit:.6f}")

        print(f"p2  = {p2_fit:.6f}")

        print(f"2  = {mu2_fit:.6f}")

        print(f"NLL = {result_local.fun:.6f}")

        print("============================================================\n")



    return {

        "raw_params": raw_final,

        "params": np.array([eta_fit, p1_fit, p2_fit, mu2_fit]),

        "NLL": result_local.fun,

        "result_local": result_local,

    }
```

```
5264
5265
5266
5267
5268
5269 # In[ ]:
```

Now it's time for the tequila.

Sebastian Andres Malewicz